

First-order finite-Larmor-radius effects on magnetic tearing  
and relaxation in pinch configurations

by  
Jacob King

A dissertation submitted in partial fulfillment  
of the requirements for the degree of

Doctor of Philosophy

(Physics)

at the

UNIVERSITY OF WISCONSIN-MADISON

2011

### Abstract

Drift and Hall effects on magnetic tearing, island evolution, and relaxation in pinch configurations are investigated using a non-reduced fluid model with first-order FLR effects. When the tearing layer width is smaller than the ion sound gyroradius ( $\rho_s$ ), cylindrical computations show that kinetic-Alfvén-wave (KAW) physics increases linear growth rates relative to resistive MHD. An unexpected result with a uniform pressure profile is a drift effect that reduces the growth rate at intermediate- $\rho_s$  values. This drift is present only with warm-ions FLR modeling, and analytics show that it arises from  $\nabla B$  and poloidal curvature represented in the Braginskii gyroviscous stress. While the flux-surface average contribution from these drifts are small relative to diamagnetic drifts in tokamaks, they are dominant in pinch profiles. Growth rates and rotation frequencies are derived for a heuristic dispersion relation using the ion-drift effects and a resistive-MHD Ohm's law. This dispersion relation is in agreement with numerical results in the intermediate drift regime before KAW effects are significant. Nonlinear single-helicity computations with experimentally-relevant  $\rho_s$  values show that the warm-ion gyroviscous effects reduce saturated island widths. In contrast to diamagnetic drift-tearing, the  $\nabla B$  and poloidal curvature profiles are largely unaffected by magnetic islands. The result suggests an increasing tendency to obtain quasi-single helicity in reversed-field pinches with increasing ion temperature. [King et al., Phys. Pl. 2011]

Multihelicity simulations show that mode amplitudes are suppressed during warm-ion computations through the influence of ion gyroviscosity as in our single-helicity results. Both MHD and Hall dynamos contribute to relaxation events. The presence of Hall dynamo implies a fluctuation-induced Maxwell stress, and the simulation results show net transport of parallel momentum. The magnitude of force densities from the Maxwell stress and a competing Reynolds stress, and changes in the parallel flow profile are within a factor of 2-3 of measurements [Kuritsyn et al., Phys. Pl. 2009] during a relaxation event in the Madison Symmetric Torus.

## Acknowledgements

I would like to thank my advisor, Carl Sovinec, as without his scientific, computational, editorial and professional guidance this thesis would not be possible. I owe sincere gratitude to Vladimir Mirnov, with whom I spent countless hours discussing tearing and RFP theory. I am obliged to many who supported me by simply asking the right questions: John Sarff, Dalton Schnack, Chris Hegna, James Callen, Karsten McCollam and Ping Zhu.

Without my wife, Kirsten, it is inconceivable to think I could survive the many long days of writing; her patience, understanding and logistical support have been invaluable. I am grateful to my parents, Robert and Donna, and brother, Michael, who have fostered my interest in natural science and along with Kirsten have provided love and moral support throughout graduate school.

# Contents

<b>I</b>	<b>Introduction</b>	<b>1</b>
<b>1</b>	<b>Some basic plasma concepts</b>	<b>2</b>
1.1	Nuclear fusion . . . . .	2
1.2	Guiding-center drifts . . . . .	4
1.3	Rational magnetic flux surfaces . . . . .	5
1.4	Toroidal confinement devices . . . . .	7
<b>2</b>	<b>Fluid modeling</b>	<b>14</b>
2.1	The kinetic description . . . . .	14
2.2	Moment equations . . . . .	15
2.3	Closure relations . . . . .	16
2.4	Two-fluid formulation . . . . .	18
2.5	Relation to resistive, ideal MHD . . . . .	20
<b>3</b>	<b>Reversed-field pinches</b>	<b>21</b>
3.1	Edge- $B_T$ reversal and dynamo emfs . . . . .	22
3.2	Relaxation theory . . . . .	23
3.3	RFP experimental measurements relevant to two-fluid dynamics . . . . .	26
<b>4</b>	<b>Magnetic reconnection with resistive MHD</b>	<b>30</b>
4.1	Boundary layer formulation . . . . .	31
4.2	Small- $\Delta'$ current-driven tearing modes . . . . .	34
4.3	Finite- $\beta$ effects . . . . .	40
4.4	Notes and extensions . . . . .	40
<b>5</b>	<b>First-order FLR effects on the tearing mode</b>	<b>41</b>
5.1	Diamagnetic-drift tearing . . . . .	42
5.2	Kinetic-Alfvén-wave mediated regime . . . . .	43
<b>6</b>	<b>Nonlinear growth and saturation of the tearing mode</b>	<b>49</b>
6.1	Rutherford theory . . . . .	49

6.2	FLR effects . . . . .	51
<b>7</b>	<b>Thesis</b>	<b>53</b>
<b>II</b>	<b>Methods and parameters</b>	<b>55</b>
<b>8</b>	<b>The NIMROD code</b>	<b>55</b>
8.1	Spatial discretization . . . . .	55
8.2	Temporal discretization . . . . .	57
<b>9</b>	<b>Geometric approximations and equilibria</b>	<b>59</b>
9.1	Slab . . . . .	60
9.2	Cylindrical . . . . .	61
9.3	Boundary conditions . . . . .	64
9.4	Model parameter space . . . . .	64
<b>III</b>	<b>Linear tearing modes</b>	<b>67</b>
<b>10</b>	<b>Slab geometry</b>	<b>67</b>
10.1	Benchmark to analytic theory . . . . .	67
10.2	Eigenmode structure . . . . .	68
<b>11</b>	<b>Cylindrical dispersion relation</b>	<b>71</b>
11.1	Computational result . . . . .	71
11.2	Heuristic reduced gyroviscous model . . . . .	73
11.3	Comparison . . . . .	76
<b>12</b>	<b>Cylindrical structure</b>	<b>78</b>
12.1	Eigenfunction components . . . . .	78
12.2	Dynamo contribution to the electric field inferred from the linear mode . . . . .	82
<b>13</b>	<b>Discussion</b>	<b>83</b>
<b>IV</b>	<b>Nonlinear single-helicity tearing</b>	<b>85</b>

<b>14 Island structure in a cylinder</b>	<b>85</b>
14.1 Helical projection method . . . . .	87
14.2 Flow structures . . . . .	88
<b>15 Cylindrical dynamo emfs and force balance</b>	<b>91</b>
15.1 Dynamo emfs at saturation . . . . .	91
15.2 Island force balance . . . . .	93
<b>16 Discussion</b>	<b>95</b>
<b>V Multi-helicity dynamics</b>	<b>96</b>
<b>17 Mode amplitudes</b>	<b>99</b>
17.1 Experimental comparison . . . . .	99
17.2 Equilibria and island force balance . . . . .	99
17.3 $m = 0$ magnetic energy drive . . . . .	103
<b>18 Electric-field dynamics</b>	<b>106</b>
18.1 Dynamo emfs and profile modification . . . . .	106
18.2 Experimental comparison . . . . .	108
<b>19 Momentum transport</b>	<b>112</b>
19.1 Flow profiles and mean forces . . . . .	112
19.2 Experimental comparison . . . . .	115
<b>20 Discussion</b>	<b>116</b>
<b>VI Conclusions</b>	<b>118</b>
<b>21 Summary of results</b>	<b>118</b>
21.1 Drift effects on the linear tearing mode . . . . .	118
21.2 Reduction of the saturated island width through FLR effects . . . . .	119
21.3 Multi-helicity results . . . . .	119
<b>A Formulary</b>	<b>121</b>

<b>B</b>	<b>Definitions of notation</b>	<b>123</b>
<b>C</b>	<b>Model equations</b>	<b>124</b>
<b>D</b>	<b>Parallel electric field assumptions</b>	<b>125</b>
<b>E</b>	<b>Conservation laws</b>	<b>126</b>
E.1	Momentum . . . . .	126
E.2	Magnetic energy density . . . . .	126
E.3	Kinetic energy density . . . . .	126
E.4	Internal energy density . . . . .	127
<b>F</b>	<b>Gyroviscous Mathematica code</b>	<b>129</b>
<b>G</b>	<b>Dynamo emf component derivation</b>	<b>135</b>
<b>H</b>	<b>Supplemental multi-helicity plots</b>	<b>138</b>
<b>I</b>	<b>References</b>	<b>140</b>

## Part I

# Introduction

Computational plasma physics creates and implements models which are able to provide insight into experimental plasma-confinement devices that may be difficult to observe with direct measurements. Ultimately, a goal is to develop predictive capability in order to determine device characteristics that could guide design. Computations are routinely used to reconstruct plasma equilibrium states, and to characterize these states by identifying the properties of potentially unstable modes, to examine the nature of turbulent fluctuations, and to study the nonlinear evolution. However, computation of the full plasma dynamics by simply tracking the motion of each particle in self-consistent electromagnetic fields is impractical given the enormous number of particles, and thus degrees of freedom. All models must apply some simplifying assumptions for the problem to be computationally or analytically tractable. Understanding these simplified models is essential for confidence in predictive computations, and effort is being made to compare the results of plasma computations with experimental measurements to validate a given model as reproducing the underlying physics. Equally important is ensuring that a given code faithfully reproduces a model, and this is verified by comparing codes relative to each other or specific cases that can be treated analytically.

Initially the path to a fusion reactor appeared straightforward, however most concepts are subject to plasma instabilities and turbulence which degrade the confinement time and/or disrupt the discharge. Advances in our understanding of basic high-temperature plasma science directly improves our engineering capabilities for a plasma reactor. They also allow for new understanding of astrophysical phenomena. High-temperature magnetized plasma models are applicable on many astrophysical scales, for example, stellar modeling on a small scale, the dynamics of the solar wind on an intermediate scale and astrophysical jets on a large scale. Although some experimental devices are built to study basic plasma science, and some to study astrophysical phenomena, many plasma devices are constructed with fusion energy as an ultimate goal. Predictive simulation could provide a cost-efficient path to the construction of plasma reactor using nuclear fusion, as it may partially circumvent the construction of multiple experimental test reactor concepts.

Although comprehensive predictive simulation may be considered the major goal of computation, the achievement of such simulation is in the future, and the journey towards it can produce fascinating new results. The work presented here is part of this journey. While both the plasma device, the reversed-field pinch (RFP), and model, a magnetohydrodynamic (MHD) fluid model with effects first-order in Larmor radius

(or particle gyroradius), have been studied for almost 50 years, we are still able to find new, experimentally relevant physics. Before a detailed statement of our thesis in Sec. 7, we will review the bare minimum of necessary fundamental plasma physics. The concepts presented are more fully treated in textbooks, for example Refs. [1, 2, 3].

We have three new results from this work, covered in Parts III-V, respectively. For the first, we use a two-fluid model to show the growth of the tearing mode in the RFP is reduced by a drift response related to the gradient of the magnetic field and poloidal curvature when the drift frequency is on the order of the growth rate of the mode. This effect is manifest through contributions from ion gyroviscosity in the momentum equation, and is relevant to pinch configurations but not tokamaks as the latter have relatively small field gradients and poloidal curvature. (Additionally, the drift from the significant toroidal curvature in tokamaks is not aligned with the resonant flux surfaces of the tearing modes.) For our second result we show that the saturated width of an island formed by tearing activity is reduced by contributions from the ion gyroviscous force when the ion gyroradius is significant. This reduction in the saturated width occurs for parameters that are experimentally relevant to modern RFPs. This effect is present in our highly nonlinear computations with multiple modes which approximate the dynamic activity of RFP operation where we find the mode amplitudes with the two-fluid model are reduced relative to single-fluid MHD, and compare well with experimental measurements. Our final result examines the modification of the mean fields by the tearing fluctuations; with two-fluid modeling both the MHD and Hall dynamo emfs act to flatten the current profile during a relaxation event. There is a Maxwell stress associated with the Hall dynamo. The momentum transport is largely determined by the interplay between the Maxwell stress and a self-consistently-modeled nonlinear Reynolds stress. We find these stresses generally oppose as a function of radius, and although the computation exhibits momentum transport, it would be much larger if the stresses did not nearly cancel. The opposing nature and magnitude of these stresses, and associated momentum transport has been experimentally measured. These measurements qualitatively agree with our two-fluid computations, and these effects are not present in previous single-fluid modeling.

## 1 Some basic plasma concepts

### 1.1 Nuclear fusion

Nuclear fusion is achieved when two nuclei overcome the Coulomb barrier of their electric repulsion and fuse to produce a heavier nuclei. The easiest reaction, in terms of required temperatures and densities, being

considered for fusion reactor purposes is the fusion of the hydrogen isotopes deuterium and tritium. This process creates a fast neutron and an alpha particle and releases  $17.7\text{MeV}$  of energy:



The cross section for this reaction to occur requires a high plasma temperature, and peaks around  $25\text{keV}$  or  $3 \times 10^8\text{K}$ , in order to overcome the Coulomb barrier. Lawson determined that the triple product  $n_e\tau_E T \geq 10^{21}\text{keV s/m}^3$  is sufficient for the D-T reaction to ensure the thermal energy gained from the reactions sustains the plasma temperature without energy input (this condition is known as ignition) [4]. Here  $n_e$  is the electron density,  $T$  is the temperature, and  $\tau_E$  is the energy confinement time defined as the ratio of the energy stored in the plasma divided by the energy loss rate.

In general, fusion plasma confinement concepts may be categorized as either inertial or magnetic confinement. Inertial confinement involves the isotropic compression and heating of the fusion products to extremely high densities and temperatures to achieve ignition. Modeling of inertial confinement fusion must be able accurately determine the physics of the propagating shocks, or steep gradients in the density, temperature and field quantities, that result from this scheme. This process is typically very fast and the target fuel must be consumed quickly to get a fusion yield before instabilities associated with the steep gradients degrade the confinement. In principle, it must be repeated in short regular intervals to get a steady state reactor.

Alternatively magnetic confinement relies on the magnetic field to trap ionized particles. A charged particle moving perpendicular to a magnetic field is subject to a Lorentz force which causes it to orbit the magnetic field line. This basic concept is used in magnetic confinement to confine the plasma with a longer  $\tau_E$  but lower density than compared to inertial confinement. Magnetic confinement models typically do not need to resolve shocks, but must determine the plasma properties on longer time scales and must deal with highly anisotropic systems - particles are well confined perpendicular to the magnetic field, but their motion is unconstrained parallel to the magnetic field. Magnetic confinement devices can be further categorized as toroidal or non-toroidal. Examples of non-toroidal devices are mirror and field-reversed configurations. Toroidal confinement is characterized by magnetic-field lines that wrap back upon themselves and never leave a confining surface. The only surface which can bound a well-behaved divergence-free vector field must be topologically toroidal [5]. These configurations prevent the particles from escaping through the unconfined motion parallel to field lines.

## 1.2 Guiding-center drifts

Charged particles orbit a magnetic field with gyro-frequency  $\omega_{c\alpha} = q_\alpha B/m_\alpha$  at a radius  $\rho_\alpha = v_{\perp\alpha}/\omega_{c\alpha}$  where  $\alpha = e/i$  indicates electron or ion species, respectively,  $q_\alpha$  is the particle charge,  $B$  is the magnetic field magnitude,  $m_\alpha$  is a species mass and  $v_{\perp}$  is the particle velocity perpendicular to the magnetic field. A particle with a non-zero perpendicular velocity orbits a magnetic field-line with a finite gyroradius (or finite-Larmor radius, FLR) given by  $\rho_\alpha$ . Note that  $\rho_\alpha/L \ll 1$  over at least part of the configuration, where  $L$  is a characteristic device length scale, must be satisfied by the definition of magnetic confinement.

We now consider a particle in the presence of both a magnetic field,  $\mathbf{B}$ , and electric field  $\mathbf{E}$ . For confinement considerations, we are interested in the perpendicular motion, relative to  $\mathbf{B}$ . As the fast gyro-motion is unimportant to confinement, what we really want to know is the average drift, or the velocity of the particle guiding center, defined at the axis of the gyro-rotation. As shown in Chap. 2 of Ref. [1], using  $\rho_\alpha/L$  as a small ordering parameter, the zeroth-order guiding-center drift (the limit of vanishing  $\rho_\alpha$ ) is the  $\mathbf{E} \times \mathbf{B}$  drift,

$$\mathbf{v}_{E \times B} = \frac{\mathbf{E} \times \mathbf{B}}{B^2} \quad (1.2)$$

and the first-order drifts ( $\sim \rho_\alpha/L$ ) are the  $\nabla B$  and inertial drifts:

$$\mathbf{v}_{\nabla B} = \frac{m_\alpha v_{\perp\alpha}^2}{2q_\alpha B^2} \hat{\mathbf{b}} \times \nabla B \quad (1.3)$$

$$\mathbf{v}_{inertial} = \frac{m_\alpha}{q_\alpha B^2} \mathbf{B} \times \frac{d\mathbf{v}_0}{dt} . \quad (1.4)$$

We define  $\hat{\mathbf{b}} = \mathbf{B}/B$  as the magnetic-field unit vector and  $\mathbf{v}_0$  is the zeroth-order drift,  $\mathbf{v}_0 = v_{\parallel} \hat{\mathbf{b}} + \mathbf{v}_{E \times B}$ , where  $v_{\parallel}$  is the unconstrained motion along the field line. The inertial drift can be decomposed into several terms, an important term for our purposes is the curvature drift,

$$\mathbf{v}_\kappa = \frac{m_\alpha v_{\parallel}^2}{q_\alpha B^2} \mathbf{B} \times \kappa \quad (1.5)$$

where  $v_{\parallel\alpha}$  is a specie's parallel velocity and  $\kappa = \hat{\mathbf{b}} \cdot \nabla \hat{\mathbf{b}}$  is the curvature vector. The first-order drifts are proportional to  $|q_\alpha|$ , unlike the  $\mathbf{E} \times \mathbf{B}$  drift. Thus the  $\nabla B$  and curvature drifts will cause relative ion and electron motion, unlike the  $\mathbf{E} \times \mathbf{B}$  drift where the motion is in the same direction.

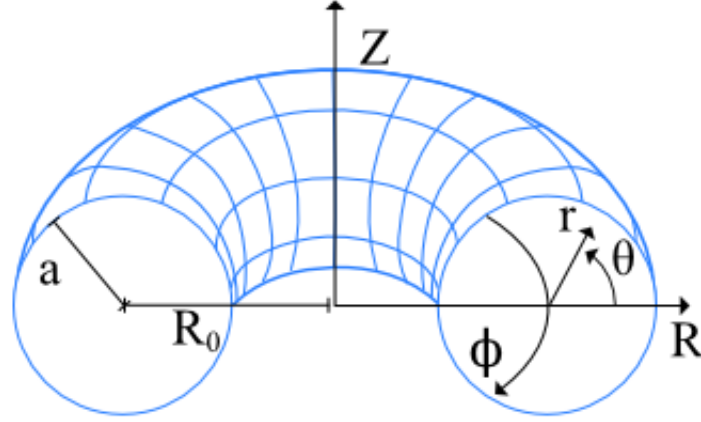


Figure 1: Illustration of toroidal coordinates,  $R$ ,  $Z$ , and approximate cylindrical coordinates,  $r, \chi$ , of the poloidal cross-section (right-side) for an axisymmetric torus with a circular cross-section. The minor radius ( $a$ ) and major radius ( $R_0$ ) are labeled on the left-side.

### 1.3 Rational magnetic flux surfaces

It is clear from Eqns. (1.3) and (1.5) that the first-order drift motion is determined by the magnetic field configuration. We may describe this configuration in terms of toroidal coordinates,  $R$ ,  $Z$ , and approximate cylindrical coordinates,  $r, \chi$ , are illustrated in Figure 1. Flux surfaces are defined such that an unperturbed, axisymmetric magnetic field line lies on the surface. The poloidal flux is defined as

$$\Psi_P = \int_{S_P} \mathbf{B} \cdot d\mathbf{S} \quad (1.6)$$

where  $S_P$  is a ring-like surface bounded by the flux surface on one edge and the magnetic axis on the other edge with its normal vector in the poloidal direction. The magnetic differential equation  $\mathbf{B} \cdot \nabla \Psi_P = 0$  is satisfied simply by the definition of  $\Psi_P$ . Thus the variation of  $\Psi_P$  is perpendicular to  $\mathbf{B}$  and constant on a flux surface, and  $\Psi_P$  is *flux-surface quantity*. As  $\Psi_P$  increases monotonically as a function of flux surface for the configurations discussed here, we may label each flux surface by a unique value of  $\Psi_P$ . In other words,  $\Psi_P$  is also a flux-surface label. Along the same lines, the toroidal flux is defined as

$$\Psi_T = \int_{S_T} \mathbf{B} \cdot d\mathbf{S} \quad (1.7)$$

where  $S_T$  is a disk-like surface bounded by a flux surface with normal vector in the toroidal direction. We

note  $\Psi_T$  is also a flux surface quantity, however as we will discuss, it is poor flux surface label for the RFP as it is not monotonic for this configuration.

An essential quantity in plasma stability analysis is the safety factor,  $q(\Psi_P)$ , defined by

$$q(\Psi_P) \equiv \frac{d\Psi_T}{d\Psi_P}. \quad (1.8)$$

Physically the safety factor is the average number of times a field-line orbits about the center of the torus divided by the number of times it orbits about the magnetic axis before closing on itself. If  $q$  is irrational the field-line never closes on itself, and passes arbitrarily close to every point of the magnetic flux surface. For rational surfaces, defined by where  $q$  is rational, we may write  $q = -m/n$  where  $m$  is the number of toroidal and  $n$  is the number of poloidal transits required for a field-line to close on itself. If  $q > 0$ ,  $\Psi_T$  increases as a function of flux surface, and if  $q < 0$ ,  $\Psi_T$  decreases as a function of flux surface. The reversed-field pinch is characterized by the reversal of  $B_T$  at the wall relative to the core, thus we may expect  $q > 0$  in the core and  $q < 0$  at the edge. The flux surface where  $q = 0$  is known as the *reversal surface*, and contains purely poloidal magnetic field. Additionally, as  $\Psi_T$  is not monotonic as a function of flux surface, it does not constitute a good flux label for the RFP.

By using a straight cylinder with coordinates  $r\theta z$  we approximate a toroidal configuration, and the physical conclusions of the next two paragraphs are generalizable to toroidal cases. The cylindrical approximation is reasonable when poloidal localization and toroidal curvature effects are small, conditions to be discussed in Sec. 1.4. In this approximation the torus is ‘unwrapped’ and the toroidal direction then becomes the axial  $\hat{z}$  direction with length  $2\pi R_0$ , the poloidal direction is  $\hat{\theta}$ , and the end-caps are periodic. Assuming axisymmetric fields which allow us to use the radius as a flux label, we may simplify the safety factor as

$$q(r) = \frac{\mathbf{B}_z \cdot d\mathbf{S}_T}{\mathbf{B}_\theta \cdot d\mathbf{S}_P} = \frac{B_z(r) d(\pi r^2)}{B_\theta(r) d(2\pi R_0 r)} = \frac{r B_z(r)}{R_0 B_\theta(r)}. \quad (1.9)$$

Next we consider a general magnetic differential equation,  $\mathbf{B} \cdot \nabla \tilde{f}(\mathbf{r}) = C(\mathbf{r})$ , where  $\tilde{f}(\mathbf{r})$  is a cylindrical perturbation and  $C(\mathbf{r})$  is a known function. As we shall see, equations of this form are common with a fluid plasma model. We are interested in solving for  $\tilde{f}(r)$ , and express it in a separation-of-variables form such that the spatial structure varies as  $\sim \tilde{f}(r) \exp(im\theta + inz/R_0) + c.c.$ . Thus the left-hand side (LHS) of  $\mathbf{B} \cdot \nabla \tilde{f}(\mathbf{r}) = C(\mathbf{r})$  becomes

$$\mathbf{B} \cdot \nabla \tilde{f}(\mathbf{r}) = \frac{B_\theta}{r} \frac{\partial \tilde{f}}{\partial \theta} + B_z \frac{\partial \tilde{f}}{\partial z} = \left( B_\theta \frac{im}{r} + B_z \frac{in}{R_0} \right) \tilde{f}(r). \quad (1.10)$$

The equation is singular, i.e.  $\tilde{f}(r_s)$  is undetermined, if  $B_\theta m/r_s + B_z n/R_0 = 0$ . We may rewrite this as  $rB_z/R_0B_\theta = -m/n$ , or  $q(r_s) = -m/n$ . Here  $r_s$  is defined as the resonant surface of the perturbation where  $\tilde{f}(r_s)$  is undetermined. In this sense, the amplitude of  $\tilde{f}(r_s)$  is arbitrary. The singularity is resolved when other, typically diffusive, terms with factors of  $\tilde{f}(r_s)$  are included in the model. As we shall see, the concept of resonance will be important for a class of instabilities in the RFP, tearing modes, which we will discuss at length throughout this document.

## 1.4 Toroidal confinement devices

Before discussing the RFP in detail, we will contrast it with two more-well-known toroidal-confinement devices, tokamaks and stellarators. By no means do we intend this as an exhaustive treatment of the latter devices. We begin by considering the magnetic field generated by a current from a solenoidal coil bent into a torus with major radius  $R_0$  and minor radius  $a$  as shown in Fig. 1. Using the steady-state Ampere's law, i.e. without displacement current,

$$\mu_0 \mathbf{J} = \nabla \times \mathbf{B} \quad (1.11)$$

the magnetic field distribution without a plasma is  $B_T = \mu_0 I_{coil}/2\pi R$ , where  $I_{coil}$  is the coil current,  $\mathbf{J}$  is the current density, and  $\mu_0$  is the vacuum permeability. Thus the magnetic-field magnitude on the inboard side of the torus ( $R < R_0$ ) is larger than the outboard, which creates a magnetic-field gradient pointing in the negative  $\hat{R}$ -direction. The  $\nabla B$  and curvature drifts, Eqns. (1.3) and (1.5), will be in the vertical  $\hat{Z}$ -direction for this 'vacuum' magnetic-field distribution, and charged particles confined by this field will drift into the wall on the top or bottom of the torus depending on the sign of their charge.

This configuration is uncharacteristic of confinement devices as  $q$  is infinite everywhere without poloidal field. With poloidal magnetic field and symmetry in the vertical  $\hat{Z}$  direction, the flux-surface average of drifts normal to the surface vanishes. For configurations with toroidal axisymmetry, poloidal field cannot be imposed with external coils and must be introduced by driving toroidal current in the plasma, typically with an inductive electric field. Another method is to abandon axisymmetric configurations, and use external coils to construct a fully 3D vacuum field. This field may be designed to minimize the particle drifts which result in the loss of confinement, along with other constraints not discussed here. The use of a fully 3D configuration to construct a finite- $q$  profile was first proposed by Spitzer in 1958, who called the concept a stellarator [6]. Internal plasma currents modify the vacuum magnetic configuration, for example stellarators with finite pressure gradients must account for Pfirsch-Schlüter currents. However, stellarator configurations

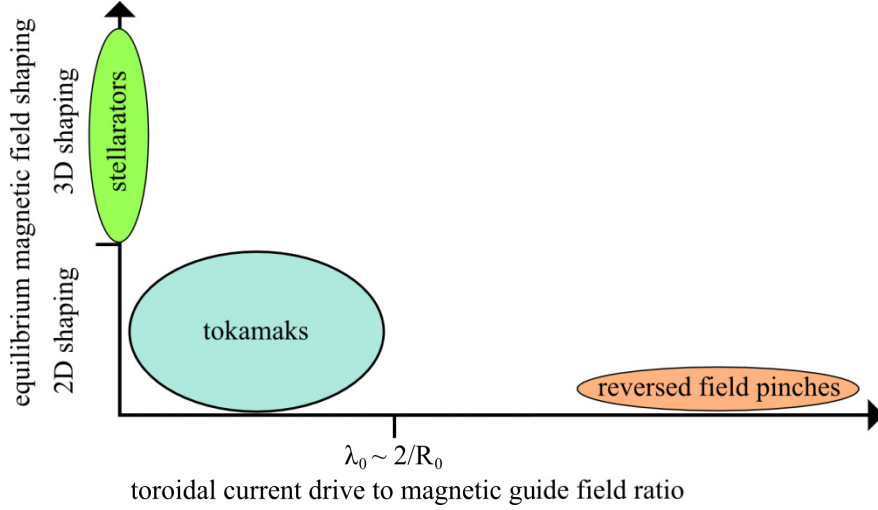


Figure 2: The spectrum of toroidal magnetic confinement devices, as they relate to magnetic-field shaping through external coils (vertical axis) and the ratio of net toroidal current to toroidal magnetic guide field (horizontal axis).

typically have no inductive electric field or associated inductively-driven current.

Returning to configurations with toroidal axisymmetry we distinguish configurations with small toroidal current to guide-field ratio, tokamaks, from pinches which have a large ratio. Tokamak devices are typically operated such that the  $q = 1$  surface is either close to the magnetic axis or not resonant in the plasma, in order to avoid the  $m = 1, n = 1$  kink instability. For a cylindrical  $q(r)$ , Eqn. (1.9), we note

$$\lim_r q(r) = q_0 = \frac{2B_z(0)}{R \int_0^R J_z(r) r dr} = \frac{2}{\phi(0) R} \quad (1.12)$$

where we have made use of Ampere's law and define the parallel current density as

$$\phi(r) = \frac{\int_0^r J_z(r') r' dr'}{B^2} \quad (1.13)$$

Thus tokamak operation uses  $\phi(0) \approx 2/R$ , and reversed-field pinches have  $\phi(0) > 2/R$ . Figure 2 illustrates the relation between stellarators, tokamaks, and RFP in terms of magnetic-field structure, and toroidal-current drive to guide-field ratio. As indicated in the figure and discussed further in the remainder of this section, tokamak equilibria have largely non-circular poloidal shaping in comparison to RFP equilibria.

We now turn to a discussion of toroidal 2D axisymmetric equilibria force balance based on

$$\mathbf{J} \times \mathbf{B} = \nabla p \quad (1.14)$$

where the force from pressure gradients is balanced by the Lorentz force from particles moving perpendicular to  $\mathbf{B}$ , which is a valid description if plasma flows and gyroradii are small. Since  $\mathbf{B} \cdot \nabla p = 0$ , pressure is a flux function,  $p(\Psi_P)$ . In an axisymmetric system we may express  $\mathbf{B}$  as

$$\mathbf{B} = \frac{\nabla \Psi_P}{R} \times \hat{\Phi} + B_\Phi \hat{\Phi} \quad (1.15)$$

and through Ampere's law,

$$\mu_0 \mathbf{J} = \frac{\nabla F}{R} \times \hat{\Phi} - \frac{\Delta^* \Psi_P}{R} \hat{\Phi} \quad (1.16)$$

where  $F(\Psi_P) = RB_\Phi$  and  $\Delta^* \equiv R^2 \nabla \cdot (R^{-2} \nabla)$ . (See Ref. [1], Chap. 3.9) In general, we may also write

$$\mu_0 \mathbf{J} = \lambda \mathbf{B} + \mu_0 \mathbf{J}_\perp \quad (1.17)$$

with  $\mathbf{J}_\perp$  determined from the crossing the force balance equation, Eqn. (1.14), with  $\mathbf{B}$ :

$$\mathbf{J}_\perp = \frac{p' \mathbf{B} \times \nabla \Psi_P}{B^2} \quad (1.18)$$

where the prime indicates differentiation with respect to  $\Psi_P$  and  $\nabla p = p' \nabla \Psi_P$ . Explicitly, the components of Eqn. (1.17) are

$$\Delta^* \Psi_P + \lambda F + (\nabla \Psi_P)^2 \frac{\mu_0 p'}{B^2} = 0 \quad (1.19)$$

and

$$F' = \lambda - F \frac{\mu_0 p'}{B^2} . \quad (1.20)$$

By eliminating  $\lambda$  from this set of equations we arrive at the well-known equation of axisymmetric toroidal force balance, the Grad-Shafranov equation [7, 8],

$$\Delta^* \Psi_P = -FF' - \mu_0 p' R^2 . \quad (1.21)$$

	$B_{\Phi}(0)$	$a\lambda(0)$	$\alpha$	$T_e(a)$	$T_e(0)$
(a) tokamak-like, force-free	$2T$	0.6	1.5	$100eV$	$100eV$
(b) tokamak-like	$2T$	0.6	1.5	$100eV$	$1keV$
(c) pinch-like, force-free	$0.4T$	3.9	3	$50eV$	$50eV$
(d) pinch-like	$0.4T$	3.9	3	$50eV$	$350eV$

Table 1: Input parameters to Eqns. 1.22 and 1.23 used to solve the Grad-Shafranov equation, Eqn. 1.21, for four cases (a)-(d) with  $T_e = T_i$ ,  $R_0 = 3$  and  $a = 1$ .

An equilibrium  $\Psi_P$  can be found after specifying  $F(\Psi_P)$  and  $p(\Psi_P)$ , typically motivated by experimental measurements. We will use this equation to illustrate some of the differences between tokamak-like and pinch-like toroidal equilibria.

Note for force-free configurations ( $p' = 0$ ) the parallel current profile is specified through  $F'$ , as expressed in Eqn. 1.20. To illustrate equilibrium conditions for tokamaks and RFPs, we specify  $F$  as an alpha-like model such that

$$F'(\psi) = \lambda(0) \left(1 - \psi^{-\alpha/2}\right) \quad (1.22)$$

where  $\psi$  is a normalized flux bounded by 0 (magnetic axis) and 1 (wall), and  $\lambda(0)$  is an input parameter which sets the parallel current on the magnetic axis if  $p'(0) = 0$ . The constant of integration,  $F_0$ , is used to specify  $F(0)$ . Additionally, we use a parabolic pressure profile

$$p(\psi) = p_0 + p_1 (1 - \psi^2) . \quad (1.23)$$

The four cases, listed in Table 1, then allow us to contrast and compare pinch and tokamak profiles.

Figures 3 and 4 show surfaces of constant  $\psi$ ,  $|B|$ ,  $\lambda$ ,  $B_{\Phi}$ ,  $B_{pol}$ , and  $T_e$  from solutions of the Grad-Shafranov equation with the NIMEQ code [9], for the cases listed in Table 1 assuming a constant density profile. Compared to the tokamak-like cases, (a) and (b), the pinch-like profiles, (c) and (d), have  $|B|$  surfaces which are roughly aligned with flux surfaces. Thus we expect the  $\nabla B$  and curvature drifts to be dominantly within a flux surface for the pinch cases, unlike the tokamak-like profiles where the  $|B|$  distribution is very similar to the vacuum field. In addition, the trapping of particles by the variation of  $|B|$  on a flux surface leads to important effects for tokamaks. We note that for the pinch this trapping will be smaller in comparison. From these considerations, the tokamak theory must include the full 2D field topology, however a pinch may be well-approximated as a 1D periodic cylinder. (Where the axial direction of the

cylinder approximates the toroidal direction) Many results from RFP computation discussed in Sec. 3 use this cylindrical approximation.

Tearing modes [10], introduced in Sec. 4.2 and discussed in detail in Part III, are sensitive to the drift dynamics at their resonant surfaces, i.e. a flux-surface-averaged drift. We now make an order of magnitude estimate of the flux-surface-averaged ion diamagnetic (which is a fluid effect from the  $\mathbf{J}_\perp = ne(\mathbf{v}_{e\perp} - \mathbf{v}_{i\perp})$  that balances the equilibrium  $\nabla p$ ), curvature and  $\nabla B$ -drift frequencies for the tokamak and pinch equilibria:

$$\omega_{*i} \sim k_\perp \frac{\hat{r} \cdot \nabla p_i}{m_i n \omega_{ci}}, \quad (1.24)$$

$$\omega_{*\kappa} \sim k_\perp \frac{k_B T_i}{m_i \omega_{ci}} \frac{B_{pol}^2}{B^2 r}, \quad (1.25)$$

$$\omega_{*\nabla B} \sim k_\perp \frac{k_B T_i}{m_i \omega_{ci}} \frac{\hat{r} \cdot \nabla B}{B}, \quad (1.26)$$

where  $k_B$  is Boltzmann's constant and  $k_\perp$  is the perpendicular wave number of the mode. For a tokamak, we may write  $\hat{r} \cdot \nabla \sim 1/a \sim 1 \text{ m}^{-1}$  and  $B_{pol}^2/B^2 r \sim (0.25 \text{ T})^2 / ((2 \text{ T})^2 \times 0.5 \text{ m}) \sim (1/32) \text{ m}^{-1}$ . Thus  $\omega_{*i}/\omega_{*\kappa} \sim 32$ , and the diamagnetic effect will be the dominant drift. From radial force balance,  $\hat{r} \cdot \nabla B/B \sim B_{pol}^2/rB^2$ , thus  $\omega_{*i} \gg \omega_{*\kappa} \sim \omega_{*\nabla B}$ , for the drift contained within a flux surface. For a pinch profile, again  $\hat{r} \cdot \nabla \sim 1/a \sim 1 \text{ m}^{-1}$  but now  $B_{pol}^2/B^2 r \sim (0.2 \text{ T})^2 / ((0.2 \text{ T})^2 \times 0.5 \text{ m}) \sim 2 \text{ m}^{-1}$ . In addition, we note  $\hat{r} \cdot \nabla B/B \sim 0.2 \text{ T} / (0.2 \text{ T} \times 1 \text{ m}) \sim 1 \text{ m}^{-1}$  such that we conclude  $\omega_{*i} \sim \omega_{*\kappa} \sim \omega_{*\nabla B}$ . In this sense, the  $\nabla B$  and curvature drifts are at least as important to the tearing dynamics as the diamagnetic drift in pinch configurations. Additionally, as discussed in Sec. 6, for finite island widths the pressure profile is flattened through thermal conduction or sound wave mixing and diamagnetic effects are diminished. However, the equilibrium magnetic profile is not greatly affected, and in this sense the  $\nabla B$  and curvature drifts may be more important than the diamagnetic drift to the nonlinear dynamics.

Returning to the comparison of the profiles in Figs. 3 and 4, we note that the inclusion of a pressure gradient does not greatly affect the magnetic profiles. This is evident upon examining the differences between cases (a) and (b), and (c) and (d). Thus the use of profiles without a pressure gradient but with nonzero uniform pressure to study the effect of the  $\nabla B$  and curvature drifts is justified.

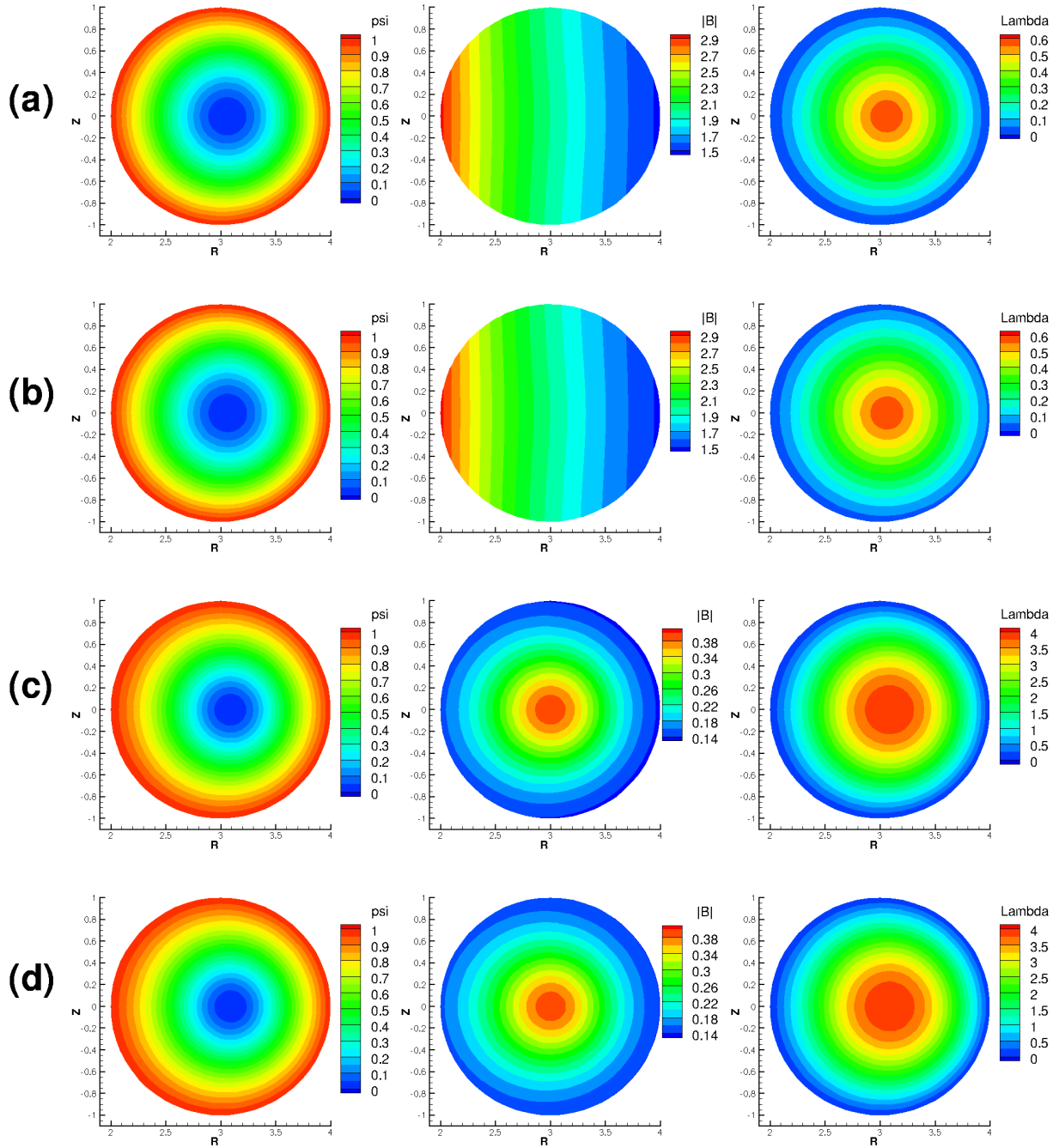


Figure 3: Surfaces of constant  $\psi$ ,  $|B|$ , and  $\lambda$  for cases (a)-(d) with parameters as listed in Table 1

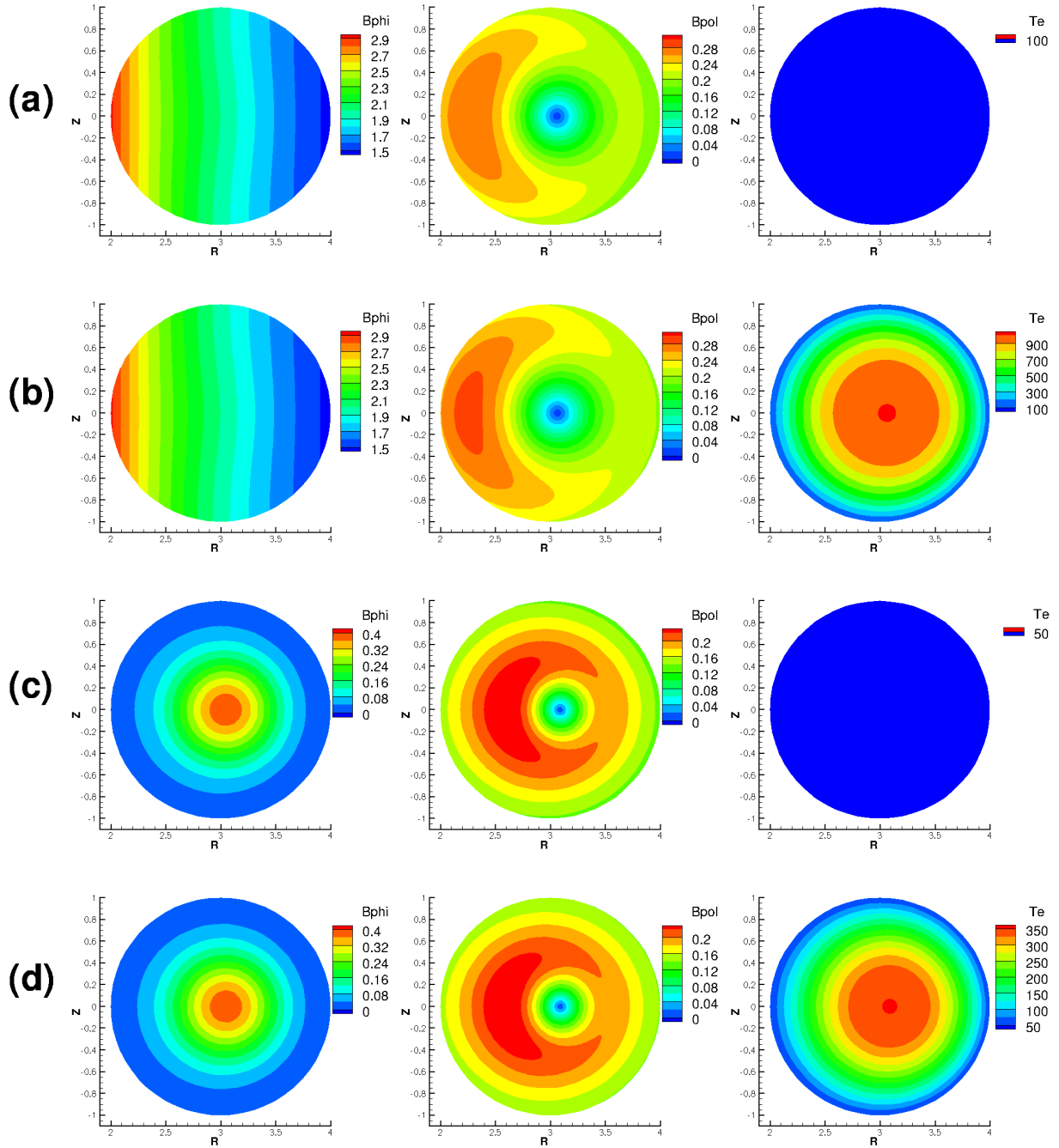


Figure 4: Surfaces of constant  $B_\Phi$ ,  $B_{pol}$ , and  $T_e$  for cases (a)-(d) with parameters as listed in Table 1

## 2 Fluid modeling

The degree of detail required in a model to describe a particular aspect of the physics in a device varies widely, even when considering only toroidal confinement devices. Given the enormous complication of a first-principles approach, approximations are needed to treat any physically relevant problem. In this section we describe the approximations used to derive the first-order FLR fluid model used here, and relate this model to the well-known resistive and ideal-MHD models.

### 2.1 The kinetic description

The first-principles approach is to solve Maxwell's equations,

$$\nabla \times \mathbf{E} = -\frac{\partial \mathbf{B}}{\partial t} \quad (2.1)$$

$$\nabla \times \mathbf{B} = \epsilon_0 \mu_0 \frac{\partial \mathbf{E}}{\partial t} + \mu_0 \mathbf{J} \quad (2.2)$$

$$\nabla \cdot \mathbf{E} = \frac{\rho_c}{\epsilon_0} \quad (2.3)$$

$$\nabla \cdot \mathbf{B} = 0 \quad (2.4)$$

by specifying the charge density,  $\rho_c(\mathbf{r}, t) = \sum_p n_p q_p$ , and current density,  $\mathbf{J}(\mathbf{r}, t) = \sum_p n_p q_p \mathbf{v}_p$ , through the solution to the equation of motion for each particle,  $\mathbf{F}_p = m_p \partial \mathbf{v}_p / \partial t$ . Here  $p$  is a particle label and  $\epsilon_0$  is the vacuum permittivity. In the non-relativistic limit, the electromagnetic forces are  $\mathbf{F}_p = q_p [\mathbf{E} + \mathbf{v}_p \times \mathbf{B}]$ . Although the solution to these equations provides a nearly complete description of the plasma motion, with realistic plasma densities of  $10^{19} m^{-3}$  the problem is intractable for realistic geometries even computationally. Simplifying approximations are necessary.

A first step is to treat the plasma statistically by introducing a distribution function,  $f_\alpha(\mathbf{r}, \mathbf{v}', t)$  which specifies the probability of finding a particle of species  $\alpha$  in the phase space volume  $d\mathbf{r}d\mathbf{v}'$ . This allows us to write the kinetic equation,

$$\frac{\partial f_\alpha}{\partial t} + \mathbf{v}' \cdot \nabla f_\alpha + \frac{\mathbf{F}_\alpha}{m_\alpha} \cdot \frac{\partial f_\alpha}{\partial \mathbf{v}'} = C(f_\alpha) \quad (2.5)$$

where the LHS describes the motion of non-interacting particles, and the right-hand side (RHS) describe the effects of particle interactions, or collisions where  $C(f_\alpha)$  is the collision operator. The appropriate expressions for charge density, current and force become  $\rho_c(\mathbf{r}, t) = \sum_\alpha n_\alpha q_\alpha$ ,  $\mathbf{J}(\mathbf{r}, t) = \sum_\alpha n_\alpha q_\alpha \mathbf{v}_\alpha$ , and  $\mathbf{F}_\alpha = q_\alpha [\mathbf{E} + \mathbf{v}_\alpha \times \mathbf{B}]$ , respectively. If the number of particles in a Debye sphere,  $N_D = 4\pi\lambda_D^3 n / 3$  where  $\lambda_D = \sqrt{\epsilon_0 k_B T_e / n_e q_e^2}$ , is large the system exhibits collective motion that defines a plasma. If characteristic

length scales are large such that  $L \gg \lambda_D$ , particle motion screens out electric fields and ion and electron charge densities are roughly equal. For ions with  $Z = 1$ , where  $q_i = Ze$ , this implies  $n_e \simeq n_i$ . Including the effect of the charge screening, the electric field from a particle is proportional to  $\exp(-r/\lambda_D)/r$  instead of  $1/r^2$ . In this sense, plasmas are weakly interacting, and tractable analytic forms of the collision operator may be obtained. (See Ref. [3], Chap. 12 for a detailed overview)

## 2.2 Moment equations

The distribution function may be transformed into fluid variables by integration over velocity space. The particle density, velocity, pressure, stress tensor, heat flux are defined as

$$n_\alpha(\mathbf{r}, t) = \int f_\alpha(\mathbf{r}, \mathbf{v}', t) d\mathbf{v}' \quad (2.6)$$

$$n_\alpha \mathbf{v}_\alpha(\mathbf{r}, t) = \int \mathbf{v}' f_\alpha(\mathbf{r}, \mathbf{v}', t) d\mathbf{v}' \quad (2.7)$$

$$p_\alpha = n_\alpha k_B T_\alpha = (\Gamma - 1) \frac{m_\alpha}{2} \int c_\alpha^2 f_\alpha(\mathbf{r}, \mathbf{v}', t) d\mathbf{v}' \quad (2.8)$$

$$\mathbf{P}_\alpha(\mathbf{r}, t) = m_\alpha \int \mathbf{v}' \mathbf{v}' f_\alpha(\mathbf{r}, \mathbf{v}', t) d\mathbf{v}' \quad (2.9)$$

$$\mathbf{q}_\alpha(\mathbf{r}, t) = \frac{m_\alpha}{2} \int c_\alpha^2 \mathbf{c}_\alpha f_\alpha(\mathbf{r}, \mathbf{v}', t) d\mathbf{v}' \quad (2.10)$$

where  $\mathbf{c}_\alpha = \mathbf{v}' - \mathbf{v}_\alpha(\mathbf{r}, t)$  is the random velocity with respect to the rest frame,  $k_B$  is the Boltzmann constant, and  $\Gamma$  is the ratio of specific heats. Moment equations for the fluid variables are obtained by taking the appropriate moments of the kinetic equation, Eqn. (2.5). For example, the moments with respect to 1,  $m\mathbf{v}'$  and  $mv'^2/2$  yield equations for the evolution of density, momentum and energy equations:

$$\frac{\partial n_\alpha}{\partial t} + \nabla \cdot (n_\alpha \mathbf{v}_\alpha) = 0 \quad (2.11)$$

$$m_\alpha n_\alpha \frac{d^\alpha \mathbf{v}_\alpha}{dt} + \nabla p_\alpha + \nabla \cdot \mathbf{\Pi}_\alpha - n_\alpha q_\alpha (\mathbf{E} + \mathbf{v}_\alpha \times \mathbf{B}) = \mathbf{R}_\alpha \quad (2.12)$$

$$\frac{n_\alpha}{\Gamma - 1} \frac{\partial k_B T_\alpha}{\partial t} + \frac{n_\alpha}{\Gamma - 1} \mathbf{v}_\alpha \cdot \nabla k_B T_\alpha + n_\alpha k_B T_\alpha \nabla \cdot \mathbf{v}_\alpha + \mathbf{P}_\alpha : \nabla \mathbf{v}_\alpha + \nabla \cdot \mathbf{q}_\alpha = Q_\alpha \quad (2.13)$$

where  $\mathbf{P}_\alpha = \mathbf{\Pi}_\alpha + \mathbf{I}p_\alpha$ ,  $d^\alpha/dt \equiv \partial/\partial t + \mathbf{v}_\alpha \cdot \nabla$ , and Eqns. (2.11) and (2.12) have been substituted into Eqn. (2.13). The moments of the collision operator have been defined as

$$0 = \int C(f_\alpha) d\mathbf{v}' \quad (2.14)$$

$$\mathbf{R}_\alpha = \int m_\alpha \mathbf{v}' C(f_\alpha) d\mathbf{v}' \quad (2.15)$$

$$Q_\alpha = \int \frac{m_\alpha}{2} \mathbf{v}'^2 C(f_\alpha) d\mathbf{v}' - \mathbf{v}_\alpha \cdot \mathbf{R}_\alpha \quad (2.16)$$

which obey the conservation properties  $\sum_\alpha \mathbf{R}_\alpha = 0$  and  $\sum_\alpha Q_\alpha = 0$ . (See Ref. [11], Chap. 1)

### 2.3 Closure relations

Formulation of the higher-order and collision operator moments ( $\mathbf{\Pi}_\alpha$ ,  $\mathbf{q}_\alpha$ ,  $\mathbf{R}_\alpha$  and  $Q_\alpha$  for our purposes) in terms of moments evolved by the lower-order moment equations ( $n_\alpha$ ,  $\mathbf{v}_\alpha$ , and  $T_\alpha$  in Eqns. (2.11), (2.12) and (2.13)) is referred to as a closure problem. In 1965 Braginskii reviewed a closure that we will use to motivate our model. (Ref. [11], Chap. 2) In the absence of forcing, the equilibrium state of the kinetic equation is a Maxwellian distribution,

$$f_{M\alpha}(\mathbf{r}, \mathbf{v}', t) = \frac{n_\alpha}{(2\pi k_B T_\alpha / m_\alpha)^{3/2}} \text{Exp}\left[-\frac{m_\alpha}{2k_B T_\alpha} (\mathbf{v}' - \mathbf{v}_\alpha)^2\right] \quad (2.17)$$

and it can be shown that a non-Maxwellian distribution will relax to this state within a characteristic time,  $\tau_\alpha$ , determined by collisions. For ions the collisional relaxation time is determined by ion-ion collisions,

$$\tau_i = \frac{4\epsilon_0^2 \sqrt{\pi^3 m_i k_B^3 T_i^3}}{\Lambda q_i^4 n_i} \quad (2.18)$$

and for electrons it is determined by ion-electron collisions,

$$\tau_e = \frac{4\epsilon_0^2 \sqrt{\pi^3 m_e k_B^3 T_e^3}}{\sqrt{2} \Lambda q_i^2 q_e^2 n_i} \quad (2.19)$$

where  $\Lambda$  is the Coulomb logarithm, typically  $\sim 15$ . The Braginskii closure relations assume the distribution is dominantly a local Maxwellian at each point in space, thus  $\omega \tau_\alpha \ll 1$  where  $\omega$  is a characteristic frequency of the effect being studied with the model. Finally, the spatial gradient length scale,  $L_\parallel$ , in the direction parallel to the magnetic field must be large in comparison to the mean-free path for particle collisions,  $v_{T\alpha} \tau_\alpha / L_\parallel \ll 1$  where  $L_\parallel \sim 1 / \nabla_\parallel$  and  $v_{T\alpha} = \sqrt{k_B T_\alpha / m_\alpha}$  is the thermal speed. We will consider relations which apply to a strongly magnetized plasma, where a particle makes many orbits between collisions and

thus  $\omega_{c\alpha}\tau_\alpha \gg 1$ , although Braginskii's relations are more general. Other closures consider the related limit of small gyroradius compared to the perpendicular length scale,  $\rho_\alpha/L_\perp = v_{T\alpha}\tau_\alpha/(\omega_{c\alpha}\tau_\alpha L_\perp) \ll 1$ , see Ref. [12] and references contained within.

With these assumptions, the  $\Pi_\alpha$  may be characterized by the anisotropic properties of the magnetized system as a viscosity with perpendicular ( $\sim 1/\omega_{c\alpha}^2\tau_\alpha$ ), gyro (cross field,  $\sim 1/\omega_{c\alpha}$ ), and parallel ( $\sim \tau_\alpha$ ) contributions. Additionally, part of  $\mathbf{R}_\alpha$  captures the effect of collisions between ions and electrons, analogous to electrical resistance. We will presently discuss the gyro and parallel viscosity, and the resistive part of  $\mathbf{R}_\alpha$  for a plasma with  $Z = 1$ .

The ion-gyroviscous stress from Ref. [12] with arbitrarily-oriented magnetic field is

$$\mathbf{\Pi}_{gv} = \frac{m_i p_i}{4eB} \left[ \hat{\mathbf{b}} \times \left( \mathbf{W} + \frac{5}{2} \frac{\nabla \mathbf{q}_i + \nabla \mathbf{q}_i^T}{p_i} \right) \cdot (\mathbf{I} + 3\hat{\mathbf{b}}\hat{\mathbf{b}}) + \text{transpose} \right] \quad (2.20)$$

where  $\mathbf{W} = \nabla \mathbf{v}_i + \nabla \mathbf{v}_i^T - (2/3)\mathbf{I}\nabla \cdot \mathbf{v}_i$  is the rate of strain tensor, and  $\hat{\mathbf{b}} = \mathbf{B}/B$  is the magnetic-field unit direction. Braginskii considered the limit with flows on the order of  $v_{Ti}$  where contributions from  $\mathbf{q}$  may be ignored. Although the measured flows in the RFP are small compared to  $v_{Ti}$  as discussed in Sec. 2.5, we will also ignore contributions from  $\mathbf{q}$ . Our studies will concentrate on the tearing modes in the RFP core where the pressure profile is relatively flat, and we argue the associated finite- $\beta$  corrections from  $\mathbf{q}$  are small. Thus the form of gyroviscosity used in our studies is

$$\mathbf{\Pi}_{gv} \simeq \frac{m_i p_i}{4eB} \left[ \hat{\mathbf{b}} \times \mathbf{W} \cdot (\mathbf{I} + 3\hat{\mathbf{b}}\hat{\mathbf{b}}) - (\mathbf{I} + 3\hat{\mathbf{b}}\hat{\mathbf{b}}) \cdot \mathbf{W} \times \hat{\mathbf{b}} \right] \quad (2.21)$$

Kaufman showed gyroviscosity captures gyro-orbit frequency shifts and ellipticity resulting from the gyro-orbit averaging of  $\nabla \mathbf{E}$  and is non-dissipative [13]. Compared to a characteristic inertial frequency  $\omega$ , the gyroviscous stress scales as  $\rho_i v_{Ti}/L^2$ , where  $\rho_i = v_{Ti}/\omega_{ci}$  is the ion gyroradius and  $L$  is a characteristic gradient length. In this sense, it is a first-order FLR effect and important only with warm ions ( $T_i \neq 0$ ).

The parallel and perpendicular contributions to the ion stress tensor are modeled as

$$\mathbf{\Pi}_{\parallel} = -\frac{3}{2} m_i n \nu_{\parallel} \mathbf{b} \cdot \mathbf{W} \cdot \hat{\mathbf{b}} \left[ \hat{\mathbf{b}}\hat{\mathbf{b}} - \frac{\mathbf{I}}{3} \right] \quad (2.22)$$

$$\mathbf{\Pi}_{\perp} = -m_i n \nu_{\perp} \mathbf{W} \quad (2.23)$$

where contributions from  $\mathbf{q}$  have again been ignored. The parallel viscous coefficient scales as  $\nu_{\parallel} \simeq v_{Ti}^2 \tau_i \sim T_i^{5/2}$  and is significant for high temperature fusion plasmas, whereas the perpendicular viscous coefficient  $\nu_{\perp}$

is proportional to  $1/\tau_i$  and is expected to be relatively small. Instead of concentrating on the exact form of the small contribution of perpendicular stress tensor we simply model it as isotropic diffusion.

Finally, the contribution to  $\mathbf{R}_e$  from ion-electron collisions is

$$\mathbf{R}_{ef} = n_e e \eta \mathbf{J} \quad (2.24)$$

where  $\eta$  is an isotropic resistivity,  $\eta = m_e/n_e e^2 \tau_e$ . Effects associated with an anisotropic conductivity ( $\sigma = \eta^{-1}$ ) only contribute a factor of 2 and are neglected in the computations described here.

## 2.4 Two-fluid formulation

For our model of a two-species quasi-neutral plasma, electrons and ions with  $Z = 1$  and  $n = n_e = n_i$ , we include the necessary terms to model low-frequency current-driven instabilities with first-order FLR effects in the RFP. Transport effects associated with the modes are left for future work. As previously mentioned contributions from heat flux are ignored, and we will only include the necessary terms in the energy equation to capture the finite- $\beta$  effects that are necessary for kinetic-Alfvén-wave-tearing response described in Sec. 5.2.

Instead of using  $\mathbf{v}_i$  and  $\mathbf{v}_e$  to describe the fluid motion, we transform the equations in terms of the equivalent  $\mathbf{v}$  and  $\mathbf{J}$ , where  $\mathbf{v}$  is the center of mass velocity,

$$\mathbf{v} = \frac{m_i \mathbf{v}_i + m_e \mathbf{v}_e}{m_i + m_e} \simeq \mathbf{v}_i. \quad (2.25)$$

By adding together the ion and electron momentum equations, Eqn. (2.12), and transforming to  $\mathbf{v}$  and  $\mathbf{J}$  we find what is known simply as the *momentum equation*,

$$m_i n \frac{d\mathbf{v}}{dt} = \mathbf{J} \times \mathbf{B} - \nabla p - \nabla \cdot (\mathbf{\Pi}_{\parallel} + \mathbf{\Pi}_{gv}) - \nabla \cdot \nu_{\perp} m_i n \mathbf{W} \quad (2.26)$$

where we have dropped terms  $\sim m_e/m_i$  and define  $p = p_e + p_i$ . Ion gyroviscosity, Eqn. (2.20), and parallel viscosity, Eqn. (2.22), have been included along with a perpendicular-like isotropic viscosity as the last three terms in Eqn. (2.26). The addition of the momentum equations exactly cancel the friction force through the conservation properties of  $\mathbf{R}_\alpha$ , and the electric field force is canceled with quasi-neutral conditions.

As  $\mathbf{v} \simeq \mathbf{v}_i$  the momentum equation specifies the ion fluid evolution. Alternatively, the fast motion of the mobile electron fluid evolution is used to specify the electric field by solving the electron momentum

equation to produce a *generalized Ohm's law*,

$$\mathbf{E} = -\mathbf{v} \times \mathbf{B} + \frac{\mathbf{J} \times \mathbf{B}}{ne} - \frac{\nabla p_e}{ne} + \eta \mathbf{J} + \frac{m_e}{ne^2} \frac{\partial \mathbf{J}}{\partial t}. \quad (2.27)$$

We have used the definition of current density,  $\mathbf{J} = ne\mathbf{v}_i - ne\mathbf{v}_e$  to eliminate electron flow velocity resulting in the first two terms on the RHS, the ideal-MHD and Hall contributions. The combination of these terms is equivalent to  $-\mathbf{v}_e \times \mathbf{B}$ , and when the Hall term is large in comparison with  $\mathbf{v} \times \mathbf{B}$ , it signifies decoupling of the electron and ion perpendicular dynamics. To the extent that the last three terms of Eqn. (2.27) are small,  $\mathbf{E} \cong -\mathbf{v}_e \times \mathbf{B}$ , and the magnetic flux is frozen into the electron fluid. Instead of evolving the electric field independently with Ampere's law, we use the constitutive relationship established through the generalized Ohm's law for  $\mathbf{E}$ . Since the phenomena we study involves only the low-frequency dynamics, we use an approximate Ampere's law where the displacement current is dropped,

$$\mu_0 \mathbf{J} = \nabla \times \mathbf{B}, \quad (2.28)$$

to determine  $\mathbf{J}$  and thus the electron response,  $\mathbf{v}_e$ . By substituting the generalized Ohm's law into Faraday's law, Eqn. (2.1), the magnetic field is evolved through the *induction equation*.

The last three terms on the RHS of Ohm's law are electric field contributions from the electron pressure gradient, the resistive term,  $\mathbf{R}_e/ne$ , and electron inertia. Electron inertia is reduced to the form of Eqn. (2.27) by expanding it as

$$\frac{m_e}{e} \frac{d^e \mathbf{v}_e}{dt} = \frac{m_e}{e} \left( \frac{\partial \mathbf{v}_e}{\partial t} - \mathbf{v}_e \cdot \nabla \mathbf{v}_e \right) = \frac{m_e}{e} \left( \frac{\partial \mathbf{v}}{\partial t} - \frac{\partial}{\partial t} \left( \frac{\mathbf{J}}{ne} \right) - \mathbf{v} \cdot \nabla \mathbf{v} + \mathbf{v} \cdot \nabla \frac{\mathbf{J}}{ne} + \frac{\mathbf{J}}{ne} \cdot \nabla \mathbf{v} - \frac{\mathbf{J}}{ne} \cdot \nabla \frac{\mathbf{J}}{ne} \right). \quad (2.29)$$

The dominant term is  $\sim \partial \mathbf{J} / \partial t$  as described in Ref. [14]. We will concentrate on cases physically relevant to the RFP where effects proportional to  $m_e$  are small. Thus the contribution from electron inertia and the implicitly ignored  $\mathbf{\Pi}_e$  are unimportant.

Finite- $\beta$  effects are captured through the *continuity* and *energy equations*,

$$\frac{dn}{dt} = -n \nabla \cdot \mathbf{v} + D_n \nabla^2 n \quad (2.30)$$

and

$$\frac{n}{\Gamma - 1} \frac{dk_B T}{dt} = -p \nabla \cdot \mathbf{v} + \nabla \cdot \chi n \nabla k_B T . \quad (2.31)$$

We model both the electron and ion temperatures through the ion energy equation as remaining at a fixed fraction of  $T$ , i.e.  $T_i = f_{Ti}T$  and  $T_e = (1 - f_{Ti})T$ , where  $f_{Ti}$  is a specified parameter. Separate sets of computations reported in Parts III and IV consider the cold-ion ( $f_{Ti} = 0$ ) and rapid-equilibration ( $f_{Ti} = 0.5$ ) limits. Heating effects from  $Q_{i/e}$  are neglected, and  $\mathbf{q}_i$  is simply a diffusive term with small thermal diffusivity  $\chi$ . Additionally we use a small particle diffusivity,  $D_n$ , in the density equation for numerical stability. In cases presented here, their coefficients are chosen to be small with respect to resistivity, such that  $D_n = \chi = 0.1\eta/\mu_0$ . The magnetic Prandtl number, specifying ratio of the resistive and perpendicular viscous diffusivities  $P_m = \mu_0\nu/\eta$ , is either 0.1 or 1.

Our model uses Eqns. (2.26), (2.1), (2.11), (2.13) to specify the evolution of  $\mathbf{v}$ ,  $\mathbf{B}$ ,  $n$ , and  $T$  with the constitutive relations from Eqns. (2.27) and (2.28) which specify  $\mathbf{E}$  and  $\mathbf{J}$ . After prescribing the relation among diffusion coefficients, a set of five dimensionless parameters describes the plasma in the model: (1)  $f_{Ti}$ , (2) the plasma- $\beta$  ( $2\mu_0 p/B_0$ ), (3, 4) the normalized ion and electron skin depths,  $d_\alpha/a = c/\omega_{p\alpha}a$ , where  $\omega_{p\alpha} = \sqrt{ne^2/\epsilon_0 m_\alpha}$  is the plasma frequency for species  $\alpha$ , and (5) the Lundquist number,  $S = \tau_R/\tau_A$ , where  $\tau_R = \mu_0 a^2/\eta$  is the resistive time and  $\tau_A = a/v_A = a\sqrt{\mu_0\rho_0}/B_0$  is the Alfvén time. In reality, the ion and electron skin depths are not independent, as their ratio is determined by the electron and ion masses.

## 2.5 Relation to resistive, ideal MHD

If the flows associated with the  $\mathbf{E} \times \mathbf{B}$  drift dominate the perpendicular macroscopic dynamics,

$$\mathbf{v}_\perp \sim \mathbf{v}_{E \times B} \sim v_T \quad (2.32)$$

then MHD ordering is valid and one may approximate Ohm's law with only the advective term as

$$\mathbf{E} = -\mathbf{v} \times \mathbf{B} . \quad (2.33)$$

This equation is known as the ideal Ohm's law, and it captures only the effect of the large  $\mathbf{E} \times \mathbf{B}$  flow. Additional terms must be included to determine the parallel electric field (note  $E_\parallel = 0$  with ideal MHD) and at resonant surfaces where contributions to the induction equation from the line-bending term,  $\mathbf{B} \cdot \nabla \mathbf{v}$ , become a magnetic differential equation (Sec. 1.3) and vanish as described later in Sec. 4.1. Resistive MHD

resolves these issues and is appropriate when the gyroradius is small,  $\rho_i/a \ll 1$ , and terms  $\sim d_i$  in the generalized Ohm's law, Eqn. (2.27), may be neglected. Thus

$$\mathbf{E} = -\mathbf{v} \times \mathbf{B} + \eta \mathbf{J} . \quad (2.34)$$

To the extent the Hall term may be ignored in both formulations  $\mathbf{v}_{e\perp} \simeq \mathbf{v}_{i\perp}$ , and the ion and electron fluids are coupled. In this sense, we refer to ideal- and resistive-MHD as single-fluid models. For a more complete discussion of these approximations, see Ref. [1], Chap. 6, for example.

Before reviewing RFP dynamics, we motivate their study with a two-fluid model by considering ion flow measurements in the Madison Symmetric Torus (MST, see [15]) RFP. Using a characteristic temperature of  $300\text{eV}$ , the thermal speed of a deuterium plasma is  $v_{Ti} = 120\text{km/s}$ . From mean flow measurements in Ref. [16], we note  $v_{mean} = 30\text{km/s}$  and  $v_{mean}/v_{Ti} \sim 0.25$ . More importantly, from measurements of the fluctuations associated with the instabilities in Ref. [17],  $v_{fluct} = 1 - 5\text{km/s}$  and  $v_{fluct}/v_{Ti} \sim 0.04$ . Given the small instability flows we may anticipate  $\mathbf{v}_{E \times B}$  does not strictly dominate the instability dynamics, and two-fluid effect may be significant.

### 3 Reversed-field pinches

The considerations of pinch equilibria in Sec. 1.4 are only based on axisymmetric steady-state solutions to force balance,  $\mathbf{J} \times \mathbf{B} = \nabla p$ . However a true steady state would have  $\partial/\partial t \rightarrow 0$  for all the equations which describe a plasma. In practice, magnetically-confined plasma are always in a state of approximate force balance as it is enforced on the fast Alfvénic time scale,  $\tau_A = v_A/a$  with the Alfvén speed defined as  $v_A = B/\sqrt{\mu_0 m_i n}$ . For dynamics that are slow relative to Alfvénic propagation, the plasma evolution can be conceptualized as a sequence of equilibrium states described by force balance. Additionally, the assumption of axisymmetry does not hold in the RFP. In fact many unstable and nonlinearly driven modes are present, and a fully 3D configuration develops. In the next section we discuss how these effects impact standard RFP dynamics, particularly the quasi-periodic sawtooth cycle and edge reversal of the toroidal field, compared to the magnetic axis, which distinguishes an RFP from a simple pinch.

### 3.1 Edge- $B_T$ reversal and dynamo emfs

Consider the cylindrical, force-free, Ohmic ( $\partial \mathbf{B} / \partial t = 0$ ) equilibrium described by Robinson as a paramagnetic pinch [18]. These conditions may be expressed by components of Faraday's law

$$\frac{\partial B_\theta}{\partial t} = -\frac{\partial E_z}{\partial r} = 0 \quad \rightarrow \quad E_z(r) = \frac{V_T}{2\pi R} = \text{const.} \quad (3.1)$$

$$\frac{\partial B_z}{\partial t} = \frac{1}{r} \frac{\partial}{\partial r} (r E_\theta) = 0 \quad \rightarrow \quad E_\theta(r) = 0 \quad (3.2)$$

where  $V_T$  is the inductive toroidal loop voltage. With a simple resistive Ohm's law we may write  $-v_r B_\theta + \eta J_z = V_T / 2\pi R$  and  $v_r B_z + \eta J_\theta = 0$ , where  $v_r$  is a radially-inward pinch flow,  $v_{pinch}$ . Solving these equations we find

$$\lambda_{para}(r) = \lambda(0) B_z(0) \frac{B_z}{B^2} \quad (3.3)$$

and

$$v_{pinch}(r) = -\frac{\eta}{\mu_0} \lambda(0) B_z(0) \frac{B_\theta}{B^2}. \quad (3.4)$$

Energy flows from the boundary through the  $\mathbf{E} \times \mathbf{B}$  flux associated with the pinch flow, and is dissipated resistively throughout the profile. In this sense the loop voltage drives both toroidal and poloidal components of the parallel current. With experimentally relevant values for resistivity and inductive loop voltage, the paramagnetic profile has a large gradient in  $\lambda_{para}(r)$  which provides a free-energy source for core-resonant instabilities.

Standard operation of reversed-field pinch (RFP) experiments relies on macroscopic magnetohydrodynamic-like modes to distribute  $\lambda(\psi)$  over the profile and relax the gradient in  $\lambda(\psi)$  compared to Robinson's paramagnetic pinch. The resulting broad distribution gives the configuration its characteristic reversal of the toroidal magnetic field near the wall. (Reversal of the magnetic field requires poloidal current driven by the modes) With some possible exceptions, the dominant unstable modes of standard RFP profiles are tearing modes that saturate nonlinearly by coupling to stable resonant modes [19] and by reducing their drive through profile modification [20]. We separate fields into mean and fluctuating components,  $A = \langle A \rangle + \tilde{A} = A_0 + \tilde{A}$ , where the tilde indicates a perturbed field and  $\langle \rangle$  indicates an axial and poloidal average. Mean-field analysis [21] of the parallel generalized Ohm's law (see Appendix D),

$$E_{0\parallel} \simeq -\left\langle \tilde{\mathbf{v}} \times \tilde{\mathbf{B}} \right\rangle_{\parallel} + \left\langle \frac{\tilde{\mathbf{J}} \times \tilde{\mathbf{B}}}{ne} \right\rangle_{\parallel} + \eta J_{0\parallel}, \quad (3.5)$$

shows that part of the parallel-current-density profile may be sustained against resistive dissipation by an emf produced from the correlation of fluctuations instead of being driven directly by the inductive loop voltage. Through-out this document we use perpendicular ( $\perp$ ), and parallel ( $\parallel$ ) to refer to the magnetic coordinates ( $\hat{\mathbf{r}}, \hat{\mathbf{e}}_{\perp} = \hat{\mathbf{b}}_0 \times \hat{\mathbf{r}}, \hat{\mathbf{e}}_{\parallel} = \hat{\mathbf{b}}_0$ ) where  $\hat{\mathbf{b}}_0 = \mathbf{B}_0/B_0$ . In single-fluid models, the correlation of fluctuating flows and magnetic field induces the MHD dynamo effect,  $\langle \tilde{\mathbf{v}} \times \tilde{\mathbf{B}} \rangle$  [22]. Two-fluid models allow a Hall dynamo effect,  $\langle \tilde{\mathbf{J}} \times \tilde{\mathbf{B}}/ne \rangle$ , from the correlation of the fluctuating current density and magnetic field [23, 24], in addition to the MHD dynamo effect.

In MST, the dynamo emfs are not steady-state, and instead are correlated with quasi-periodic relaxation events, or ‘sawteeth.’ These events are characterized by an increase in mode activity and fast changes in the profiles, and are typically separated by a quiescent period of approximately  $\sim 5 - 10$  ms. With our simple model, the process can be described as a quick modification of the profile through dynamo emfs, stabilization of the profile and decay of the mode energies and their associated dynamo emfs, a quiescent period where the current profile modification from the dynamo resistively decays, followed by destabilization of the instabilities and a repeat of the cycle. Figure 5 shows experimental measurements of the mode magnetic amplitudes at the wall during a sawtooth crash for an MST standard 400 kA discharge.

### 3.2 Relaxation theory

In contrast to the computational models, which track the mode dynamics, RFP relaxation theory predicts the plasma will tend towards a ‘relaxed’ state where the plasma energy,  $W$ , is minimized subject to constraints. In 1958 Woltjer was interested in explaining force-free configurations in astrophysical phenomena [26]. He noted the global magnetic helicity,

$$K_0 = \int_{V_0} dV \mathbf{A} \cdot \mathbf{B} \quad (3.6)$$

where  $\mathbf{A}$  is the magnetic vector potential and  $V_0$  is the full plasma volume, is a constant of the plasma motion with astrophysical (or conducting wall) boundary conditions and  $\mathbf{E} \cdot \mathbf{B} = 0$  as in ideal MHD. Woltjer demonstrated that if the energy of the system is minimized with the constraint of constant  $K_0$ , the plasma tends to a force-free state,  $\mu_0 \mathbf{J} = \lambda_c \mathbf{B}$  where  $\lambda_c$  is a constant. This work was soon extended to include a second global invariant of dissipationless single-fluid MHD, global cross helicity,

$$M_0 = \int_{V_0} dV \mathbf{v} \cdot \mathbf{B}, \quad (3.7)$$

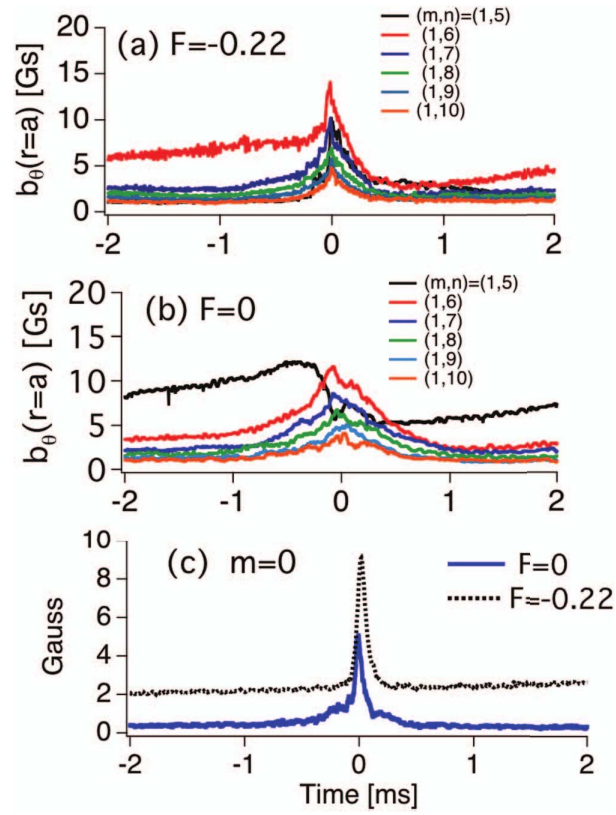


Figure 5: MST experimental measurements of temporal dynamics of core resonant ( $m = 1$ ) modes over sawtooth cycle for (a) standard plasma ( $F = -0.22$ ) and (b) non-reversed plasma ( $F = 0$ ); and (c)  $m = 0$  mode amplitude for standard ( $F = -0.22$ ) and non-reversed ( $F = 0$ ) plasmas. Crash denoted by  $t = 0$ . This figure is from Ding et al., Ref. [25].

where the minimum energy state is force-free with constant  $\lambda$  but additionally has field aligned flows [27]. However in ideal systems, it can be shown that the helicity is not just a global invariant, but is invariant for the volume bounded by each good flux surface [28]. Thus for a plasma with good nested flux surfaces there are an infinite number of constraints.

In 1974 Taylor postulated that in the RFP finite-resistivity tearing-mode dynamics allow helicity on individual flux surfaces to change during relaxation while global helicity is relatively well conserved [5]. This conjecture allowed Taylor to predict that relaxation flattens the current profile to move the plasma towards towards a constant- $\lambda$  state. He used the constant- $\lambda$  profile to find the fields in a cylinder in terms of Bessel functions. The normalized current,

$$\Theta = \frac{B_{\theta 0}(a)}{\langle\langle B_z \rangle\rangle} \quad (3.8)$$

where  $\langle\langle \rangle\rangle$  is a volume average, and edge-field reversal parameter,

$$F = \frac{B_{z0}(a)}{\langle\langle B_z \rangle\rangle}, \quad (3.9)$$

calculated from the modified-Bessel-function model behave qualitatively similar to plasma experiments [29]. Measurements of  $K$  and  $W$  in MST also provides some support for the hypothesis that  $K$  is nearly constant in comparison to  $W$  during a relaxation event [30].

With a two-fluid model, the invariant quantities become the hybrid ion and electron helicities

$$K_\alpha = \int \left( \mathbf{A} + \frac{m_\alpha \mathbf{v}_\alpha}{q_\alpha} \right) \cdot \left( \mathbf{B} + \frac{m_\alpha \mathbf{U}_\alpha}{q_\alpha} \right) \quad (3.10)$$

where  $\mathbf{U}_\alpha = \nabla \times \mathbf{v}_\alpha$  is the vorticity [31, 32, 33, 34, 35]. To the extent the electron mass is small, the hybrid electron helicity is equivalent to the magnetic helicity  $K$ . Cross helicity, Eqn. (3.7), is no longer an invariant with the two-fluid model. However in the MHD limit, the hybrid ion helicity reduces to cross helicity [36]. The two-fluid relaxed states, found when both  $K_i$  and  $K_e$  are used as constraints and  $W$  is minimized, no longer must be force-free, and plasma flows are specified in addition to the field configurations. Thus coupling between flows and fields occurs naturally for two-fluid relaxation.

This coupling is apparent by considering the parallel momentum equation with mean-field theory,

$$m_i n \frac{\partial v_{\parallel}}{\partial t} + m_i n \langle \tilde{\mathbf{v}} \cdot \nabla \tilde{\mathbf{v}} \rangle_{\parallel} = \langle \tilde{\mathbf{J}} \times \tilde{\mathbf{B}} \rangle_{\parallel} - \langle \nabla \cdot \mathbf{\Pi} \rangle_{\parallel} \quad (3.11)$$

where the second term on the LHS comes from the Reynolds stress and the first term on the RHS is from

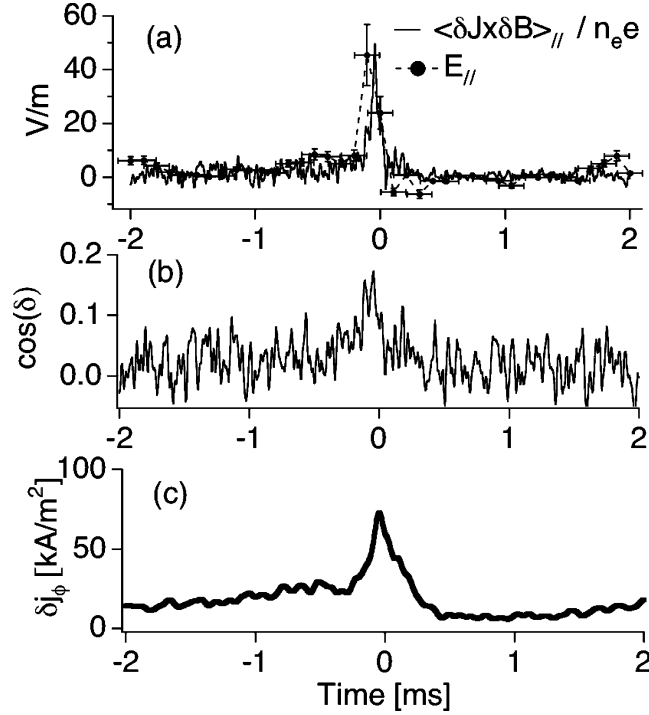


Figure 6: (a) Dynamics of Hall dynamo (solid line) and inductive electric field (dashed line) during magnetic relaxation event. Time  $t = 0$  denotes the sawtooth crash. Data have been ensemble averaged over 380 independent sawtooth events. (b) Phase difference between current and magnetic field fluctuations and (c) current density fluctuations dynamics over sawtooth crash. This figure is from Ding et al., Ref. [25].

the Maxwell stress, along with the parallel generalized Ohm's law, Eqn. (3.5). Clearly the Hall dynamo is closely related to the Maxwell stress, and it is no surprise that in two-fluid relaxation the flows are naturally coupled to the fields.

### 3.3 RFP experimental measurements relevant to two-fluid dynamics

Direct experimental measurements on MST during relaxation events have provided a window into the two-fluid dynamics of the RFP. In the core, Ding et al. made laser polarimetry measurements during 400 kA discharges that demonstrate the Hall-dynamo effect from the inner-most core-resonant mode ( $m = 1, n = 6$ ) is significant, as shown in Figs. 6 and 7 [37, 25]. These measurements indicate that the effect is anti-dynamo in the sense that it reduces the parallel current and that it is peaked around the resonant surface of the mode. Additionally, measurements made without significant edge reversal and its associated strong  $m = 0$  mode show the Hall dynamo effect is small and indicate the strong nonlinear coupling provided through this mode is important. (For example, the  $m = 0, n = 1$  mode couples the  $m = 1, n = 6$  and  $m = 1, n = 7$  modes as described in Ref. [20])

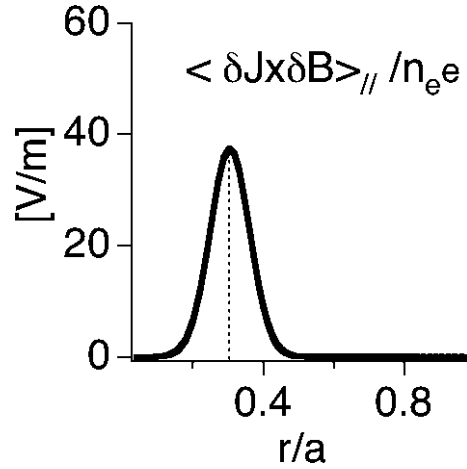


Figure 7: Hall dynamo spatial profile for (1,6) mode showing a peak at the resonant surface. This figure is from Ding et al., Ref. [25].

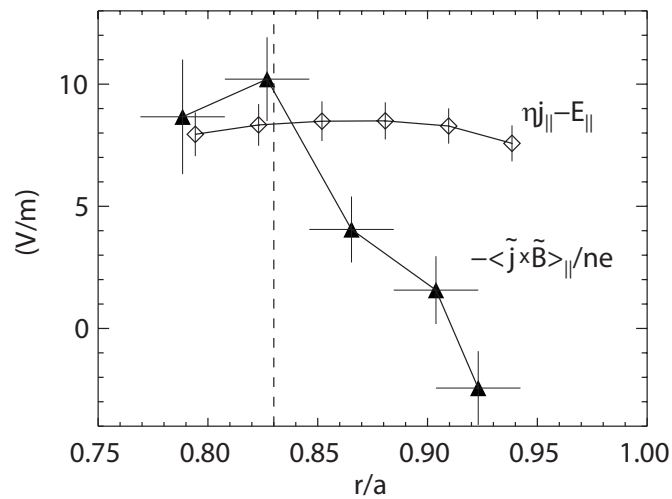


Figure 8: Edge radial profiles of the resistive term (diamonds) and the Hall dynamo (triangles) averaged over 0.15 ms at the peak of the reconnection event. The dashed line shows the location of the reversal surface. This figure is from Kuritsyn et al., Ref. [16].

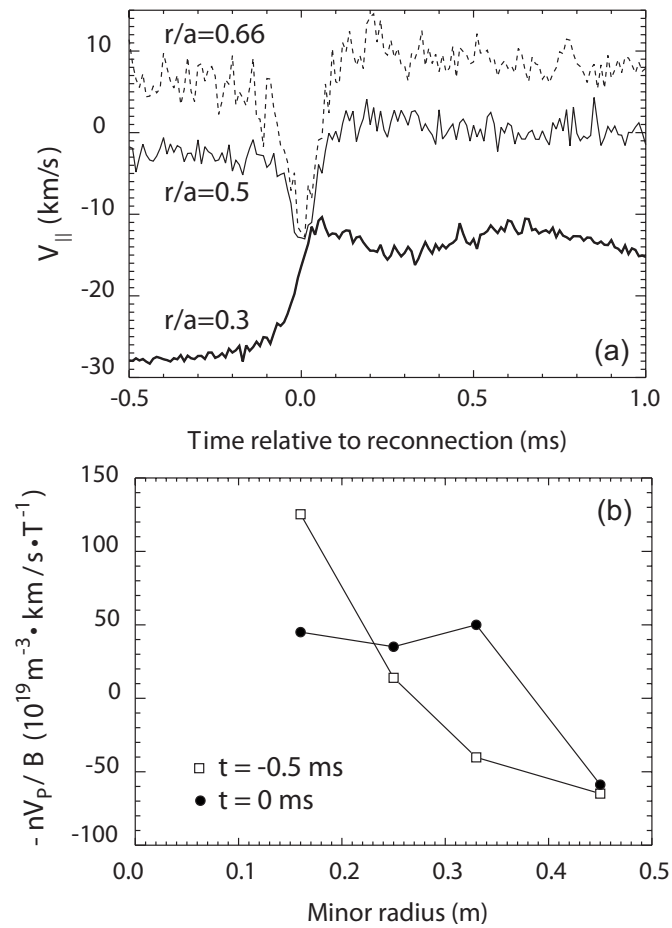


Figure 9: (a) Parallel velocity at three radial locations. (b) Radial profile of the parallel momentum evolution normalized by the magnetic field before (squares) and during (circles) the reconnection event in MST. This figure is from Kuritsyn et al., Ref. [16].

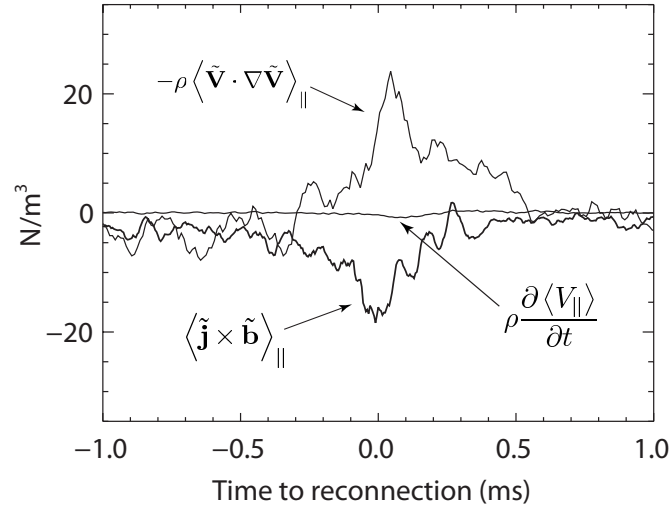


Figure 10: Parallel momentum balance near the reversal surface ( $r/a = 0.83$ ) through the reconnection event. Rapid oscillations on the data curves indicate experimental uncertainty. This figure is from Kuritsyn et al., Ref. [16].

Magnetic probe measurements in the edge for 200 kA discharges analyzed by Kuritsyn et al. show the Hall dynamo is also significant near the reversal surface during relaxation events and small near the plasma boundary as shown in Fig. 8 [16]. Additionally, Kuritsyn et al. investigated the momentum transport induced by the fluctuations during a relaxation event by examining the terms in Eqn. (3.11). By combining Rutherford scattering measurements of the core poloidal bulk velocity and mode rotation measurements to infer the core toroidal velocity, along with Mach probe measurements at the edge, they were able to examine the flow profile evolution through a sawtooth crash. The measurements of the parallel flow shown in Fig. 9 demonstrate in the core,  $r/a \approx 0.3$ ,  $v_{\parallel}$  is increased while it is decreased in the mid-radius region,  $r/a \approx 0.5 - 0.7$ , and unchanged at the edge. These measurements indicate the flow is strongly coupled to current-profile relaxation as discussed in the previous section. Near the wall where the plasma temperature and gyro-radius are small, both the Hall dynamo and flow-profile-modification effects vanish.

In order to gain insight into these flow-profile modification, Kuritsyn et al. calculated the Maxwell and Reynolds stresses of Eqn. (3.11) from the edge to just inside the reversal surface with probe and optical-Doppler-spectroscopy measurements. Their results, in Figs. 10 and 11, found both were large in magnitude relative to the change in the flow profile (the inertial term on the RHS of Eqn. (3.11)), and that there was a near cancellation of the two terms - an unexpected result. In the core, the Faraday rotation measurements indicate the Maxwell stress is large relative to ion inertia and must be balanced by something in the parallel momentum equation, however the Reynolds stress was not measured. Finally, the authors note that the

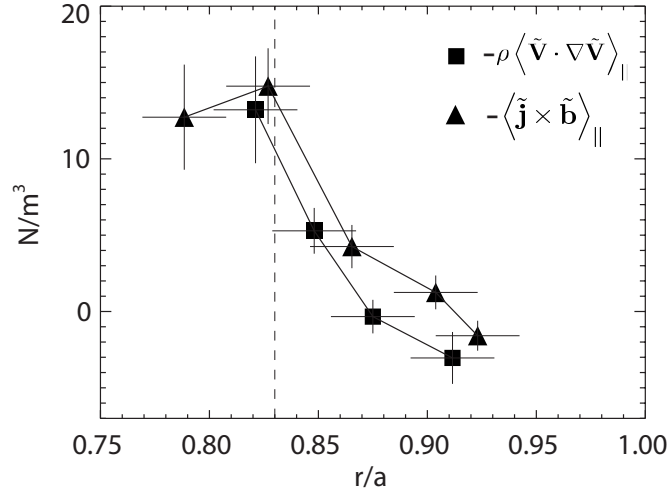


Figure 11: Radial profiles of the Maxwell (triangles) and Reynolds (squares) stresses averaged over 0.15 ms at the peak of the reconnection event. The dashed line marks the toroidal magnetic field reversal surface. This figure is from Kuritsyn et al., Ref. [16].

momentum transport effects are minimal without significant edge reversal and  $m = 0$  mode activity during a sawtooth crash, as seen in Fig. 12. Similar to the Hall-effect observations by Ding et al., the strong nonlinear coupling of the modes is critical for the two-fluid relaxation effects.

## 4 Magnetic reconnection with resistive MHD

Our description of the RFP so far has concentrated on relaxation and mean-field theories which rely on fluctuations in their underlying formulation but do not specify their form or internal structure. We now turn to what is typically considered the dominant instability and source of long-wavelength fluctuations in the RFP - the tearing mode. This mode belongs to a broader class of instabilities which cause magnetic reconnection, and before discussing the specifics of tearing, we describe the reconnection process in general terms.

Magnetic reconnection occurs when magnetic field-lines are broken and reassembled in a topologically-different configuration. Magnetic-topology change may be described by a simple resistive Ohm's law,  $\mathbf{E} = -\nabla\phi - \mathbf{J}$ , which combined with Faraday's law, Eqn. (2.1), gives  $\tau \nabla^2 \mathbf{B} = -\nabla \times \mathbf{J}$ . This diffusive process takes place on a resistive time scale  $\sigma_R = \mu_0 a^2 / \eta$ , and in many common circumstances it is reasonably fast as resistance is large. However a plasma is a nearly perfect conductor, thus  $\sigma_R$  is large and one would expect topological changes through resistive diffusion to take an extremely long time. In reality, observations of magnetic-topology change in confinement devices indicate that it occurs on a hybrid-resistive-Alfvén time

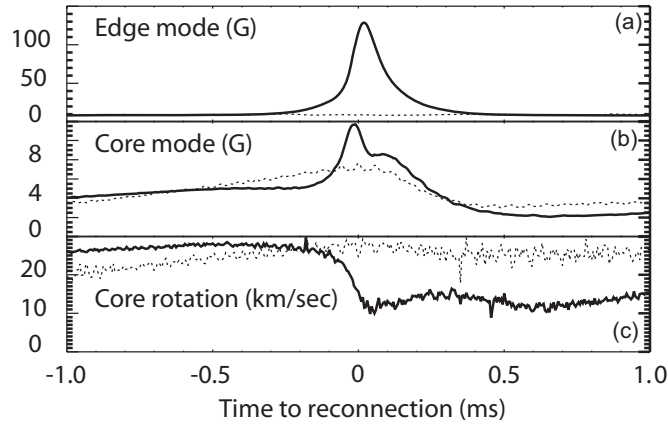


Figure 12: Amplitudes of (a) edge  $m = 0$ ,  $n = 1$  mode, (b) core  $m = 1$ ,  $n = 6$  mode, and (c) core plasma rotation. When  $m = 0$  mode is not excited (dashed curves) there is no change in the core plasma rotation. This figure is from Kuritsyn et al., Ref. [16].

scale faster than  $\sigma_R$ . Of course a purely resistive Ohm's law is an incomplete description of a plasma, and in the next section we will consider the separation of scales that occurs with a boundary layer formulation where different physical mechanisms dominate each region. In this sense, magnetic reconnection in a plasma involves both topological change and scale separation. In particular, we describe the current-driven tearing mode with a resistive-MHD model, an instability associated with reconnection in Sec. 4.2. This picture is extended in Sec. 5 where first-order FLR effects on the tearing mode, drift tearing and modification by kinetic-Alfvén waves, is discussed. The nonlinear growth and saturation of the tearing mode is reviewed in Sec. 6. The effects described here in addition to the considerations of Part III comprise a reasonable model for tearing activity in the RFP.

#### 4.1 Boundary layer formulation

The Lundquist number roughly compares the advective and resistive terms in a resistive MHD Ohm's law, Eqn. (2.34), with dimensional analysis,

$$S = \frac{v_A B L}{\mu_0 (B L^2)} = \frac{\mu_0 B L}{m_i n} = \frac{\sigma_R}{\sigma_A} \quad (4.1)$$

where  $L$  is a characteristic gradient length. If  $S$  is large, the advective term dominates and resistivity may be neglected in  $\mathbf{E}$ . As  $S \ll L$  we note that for small length scales the resistive term can be significant. In general, these length scales are far too small to impact the instability dynamics as fusion plasmas typically have  $S \sim 10^6$  for  $L \sim a$ , and thus a very small resistive length scale,  $L_R \sim 10^{-6} a$ .

However, the linearized radial component of the advective term in the induction equation is a magnetic differential equation,

$$\hat{r} \cdot \nabla \times (\tilde{\mathbf{v}} \times \mathbf{B}_0) = \hat{r} \cdot [-\mathbf{B}_0 \nabla \cdot \tilde{\mathbf{v}} + (\mathbf{B}_0 \cdot \nabla) \tilde{\mathbf{v}} - (\tilde{\mathbf{v}} \cdot \nabla) \mathbf{B}_0] = (\mathbf{B}_0 \cdot \nabla) \tilde{v}_r \quad (4.2)$$

where we assume cylindrical geometry and note there is no radial component of the mean magnetic field. The tilde indicates a perturbed quantity with spatial and time dependence,  $\tilde{a} = \tilde{a}(r) \text{Exp}(-i\omega t + im\theta + inz/R) = \tilde{a}(r) \text{Exp}(-i\omega t + i\mathbf{k} \cdot \mathbf{r})$  where the wave-vector  $\mathbf{k} = \hat{\theta}m/r + \hat{z}n/R$ , and the equilibrium is denoted with a subscript ‘0’. The radial component of the resistive-MHD magnetic-induction equation is then

$$\gamma \tilde{B}_r = (\mathbf{B}_0 \cdot \nabla) \tilde{v}_r + \frac{\eta}{\mu_0} \hat{r} \cdot \nabla^2 \tilde{\mathbf{B}}, \quad (4.3)$$

where  $\gamma = -i\omega$ . If  $\eta \rightarrow 0$  this equation is singular at the resonant surface of the mode, as discussed in Sec. 1.3, and the only solution is  $\tilde{B}_r(r_s) = 0$ . Indeed this is the case for ideal instabilities. The inclusion of finite resistivity resolves the singularity and allows resistive instabilities, solutions with  $\tilde{B}_r(r_s) \neq 0$ . Non-zero  $\tilde{B}_r(r_s)$  leads to magnetic-field topology change and associated reconnection. Since the Lundquist number, defined by the length scale of the minor radius in our cases, is large for experimental cases, we may neglect resistivity everywhere but in a thin boundary layer near the resonant surface. This property of the induction equation permits a boundary-layer formulation of the problem: near the resonant surface at least the resistive-MHD equations are used - referred to as the inner region, and away from the resonant surface, the outer region, the ideal-MHD equations are sufficient. The solutions from each region are then matched at the interface between the layers.

Figure 13 sketches the structure of the tearing mode. The figure assumes both the wavenumber and reconnecting field are oriented in the perpendicular vertical direction. The reconnecting field reverses sign at the resonant surface, and thus  $\mathbf{k} \cdot \mathbf{B}_0(r_s) = 0$ . Perturbed flows form a vortex structure which advects flux to the resonant surface, and when the perturbation is large an island will form. However in the linear stage the amplitude is small such that the island width is negligible. In a simple slab geometry, the flow symmetrically advect flux to the resonant surface where the gradient of  $\tilde{B}_\perp$  is large and the resistive term can balance  $\gamma \tilde{B}_r$  in Eqn. (4.3).

With a resistive-MHD model the tearing mode dispersion relation may be obtained from the radial

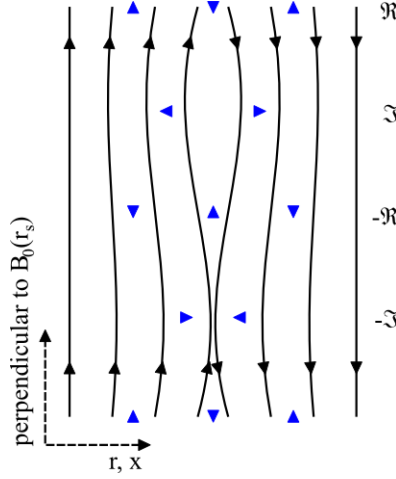


Figure 13: A sketch of the perturbed velocity (blue arrows) and reconnecting magnetic field lines (black lines) of the tearing mode. The normalized phase of the complex eigenfunction coefficients used in Part III are indicated on the right.

component of the induction equation, Eqn. (4.3), and the parallel vorticity equation,

$$\mathbf{b}_0 \left( \rho \frac{d\mathbf{v}}{dt} + \nabla \times \mathbf{b}_0 \right) = \mathbf{b}_0 \left( \mathbf{J} \times \mathbf{B} \right) \quad (4.4)$$

where  $\mathbf{b}_0 = \mathbf{B}_0 / B_0$ . In the outer region ion inertia, viscosity and resistivity may be neglected, such that

$$0 = \mathbf{b}_0 \left( \mathbf{J} \times \mathbf{B}_0 + \mathbf{J}_0 \times \mathbf{B} \right) \quad (4.5)$$

$$\pi B_r = (\mathbf{B}_0 \cdot \nabla) v_r \quad (4.6)$$

The solution to the first of these equations is given by Newcomb (Ref. [38]) and specifies the perturbed magnetic field, and evaluating the second then provides a relation for the flow. By taking advantage of the divergence-free nature of  $\mathbf{B}$ ,  $\nabla \cdot \mathbf{B} = 0$ , we transform the perturbed magnetic field to a flux representation,

$$\mathbf{B} = \mathbf{B}_0 + B \mathbf{b}_0 \quad (4.7)$$

and it is useful to express the perturbed flow as a streamfunction representation which captures the dominant vortical nature of the flows,

$$\mathbf{v} = \mathbf{b}_0 \times \nabla \psi + v \mathbf{b}_0 \quad (4.8)$$

Thus

$$\tilde{B}_r = ik_{\perp} B_0 \tilde{\psi} \quad (4.9)$$

$$\tilde{B}_{\perp} = -B_0 \tilde{\psi}' \quad (4.10)$$

$$\tilde{v}_r = -ik_{\perp} \tilde{\phi} \quad (4.11)$$

$$\tilde{v}_{\perp} = \tilde{\phi}' \quad (4.12)$$

where the perpendicular direction is  $\hat{\mathbf{b}}_0 \times \hat{\mathbf{r}}$ , such that  $k_{\perp} = (\hat{\mathbf{b}}_0 \times \hat{\mathbf{r}}) \cdot \mathbf{k}$ , and primes indicate radial derivatives. As in Ref. [39] the outer equations in cylindrical geometry may be written in terms of  $\tilde{\psi}$  and  $\tilde{\phi}$  as

$$(f\tilde{\psi}')' - fg\tilde{\psi} = 0 \quad (4.13)$$

$$\gamma\tilde{\psi} = -ik_{\parallel}\tilde{\phi} \quad (4.14)$$

where

$$f = \frac{r}{k^2} \quad (4.15)$$

and

$$g = k^2 + \frac{(m/r)^2 - (n/R)^2}{r^2 k^2} + \left(\frac{n}{R}\right)^2 \frac{2\mu_0 p'_0}{(\mathbf{k} \cdot \mathbf{B}_0)^2 r} + \frac{(mB_{\theta}/r - nB_z/R)}{\mathbf{k} \cdot \mathbf{B}_0} \left( \frac{2\mu_0 p'_0}{rB_0^2} - \frac{2\mu_0 p'_0}{B_0^2} \lambda_0 + \lambda'_0 \right) - \frac{1}{r} \left( \frac{r\mu_0 p'_0}{B_0^2} \right)' + \frac{2}{k^2 r} \left(\frac{n}{R}\right)^2 \frac{\mu_0 p'_0}{B_0^2} + \left( \frac{\mu_0 p'_0}{B_0^2} \right)^2 - \frac{2mn}{r^2 R k^2} \lambda - \lambda^2. \quad (4.16)$$

## 4.2 Small- $\Delta'$ current-driven tearing modes

Equations (4.13) and (4.14) may be solved for  $\tilde{\psi}$  and  $\tilde{\phi}$  by integrating from the edge of the domain with specified boundary conditions and a dispersion relation is obtained after mapping onto solutions from the inner region. The matching parameter is defined as

$$\Delta' \equiv \frac{1}{\tilde{\psi}} \frac{\partial \tilde{\psi}}{\partial r} \Big|_{-r_s}^{+r_s} = \frac{1}{\tilde{B}_r} \frac{\partial \tilde{B}_r}{\partial r} \Big|_{-r_s}^{+r_s}. \quad (4.17)$$

We immediately note  $\tilde{\psi} \Delta' \sim \tilde{\psi}'$ . For modes not too close to marginal stability,  $\Delta' \sim a^{-1} \sim \mathcal{O}(1)$  there is a large jump in  $\tilde{\psi}'$  over the layer, and we may assume  $\tilde{\psi}'' \sim (\tilde{\psi} \Delta')' \sim (\tilde{\psi} \Delta')/l$ . The layer width,  $l$ , is defined by the region where  $\tilde{\psi}''$  (or  $\tilde{E}_{\parallel}$ ) is large, and as we shall see it is small,  $l \ll k^{-1} \sim a$ . Thus we may order

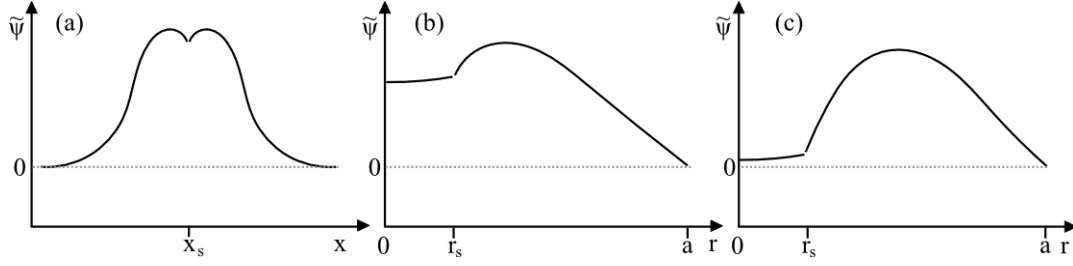


Figure 14: A sketch of (a) small- slab, cylindrical (b) small- and (c) large- solutions for in the outer region.

$\gg k^2$   $k$ . As  $B = B_0$ , the largeness of is physically related to the large gradient of  $B$  at the resonant surface. Additionally modes may be characterized as either small-,  $l < 1$ , or large-,  $l > 1$ . We will concentrate on the small- regime where it is appropriate to assume very slow growth of the mode. Using these approximations we be able to obtain the growth rate of the tearing mode, compute  $l$ , and confirm the small- tearing orderings: small layer width and growth rate and large.

Figure 14 sketches some characteristic solutions of . Figure 14(a) represents a solution with  $l \ll 1$  or small- behavior in symmetric slab geometry where the tearing approximations are valid. Figures 14(b) and (c) represent cylindrical solutions with small- and large- respectively. The small- solutions are similar to the behavior of the modes in Part III, for example compare with Fig. 26. The large- solution is an example of the regime where the mode transitions to ideal behavior as  $0$  at  $r_s$ .

As discussed in Chapter 7 of Ref. [1], one may open the term on the RHS of the parallel vorticity equation, Eqn. (4.4), and eliminate a term  $B$  after writing the Lorentz force on the right-hand side in terms of the curvature vector . With uniform background mass density, the linear version of the parallel vorticity equation is

$$m_i n_0 (\pi + \mathbf{v}_0 \cdot \nabla) U = B_0 (\mathbf{B}_0 \cdot \nabla) \frac{J}{B_0} + B_0 \left\langle \mathbf{B} \cdot \nabla \right\rangle \frac{J_0}{B_0} + 2\mathbf{b}_0 \cdot \nabla \left\langle p + \frac{1}{2} \mathbf{v}_0^2 \right\rangle \mathbf{b}_0 \quad (4.18)$$

where  $\mathbf{b}_0 = \mathbf{B}_0 / B_0$ ,  $\mathbf{b}_0 = r b^2 \mathbf{e}_r$ ,  $b = B_0 / B$ , and the parallel vorticity is  $U = \mathbf{b}_0 \cdot \nabla \psi$ . Our considerations will neglect both the coupling to pressure and viscous contributions until Sec. 11. In the inner layer, the line-bending and kink terms (the second and third terms on the RHS of Eqn. (4.18)) may be written as

$$B_0 (\mathbf{B}_0 \cdot \nabla) \frac{J}{B_0} + B_0 \left\langle \mathbf{B} \cdot \nabla \right\rangle \frac{J_0}{B_0} = \frac{B_0^2}{0} \left\{ ik \frac{d\phi_0}{dr} + ik \phi_0 \frac{d}{dr} - n_0 v_A^2 ik \right\} \quad (4.19)$$

where the kink term may be neglected given the small layer width and  $l\tilde{\psi}'' \sim \Delta'\tilde{\psi}$ , and

$$\mu_0\tilde{J}_{\parallel} \simeq -B_0\tilde{\psi}'' . \quad (4.20)$$

The kink term is still associated with instability drive, however for the tearing mode this drive is provided through the solution to the equations in the outer region and the determination of  $\Delta'$ . We make a Taylor expansion of equilibrium quantities in the small layer around  $r_s$ , where  $x \equiv r - r_s$ ,  $x \sim \epsilon r_s$ , and  $\epsilon$  is a small parameter:

$$\hat{\mathbf{b}}_0 \rightarrow \hat{\mathbf{b}}_{0s} + x\hat{\mathbf{b}}'_{0s} + \frac{1}{2}x^2\hat{\mathbf{b}}''_{0s} + \mathcal{O}(\epsilon^3) \quad (4.21)$$

$$\mathbf{k} \rightarrow \mathbf{k}_s + x\mathbf{k}'_s + \frac{1}{2}x^2\mathbf{k}''_s + \mathcal{O}(\epsilon^3) . \quad (4.22)$$

Finally, assuming the flow is nearly incompressible and noting that the inner-region aspect ratio is small,  $kl \sim \mathcal{O}(\epsilon)$ , due to the smallness of the layer width, we may order  $\tilde{v}_r \sim \epsilon\tilde{v}_{\perp}$  and  $\tilde{\phi} \sim \mathcal{O}(1)$  implies  $\tilde{\phi}' \sim \mathcal{O}(\epsilon^{-1})$ . We order each successive radial derivative of  $\tilde{\phi}$  as  $\epsilon^{-1}$  and may write the vorticity to leading order as

$$\tilde{U} = \tilde{\phi}'' + \mathcal{O}(\epsilon^{-1}) .$$

We choose the ion-rest frame where  $\mathbf{v}_0 = 0$ , and neglect viscosity and the coupling to  $\tilde{p}$  through curvature effects. Thus to leading order in each term the inner layer equations for parallel vorticity and magnetic flux (the radial induction equation, Eqn. (4.3)) become

$$\gamma\tilde{\phi}'' = -v_A^2 ik'_{\parallel s} x\tilde{\psi}'' \quad (4.23)$$

$$\gamma\tilde{\psi} = -ik'_{\parallel s} x\tilde{\phi} + \frac{\eta}{\mu_0}\tilde{\psi}'' \quad (4.24)$$

where we make use of the fact that  $k_{\parallel s} = 0$ . Contributions from cylindrical curvature are small with this ordering, and the inner layer equations are the same for slab geometry.

These coupled equations may be expressed as a single integro-differential equation via the following substitutions: Following the method described in Ref. [1], we substitute  $\tilde{E} = -\tilde{\phi}'$ , where the significance of notation connects the streamfunction,  $\tilde{\phi}$ , to the electric potential,  $\tilde{\Phi}$  through the perpendicular  $\mathbf{E} \times \mathbf{B}$  flow. If this flow dominates,

$$\tilde{\mathbf{v}}_{E \times B} = \frac{\tilde{\mathbf{E}} \times \mathbf{B}_0}{B_0^2} \simeq -\frac{\nabla\tilde{\Phi}}{B_0} \times \hat{\mathbf{b}}_0 \simeq -\nabla\tilde{\phi} \times \hat{\mathbf{b}}_0 . \quad (4.25)$$

We may also relate  $\tilde{\psi}$  to parallel component of the vector potential,  $\tilde{A}_{\parallel}$ , given the representation of  $\tilde{B}$  in Eqn. (4.7). In fact, some formulations use the parallel component of Maxwell's equation,  $\tilde{E}_{\parallel} = -\hat{\mathbf{b}}_0 \cdot \nabla \tilde{\Phi} - \partial \tilde{A}_{\parallel} / \partial t$ , with  $\tilde{E}_{\parallel} = \eta \tilde{J}_{\parallel}$  to derive Eqn. (4.24) instead of the radial induction equation. Returning to our initial point, we substitute  $\tilde{E} = -\tilde{\phi}'$  into Eqn. (4.23),

$$\gamma \tilde{E}' = v_A^2 i k'_{\parallel s} x \tilde{\psi}'' = v_A^2 i k'_{\parallel s} \left[ x^2 \left( \frac{\tilde{\psi}}{x} \right)' \right]' . \quad (4.26)$$

Integrating this equation yields

$$\gamma \tilde{E} = v_A^2 i k'_{\parallel s} x^2 \left( \frac{\tilde{\psi}}{x} \right)' + C \quad (4.27)$$

where  $C$  is a constant of integration to be determined by the matching conditions. Dividing Eqn. (4.24) by  $x$  and taking the derivative we find

$$\gamma \left( \frac{\tilde{\psi}}{x} \right)' = i k'_{\parallel s} \tilde{E} + \frac{\eta}{\mu_0} \left( \frac{\tilde{\psi}''}{x} \right)' \quad (4.28)$$

which after substituting in Eqns. (4.26) and (4.27), may be written

$$\left[ 1 - \left( \frac{v_A k'_{\parallel s} x}{\gamma} \right)^2 \right] \tilde{E} - \frac{\eta}{\mu_0} \frac{x^2}{\gamma} \left[ \frac{\tilde{E}'}{x^2} \right]' = \frac{C}{\gamma} . \quad (4.29)$$

To match to the outer solution we examine the behavior of this equation at large  $x$ ,  $x \gg l$ , which gives a balance of the second term on the LHS and the term on the RHS,  $\left( v_A k'_{\parallel s} x \right)^2 \tilde{E} \simeq \gamma C$ . Thus we may expect

$$\tilde{\phi}' \simeq - \frac{\gamma C}{\left( v_A k'_{\parallel s} x \right)^2}, \quad x \gg l \quad (4.30)$$

The zero- $\beta$  asymptotic behavior of the outer solution as it approaches the singular layer is given by Hazeltine and Meiss as

$$\tilde{\phi}_{outer} \rightarrow \tilde{\phi}_{R,L} + \frac{\tilde{\phi}_0}{x} \quad (4.31)$$

where  $\tilde{\phi}_0$  and  $\tilde{\phi}_{R,L}$  are constants and  $\tilde{\phi}_{R,L}$  may differ on each side of the layer. Given Eqn. (4.14) the associated behavior of  $\tilde{\psi}$  is

$$\tilde{\psi}_{outer} \rightarrow \tilde{\psi}_{R,L} x + \tilde{\psi}_0 \quad (4.32)$$

where  $\gamma \tilde{\psi}_0 = -i k'_{\parallel s} x \tilde{\phi}_0$  and  $\tilde{\psi}_{R,L}$  and  $\tilde{\phi}_{R,L}$  are similarly related. Combining Eqns. (4.30)-(4.32), we find the

relation

$$\tilde{\psi}_0 = -\frac{iC}{v_A^2 k'_{\parallel}}. \quad (4.33)$$

Finally, we integrate  $\tilde{J}_{\parallel}$  over the layer,

$$\int \tilde{J}_{\parallel} dx \simeq \int \tilde{\psi}'' dx = \Delta' \tilde{\psi}_0 = -\frac{iC\Delta'}{v_A^2 k'_{\parallel}} \quad (4.34)$$

$$= \frac{\gamma}{v_A^2 i k'_{\parallel}} \int \frac{\tilde{E}'}{x} dx \quad (4.35)$$

where the relation on the first line is established through the definition of  $\Delta'$ , Eqn. (4.17), and the relation on the second line from the parallel vorticity equation, Eqn. (4.23). Using this to establish a relation between  $C$  and  $\tilde{E}$ , we may now rewrite Eqn. (4.29) as

$$\left[ 1 - \left( \frac{v_A k'_{\parallel s} x}{\gamma} \right)^2 \right] \tilde{E} - \frac{\eta}{\mu_0} \frac{x^2}{\gamma} \left[ \frac{E'}{x^2} \right]' = \frac{1}{\Delta'} \int \frac{\tilde{E}'}{x} dx. \quad (4.36)$$

Ref. [1] describes the terms on the LHS as inertial, line-bending, and resistive contributions, respectively. The term on the RHS is the contribution from the kink term as it is linked to the solution in the outer region, and thus the kink drive of the mode, through  $\Delta'$ . For small- $\Delta'$  tearing the mode is close to marginal stability and the growth rate is small enough that the inertial term may be ignored. This is equivalent to the constant- $\tilde{\psi}$  approximation used by Furth, Kileen and Rosenbluth (FKR) [10].

We may estimate the layer width and the growth rate through a balance of the line-bending, resistive and kink terms. Using  $x \rightarrow l$  and  $\tilde{E}' \sim \tilde{E}/l$ , the balance of the line-bending and resistive terms,  $\left( v_A k'_{\parallel s} l / \gamma \right)^2 \sim (\eta / \mu_0 l^2 \gamma)$ , gives an expression for the layer width,

$$l^2 \sim \left( \gamma \frac{\eta}{\mu_0} \right)^{1/2} \frac{1}{v_A k'_{\parallel s}}. \quad (4.37)$$

The balance of the resistive and kink terms,  $(\eta / \mu_0 l^2 \gamma) \sim 1 / \Delta' l$ , after substitution for  $l$  gives

$$\gamma \sim \Delta'^{4/5} \left( \frac{\eta}{\mu_0} \right)^{3/5} \left( v_A k'_{\parallel s} \right)^{2/5}. \quad (4.38)$$

The exact solution to the integro-differential equations for  $\tilde{E}$ , Eqn. (4.36) without the first term on the LHS gives may be solved for in terms of parabolic cylinder functions. The exact result is (see Ref. [1] for the

solution method, this is the result of FKR, Ref. [10]),

$$\gamma_{MHD} = \left[ \frac{\Delta' \Gamma(1/4)}{2\pi \Gamma(3/4)} \right]^{4/5} \left( \frac{\eta}{\mu_0} \right)^{3/5} \left( v_{As} k'_{\parallel s} \right)^{2/5}. \quad (4.39)$$

The tearing mode grows on a hybrid-resistive-Alfvén-time scale,  $\gamma_{MHD} \sim S^{-3/5}$ , as expected. The sign of  $\gamma_{MHD}$  depends on the sign of  $\Delta'$ , thus  $\Delta'$  is also a stability parameter where instability is characterized by  $\Delta' > 0$ . Thus for considerations of tearing stability only the solution to the Newcomb equation in the outer region is necessary. Marginal stability has  $\Delta' = 0$  and we expect modes which become unstable though the slow profile evolution on a transport-time scale to be in the small- $\Delta'$  regime. In fact estimates from the relaxed profiles of MST indicate  $\Delta' \sim 1 - 10$ , and make the constant- $\tilde{\psi}$  approximation fitting for the tearing activity in the RFP.

To find the layer width, where  $\tilde{E}_{\parallel}, \tilde{\psi}'' \rightarrow 0$ , we take  $x \rightarrow l$  in our inner layer equations. Dropping the last term  $\sim \eta \tilde{\psi}''$  in Eqn. (4.24) and combining this with Eqn. (4.23) with  $\tilde{\phi}'' \rightarrow \tilde{\phi}/l^2$  we find

$$\gamma \tilde{\psi} \simeq -i k'_{\parallel s} l \tilde{\phi} \simeq \left( i k'_{\parallel s} v_A \right)^2 l^4 \frac{\tilde{\psi}''}{\gamma} \simeq \left( k'_{\parallel s} v_A \right)^2 l^4 \frac{\left( \Delta' \tilde{\psi} \right)'}{\gamma} \simeq \left( k'_{\parallel s} v_A \right)^2 l^3 \frac{\Delta' \tilde{\psi}}{\gamma}. \quad (4.40)$$

Solving for  $l$  after substitution of Eqn. (4.39) to eliminate  $v_A k'_{\parallel s}$  and dropping a factor of 1.28 gives the layer width,

$$l \simeq \Delta' \delta_{\eta}^2. \quad (4.41)$$

Where we define the resistive skin depth,  $\delta_{\eta}/a = 1/\sqrt{S\gamma\tau_A}$ , by the characteristic gradient length scale required for the resistive term to balance the inertia term in the radial induction equation, Eqn. (4.3). The tearing mode is a slowly growing mode with  $\gamma \sim S^{-3/5}$ , thus we expect  $\delta_{\eta} \sim S^{-1/5}$ ,  $l \sim S^{-2/5}$  and the layer width to be small in the physically-relevant asymptotic limit of large  $S$ . These arguments justify our assumptions.

In Sec. 9.1, we show  $\Delta' L_B = 2(1/kL_B - kL_B)$  for our particular periodic slab configuration with an infinite current sheet enclosed by distant conducting walls, where  $L_B$  is the gradient scale length of the magnetic field. As the positive contribution to  $\Delta'$  is proportional to  $(kL_B)^{-1}$  the most unstable mode corresponds the longest wavelength, and the negative contribution,  $-2kL_B$ , stabilizes modes with large wavenumber. This behavior is similar for cylindrical configurations [18]. Thus the most unstable tearing mode has a long wavelength, is easy to detect experimentally, and its global structure greatly impacts plasma confinement.

### 4.3 Finite- $\beta$ effects

Of course, the tearing mode is not the only source of reconnection. Coppi, Greene and Johnson extended FKR's result to cases with finite pressure and distinguished a spectrum of modes from resistive interchange to tearing [39]. The distinction between being that the tearing drive is provided by the kink term, through the matching condition  $\Delta'$ ; whereas resistive interchange is an instability driven through the equilibrium quantities at the resonant surface with non-zero curvature and  $p'_0$ . It is manifest through the interchange term in the parallel vorticity equation (Eqn. (4.18)),  $2\hat{\mathbf{b}}_0 \times \boldsymbol{\kappa}_0 \cdot \nabla \tilde{p}$ .

The linearized energy equation, Eqn. (2.31), is used to find an expression for  $\tilde{p}$ ,

$$\gamma \tilde{p} = ik_{\perp} \tilde{\phi} p'_0 - \Gamma p_0 \nabla \cdot \tilde{\mathbf{v}} \quad (4.42)$$

where we have assumed  $\mathbf{v}_0 = 0$  and  $\mathbf{q} = 0$ . Thus the interchange term becomes

$$2\hat{\mathbf{b}}_0 \times \boldsymbol{\kappa}_0 \cdot \nabla \tilde{p} = 2\hat{\mathbf{b}}_0 \times \boldsymbol{\kappa}_0 \cdot \nabla \left( \frac{ik_{\perp} \tilde{\phi} p'_0 - \Gamma p_0 \nabla \cdot \tilde{\mathbf{v}}}{\gamma} \right) \simeq 2 \frac{b_{0\theta}^2}{r} \frac{k_{\perp s}^2}{\gamma} p'_0 \tilde{\phi} - 2 \frac{b_{0\theta}^2}{r} \Gamma p_0 ik_{\perp s} \nabla \cdot \tilde{\mathbf{v}} \quad (4.43)$$

where we have assumed the dominant curvature is poloidal,  $\boldsymbol{\kappa}_0 = -b_{0\theta}^2/r$  with  $b_{0\theta} = B_{0\theta}/B_0$ , as is the case for the RFP. In a cylinder, Coppi et al. find instability driven by the first term on the RHS through  $p'_0$  evaluated at  $r_s$ . This interchange mode is unstable in regions of bad curvature which for the RFP is approximately whenever the equilibrium pressure decrease is radially outward. The second term on the RHS is first time  $\nabla \cdot \tilde{\mathbf{v}}$  has appeared explicitly in our equations, and through this term the mode is coupled to compressible motions. For slab cases  $\boldsymbol{\kappa}_0 \rightarrow 0$  and there is no contribution from the interchange term, thus no dependence on  $\beta$  through coupling to  $\nabla \cdot \tilde{\mathbf{v}}$  with a resistive-MHD model.

### 4.4 Notes and extensions

The configuration itself has implications on the appropriate model as well, our considerations use conducting walls placed on each horizontal side of Fig. 13 and vertical periodic boundary. The flux is then conserved, and the tearing instability can reconnect at most the available flux before nonlinear saturation. This is the case for *spontaneous reconnection* as there is no drive from the boundary. An alternative configuration is that of *driven reconnection*, where flux is pushed in through the horizontal boundary and allowed to flow out the vertical boundary. Studies of driven configurations may approximate astrophysical effects such as solar

flares or the Earth’s magneto-tail. Analytic studies typically use a model to establish a reconnection rate, which measures how quickly the flux passes through the inner region, as opposed to a growth rate which measures the exponential time-rate of change of the amplitude of the perturbation.

The flux in MST undergoes a rapid change during sawtooth events. For example, in the low-current discharges studied by Kuritsyn et al. the toroidal flux increases by 7 – 10% over approximately a tenth of a millisecond, even though the associated toroidal-field reversal is deepened. Our cases with a conducting wall boundary condition do not capture this effect as flux is conserved with a specified constant electric field at the boundary. However, one expects that core-resonant tearing modes in a RFP are spontaneously unstable in experimental cases, and our model is sufficient to qualitatively capture their dynamics.

The edge-resonant  $m = 0$  modes are typically nonlinearly driven through core-mode coupling during a large sawtooth event, as predicted computationally in Ref. [20]. Experimentally this has been observed, as Choi et al. measured the drive through the  $m = 0$  nonlinear advective term of Ohm’s law [40], and Tharp et al. measured the Hall-term drive [41]. As we model both terms in our two-fluid computations present in Part V, we self-consistently capture both the core-mode spontaneous drive through an unstable-profile configuration and the nonlinear drive of the  $m = 0$  mode.

## 5 First-order FLR effects on the tearing mode

As discussed in Secs. 2 and 3, in the experimentally-relevant parameter regimes of interest, important non-MHD effects arise from particle motions as finite-Larmor-radius (FLR) contributions. The FLR effects may be included in a fluid model, to first order, with a two-fluid Ohm’s law and ion gyroviscosity. Their influence on tearing modes has been the subject of many theoretical studies over more than four decades. Important FLR effects on RFP tearing, drift-tearing and kinetic-Alfvén-wave (KAW) effects, are discussed in the next two subsections. These effects are considered via the inclusion of the linearized Hall term in Ohm’s law:  $(\mathbf{J}_0 \times \tilde{\mathbf{B}} + \tilde{\mathbf{J}} \times \mathbf{B}_0) / n_0 e$ . In Sec. 5.1 we include the  $\mathbf{J}_0 \times \tilde{\mathbf{B}}$  contribution along with  $\mathbf{v}_0 \neq 0$ , which together represent advection of  $\tilde{\mathbf{B}}$  by  $\mathbf{v}_{e0}$  and leads to a drift-tearing response. In Sec. 5.2 we include the second contribution,  $\tilde{\mathbf{J}} \times \mathbf{B}_0$ , which couples the equations to  $\tilde{B}_{\parallel}$  and introduces two-fluid responses via the whistler- and kinetic-Alfvén-waves.

We will not carry out calculations in complete detail, but intend to only illustrate the physical importance and origin of these FLR effects. Thus the dispersion relations we find will only constitute a heuristic model, and references to more complete works will be indicated.

## 5.1 Diamagnetic-drift tearing

Previous drift-tearing work begins with Coppi's analysis of ion FLR effects, which identifies a stabilizing drift-tearing behavior resulting from pressure gradients at the resonant surface [42]. As appropriate for large-aspect ratio tokamaks, this study orders both the perturbed pressure and the reconnecting component of magnetic field to be small. A drift-tearing response occurs when the ion and electron dynamics separate parallel to  $\mathbf{k}$  at the resonant flux surface.

The steady-state mean fluid velocities may be found by crossing Eqn. (2.12) with  $\mathbf{B}$ , and neglecting contributions from  $\mathbf{\Pi}_\alpha$  and  $\mathbf{R}_\alpha$ :

$$\mathbf{v}_{i\perp} = \frac{\mathbf{E} \times \mathbf{B}}{B^2} + \frac{\mathbf{B} \times \nabla p_i}{neB^2}, \quad (5.1)$$

$$\mathbf{v}_{e\perp} = \frac{\mathbf{E} \times \mathbf{B}}{B^2} - \frac{\mathbf{B} \times \nabla p_e}{neB^2}, \quad (5.2)$$

and associated current density,

$$\mathbf{J}_\perp = ne(\mathbf{v}_{i\perp} - \mathbf{v}_{e\perp}) = \frac{\mathbf{B} \times \nabla p}{neB^2} \quad (5.3)$$

consistent with Eqn. (1.18). As noted, the  $\mathbf{E} \times \mathbf{B}$  drifts do not depend on charge and do not lead to separation of the fluid species, unlike the diamagnetic drift. Diamagnetic-drift tearing may be examined by including contributions from the  $\mathbf{v}_{i\perp 0}$ ,  $\mathbf{v}_{e\perp 0}$ , and  $\mathbf{J}_\perp 0$  in our inner layer equations.

There are additional terms to consider in the parallel vorticity equation, Eqn. (4.18): the advective term  $\mathbf{v}_0 \cdot \nabla \tilde{U}$ , and  $-\hat{\mathbf{b}}_0 \cdot \nabla \times \nabla \cdot \mathbf{\Pi}$ . As shown in Part III, there is a contribution from  $-\hat{\mathbf{b}}_0 \cdot \nabla \times \nabla \cdot \mathbf{\Pi}_{gv}$  proportional to  $p'_0$  which exactly cancels with the diamagnetic contribution to the advective term. Thus the parallel vorticity equation, with an advective contribution from the  $\mathbf{E} \times \mathbf{B}$  flow, becomes

$$(\gamma + i\omega_{E \times B}) \tilde{\phi}'' = -v_A^2 ik'_{\parallel s} x \tilde{\psi}'' \quad (5.4)$$

where  $\omega_{E \times B} = k_{\perp s} v_{E \times B}$ .

The radial-induction equation will now have a contribution from the advective term  $\nabla \times (\mathbf{v}_{e0} \times \tilde{\mathbf{B}})$ ,

$$\hat{r} \cdot \nabla \times (\mathbf{v}_{e0} \times \tilde{\mathbf{B}}) = \hat{r} \cdot \left[ (\tilde{\mathbf{B}} \cdot \nabla) \mathbf{v}_{e0} - (\mathbf{v}_{e0} \cdot \nabla) \tilde{\mathbf{B}} \right] = -i\mathbf{k} \cdot \mathbf{v}_{e0} \tilde{B}_r \simeq -(ik_{\perp s})^2 v_{e0} B_0 \tilde{\psi} \quad (5.5)$$

where  $\mathbf{v}_{e0}$ , as determined by Eqn. (5.2), is incompressible and has no radial component. With this term, the

inner-region radial-induction equation becomes

$$(\gamma + i\omega_{*e} + i\omega_{E \times B}) \tilde{\psi} = -ik'_{\parallel s} x \tilde{\phi} + \frac{\eta}{\mu_0} \tilde{\psi}'' \quad (5.6)$$

where  $\omega_{*e} = k_{\perp s} v_{*e0} = -k_{\perp s} p'_{e0} / n_0 e B_0$  (mean quantities evaluated at  $r_s$ ) is the diamagnetic-drift modification.

Using Eqns. (5.4) and (5.6) as the inner layer equations we find the dispersion relation relative to the MHD growth rate is

$$(\gamma + i\omega_{*e} + i\omega_{E \times B})^4 (\gamma + i\omega_{E \times B}) = \gamma_{MHD}^5. \quad (5.7)$$

When  $\omega_{*e} \rightarrow 0$ ,  $\gamma = \gamma_{MHD} - i\omega_{E \times B}$  and the growth rate of the mode is unchanged, however it acquires a real frequency associated with the Doppler shift of the  $\mathbf{E} \times \mathbf{B}$  flow common to both species. When  $\omega_{*e} \gtrsim \gamma_{MHD}$  the drift effect reduces the growth rate of the mode. We stress that the effects from  $\tilde{\mathbf{J}} \times \mathbf{B}_0$  have been ignored so far; this term enters the equations on the same order and is discussed in the next section. Thus we only present this relation as a heuristic description - for more complete treatments see Refs. [43, 44, 45]. As a final note, the contribution from  $\nabla p_e / ne$  to the radial induction equation vanishes as

$$\hat{r} \cdot \nabla \times \frac{\nabla \tilde{p}_e}{n_0 e} = \hat{r} \cdot \left[ \frac{\nabla \times \nabla \tilde{p}_e}{n_0 e} + \nabla \left( \frac{1}{n_0 e} \right) \times \nabla \tilde{p}_e \right] = 0. \quad (5.8)$$

## 5.2 Kinetic-Alfvén-wave mediated regime

Drake and Lee identify the importance of the parallel component of perturbed electric field in the collisionless ( $\gamma \gg 1/\tau_e$ , or equivalently  $d_e^2 \gg 1/\gamma \tau_A S$  and  $\rho_i \gg l$ ) and semi-collisional ( $\gamma \ll 1/\tau_e$  and  $\rho_i \gg l$ ) regimes that occur when the reconnection scale is smaller than the ion gyroradius [46]. The resistive-MHD regime occurs when both  $\gamma \ll 1/\tau_e$  (neglect electron inertia) and  $\rho_i \ll l$  (neglect FLR corrections), and was described in detail with our model in Sec. 4.2. Consideration of the radial component of Faraday's law without specification of  $\tilde{\mathbf{E}}$ ,

$$\gamma B_0 i k_{\perp} \tilde{\psi} = -\hat{r} \cdot \nabla \times \tilde{\mathbf{E}} = -i k_{\perp} \tilde{E}_{\parallel} + i k_{\parallel} \tilde{E}_{\perp} \quad (5.9)$$

demonstrates the significance of  $\tilde{E}_{\parallel}$ , given  $k_{\parallel} \rightarrow 0$  at  $r_s$ . The perpendicular electric field may be written as

$$\tilde{E}_{\perp} = -i k_{\perp} \tilde{\phi} B_0 - i k_{\perp} \tilde{\psi} B_0 \mathbf{v}_{e0\parallel} - \frac{\tilde{J}_r B_0}{n_0 e} - \frac{i k_{\perp} \tilde{p}_e}{n_0 e} + \eta \tilde{J}_{\perp} + \frac{m_e}{n e^2} \gamma \tilde{J}_{\perp}. \quad (5.10)$$

Thus the contribution from  $\tilde{\mathbf{v}} \times \mathbf{B}_0$  gives the ion advective contribution,  $ik_{\perp}\tilde{\phi}$ , in Eqn. (4.24) through  $\tilde{E}_{\perp}$ . When  $\rho_i \gg l$ , the ions become demagnetized and are no longer sensitive to the dynamics in the thin tearing layer. Thus in the collisionless and semi-collisional limits, Drake and Lee ignore the advective contribution from  $\tilde{E}_{\perp}$  to Eqn. (5.9), and the dynamics in the layer are determined fully by  $\tilde{E}_{\parallel}$ ,

$$\tilde{E}_{\parallel} = -\hat{\mathbf{b}}_0 \cdot \left[ \mathbf{v}_{e0} \times \tilde{\mathbf{B}} + \frac{\nabla \tilde{p}_e}{ne} \right] + \eta \tilde{J}_{\parallel} + \frac{m_e}{ne^2} \gamma \tilde{J}_{\parallel}. \quad (5.11)$$

We will ignore the drift contribution,  $\mathbf{v}_{e0} \times \tilde{\mathbf{B}}$ , discussed in the last section, note  $\hat{\mathbf{b}}_0 \cdot \nabla \tilde{p}_e \simeq ik'_{\parallel s} x \tilde{p}_e$  cancels with a contribution from  $\tilde{E}_{\perp}$  consistent with Eqn. (5.8), and use the tearing layer ordering to justify  $k_{\perp s} \tilde{J}_{\parallel} \gg k'_{\parallel s} x \tilde{J}_{\perp}$  in the resistive and electron inertia contributions. The distinction between the collisionless and semicollisional regimes may be understood with a fluid model by comparing the resistive  $\sim \eta$  and electron inertia  $\sim \gamma m_e / ne^2$  terms in the parallel Ohm's law, Eqn. (5.11). Using the definition of resistivity from Sec. 2.3,  $\eta = m_e / ne^2 \tau_e$ , we note the resistive term dominates in the semi-collisional regime, and the electron inertia term dominates in the collisionless regime, as one would expect from the nomenclature.

### Collisionless regime

In the collisionless regime at  $r_s$ ,  $\tilde{E}_{\parallel} \simeq m_e \gamma \tilde{J}_{\parallel} / ne^2 = \gamma d_e^2 \mu_0 \tilde{J}_{\parallel} \simeq -\gamma d_e^2 B_0 \tilde{\psi}''$ , where we have used Eqn. (4.20), thus Eqn. (5.9) at  $r_s$  becomes

$$\tilde{\psi} \simeq -d_e^2 \tilde{\psi}'' \simeq d_e^2 \frac{\tilde{\psi} \Delta'}{l_k}. \quad (5.12)$$

This gives an expression for the collisionless layer width,

$$l_k = \Delta' d_e^2. \quad (5.13)$$

Individual electrons slightly off the resonant surface experience a Doppler shift,  $\omega_D = \mathbf{k} \cdot \hat{\mathbf{b}}_0 v_{Te} \simeq k'_{\parallel s} x v_{Te}$ , from their random-thermal parallel motion along a field-line. If  $\omega_D > \gamma$  these electron are subject to an ac rather than a dc electric field. Drake and Lee point out the layer width of the mode is limited by this Doppler shift, such that  $\gamma_k \simeq \omega_D$ . Thus the collisionless growth rate is

$$\gamma_k \simeq k'_{\parallel s} l_k v_{Te} \simeq k'_{\parallel s} \Delta' d_e^2 v_{Te}. \quad (5.14)$$

A significant feature of the collisionless regime is neither  $l_k$  or  $\gamma_k$  depend on  $S$ . Rather they are determined by electron inertia and  $\sim d_e^2$ . This regime is of interest for hot fusion plasmas, however typical RFP discharges

are semi-collisional and thus our regime of study is that which resistivity dominates.

### Semi-collisional regime

In the semi-collisional regime  $\tilde{E}_{\parallel} \simeq \eta \tilde{J}_{\parallel} \simeq -(\eta/\mu_0) B_0 \tilde{\psi}''$ , and we may write Eqn. (5.9) as

$$\gamma_{sc} \tilde{\psi} \simeq -\frac{\eta}{\mu_0} \tilde{\psi}'' \simeq \frac{\eta}{\mu_0} \frac{\tilde{\psi} \Delta'}{l_{sc}}. \quad (5.15)$$

The parallel electron motion is no longer free streaming, but limited by collisions thus  $\omega_D \simeq (k'_{\parallel s} x v_{Te})^2 \tau_e$ . Again, this Doppler shift limits the growth rate at the semi-collisional layer width,  $l_{sc}$ , thus  $\omega_D(l_{sc}) \simeq \gamma_{sc}$ . Combining this equation with Eqn. (5.15), expressions for the layer width and growth rate in the semi-collisional regime are

$$l_{sc} \simeq \Delta' \delta_{sc}^2 \simeq \left( \frac{\eta}{\mu_0} \frac{1}{d_e k'_{\parallel s} v_{Te}} \right)^{2/3} \Delta'^{1/3} \quad (5.16)$$

and

$$\gamma_{sc} \simeq \left( \frac{\eta}{\mu_0} \right)^{1/3} \Delta'^{2/3} (d_e k'_{\parallel s} v_{Te})^{2/3}. \quad (5.17)$$

The semi-collisional growth rate scales as  $S^{-1/3}$  and the layer width as  $S^{-2/3}$ . The layer width has the same form as the collisional case,  $\Delta' \delta_{sc}^2$ , where  $\delta_{sc}/a = 1/\sqrt{S\gamma_{sc}\tau_A}$ .

Given the expressions for layer width in the three regimes, Eqns. (4.41), (5.13) and (5.16), we define the tearing skin depth as

$$\delta = \sqrt{\frac{a^2}{S\gamma_{\tau_A}} + d_e^2} \quad (5.18)$$

which allows us to write a single expression for the small- $\Delta'$  layer width valid everywhere,

$$l \simeq \Delta' \delta^2. \quad (5.19)$$

### Kinetic-Alfvén-wave mediated regime

That the separation of the electron and ion responses in both the semi-collisional and collisionless regimes is not specifically dependent on ion thermal energy ( $\rho_i$ ) but also arises at scales below the ion-sound gyroradius,  $\rho_s = c_s/\omega_{ci}$ , from electron thermal energy was emphasized in Ref. [47] for the  $m = 1$  tokamak mode. This type of separation is discussed in general terms for reconnection in Ref. [48] as a kinetic-Alfvén-wave type dispersive response that maintains reconnection outflows at scales below  $\rho_s$ . We may illustrate this response in a fluid model with the inclusion of the Hall term in the radial induction equation. In addition to drift

terms from Eqn. (5.5), we include

$$\hat{r} \cdot \nabla \times [\tilde{\mathbf{J}} \times \mathbf{B}_0] = \hat{r} \cdot [(\mathbf{B}_0 \cdot \nabla) \tilde{\mathbf{J}} - (\tilde{\mathbf{J}} \cdot \nabla) \mathbf{B}_0] = (i\mathbf{k} \cdot \mathbf{B}_0) \tilde{J}_r. \quad (5.20)$$

Using Ampere's law to solve for  $\tilde{J}_r$ ,

$$\mu_0 \tilde{J}_r = ik_{\perp} \tilde{B}_{\parallel} + ik_{\parallel} B_0 \tilde{\psi}'. \quad (5.21)$$

Thus the full contribution from the Hall term, with the inner layer ordering, is

$$\hat{r} \cdot \nabla \times [\tilde{\mathbf{J}} \times \mathbf{B}_0 + \mathbf{J}_0 \times \tilde{\mathbf{B}}] = -k_{\perp s} k'_{\parallel s} x \frac{B_0 \tilde{B}_{\parallel}}{\mu_0} - (k'_{\parallel s} x)^2 \frac{B_0^2}{\mu_0} \tilde{\psi}' + (k_{\perp s})^2 J_{0\perp} B_0 \tilde{\psi} + k_{\perp s} k'_{\parallel s} x J_{0\parallel} B_0 \tilde{\psi} \quad (5.22)$$

where the last two terms are associated with the drift effects described in Sec. 5.1. We may neglect the second ( $\mathcal{O}(\epsilon^2)$ ) and fourth ( $\mathcal{O}(\epsilon)$ ) terms, thus the inner layer radial induction equation becomes

$$(\gamma + i\omega_{*e} + i\omega_{E \times B}) \tilde{\psi} = ik'_{\parallel s} x \left( -\tilde{\phi} + \frac{\tilde{B}_{\parallel}}{\mu_0 n_0 e} \right) + \frac{\eta}{\mu_0} \tilde{\psi}'' \quad (5.23)$$

and the solution is now coupled to  $\tilde{B}_{\parallel}$  when  $1/\mu_0 n_0 e \sim d_i^2 e/m_i$  is appreciable. The expression for  $\tilde{B}_{\parallel}$  from the parallel induction equation has considerably more terms than the radial component. Until now our equations have been general for both slab and cylindrical cases, for simplicity we consider  $\tilde{B}_{\parallel}$  for a slab without profile gradients ( $\nabla B_0 = p'_0 = 0$ ) or a mean flow ( $\mathbf{v}_0 = 0$ ). In this case

$$\gamma \tilde{B}_{\parallel} = -B_0 \nabla_{\perp} \cdot \tilde{\mathbf{v}} + d_i v_A ik'_{\parallel s} x B_0 \tilde{\psi}'' + \eta \nabla^2 \tilde{B}_{\parallel}. \quad (5.24)$$

where the first term on the RHS comes from  $\hat{\mathbf{b}} \cdot \nabla \times (\tilde{\mathbf{v}} \times \mathbf{B}_0)$  and the second from  $\hat{\mathbf{b}} \cdot \nabla \times (\tilde{\mathbf{J}} \times \mathbf{B}_0)$ . Unlike the resistive-MHD cases where the guide field,  $B_0(r_s)$ , was unimportant, the cases where the contribution from  $\tilde{B}_{\parallel}$  is large will have a critical dependence. Additionally, it is evident that mode is now coupled to the perpendicular compression,  $\nabla_{\perp} \cdot \tilde{\mathbf{v}} = \nabla \cdot \tilde{\mathbf{v}} - ik'_{\parallel s} x \tilde{v}_{\parallel}$ , through the first term on the RHS.

Mirnov et al. (and references contained within) discuss the two-fluid responses through the coupling to  $\tilde{B}_{\parallel}$  as whistler-mediated and kinetic-Alfvén-mediated regimes with a double layer formulation [14]. Their study of slab geometry with uniform pressure orders the ratio of the reconnecting and guide fields to be small,  $\epsilon_B \ll 1$ , includes contributions from nonzero  $\nabla \cdot \tilde{\mathbf{v}}$ , and considers the regime of  $\rho_s, d_i > \delta$ . The whistler-mediated regime may be described without coupling to the perturbed pressure through  $\nabla_{\perp} \cdot \tilde{\mathbf{v}}$ , and occurs when  $d_i/a \gg (m_i/m_e)^{1/4} (L_B/a) \epsilon_B^{-1/2}$ . This corresponds to either the large  $\epsilon_B$  or small guide field limit,

which is important in astrophysical situations but rare for confinement devices, or a small magnetic field gradient scale length,  $L_B$ . For small  $L_B$ ,  $\Delta' \sim 2/kL_B^2$  and we expect whistler-mediated reconnection to be important for large- $\Delta'$  cases. In MST,  $d_i/a \sim 0.2$ ,  $L_B/a \sim 1$ , and  $\epsilon_B \sim 1$ , thus  $(m_i/m_e)^{1/4} (L_B/a) \epsilon_B^{-1/2} \sim 8$  and whistler-mediated is not the relevant regime. Alternatively, finite- $\beta$  effects must be included to model the kinetic-Alfvén-mediated regime which occurs when  $\rho_s \gtrsim l$ . This is the relevant regime for MST. For example, in the discharges described by Ding et al. in Ref. [37], the ion-sound gyroradius is approximately  $1\text{cm}$ , less than a tenth of the minor radius but comparable to a tearing layer width. As a new result, Mirnov et. al. identify a limitation on the electron response from the diffusion of  $\tilde{B}_{\parallel}$  and find the dispersion relation

$$\frac{\Gamma_n \rho_s}{G(\Gamma_n/\sqrt{\beta})} + \frac{2}{\Delta'} = \frac{2\delta G(\Gamma_n/\sqrt{\beta})}{\pi \Gamma_n} \quad (5.25)$$

which is valid for both small- and large- $\Delta'$ . Here  $\Gamma_n$  is the normalized growth rate,  $\Gamma_n = \gamma\tau_A/\rho_s k_{\perp}$ , and the  $G$  function is defined as

$$G(x) = \frac{x^{1/2} \Gamma(1/4 + x/4)}{2\Gamma(3/4 + x/4)}. \quad (5.26)$$

Ahedo and Ramos use a different ordering to include both the transition to and the MHD regime in Ref. [49]. Their ordering allows for arbitrary  $\epsilon_B$  and  $d_i$ , but requires finite- $\beta$ ,  $\beta \gg (\gamma/v_A k_{\perp})^2$  and small- $\Delta'$ . The restriction on  $\beta$  is easily met as long as  $\beta \neq 0$  as  $(\gamma/v_A k_{\perp})^2$  is very small for tearing modes. This ordering allows them to consider the MST-relevant kinetic-Alfvén-mediated regime, while neglecting the effect of whistler waves. Their dispersion relations smoothly transition between six regimes parameterized by  $\beta$  and  $d_i$ :

1. the collisional (resistive-MHD) regime [ $\rho_s \ll l$  or  $d_i^2 \Delta' \ll l$ ],
2. at high  $\beta$ , the transition between (1) and (3) [ $\sqrt{\beta} \gg \Delta' \delta$  and  $d_i^2 \Delta' \sim l$ ],
3. the large- $d_i$ ,  $\tilde{B}_{\parallel}$ -diffusion dominated regime [ $\sqrt{\beta} \gg \Delta' \delta$  and  $d_i^2 \Delta' \gg l$ ],
4. at large  $d_i$ , the transition to between (3) and (5) [ $\rho_s \gg l$  and  $\sqrt{\beta} \sim \Delta' \delta$ ],
5. the semi-collisional regime [ $\rho_s \gg l$  and  $\sqrt{\beta} \ll \Delta' \delta$ ], and
6. at low  $\beta$ , the transition back to resistive-MHD [ $\rho_s \sim l$  and  $\sqrt{\beta} \ll \Delta' \delta$ ].

In the collisionless regime ( $\gamma \gg 1/\tau_e$ ), the transition of regime (4) may be characterized by the relation of the electron gyroradius to the layer width,  $\rho_e \gtrsim l$ . These regimes are shown in Fig. 15 with the normalized

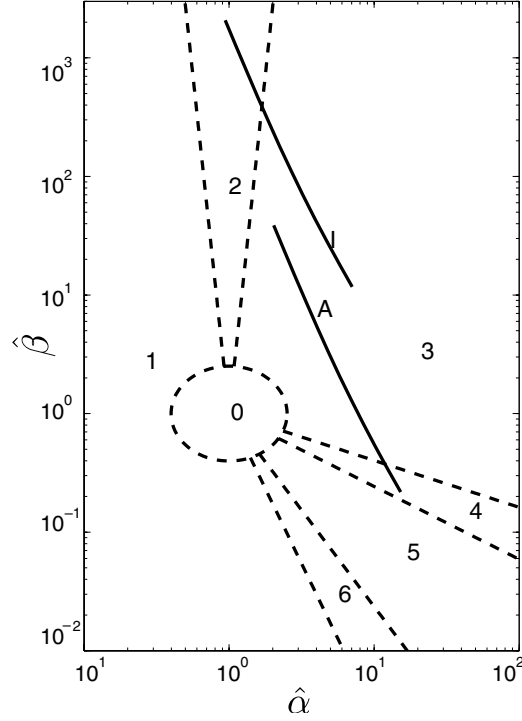


Figure 15: Dashed lines indicate the boundaries of the different parametric regions in the plane of primary input parameters. Solid lines show the location of characteristic parameters for (A) Alcator C-MOD and (I) ITER for  $k^{-1}\Delta'$  ranging from 0.1 (top) to 10 (bottom). This figure is from Ahedo and Ramos, Ref. [49].

parameters

$$\hat{\alpha} = \frac{k d_i}{\epsilon_\eta^{1/5}} \left( \frac{\epsilon_B \Delta'^2}{C^2 k_\perp^3 L} \right)^{1/5}, \quad (5.27)$$

and

$$\hat{\beta} = \frac{\beta}{\epsilon_\eta^{2/5} (\Gamma/2 + \beta)} \left( \frac{C^8 \epsilon_B k_\perp^2}{\pi^5 L \Delta'^3} \right)^{2/5}, \quad (5.28)$$

where  $\epsilon_\eta = k_\perp \eta / \mu_0 v_A$  and  $C \simeq 2.12$ . Regimes 3-5 correspond to those covered by Mirnov et al. in Ref. [14].

We will use the analytic slab dispersion relations of Refs. [14] and [49] in the transition from resistive-MHD to large  $d_i$  at high  $\beta$  (compare to Ahedo et al.) and the transition at large  $d_i$  from high  $\beta$  to small  $\beta$  (compare to Mirnov et al.) for code verification in Sec. 10. Our linear cylindrical computations with  $\Delta' \delta \sim 1$  confirm that electron-fluid separation increases the tearing growth rates in pinch profiles when  $\rho_s$  exceeds the tearing layer width.

In addition, a portion of our computations include warm-ion effects through fluid gyroviscosity. This effect only entered the preceding discussion through the gyroviscous cancellation of the diamagnetic drift in the ion momentum equation. In cylindrical geometry, our warm-ion computations show an intermediate

drift-regime with reduced growth rates at  $\rho_s$ -values that are smaller than the tearing layer width. These computations are force-free thus there is no diamagnetic-drift effect ( $\omega_{*e} = 0$ ). We will show in Sec. 11 that the drift effect results from  $\nabla B_0$  and poloidal curvature, absent in force-free slab cases. Although our model only includes first-order FLR effects, in warm-ion conditions where  $\rho_s$  is comparable to the resistive skin depth the electron dynamics are decoupled and the tearing mode becomes less sensitive to the ion dynamics. Thus first-order FLR modeling for warm ions should provide at least a semi-quantitative description of tearing through the transition from MHD to electron-MHD.

## 6 Nonlinear growth and saturation of the tearing mode

We next describe nonlinear effects on the tearing mode relevant when the island size becomes comparable or greater than the layer width. The nonlinear effects with a resistive-MHD model as described by Rutherford are reviewed in Sec. 6.1. Work on island evolution with drift and semi-collisional FLR effects is considered in Sec. 6.2. These studies will be used contextualize our nonlinear results where drift effects enter the equations through ion gyroviscosity.

### 6.1 Rutherford theory

In Rutherford theory for the resistive MHD evolution of islands, the perturbed current produces a third-order  $\mathbf{J} \times \mathbf{B}$  force, where the ordering refers to the perturbation amplitude, that counteracts the linear forces driving the island growth [50]. Figure 16 sketches this magnetic island structure. The components  $\tilde{B}_r$  and  $\tilde{J}_\parallel$  are indicated at the resonant surface, where the phase shift is specified by Eqns. (4.9) and (4.20). Additionally, the perpendicular components of  $\tilde{\mathbf{v}}$  are shown, with phases in agreement with Eqns. (4.11) and (4.12) and the phase relationship to the perturbed flux established by the radial induction equation in the outer and inner regions, Eqns. (4.14) and (4.24). Using mean-field theory we note that correlations of  $\tilde{\mathbf{v}}$  and  $\tilde{\mathbf{B}}$  can induce a second-order mean emf,  $-\langle \tilde{\mathbf{v}} \times \tilde{\mathbf{B}} \rangle_\parallel$ , as it is proportional to the square of the perturbed amplitude. This emf will drive a perturbed mean current,  $\mathcal{J}_0 \equiv \langle \mathbf{J} \rangle - \mathbf{J}_{eq}$ , which will oppose the initial equilibrium current,  $\mathbf{J}_{eq}$ , at the resonant surface. The effect is described by Eqn. (3.5) and may also be seen through consideration of the perturbations in Fig. 16. One conceptual picture of the island saturation is to consider the effect of  $\mathcal{J}_0$  on the solution of the outer region equations. This modifies  $\Delta'$ , and saturation is achieved when  $\Delta' \rightarrow 0$ . However, care must be taken as the nonlinear island may be of significant width, such that the small layer width ordering of Sec. 4 may no longer be valid.

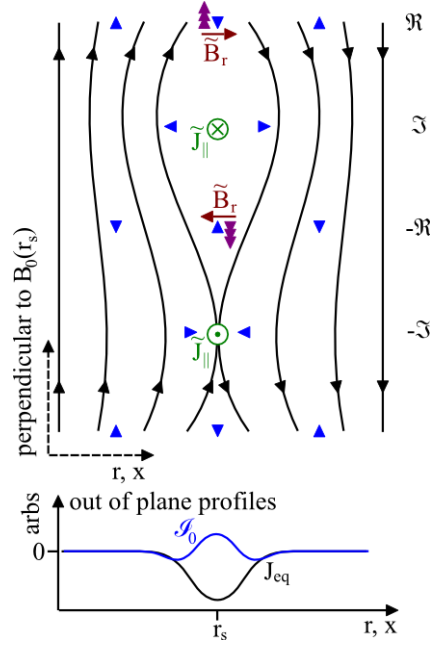


Figure 16: A sketch of the dominant perturbed velocity (blue arrows) and reconnecting magnetic field lines (black lines) of a magnetic island. Components of  $B_r$  and  $J_{\parallel}$  at the rational surface are labeled and profiles of the out of plane equilibrium and perturbed current are sketched below. The direction of the ‘third-order’ force described in the text is indicated by the purple triple arrows. The normalized phase of the complex eigenfunction coefficients used in Part III are indicated on the right.

We will make use of an alternative picture by considering the  $m = 1$  force-balance equation,

$$\rho_0 \frac{d\mathbf{v}}{dt} = \mathbf{f}_d + \mathbf{f}_3 \quad (6.1)$$

where  $\mathbf{f}_d$  is the driving force, and  $\mathbf{f}_3$  is a third-order force. The driving force,  $\mathbf{f}_d = \mathbf{J}_{eq} \times \mathbf{B} + \mathbf{J} \times \mathbf{B}_{eq} - \nabla p$ , is the interaction of the tearing perturbation with the initial equilibrium fields. Whereas the third-order force,  $\mathbf{f}_3 = \mathcal{J}_0 \times \mathbf{B}_1 + \mathbf{J}_1 \times \mathcal{B}_0$  with  $\mathcal{B}_0 = \mathbf{B} \sim \mathbf{B}_{eq}$ , is the interaction of the tearing perturbation with the profile modification from the dynamo emf. This description ignores contributions from advective terms and the harmonics of the mode, as will be appropriate for our numerical cases.

When  $\omega = 0$ , Rutherford showed that in the early nonlinear regime the island growth rate becomes algebraic:

$$\frac{\tau w}{\tau t} = A \frac{1}{0} \quad (6.2)$$

where  $w$  is the island width and  $A$  is a geometric coefficient of order unity[50]. His derivation assumes the same ordering at the linear theory of Sec. 4, and that harmonics of the resonant mode are small. The theory

does not capture the saturation of the island, only a slowing of the growth, and the regime of validity is referred to as the Rutherford stage. Recent theories perturbatively use the island size as a small parameter, and find relations for the saturated width in a slab, Ref. [51], and cylindrical paramagnetic pinch, Ref. [52].

## 6.2 FLR effects

Previous work has typically considered slab geometries or large-aspect-ratio tokamak ordering where the only contribution from  $\Pi_{gv}$  leads to the cancellation of advection from the ion diamagnetic drift. As described in Part III, we will demonstrate there is a linear drift effect proportional to  $\nabla B_0$  and curvature in pinch profiles which is manifest through contributions from  $\Pi_{gv}$  with a response similar to the diamagnetic-drift tearing described in Sec. 5.1. In order to provide a basis for interpretation of the contributions from  $\Pi_{gv}$  to Eqn. (6.1), we now review the nonlinear work on diamagnetic-drift tearing and FLR effects in tokamaks.

Early nonlinear results on drift-tearing modes showed magnetic islands evolve to the same saturated width found with resistive MHD modeling [53, 54]. These results assume drift effects are manifest only through  $n'_0$  and  $T'_{i0}$  as the large parallel thermal conductivity,  $\kappa_{\parallel e} \sim T_e^{5/2}$ , flattens  $T'_{e0}$  locally at the resonant surface for small perturbations [55]. In Ref. [53], Biskamp makes a quasilinear mixing-length argument when the island width is greater than the tearing layer width,  $w > l$ , to justify an assumption of particle density and ion temperature flattening over magnetic island flux surfaces. Thus  $\omega_* \rightarrow 0$  at finite island width which leads to resistive-MHD evolution in quasilinear computation. In Ref. [54], Monticello and White do not assume the density profile flattens over the evolving island width in nonlinear computations. While this affects rotation during the evolution, the helical flux evolution is shown to be independent of rotation, and the saturated state again matches resistive MHD predictions. Their description points out the free energy available to the drift-tearing mode is the same as resistive-MHD through consideration of  $\Delta'(w)$ . Both Biskamp and Monticello and White consider the fluid-gyroviscous effect only from the dominant ion-pressure-gradient contribution as appropriate in large-aspect-ratio tokamaks.

More complete nonlinear modeling by Scott et al. confirms the density-flattening effect through sound-wave mixing [56, 57]. In their description, the density profile flattens when

$$\omega_{*n} \sim (k_{\perp s} v_{T\alpha}^2 / \omega_{c\alpha}) (n'_0 / n_0) \sim k'_{\parallel} w c_s \quad (6.3)$$

and temperature profiles flatten when

$$\omega_{*\alpha} \sim k_{\parallel}^2 w^2 \kappa_{\parallel\alpha} / n_0. \quad (6.4)$$

The parallel thermal conductivity can be included in our model through  $\mathbf{q}_{\parallel\alpha} = \kappa_{\parallel\alpha} \hat{\mathbf{b}}_0 \cdot \nabla k_B T_\alpha$  where  $\kappa_{\parallel\alpha} \simeq nk_B T_\alpha \tau_\alpha / m_\alpha$ . With roughly equal species temperatures, we expect the electron thermal diffusivity to be greater than that of the ions by a factor of  $\sqrt{m_i/m_e}$ , and the electron temperature gradient to relax faster. Given the large parallel thermal conduction of both species, the temperature profiles flatten at a smaller magnetic perturbation amplitude than the density profile, and once  $w > \omega_{*n}/k'_{\parallel} c_s$  the island evolution is well described by resistive MHD. Drake et al. demonstrate that inclusion of the large parallel thermal conductivity with the drift-tearing response leads to a linear stabilization of the mode through a screening effect [58]. At the resonant surface, the mode rotates with frequency  $\omega_{*e}$ , but slightly off the resonant surface where temperature profile flattens, as described by Eqn. (6.4) with  $w \rightarrow l$ , it rotates with frequency  $\omega_{*n}$ . This differential mode rotation leads to a stabilizing effect. However, Scott and Hassam show this linear-stabilization effect is only relevant to the nonlinear dynamics at very small perturbation amplitude, and for perturbations on the order of the tearing layer width, the standard algebraic growth described by Rutherford is again valid [59].

Large perturbations occur in the RFP, and thus from these consideration we expect the diamagnetic-drift effects and stabilization associated with the large parallel thermal conduction are small. Additionally as the pressure-profile gradients relax with increasing island width, the interchange effects associated with  $p'_0$  described in Sec. 4.3 become progressively less important [60]. Our modeling does not consider large parallel thermal conduction or profiles with pressure gradients; however, given the decreasing importance of these effects for large islands, we believe the effects associated with  $\nabla B_0$  and curvature that we study in detail are more relevant to the RFP.

Our nonlinear two-fluid computations with cold ions, where contributions from  $\mathbf{\Pi}_{gv}$  vanish, show magnetic islands that evolve to the same saturated width found with resistive-MHD modeling. In contrast, our computations with warm ions show that the ion-gyroviscous stress in pinch configurations affects nonlinear island evolution and saturation. The gyroviscous stress supplements the nonlinear Lorentz force that occurs in resistive MHD and reduces the saturated island width. Moreover, the  $\nabla B_0$  and poloidal curvature profiles, which lead to the important gyroviscous contributions in our linear cases, are largely unaffected by the nonlinear evolution unlike the pressure-gradient effects considered in other studies.

## 7 Thesis

To provide a basis for understanding two-fluid effects in MST, the computations presented here consider linear (Part III) and nonlinear (Part IV) properties of individual tearing modes in cylindrical pinch profiles with uniform density and temperature. These equilibrium conditions approximate the core of relaxed pinches that largely confine particles and energy in their outer region. When the tearing layer width is smaller than the ion sound gyroradius, our cylindrical computations show that kinetic-Alfvén-wave (KAW) physics increases linear growth rates relative to resistive MHD. An unexpected new result is a drift effect that reduces the growth rate at intermediate- $\rho_s$  values. This drift is present only with warm-ions FLR modeling, and arises from  $\nabla B$  and poloidal curvature represented in the Braginskii gyroviscous stress. As our computations have a uniform pressure profile, there are no diamagnetic-drift effects. Using the orderings described in Sec. 4, we find the contributions from  $\Pi_{gv}$  to the parallel momentum equation and as appropriate for the RFP we do not use large-aspect ratio ordering. We show that these contributions lead to  $\nabla B_0$  and curvature drifts. Coupling this with simple resistive-MHD flux evolution through the radial induction equation, we derive a heuristic dispersion relation. The growth rates and rotation frequencies from this dispersion relation are in agreement with numerical results in the intermediate drift regime before KAW effects are significant [61].

Unlike the diamagnetic effects which diminish in importance with nonlinear considerations, in Part IV we demonstrate that the gyroviscous effects are relevant to the nonlinear evolution and limit the saturated island width. As described in previous work, the  $\nabla p_0$  profile is flattened by finite-island-width effects; however, we note the magnetic profile associated with drift effects is largely unchanged by island saturation. We examine terms of the saturated-island force balance, and show that for warm ion cases the ion gyroviscous force can supplement the nonlinear Lorentz force described in Sec. 6.1. Given the nonzero contribution from  $\nabla \cdot \mathbf{\Pi}_{gv}$ , there is an incomplete cancellation of the nonlinear Lorentz force and the driving forces in Eqn. (6.1), and thus the perpendicular current density and Hall dynamo effect are nonzero at saturation. We make a helical projection of the island magnetic and ion flow structures. Unlike cold-ion cases where the ion flows advect flux into the magnetic island, the warm-ion cases exhibit flows that are significantly distorted by the ion gyroviscosity [61].

Our studies of single tearing-mode dynamics are not directly applicable to the inherently multi-mode discharges present in MST, although they provide a clear understanding of the physics governing the mode growth rate and island saturation width. Part V considers computationally challenging cases with full multi-helicity dynamics. The magnetic perturbations are smaller with a two-fluid computation than that with a resistive-MHD model, as to be expected from the single-helicity results of Part IV. We compare

both our single- and two-fluid computations with edge measurements of the perturbed-field amplitudes, and find the computed amplitudes without the ion gyroviscous effects tend to be approximately a factor of two larger than the experiment. These two-fluid computations show that both the MHD- and Hall-dynamo emfs contribute to the flattening of the current profile during relaxation events. The decomposition of the Hall dynamo and assumption of one dominant term that are used in the measurement of Ding et al. is checked, and our computation produces results similar to their measurement. The presence of Hall dynamo implies a fluctuation-induced Maxwell stress. The magnitude of force densities from the Maxwell stress and a competing Reynolds stress, and associated changes in the parallel-flow profile are comparable to measurements by Kuritsyn et al. These measurements do not compare well with our single-fluid computation, and we conclude that at least two-fluid modeling is necessary to capture the dynamics of RFP experimental discharges.

## Part II

# Methods and parameters

We now turn to the practical matters of code implementation (Sec. 8), the configuration of the computational domain for our various cases (Secs. 9.1 and 9.2), and the characterization of the various geometric, equilibrium, dissipative, and physics parameters that describe the model (Secs. 9.3 and 9.4).

## 8 The NIMROD code

We solve the model equations, summarized in Appendix C and described in Sec. 2.4, using the initial-value, extended-MHD NIMROD (Non-Ideal MHD with Rotation, Open Discussion) code [62]. The implementation evolves perturbations from a prescribed steady state, and the computations may be either linear or fully nonlinear. Results on pinch tearing modes reported in Part III are computed with the linear option. In Parts IV and V, we describe results from fully nonlinear computations, including modification of the symmetric profiles.

### 8.1 Spatial discretization

The code's spatial representation is spectral finite elements [63, 64] over a 2D plane and finite Fourier series for a periodic coordinate. The Fourier direction may be configured with either linear (straight) or toroidal geometry. This along with the finite element mesh allows the code to capture configurations with shaped 2D cross-sections and one direction of geometric symmetry. For our cases, numerical quadrature with a Gauss-Legendre rule is used to perform the integration required by the finite element representation with 49 quadrature points per element.

Our slab cases use a rectangular mesh for the  $xy$ -plane and a single Fourier component,  $m = 0$ , in the axisymmetric  $z$ -direction. The mesh has either 120 or 240 elements in the  $x$ -direction (the direction of equilibrium field variation) and 14 elements in the periodic  $y$ -direction (the direction of the wave-vector). The elements are of polynomial degree four, and the mesh is packed around the resonant surface of the mode at  $x = 0$ . The numerical convergence of our linear cases is checked by increasing the polynomial degree from 4 to 5, and using smaller time-step sizes.

In the cylindrical-pinch computations described here, we use the Fourier representation for the azimuthal

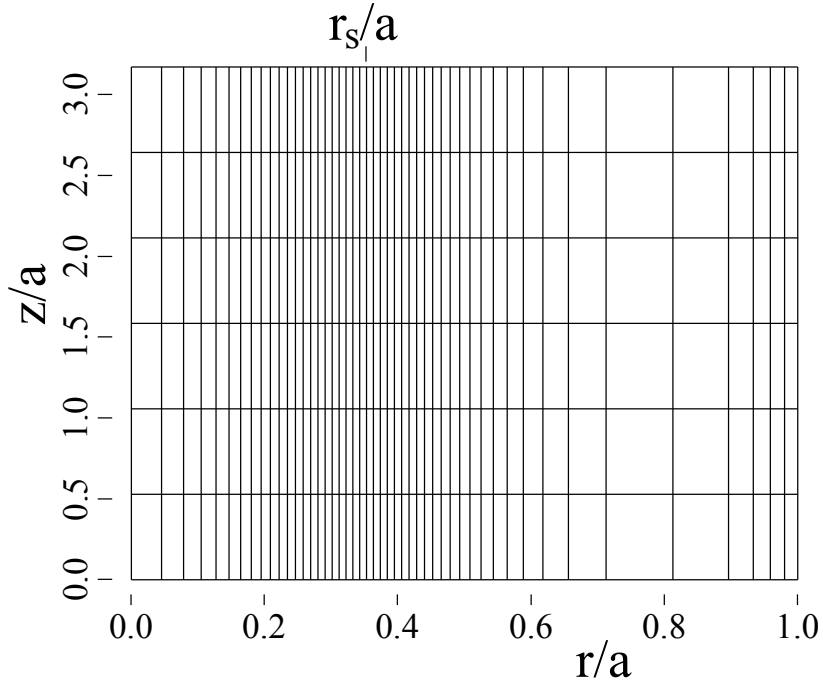


Figure 17: The packed, polynomial-degree four,  $240 \times 30$  (radial $\times$ axial) mesh as used in our single helicity computations described in Parts III and IV is displayed. Each rectangle represents  $5 \times 5$  finite elements with the similar packing, and the resonant surface is indicated.

angle and the finite-element representation for the  $rz$  plane. A periodic boundary condition is imposed in the axial direction of the cylinder, with periodicity  $2\pi R$ . Our single-helicity nonlinear computations (Part IV) have  $0 \leq m \leq 2$  Fourier components and finite-element basis functions of polynomial degree four in a  $240 \times 30$  (radial $\times$ axial) mesh that is packed about the resonant surface as shown in Fig. 17. Numerical convergence is checked by running computations with polynomial basis functions of degree five and six Fourier components,  $0 \leq m \leq 5$ . The integrated value of the  $m = 1$ -mode  $|\tilde{B}|$  changes at most by 1.6% when increasing the polynomial degree of the  $rz$  mesh and 3% when the axial resolution is doubled.

For our multi-helicity computations, described in Part V, we require additional axial and poloidal resolution, and must account for radially distributed resonant surfaces that move with the plasma profile evolution. In these cases we use an unpacked  $240 \times 60$  finite element mesh with polynomial degree four and six Fourier components,  $0 \leq m \leq 5$ . These cases push the limits of the computational resources allocated through the National Energy Research Scientific Computing center (NERSC), and we rely on our experience with the single helicity cases to give us confidence that the cases are reasonably numerically converged. Our cases represent a compromise between including all the computationally-intensive effects, and tractable but well-understood resistive-MHD modeling. The boundary of what is tractable is continuously being pushed

by improvements in computational power and algorithm and solver efficiency. The multihelicity cases are typically run on the Carver machine with 30 nodes where each has 2 quad-core Intel Xeon 5500 2.67 GHz processors, 24 GB of DDR3 1333 MHz memory per node, and QDR InfiniBand interconnects.

## 8.2 Temporal discretization

The NIMROD code uses a staggered time advance where the velocity is specified on the time steps  $(j, j + 1)$ , and density, temperature and magnetic field are specified on the half-time steps  $(j + 1/2, j + 3/2)$ . The time-discretized velocity advance is

$$\begin{aligned} m_i n^{j+1/2} \left( \frac{\Delta \mathbf{v}}{\Delta t} + \frac{1}{2} \mathbf{v}^j \cdot \nabla \Delta \mathbf{v} + \frac{1}{2} \Delta \mathbf{v} \cdot \nabla \mathbf{v}^j \right) - \Delta t L^{j+1/2} (\Delta \mathbf{v}) + \nabla \cdot \mathbf{\Pi} (\Delta \mathbf{v}) \\ = \mathbf{J}^{j+1/2} \times \mathbf{B}^{j+1/2} - m_i n^{j+1/2} \mathbf{v}^j \cdot \nabla \mathbf{v}^j - \nabla p^{j+1/2} - \nabla \cdot \mathbf{\Pi} (\mathbf{v}^j) \end{aligned} \quad (8.1)$$

where the RHS (quantities with time step label  $j$  and  $j + 1/2$ ) is known and the LHS is to be inverted to find  $\Delta \mathbf{v} = \mathbf{v}^{j+1} - \mathbf{v}^j$ . The semi-implicit differential operator  $L$  is defined as,

$$\begin{aligned} L(\Delta \mathbf{v}) = C_0 \left\{ \frac{1}{\mu_0} (\nabla \times [\nabla \times (\Delta \mathbf{v} \times \mathbf{B})]) \times \mathbf{B} + \mathbf{J} \times \nabla \times (\Delta \mathbf{v} \times \mathbf{B}) + \nabla (\Delta \mathbf{v} \cdot \nabla p + \Gamma p \nabla \cdot \Delta \mathbf{v}) \right\} \\ + C_1 p_{nl} \nabla^2 \Delta \mathbf{v}, \end{aligned} \quad (8.2)$$

and it vanishes as  $\Delta t \rightarrow 0$ . The part of  $L \sim C_0$  is the linear-ideal-MHD-force operator which is part of a fully-implicit time-advance scheme for ideal-MHD and its inclusion on the LHS of (8.1) effectively adds a wavenumber-dependent inertia. Its use limits the frequency of high- $k$  mode activity and gives the algorithm numerically favorable properties [62]. The second term  $\sim C_1$  ensures stability as non-symmetric pressures develop where the nonlinear pressure coefficient  $p_{nl}$  is defined as the maximum in the Fourier direction of the sum of the perturbed magnetic ( $\mathbf{B}^2/\mu_0$ ) and internal ( $\Gamma p$ ) energy minus the axisymmetric magnetic and internal energy. Typical values for our computations are  $C_0 = 0.3$  and  $C_1 = 0.38$ . Once  $\mathbf{v}^{j+1}$  is known, the time-discretized temperature, number density and magnetic field equations,

$$\frac{\Delta n}{\Delta t} + \frac{1}{2} \mathbf{v}^{j+1} \cdot \nabla \Delta n = -\nabla \cdot (n^{j+1/2} \mathbf{v}^{j+1}), \quad (8.3)$$

$$\frac{\bar{n}}{\Gamma - 1} \left( \frac{\Delta T}{\Delta t} + \frac{1}{2} \mathbf{v}^{j+1} \cdot \nabla \Delta T \right) = -\frac{\bar{n}}{\Gamma - 1} \mathbf{v}^{j+1} \cdot \nabla T^{j+1/2} - \bar{n} T^{j+1/2} \nabla \cdot \mathbf{v}^{j+1} \quad (8.4)$$

and

$$\begin{aligned} \frac{\Delta \mathbf{B}}{\Delta t} + \nabla \times \left[ \frac{m_e}{\mu_0 \bar{n} e^2} \nabla \times \frac{\Delta \mathbf{B}}{\Delta t} - \frac{1}{2} \mathbf{v}^{j+1} \times \Delta \mathbf{B} + \frac{1}{2} \frac{1}{\bar{n} e} \left( \mathbf{J}^{j+1/2} \times \Delta \mathbf{B} + \Delta \mathbf{J} \times \mathbf{B}^{j+1/2} \right) + \frac{1}{2} \eta \Delta \mathbf{J} \right] \\ = -\nabla \times \left[ \frac{1}{\bar{n} e} \left( \mathbf{J}^{j+1/2} \times \mathbf{B}^{j+1/2} - \nabla \bar{p}_e \right) - \mathbf{v}^{j+1} \times \mathbf{B}^{j+1/2} + \eta \mathbf{J}^{j+1/2} \right] \quad (8.5) \end{aligned}$$

are advanced to find  $n^{j+3/2}$ ,  $T^{j+3/2}$  and  $\mathbf{B}^{j+3/2}$ . Definitions used here are  $\Delta n = n^{j+3/2} - n^{j+1/2}$ ,  $\Delta T = T^{j+3/2} - T^{j+1/2}$ ,  $\Delta \mathbf{B} = \mathbf{B}^{j+3/2} - \mathbf{B}^{j+1/2}$  and  $\bar{n} = (n^{j+3/2} + n^{j+1/2})/2$ . The non-self-adjoint advective, Hall and viscous terms, are implemented implicitly, resulting in a mixed semi-implicit/implicit leapfrog advance described in Ref. [65]. In Ref. [66] von Neumann analysis of plane waves demonstrates this system is numerically stable if  $C_0 \geq 1/4$ . Additionally, further analysis demonstrates that time-centered implicit terms are essential for numerical accuracy.

Each advance equation, Eqn. (8.1) and (8.3)-(8.5), may be written in terms of a known RHS vector  $\mathbf{b}$  where each component represents the solution at a particular spatial location, a known matrix  $\mathbf{A}$  on the LHS, and an unknown solution vector  $\mathbf{x}$ , in the sense  $\mathbf{A}\mathbf{x} = \mathbf{b}$ . Thus solving an advance equation is equivalent to finding the inverse of  $\mathbf{A}$ . The deliberate choices made by the staggering scheme allow for  $\mathbf{v}$ ,  $n$ ,  $T$  and  $\mathbf{B}$  to be solved for independently in that order, as opposed to a fully-implicit time-centered scheme where they are solved for at the same time. As this choice limits the size of  $\mathbf{A}$  it improves the computational efficiency for finding its inverse. The problem is solved for  $\mathbf{x}$  with the generalized minimal residual method (GMRES)[67]. The method is iterative where the computational cost scales as each iteration squared. Therefore it is necessary to have a good preconditioner and initial guess for  $\mathbf{x}$ . The change in the fields,  $\Delta \mathbf{v}$ ,  $\Delta \mathbf{B}$ ,  $\Delta n$  and  $\Delta T$ , from the last time step is used as the initial value for  $\mathbf{x}$ . The preconditioner is based on the LU decomposition of the independent contribution from each Fourier component to  $\mathbf{A}$ . To be more specific, one may conceptualize each Fourier component as having a 2D finite element mesh associated with it and the LU decomposition associated with each 2D finite element mesh composes the preconditioner. The LU decomposition is done by the distributed SuperLU code [68]. This preconditioner does not capture the coupling between Fourier components, and although the NIMROD code has Fourier component preconditioning through Gauss-Seidel and Jacobi iteration it is not used in our cases.

The modeling of dispersive waves and largely anisotropic diffusion involves ill-conditioned matrices which may require a combination of large iteration number and small time step to solve. Thus the inclusion of the whistler waves, KAWs, large parallel thermal conduction and large parallel viscosity can increase the computational cost of a given problem. The time-step size in our cases is limited by one of four conditions:

1. an effective flow-CFL restriction [69] which requires  $\Delta t \leq 1/2k_{max}v_f$ ,  $L_{element}/2\sqrt{3}v_{mesh}$  (where  $k_{max}$  is the largest wavenumber in the Fourier direction,  $v_f$  is the maximum Fourier direction flow speed,  $L_{element}$  is a characteristic element size, and  $v_{mesh}$  is the maximum flow speed in the mesh),
2. a nonlinear-CFL restriction based on wave speeds computed with the nonlinear pressure,
3. the requirement that the solver for each field converge before 50 iterations, or
4. a hard Alfvénic limit ( $\Delta t \lesssim 3\tau_A$ ).

Linear computations are typically limited by the hard limit or the flow-CFL condition, single-helicity computations are limited by the nonlinear-CFL condition, and multihelicity by the either the flow-CFL or the solver.

The two-fluid implicit leap-frog time-advance is benchmarked to the analytic tearing dispersion relations of Sec. 5.2 for slab geometry without ion gyroviscosity in Part III, on plane-wave propagation in Ref. [66], and slab interchange with ion gyroviscosity in Ref. [70].

## 9 Geometric approximations and equilibria

We now describe the equilibrium configuration of the computational domain for slab (Sec. 9.1) and cylindrical (Sec. 9.2) cases, the conducting wall boundary condition (Sec. 9.3), and our parameter space (Sec. 9.4). In general equilibria are found using Eqn. (1.17) with specified current and pressure profiles. For cylindrical cases this becomes

$$B'_\theta = B_z\lambda - \frac{B_\theta}{r} - \frac{\mu_0 B_\theta}{B^2} p' \quad (9.1)$$

and

$$B'_z = -B_\theta\lambda - \frac{\mu_0 B_z}{B^2} p' , \quad (9.2)$$

where the prime indicates a radial derivative and we have used  $\nabla \cdot \mathbf{B} = \nabla \cdot \mathbf{J} = 0$  to eliminate the radial components of the fields. The equations in slab geometry are similar, but without the cylindrical-curvature term on the RHS of Eqn. (9.1) and with the transformation  $r\theta \rightarrow xy$ . Our computations use force-free ( $\mathbf{J}_{eq} \times \mathbf{B}_{eq} = \nabla p_{eq} = 0$ ) equilibria. Thus we use  $\mathbf{J}_{eq} = \lambda_{eq}\mathbf{B}_{eq}$  and set  $p_{eq}$  as a constant to investigate finite- $\beta$  two-fluid effects without equilibrium diamagnetic flow.

## 9.1 Slab

For our slab cases we use a ‘Harris sheet’ current profile:

$$\lambda_{slab} = \frac{\epsilon_B}{L_B} \operatorname{sech}^2 \left( \frac{x}{L_B} \right), \quad (9.3)$$

where  $\epsilon_B = \lim_{x \rightarrow \infty} B_{eqy}(x)/B_{eq0}$  and  $B_{eq0} = B_{eqz}(0)$ . With small  $\epsilon_B$ , this leads to the equilibrium fields

$$B_{eqy}(x) \simeq \epsilon_B B_{eq0} \tanh \left( \frac{x}{L_B} \right), \quad (9.4)$$

$$B_{eqz}(x) = [B_{eq0}^2 - B_{eqy}^2(x)]^{1/2} \simeq B_{eq0}, \quad (9.5)$$

$$J_{eqz}(x) \simeq \frac{\epsilon_B B_{eq0}}{\mu_0 L_B} \left( 1 - \tanh^2 \left( \frac{x}{L_B} \right) \right) = \frac{\epsilon_B B_{eq0}}{\mu_0 L_B} \operatorname{sech}^2 \left( \frac{x}{L_B} \right), \quad (9.6)$$

and

$$J_{eqy}(x) = J_{eqz}(x) \frac{B_{eqy}(x)}{B_{eqz}(x)} \simeq \frac{B_{eq0} \epsilon_B^2}{\mu_0 L_B} \operatorname{sech}^2 \left( \frac{x}{L_B} \right) \tanh \left( \frac{x}{L_B} \right). \quad (9.7)$$

To find  $\Delta'$  for this case we solve the Newcomb equation in the outer region. The expression for the Newcomb equation given in Sec. 4.1, Eqn. (4.13), is for a general cylindrical case with non-zero pressure gradient. Our slab cases are greatly simplified by the absence of curvature terms, a constant wave-vector  $\mathbf{k} = k\hat{y}$ , axisymmetry in the  $\hat{z}$ -direction such that  $\partial/\partial z \rightarrow 0$ , and no pressure gradient. We may derive an analogous equation by using  $\mathbf{J} \times \mathbf{B}$  to write

$$ikB_{eqy}\tilde{\mathbf{J}} - \tilde{J}_x\mathbf{B}'_{eq} + \tilde{B}_x\mathbf{J}'_{eq} - ikJ_{eqy}\tilde{\mathbf{B}} = 0. \quad (9.8)$$

The x-component of this equation establishes  $\tilde{J}_x = \lambda\tilde{B}_x$ . The z-component may be reduced to

$$B_{eqy}\tilde{B}_x'' - (k^2 B_{eqy} + B_{eqy}'')\tilde{B}_x = 0 \quad (9.9)$$

after using the relations  $\tilde{J}_z = \tilde{B}'_y - ik\tilde{B}_x$ ,  $\tilde{B}'_x + ik\tilde{B}_y = 0$ , and associated equilibrium conditions. After substitution of the equilibrium fields we have the relation

$$\tilde{B}_x'' = \left( k^2 - \frac{2}{L_B^2} \operatorname{sech}^2 \left( \frac{|x|}{L_B} \right) \right) \tilde{B}_x \quad (9.10)$$

where we have used the property  $\operatorname{sech}(x) = \operatorname{sech}(-x)$  to introduce the absolute value. The solution to this

equation (from, for example, Ref. [49]), valid in the outer region where  $x \neq 0$ , is

$$\tilde{B}_x = B_{x0} e^{-k|x|} \left( 1 + \frac{2}{L_B} \tanh \left( \frac{|x|}{L_B} \right) \right) \quad (9.11)$$

with

$$\tilde{B}'_x = -ik\tilde{B}_y = -B_{x0} \frac{x}{|x|} e^{-k|x|} \left[ k + \frac{1}{L_B} \tanh \left( \frac{|x|}{L_B} \right) - \frac{1}{kL_B^2} \operatorname{sech}^2 \left( \frac{|x|}{L_B} \right) \right]. \quad (9.12)$$

It is clear there is a discontinuity in  $\tilde{B}'_x$  at  $x = 0$ . Evaluating  $\Delta'$ , Eqn. (4.17), we find

$$\Delta' = \frac{2}{L_B} \left( \frac{1}{kL_B} - kL_B \right). \quad (9.13)$$

As the growth rate of the tearing mode depends on the sign of  $\Delta'$  (Eqn. (4.39)), the destabilizing term ( $1/kL_B$ ) is large for small- $k$ , and the stabilizing term ( $kL_B$ ) is small for small- $k$ , we expect the most unstable mode to correspond to the longest wavelength.

Our computations use a periodic boundary condition in the y-direction, and the length,  $Y$ , determines the most unstable  $k = 2\pi/Y$ . The analytic theory assumes an infinite domain in the x-direction,  $x \rightarrow \pm\infty$ . Of course, our mesh cannot extend to infinity and we place conducting walls at  $x = a$ , and require  $a \gg L_B$  such that these walls do not influence the mode dynamics. Given the outer solutions exponentially decay as  $\operatorname{Exp}[-k|x|]$  we do not expect this requirement to be severe. Fig. 18 shows the growth rate as a function of  $a/L_B$ , and a value of 6 is sufficient to limit the influence of the walls. This ordering creates a separation of spatial scales,  $a > L_B \gg \rho_s$ ,  $l$  where cases span the range of  $l \gg \rho_s$  and  $l \ll \rho_s$ , that makes the problem computationally challenging.

The slab cases may be related to the cylindrical through the transformation  $xy \rightarrow r\theta$ . Although the outer solution is governed by significantly different equations, compare Eqns. (4.13) and (9.9), the zero- $\beta$  resistive-MHD inner layer equations described in Sec. 4.2 are identical. However, as we shall see, in the two fluid regime the inner layer equations between slab and cylindrical cases differ. Specifically, curvature and equilibrium gradient terms in the response of  $\tilde{B}_{\parallel}$  are absent in the slab cases. When studying two-fluid effects the slab cases are useful as benchmark, but cylindrical cases must be run for experimental comparison.

## 9.2 Cylindrical

Our cylindrical computations use the force-free, cylindrical, paramagnetic-pinch equilibrium [18]. The motivation behind the choice of this equilibrium, and the specific current and radial pinch flow,  $\mathbf{v}_{eq} =$

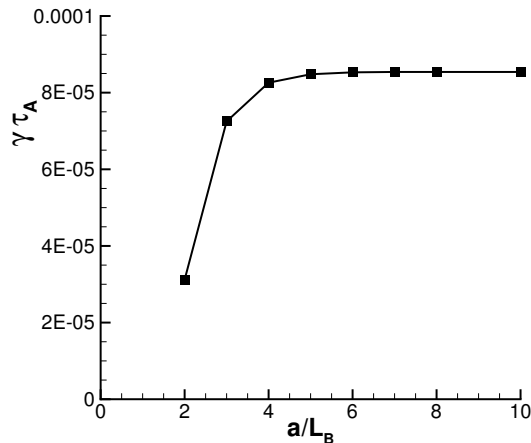


Figure 18: Slab tearing growth rate ( $\gamma\tau_A$ ) as a function of computational domain size ( $a$ ).

$\mathbf{E}_{eq} \times \mathbf{B}_{eq}/\mathbf{B}_{eq}^2$ , profiles were describe in Sec. 3.1. We include a uniform axial electric field which models the inductive loop voltage, such that the equilibrium is an Ohmic steady state  $\nabla \times \mathbf{E}_{eq} = 0$ . The particle and energy compression from  $\nabla \cdot \mathbf{v}_{eq}$  are not considered in these simulations; we assume that they are balanced by transport processes that are outside the scope of the model. Moreover, the pinch flow, Eqn. (3.4), scales as  $1/S$  and in the experimentally relevant high- $S$  regime, it is likely to be just a small part of overall transport.

### Single-helicity computations

For our single-helicity cases we set  $\lambda(0) = 3.3$  when specifying the parallel-current profile, Eqn. (3.3), which leads to the profile shown in Fig. 19(a). The pinch parameter, a measure of the normalized current, is then  $\Theta = \mathbf{B}_{\theta 0}(a)/\overline{\mathbf{B}_{z0}} = 1.38$ , where the over-bar indicates a volume average. This pinch-parameter value is roughly 10–15% below that of the MST discharges described in Ref. [37]. At larger pinch-parameter values, the parallel-current-density gradients of the paramagnetic pinch are larger, which is less representative of relaxed RFP profiles.

We limit the fluctuation spectrum of our nonlinear computations, which are three-dimensional, by using a reduced aspect ratio of  $R/a = 0.505$ . This value makes the first axial wavenumber,  $k_z a = 1.98$ , comparable to that of the dominant  $m = 1, n = 6$  mode in MST. The safety factor (Eqn. (1.9)) for the single-helicity computations is shown in Fig. 19(b), and the primary mode is resonant at the  $q = 1$  rational surface,  $r_s = 0.35$ . Unlike MST, however, the next axial wavenumber is twice as large as that of the dominant

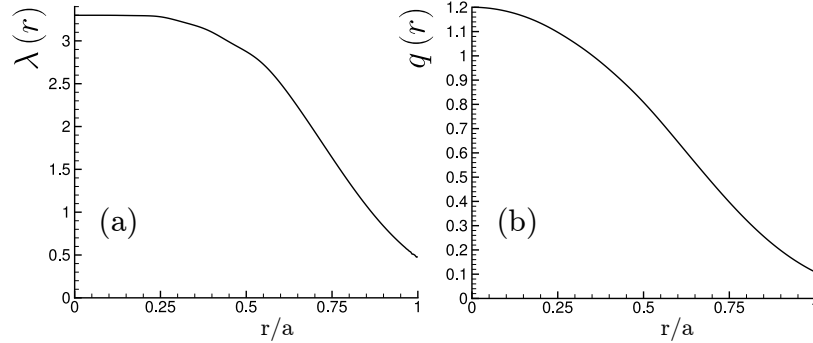


Figure 19: The (a) parallel-current profile and (b) safety factor versus radius for the paramagnetic pinch with  $\lambda_0 = 3.3$  and  $R/a = 0.505$ .

mode, which limits nonlinear coupling and allows us to focus on single-helicity behavior. The dominant  $m = 1$ ,  $k_z a = 1.98$  mode in the computations has the tearing stability parameter  $\Delta' a = 15.2$ , according to an independent eigenvalue computation which solves the cylindrical Newcomb equation, Eqn. (4.13). The only other MHD-unstable mode for this equilibrium has  $m = 1$  and  $k_z a = 3.96$ . Its stability parameter value of  $\Delta' a = 3.0$  leads to a smaller resistive-MHD growth rate, and the stabilizing gyroviscous effect described in Sec. 11 is considerably stronger for this mode. It is not observed to be significant in our nonlinear computations. Our computations allow the dominant mode to couple with its higher harmonics,  $m = 2, 3, \dots$ , so single-helicity shaping and spectral broadening are permitted numerically, but these effects are not observed to be significant in our cases. Finally, we note that the paramagnetic pinch is not a reversed state; reversal is achieved via the full RFP dynamo, which is not present in these low- $\Theta$ , reduced-aspect-ratio cases.

### Multi-helicity computations

Our multi-helicity computations use  $\lambda(0) = 3.88$  when specifying the equilibrium parallel-current profile and  $R/a = 3.03$  such that the  $m = 1$ ,  $n = 6$  axial wavenumber is the same as our single-helicity computations and similar to MST,  $k_z a = 1.98$ . However, the realistic aspect ratio leads to a profile with unstable modes for  $m = 1$ ,  $6 \leq n \leq 21$ . This multi-mode case is initialized with a low-resolution,  $S = 5000$ , resistive-MHD computation such that the  $m = 1$ ,  $n = 6$  mode is large, there is finite  $n = 7+$  activity, and the profiles are considerably more relaxed at  $t = 0$ . Thus the two-fluid multi-helicity computation begins in a nonlinear state and almost immediately a relaxation event occurs which causes the axial-magnetic-field profile to reverse.

### 9.3 Boundary conditions

Apart from a fixed effective axial voltage, which represent the transformer-driven inductive electric field, boundary conditions at  $r = a$  represent a conducting wall,

$$\hat{n} \cdot \tilde{\mathbf{B}}(a) = \hat{n} \times \tilde{\mathbf{E}}(a) = 0, \quad (9.14)$$

with a no-slip condition on flow,

$$\tilde{\mathbf{v}}(a) = 0. \quad (9.15)$$

Dirichlet conditions are used for the evolving number density and temperature,

$$\tilde{n}(a) = \tilde{T}(a) = 0, \quad (9.16)$$

which permit density and temperature to diffuse into and out of the computational domain. Edge-peaked profiles for the resistivity and isotropic viscosity increase by a factor of 10 or 20 and spread boundary-layer effects over a narrow region adjacent to the wall.

### 9.4 Model parameter space

In the high-current (400 kA) MST discharges analyzed in Refs. [37, 25], the electron and ion temperatures are approximately 300 eV,  $n \simeq 10^{19} m^{-3}$ ,  $B \simeq 0.4 T$ , the minor radius is  $a \simeq 0.5 m$ , and the major radius is  $R \simeq 1.5 m$ . With these conditions  $d_i \simeq 0.2a$  and  $\rho_s \simeq 0.02a$  in the core. If we use the linear growth rates from our single-helicity cylindrical cases of Sec. 11 to estimate the resistive skin depth and tearing-layer width we find  $l \simeq \rho_s$  for core modes in this un-relaxed but low- $\Theta$  current profile. In more relaxed profiles the growth rate is smaller, which puts the linear behavior in the MHD regime. Alternatively, nonlinearly driven modes may grow faster and have tearing-layer widths that are significantly smaller than  $\rho_s$ ; though semi-collisional conditions are still expected [71]. Understanding the transition from MHD to two-fluid tearing is therefore important for MST.

Our linear parameter scans examine the two-fluid transition by varying  $\beta$  or  $d_i$  hence  $\rho_s$  while keeping  $S$ ,  $\Delta'$ , and other parameters fixed so that the MHD response does not change for a given  $S$ -value. Table 2 summarizes the parameters of our scans and compares them with the high- and low-current MST discharges of Ref. [37, 25, 16]. In terms of the normalized two-fluid parameters,  $\hat{\alpha}$  and  $\hat{\beta}$  described in Sec. 5.2, our linear scans cover the parameter space relevant to MST. In Sec. 10 we use the slab cases to verify the

	MST 400 kA	MST 200 kA	slab $\beta$ scan	slab $d_i$ scan	cylinder $d_i$ scan
$kd_i$	0.71	0.71	0.42	0.015 – 0.95	0.12 – 6.02
$\beta$	0.015	0.04	$10^{-7} - 0.1$	0.1	0.1
$k\rho_s$	0.08	0.01	$6.8 \times 10^{-4} - 0.68$	0.01 – 0.63	$3.5 \times 10^{-3} - 1.74$
$\hat{\alpha}$	8.21	6.33	16.0	0.46 – 29.2	0.09 – 46.7
$\hat{\beta}$	0.51	0.80	$9.1 \times 10^{-5} - 84.1$	13.4	0.621
$\Delta'k^{-1}$	$\mathcal{O}(1)$	$\mathcal{O}(1)$	0.30	1.45	4.37
$S(k)$	$3.9 \times 10^5$	$1.1 \times 10^5$	$1.79 \times 10^7$	$3.50 \times 10^7$	$2.3 \times 10^4$
$P_m$	0.16	0.43	-	-	0.10
$\Delta'\delta$	$\sim 0.27$	$\sim 0.52$	0.02 – 0.07	0.06 – 0.11	0.62 – 0.98
$kl$	$\sim 0.03$	$\sim 0.09$	0.002 – 0.017	0.003 – 0.008	0.09 – 0.22

Table 2: Normalized two-fluid tearing parameters computed for a core-resonant  $m = 1$ ,  $n = 6$  mode in experimental high- and low-current discharges (left two columns), and for the linear scans of Part III (right three columns). For cylindrical cases  $k_{\perp}$  ( $r_s$ ) is used as the wavenumber and  $k_y$  is used in slab cases. The Lundquist number quoted here uses the inverse wavenumber as the characteristic length scale and is denoted  $S(k)$ , as opposed to the minor radius which is used elsewhere in the text (and is denoted simply as  $S$ ). The  $\hat{\alpha}$  and  $\hat{\beta}$  parameters are the normalized parameter space of Ahedo and Ramos (Ref. [49]) shown in Fig. 15. Finally, the linear growth rates from Sec. 11 are used to estimate the layer width in MST.

implementation of the code by benchmarking against the analytic theory. Our cylindrical scans, which are more experimentally relevant, are summarized in Secs. 11 and 12.1. For our cylindrical cases the response is dependent on the choice of a warm-ion model ( $T_i = T_e$ ) or cold-ion model ( $T_i = 0$ ) while  $\beta$  is fixed. Our slab cases are not sensitive to this choice as the effect is the result  $\nabla B_0$  and curvature drifts manifest through the ion gyroviscosity.

For convenience, the electron mass is artificially increased by a factor a 10 in most computations relative to the physical value, thus the mass ratio is  $m_e/m_i = 2.72 \times 10^{-3}$ , and the ratio of the skin depths is  $d_e/d_i = 5.21 \times 10^{-2}$ . Cylindrical computations near the collisionless limit have more realistic mass ratios such that  $d_e = \min(5.21 \times 10^{-2}d_i, 9.0 \times 10^{-3}a)$ , and the tearing conditions are in the experimentally-relevant semi-collisional regime.

The parameter space of our nonlinear computations is summarized in Table 3. Our single-helicity cases examine two particular cases with small and moderate  $d_i$ , referred to as  $k\rho_s = 0.035$  and  $k\rho_s = 0.17$  cases respectively in Part III. Varying  $d_i$  in the nonlinear computations allows us to study single-helicity tearing and subsequent magnetic island evolution in the single-fluid and two-fluid regimes. To examine the effect of warm ions, i.e. ion gyroviscosity, we run each case twice: once with warm ions ( $f_{Ti} = 0.5$ ) and once with cold ions ( $f_{Ti} = 0$ ). Our single-helicity nonlinear computations have a low  $P_m$ -value of 0.1, whereas the multihelicity cases use  $P_m = 1$ . Computational practicalities presently limit our nonlinear cases to  $S \lesssim 1 \times 10^5$ .

	MST 400 kA	MST 200 kA	SH cyl. small $d_i$	SH/MH cyl. moderate $d_i$
$kd_i$	0.71	0.71	0.12	0.60
$\beta$	0.015	0.04	0.1	0.1
$k\rho_s$	0.08	0.13	0.035	0.17
$\hat{\alpha}$	8.21	6.33	0.94	4.67
$\hat{\beta}$	0.52	0.80	0.62	0.62
$S(a)$	$1.4 \times 10^6$	$3.7 \times 10^5$	$8 \times 10^4$	$8 \times 10^4$
$P_m$	0.16	0.43	0.1	0.1/1
$\lambda(0)$	3.8	3.7	3.3	3.3/3.88

Table 3: Normalized two-fluid tearing parameters computed for a core-resonant  $m = 1$ ,  $n = 6$  mode in experimental high- and low-current discharges (left two columns), and the nonlinear cases of Parts IV and V (right two columns). The last column list both single-helicity (SH) and multi-helicity (MH) parameters. These cases use  $k_{\perp}(r_s)$  as the wavenumber. The  $\hat{\alpha}$  and  $\hat{\beta}$  parameters are the normalized parameter space of Ahedo and Ramos (Ref. [49]) shown in Fig. 15.

## Part III

# Linear tearing modes

We naturally order our discussion such that each subsequent part becomes increasingly more complex. In this part, we examine linear tearing, before moving to considerations of nonlinear effects (Part IV) and multiple nonlinearly-interacting modes (Part V). Thus our study begins with code verification by comparing our computations to analytic linear-tearing-mode theory in slab geometry in Sec. 10, and finishes with code validation through comparison to published MST measurements (Part V). With regard to the rest of our linear results, in Sec. 11 we study the dispersion relation in cylindrical geometry and find significant drift responses proportional to  $\nabla B_0$  and poloidal curvature. And in Sec. 12, we examine the modification to the eigenfunction from decoupling and drift effects and the quasi-linear mean-field emfs generated by the linear mode.

## 10 Slab geometry

### 10.1 Benchmark to analytic theory

Figure 20 shows the result of our numerical computations compared to the analytic dispersion relations of Refs. [14, 49] previously described in Sec. 5.2. In Fig. 20(a) the value of the flat equilibrium temperature profile is varied while all other parameters are held constant such that a range of  $\beta$  and thus  $\rho_s$  values are scanned. The converged growth rates from NIMROD are compared to the theory of Mirnov et al. in Ref. [14], Eqn. (5.25), with and without finite electron inertia. At large  $k\rho_s$ , the diffusion of  $\tilde{B}_{\parallel}$  described in Sec. 5.2 limits the growth rate of the mode, and this effect is captured by both the theory and numerics. At small values of  $k\rho_s$ , the numerical results asymptote to the single-fluid limit described by resistive MHD. The theory does not capture this transition as its regime of validity is restricted to stationary ions. In Fig. 20(b) the value of  $d_i$  is varied while other parameter are held constant, and the resulting numerical growth rates from NIMROD are compared to the theory of Ahedo et al. in Ref. [49]. Their assumption of  $\beta \gg (\gamma/v_A k_{\perp})^2$  and small- $\Delta'$  are less restrictive than those of Ref. [14], and there is quantitative agreement between the computations and the theory within 2.3%. Both the theory and computation capture the asymptotic limit of single-fluid behavior at small  $kd_i$ .

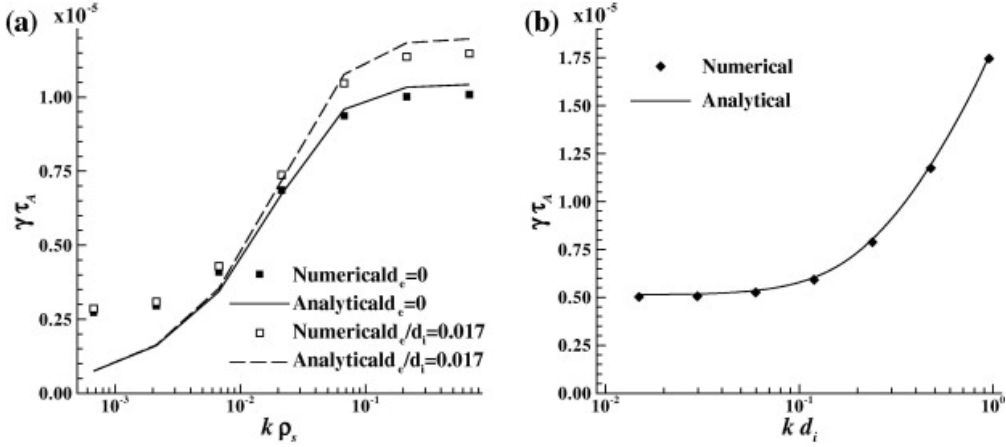


Figure 20: Comparison of numerical tearing-mode growth rates from the NIMROD code with (a) theoretical analysis of Ref. [14] for conditions of  $S = 1.79 \times 10^7$ ,  $\Delta'k^{-1} = 0.30$ ,  $\epsilon_B = 1/25$ ,  $kL_B = 0.93$ , and  $kd_i = 0.418$ , and with (b) the analysis of Ref. [49] for conditions of  $S = 3.50 \times 10^7$ ,  $\Delta'k^{-1} = 1.45$ ,  $\epsilon_B = 1/50$ ,  $kL_B = 0.76$ , and  $\beta = 0.1$ .

## 10.2 Eigenmode structure

Before studying the eigenfunction of the two-fluid tearing mode in cylindrical geometry, it is useful to start with a more idealized slab geometry. Equilibrium quantities are dependent only on the  $x$ -coordinate and are either symmetric or anti-symmetric about  $x = 0$ , where the resonant condition,  $\mathbf{k} \cdot \mathbf{B}_0 = 0$ , is satisfied. The equilibrium magnetic field has no curvature, and with uniform pressure, its magnitude is also uniform. The electron flows of tearing modes in this simple configuration symmetrically advect the reconnecting magnetic flux into a magnetic island, as illustrated schematically in Fig. 13. Given the spatial representation  $\tilde{A}Exp[im\theta + inz/R]$ , we choose the complex phase of the mode such that  $\tilde{B}_r(0)$  is positive and real, as shown in the schematic. With a single-fluid resistive MHD model, this choice makes  $\tilde{B}_r(r)$  purely real and  $\tilde{B}_\perp(r)$  and  $\tilde{B}_\parallel(r)$  purely imaginary as established by Eqns. (4.7), (4.24), and (5.24) (without the contribution from the Hall term), see Ref. [39]. The x-point inflow is then part of the purely imaginary  $\tilde{v}_r(r)$ , and the x-point outflow is part of the purely real  $\tilde{v}_\perp(r)$  as established by Eqns. (4.23), (4.11) and (4.12). How this choice of the complex-phase normalization corresponds to the tearing structure is shown on the RHS of Fig. 13.

In order to aid comparison, we choose to examine a slab case with parameters that no longer satisfy the strict scale separation of the analytic theories, but are similar to our cylindrical cases:  $S = 8 \times 10^4$ ,  $\beta = 0.1$ ,  $k\rho_s = 0.17$ ,  $\epsilon_B = 0.1$ ,  $kL_B = 0.56$ ,  $P_m = 0.1$ . These choices result in  $k^{-1}\Delta' = 4.45$  (Eqn. (9.13)),  $\gamma\tau_A = 9.6 \times 10^{-3}$  and  $kl = 0.025$  with a two-fluid model, and  $\gamma\tau_A = 5.4 \times 10^{-3}$  and  $kl = 0.040$  with a single-fluid model. Figure 21 shows the magnetic eigenfunction near the resonant surface, as  $ka = 3.48$  the plots are scaled to show  $-0.348 \leq kr \leq 0.348$ . Consistent with the discussion of the previous paragraph,

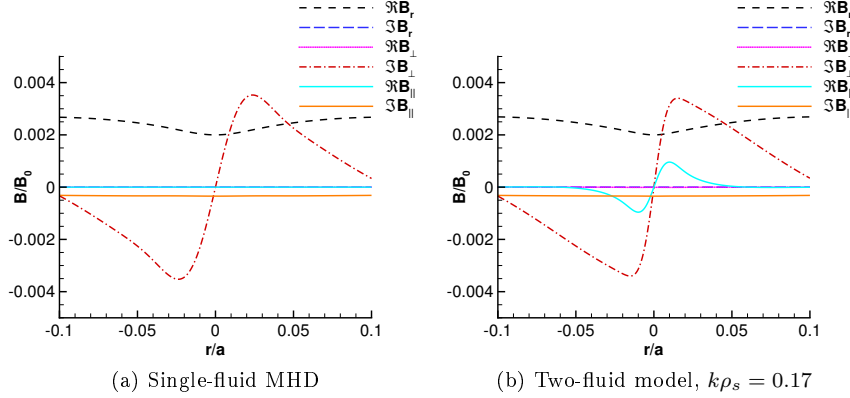


Figure 21: Eigenmode components of  $\tilde{\mathbf{B}}$  for computations with  $S = 8 \times 10^4$ ,  $\beta = 0.1$ ,  $k\rho_s = 0.17$ , and cold ions using (a) a single-fluid resistive-MHD model, and (b) a two-fluid model which includes the generalized Ohm's law.

with a single-fluid model only the set of components  $(\Re\tilde{B}_r, \Im\tilde{B}_\perp, \Im\tilde{B}_\parallel)$  are non-zero as shown in Fig. 21(a). Additionally, the small- $\Delta'$  tearing ordering established in Sec. 4 is apparent:  $\tilde{B}_r = ik_\perp B_0 \tilde{\psi} \sim \tilde{B}_\perp = -B_0 \tilde{\psi}'$  and it is clear that  $\tilde{B}'_\perp \sim \tilde{\psi}''$  will be large. Examining the magnetic eigenfunction with a two-fluid model, Fig. 21(b), we note that the component  $\Re\tilde{B}_\parallel$  is now significant. As this component is antisymmetric with respect to  $r_s$ , it creates a quadrupole field around the x-point. This term is directly related to the Hall term in Eqn. (5.24), second term on the RHS. Our phase normalization makes  $\tilde{\psi}$  purely imaginary with a single-fluid model. Thus the inclusion of the Hall term,  $\nabla \times (\tilde{\mathbf{J}} \times \mathbf{B}_0) \sim ik'_{\parallel s} x \tilde{\psi}''$ , leads to the purely real contribution that creates this quadrupole field.

The flow structure of the single- and two-fluid slab cases is plotted in Fig. 22. In all cases, the electrons flow forms symmetric eddies around the resonant surface, as sketched in Fig. 13. Relative to the single-fluid case, Figs. 22(a) and (c), the magnitude of the two-fluid electron flow, Figs. 22(b) and (d), is increased as expected from both the increase in growth rate and decrease in layer width. It is clear that there is a separation between the electron and ion flows with a two-fluid model at these parameters. This separation is associated with non-zero  $(\Im\tilde{J}_r, \Re\tilde{J}_\perp)$ . A straightforward application of Ampere's law shows that the magnetic perturbations  $(\Re\tilde{B}_r, \Im\tilde{B}_\perp, \Im\tilde{B}_\parallel)$  produce a current perturbation with the phase orientation  $(\Re\tilde{J}_r, \Im\tilde{J}_\perp, \Im\tilde{J}_\parallel)$ . The non-zero contributions from the components of the perturbed current density that lead to species-flow separation,  $(\Im\tilde{J}_r, \Re\tilde{J}_\perp)$ , are a direct consequence of the non-zero quadrupole field,  $\Re\tilde{B}_\parallel$ . As a final point, the flow structure of the plots confirms the tearing ordering of Sec. 4. The sheared structure of  $\tilde{v}_r = -ik_\perp \tilde{\phi}$  leads to a  $\tilde{v}_\perp = \tilde{\phi}'$  which is at least an order magnitude larger.

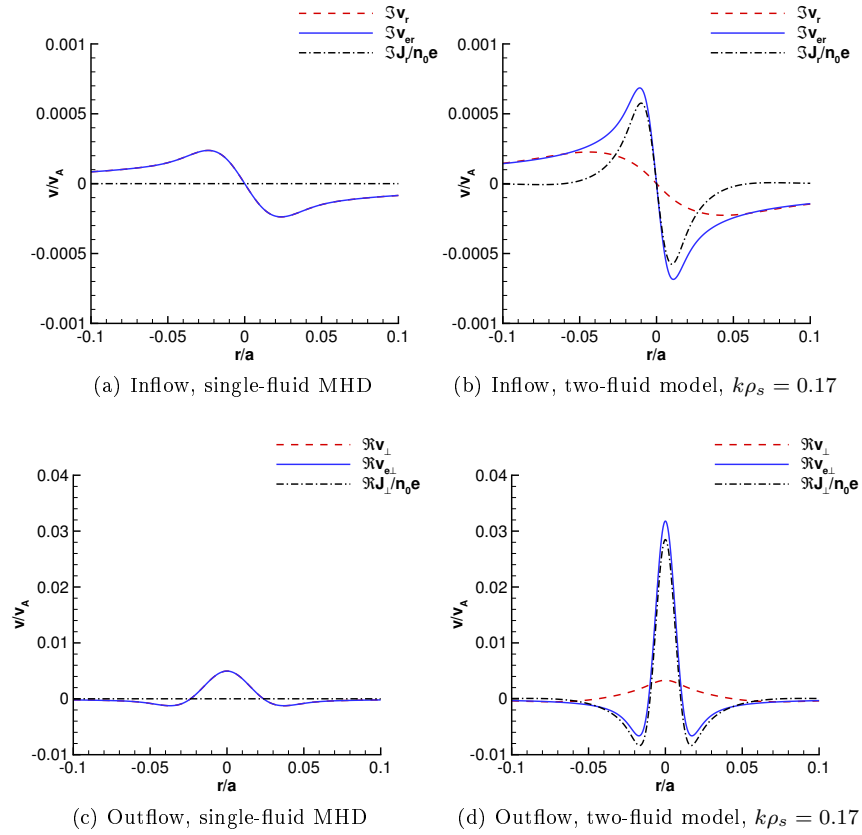


Figure 22: Eigenmode components of the tearing flow structure plots show (a,b) the tearing x-point inflow and (c,d) the tearing x-point outflow for computations with  $S = 8 \times 10^4$ ,  $\beta = 0.1$ ,  $k\rho_s = 0.17$ , and cold ions using (a,c) a single-fluid resistive-MHD model, and (b,d) and two-fluid model which includes the generalized Ohm's law.

## 11 Cylindrical dispersion relation

We now move our discussion from symmetric slab cases to more realistic cylindrical computations. These cases involve additional effects from field-line curvature, an asymmetric parallel-current profile with respect to the resonant surface, and mathematical regularity conditions at  $r = 0$ . Aside from the coupling to the perturbed pressure discussed in Sec. 4.3, with cold ions the inner-region parallel-vorticity and radial-induction equations, Eqn. (4.23) and (4.24) respectively, are identical in the slab and cylindrical cases. However, as discussed in Sec. 11.1, the cylindrical parallel-induction equation, Eqn. (5.24), includes significant effects from terms proportional to poloidal curvature and mean-magnetic-field gradients that are not present in slab cases. These additional terms cause a distortion of the eigenfunction such that the complex-phase of the components varies as a function of radius. As a consequence, the growth rate is not purely real when  $\rho_s \gtrsim l$ , where the imaginary part represents rotation of the linear mode. Additionally, there is now an important distinction in our cases between computations with cold ( $f_{Ti} = 0$ ) and warm ions ( $f_{Ti} = 0.5$ ), where the former do not include the effect of gyroviscosity.

### 11.1 Computational result

Figure 23 shows linear growth rates versus  $k\rho_s$  for calculations with cold ( $f_{Ti} = 0$ ) and warm ions ( $f_{Ti} = 0.5$ ) at  $S = 8 \times 10^4$ . Using the single-fluid growth rate to compute the skin depth, we find  $kl \simeq 0.24$  and the cold-ion trace shows growth rates that exceed the MHD result by about 20% when  $\rho_s \sim l$ . Thus, our cylindrical results with cold ions are consistent with expectations from the analytical slab theory as electron-ion decoupling and enhanced growth rates are found when  $\rho_s \gtrsim l$ . Our results with warm ions show a more complicated transition. In the small- $\rho_s$  limit, both the warm- and cold-ion results approach the single-fluid growth rate. At large- $\rho_s$  values, the electron flow decouples from the ion flow such that the warm-ion effects are not important. Thus, the warm- and cold-ion growth rates also converge at large  $\rho_s$ . In the intermediate regime, the ion response is modified by a drift effect from the ion gyroviscosity. This drift effect leads to growth rates that are smaller than the single-fluid result when  $\rho_s$  is not large enough for the KAW response to decouple the tearing from the ion fluid. Numerical results for similar warm-ion conditions in slab geometry do not show this drift regime, so the important gyroviscous effect is associated with the cylindrical geometry and equilibrium.

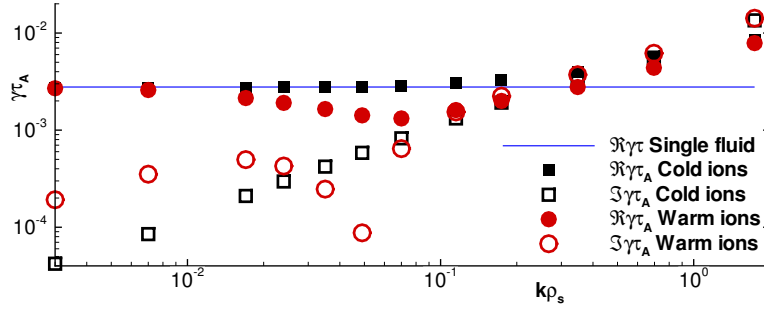


Figure 23: Growth rates ( $\Re\gamma_{\tau_A}$  and  $|\Im\gamma_{\tau_A}|$ ) as a function of the ion sound gyroradius ( $k\rho_s$ ) for linear computations with cold ions ( $f_{Ti} = 0$ , squares ( $\Re\gamma_{\tau_A}$ ) and diamonds ( $|\Im\gamma_{\tau_A}|$ )), and warm ions ( $f_{Ti} = 0.5$ , circles ( $\Re\gamma_{\tau_A}$ ) and triangles ( $|\Im\gamma_{\tau_A}|$ )). The single-fluid result is shown as the solid horizontal line. These  $\rho_s$  scans are performed at  $S = 8 \times 10^4$ ,  $P_m = 0.1$  and  $\beta = 0.1$ .

As shown in Fig. 23, the growth rate is complex for our cylindrical cases where the imaginary part is associated with mode rotation. In the intermediate regime, the mode rotation is determined by the gyroviscous drift which will be described in detail in Sec. 11.2. In the KAW-mediated regime,  $\rho_s \gtrsim l$ , the cold-ion cases start to rotate and eventually  $\Im\gamma > \Re\gamma$ . Similarly, the warm-ion cases approach the same result as the cold-ion cases as the ion fluid is decoupled. This drift effect is not present with slab geometry and can be qualitatively described through examination of the cylindrical inner-region parallel-induction equation (The analog to Eqn. (5.24) in slab cases). The  $\tilde{\mathbf{J}} \times \mathbf{B}_0$  part of the Hall term in cylindrical geometry is

$$\hat{\mathbf{b}}_0 \cdot \nabla \times (\tilde{\mathbf{J}} \times \mathbf{B}_0) = ik_{\parallel} B_0 \tilde{J}_{\parallel} - \tilde{J}_r \left( \frac{\nabla B_0}{B_0} - \frac{b_{0\theta}^2}{r} \right) \simeq -ik'_{\parallel s} x B_0 \tilde{\psi}'' - ik_{\perp s} \tilde{B}_{\parallel} \left( \frac{\nabla B_0}{B_0} - \frac{b_{0\theta}^2}{r} \right) \quad (11.1)$$

where  $b_{0\theta} = B_{0\theta}/B_0$ , the last term on the RHS is not present in slab theory and tearing ordering (Sec. 4) has been applied ( $\tilde{J}_{\parallel} \simeq -B_0 \tilde{\psi}''$  and  $\tilde{J}_r \simeq ik_{\perp s} \tilde{B}_{\parallel} + ik'_{\parallel s} x B_0 \tilde{\psi}'$ ). In particular, equilibrium quantities are Taylor expanded about the resonant surface by the small parameter  $x \equiv r - r_s$  where  $|x| \sim \epsilon r_s$  with  $\epsilon \ll 1$ . For these equilibrium and geometric quantities, primes indicate differentiation with respect to  $r$ , evaluated at  $r = r_s$ . Unlike a flute ordering, the wavenumber of the tearing mode,  $k_{\perp} = \sqrt{(m/r)^2 + (n/R)^2}$ , is order 1. The second derivative of  $\tilde{\psi}$ , which is proportional to the perturbed parallel current in the layer, is large in this ordering,  $\tilde{\psi}'' \gg k^2 \tilde{\psi} \sim k \tilde{\psi}'$ .

Adding the  $\hat{\mathbf{b}}_0 \cdot \nabla \times (\tilde{\mathbf{J}} \times \mathbf{B}_0)$  and other contributions from cylindrical curvature from the  $\mathbf{v} \times \mathbf{B}$  term to the parallel-induction equation, we find

$$(\gamma - i\omega_{*H} + i\omega_{E \times B}) \tilde{B}_{\parallel} \simeq -B_0 \nabla_{\perp} \cdot \tilde{\mathbf{v}} - B_0 \tilde{v}_r \left( \frac{\nabla B_0}{B_0} - \frac{b_{0\theta}^2}{r} \right) - ik_{\perp s} B_0 v_{e0\theta} \frac{b_{0\theta}}{r} \tilde{\psi} + d_i v_A ik'_{\parallel s} x B_0 \tilde{\psi}'' + \eta \nabla^2 \tilde{B}_{\parallel} \quad (11.2)$$

similar to the equation derived in Ref. [72]. We assume flat temperature and density profiles and define the drift frequency from the Hall effect as

$$\omega_{*H} = k_{\perp s} d_i v_A \left( \frac{b_{0\theta}^2}{r} - \frac{B'_0}{B_0} \right). \quad (11.3)$$

Comparing Eqn. (11.2) to Eqn. (5.24) we note that the  $\omega_{*H}$  term on the LHS and the second and third term on the RHS are only present in the cylindrical case. The second term on the RHS is from  $\tilde{\mathbf{v}} \times \mathbf{B}_0$  and modifies  $\Im \tilde{B}_{\parallel}$  relative to the slab cases. The third term is from  $\mathbf{v}_{e0} \times \tilde{\mathbf{B}}$ , and even without ion flow it still may contribute as  $b_{0\theta} J_{0\theta} \tilde{B}_r / n_0 e r$  if the Hall term is included. Through this term, the inclusion of mean poloidal ion flow will cause mixing of the complex-phases of the mode, even with a single-fluid model.

The  $\omega_{*H}$  term is a result of including the Hall effect in our equations, and is a drift effect which acts only on  $\tilde{B}_{\parallel}$ . Thus we expect a drift-like response of the mode to be significant when there is a large contribution from  $\tilde{B}_{\parallel}$  to the radial induction equations, Eqn. 4.24, similar to the KAW effects. Indeed Fig. 23 shows the rotation becomes large,  $|\Im \gamma \tau_A| \sim \Re \gamma \tau_A$ , at  $k \rho_s \sim kl \simeq 0.24$  just like the KAW effects which are significant for  $\rho_s \gtrsim l$ .

## 11.2 Heuristic reduced gyroviscous model

We examine the gyroviscous effects in our pinch profiles by considering the parallel component of the vorticity equation, Eqn. (4.18). A stress tensor makes two contributions: the first appears directly as the last term on the RHS of Eqn. (4.18), and the second appears when eliminating  $\nabla_{\perp} B$  after writing the Lorentz force on the right-hand side in terms of the curvature vector  $\boldsymbol{\kappa}$ . We assemble a heuristic dispersion relation using resistive-MHD magnetic-field evolution, Eqn. (4.24), and including the effect of  $\tilde{\boldsymbol{\Pi}}_{gv}$  in the parallel vorticity equation. A complete dispersion relation would include both the finite- $\beta$  effects that couple parallel flows and the two-fluid Ohm's law. However, through comparison with the results from NIMROD, we show that our heuristic model explains the stabilizing gyroviscous effect in the drift regime at intermediate- $\rho_s$  values.

We expand the gyroviscous stress operator about  $r_s$  in the inner region where the tearing flows are non-

negligible and apply tearing ordering. Consistent with the aspect ratio ordering of the flow described in Sec. (4) and confirmed in our computational slab cases of Sec. 10.2, the radial flows  $\tilde{v}_r = -ik_\perp \tilde{\phi}$  are order  $\epsilon$  smaller than the perpendicular flows,  $\tilde{v}_\perp = \tilde{\phi}'$ . For the perturbed streamfunction,  $\tilde{\phi}(x)$ , primes indicate derivatives with respect to  $x$ . The localized nature of the tearing response leads to an ordering with respect to  $x$  with each derivative of  $\tilde{\phi}$  lowering the order of a term by  $\epsilon$ . Higher-order contributions result from the expansions of  $\hat{\mathbf{b}}_0$  and  $\mathbf{k}$ .

While forces from the gyroviscous stress of the tearing vortices include terms as large as order  $\epsilon^{-3}$ , many do not contribute to the parallel vorticity. The leading-order force,  $\left(p_{i0}\tilde{\phi}'''/2\omega_{ci0}\right)\hat{\mathbf{r}}$ , for example, does not have a component in the  $\hat{\mathbf{b}}_0 \times \boldsymbol{\kappa}_0$  direction. Including terms of order  $\epsilon^{-2}$ , the force is

$$-\nabla \cdot \boldsymbol{\Pi} = \left[ \frac{p_{i0}}{2\omega_{ci0}} \left( \tilde{\phi}''' + \frac{\tilde{\phi}''}{r} \right) + \left( \frac{p_{i0}}{2\omega_{ci0}} \right)' \left( \tilde{\phi}'' + x\tilde{\phi}''' \right) \right] \hat{\mathbf{r}} + \frac{p_{i0}}{2\omega_{ci0}} ik_\perp \tilde{\phi}'' \hat{\mathbf{b}}_0 \times \hat{\mathbf{r}} + \mathcal{O}(\epsilon^{-1}) . \quad (11.4)$$

From this, we find the leading-order curvature-induced modification to  $\hat{\mathbf{b}}_0 \cdot \nabla \times (\mathbf{J} \times \mathbf{B})$ ,

$$2\hat{\mathbf{b}}_0 \times \boldsymbol{\kappa}_0 \cdot \nabla \cdot \tilde{\boldsymbol{\Pi}} = \frac{p_{i0}}{\omega_{ci0}} \frac{b_{0\theta}^2}{r} ik_\perp \tilde{\phi}'' + \mathcal{O}(\epsilon^{-1}) . \quad (11.5)$$

The leading-order forces in the radial and perpendicular directions, of order  $\epsilon^{-3}$  and  $\epsilon^{-2}$  respectively in Eqn. (11.4), may be rewritten in terms of  $\tilde{v}_r$  and  $\tilde{v}_\perp$  as

$$-\nabla \cdot \boldsymbol{\Pi} \cong \frac{p_{i0}}{2\omega_{ci0}} \left[ (\nabla^2 \tilde{v})_\perp \hat{\mathbf{r}} - (\nabla^2 \tilde{v})_r \hat{\mathbf{b}}_0 \times \hat{\mathbf{r}} \right] . \quad (11.6)$$

Figure 24 shows that when the expression on the right-hand side is computed with the flow velocity of a warm-ion cylindrical tearing mode, it provides a good approximation to the full gyroviscous force.

The gyroviscous force contains at most three radial derivatives from differential operations: the divergence of  $\boldsymbol{\Pi}$ , the  $\nabla \tilde{\mathbf{v}}$  in the rate of strain tensor, and the gradient of  $\tilde{\phi}$ . Thus, the force has lowest order terms at  $\mathcal{O}(\epsilon^{-3})$ . For the parallel ion-gyroviscous torque,  $-\hat{\mathbf{b}}_0 \cdot \nabla \times \nabla \cdot \tilde{\boldsymbol{\Pi}}$ , the radial derivatives in the curl operation act only on the perpendicular force, which is of  $\mathcal{O}(\epsilon^{-2})$ , so there is no contribution to the torque at  $\mathcal{O}(\epsilon^{-4})$ . In fact the radial derivative of the lowest-order perpendicular force,  $\mathcal{O}(\epsilon^{-2})$ , cancels exactly with the  $\mathcal{O}(\epsilon^{-3})$  term  $ik_\perp (\nabla \cdot \boldsymbol{\Pi})_r$  from the radial force during the curl operation. This cancellation is related to the nearly incompressible nature of the flows, and thus there are at most terms of  $\mathcal{O}(\epsilon^{-2})$  in the gyroviscous torque.

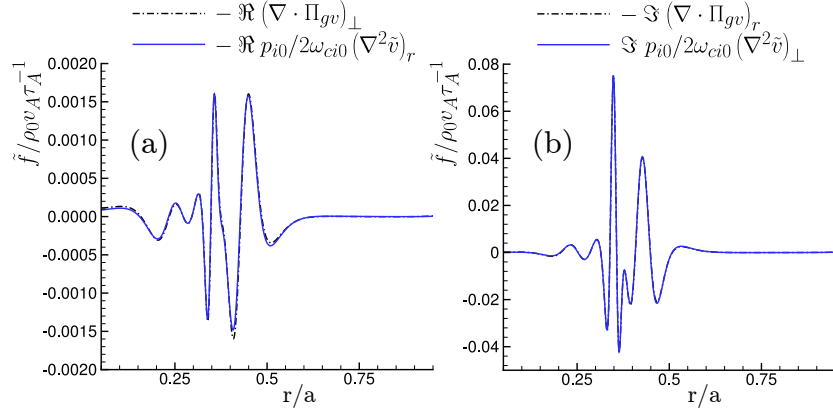


Figure 24: The perpendicular, (a), and radial, (b), ion-gyroviscous stress as well as the leading-order terms expressed in Eqn. (11.6) for a linear computation with  $S = 8 \times 10^4$ ,  $\beta = 0.1$ ,  $k\rho_s = 0.17$  and warm ions.

This requires evaluation of the perpendicular gyroviscous force to  $\mathcal{O}(\epsilon^{-1})$ , where the additional terms at  $\mathcal{O}(\epsilon^{-1})$  are

$$\frac{p_{i0}}{2\omega_{ci0}} \left[ ik'_\perp x \tilde{\phi}'' + \frac{ik_\perp \tilde{\phi}'}{r} (1 + b_\theta^2) \right] + \left( \frac{p_{i0}}{2\omega_{ci0}} \right)' ik_\perp [2\tilde{\phi}' + x\tilde{\phi}'']. \quad (11.7)$$

Applying the  $\hat{b} \cdot \nabla \times$  operation to the gyroviscous forces through  $\mathcal{O}(\epsilon^{-1})$ , we find the  $\mathcal{O}(\epsilon^{-2})$  gyroviscous torque,

$$-\hat{\mathbf{b}}_0 \cdot \nabla \times \nabla \cdot \tilde{\mathbf{\Pi}} = \frac{p_{i0}}{2\omega_{ci0}} \frac{b_{0\theta}^2}{r} ik_\perp \tilde{\phi}'' + \left( \frac{p_{i0}}{\omega_{ci0}} \right)' ik_\perp \tilde{\phi}'' + \mathcal{O}(\epsilon^{-1}) \quad (11.8)$$

which is of the same order as the leading contribution from  $2\hat{\mathbf{b}}_0 \times \boldsymbol{\kappa}_0 \cdot \nabla \cdot \tilde{\mathbf{\Pi}}$ . The calculations are detailed in Appendix F. Using  $\tilde{U} \simeq \tilde{\phi}''$  to order  $\epsilon^{-2}$  and ignoring contributions from the relatively small isotropic viscosity and perturbed pressure, we rewrite the parallel-vorticity equation as

$$(\gamma - i\omega_{*gv} + i\omega_{E \times B}) \tilde{\phi}'' = -v_A^2 ik'_{\parallel s} x \tilde{\psi}'' \quad (11.9)$$

where again the kink and line-bending terms have been reduced as in Sec. 4 and we define the gyroviscous drift frequency as

$$\omega_{*gv} = \frac{k_\perp}{m_i n_0} \frac{p_{i0}}{\omega_{ci0}} \left( \frac{3}{2} \frac{b_{0\theta}^2}{r} - \frac{B'_0}{B_0} \right) = k_\perp f_{Ti} \beta d_i v_A \left( \frac{3}{2} \frac{b_{0\theta}^2}{r} - \frac{B'_0}{B_0} \right). \quad (11.10)$$

For conditions with an ion diamagnetic drift,  $\mathbf{v}_0 = \hat{\mathbf{b}}_0 \times \nabla p_{i0} / \omega_{ci0} m_i n_0$ , the advective term of Eqn. (4.18) becomes  $-ik_\perp p'_{i0} \tilde{\phi}'' / \omega_{ci0} m_i n_0$  and cancels with the contribution from the ion-gyroviscous torque that is proportional to  $p'_{i0}$  in Eqn. (11.8). Thus, even though we study cases without an equilibrium-pressure

gradient, we recover the general lowest-order effects with respect to  $\rho_i/L$  in the ion-flow equation.

As a new result found in this work, the  $\omega_{*gv}$  term from gyroviscous stress has the form of an ion-drift effect in the parallel vorticity equation, and it provides stabilizing effects that are generally observed with drift-tearing, see Sec. 5.1. To demonstrate the stabilizing effects, we choose the ion rest frame such that  $\omega_{E \times B} \rightarrow 0$  and combine Eqn. (11.9) with resistive-MHD evolution of the perturbed magnetic flux, Eqn. (4.24). This results in a coupled pair of second-order differential equations,

$$\begin{aligned} (\gamma - i\omega_{*gv}) \tilde{\phi}'' &= -v_A^2 i k'_{\parallel} x \tilde{\psi}'' \\ \gamma \tilde{\psi} + i k'_{\parallel} x \tilde{\phi} &= \frac{\eta}{\mu_0} \tilde{\psi}'' . \end{aligned} \quad (11.11)$$

Using these as our inner-layer equations for the tearing mode, the resulting heuristic dispersion relation is  $\gamma^4 (\gamma - i\omega_{*gv}) = \gamma_{MHD}^5$  similar to the relation found in Sec. 5.1, Eqn. (5.7), where  $\gamma_{MHD}$  is the growth rate when  $\omega_{*gv} \rightarrow 0$ .

### 11.3 Comparison

The growth rates of Fig. 23 are computed with parameters that we use in our nonlinear single- and multihelicity studies. Instead of comparing our heuristic gyroviscous model with these computations, we perform a second set of computations that are in the asymptotic limit of large  $S$  ( $10^6$ ), which is important for the validity of the tearing ordering, and have small  $P_m$  ( $10^{-3}$ ) as we have ignored contributions from isotropic viscosity. We then compare the growth rate and real frequency of the heuristic dispersion relation with results from three subsets of these linear computations from NIMROD as shown in Fig. 25.

The first subset of computations uses a resistive-MHD Ohm's law with the cylindrical geometry and parameters of our pinch case, and  $\beta$  is very small in order to reproduce the simplified response assumed for the heuristic model. Thus to capture the effects of ion gyroviscosity, an ad-hoc gyroviscous coefficient is scaled to vary  $\omega_{*gv}$ . Although the numerical computations include more than just the leading-order effects with respect to  $|x|/a$ , we see that there is good agreement between our heuristic model and the growth rate and real frequency computed with NIMROD, and a strong stabilizing effect from the gyroviscous stress is apparent.

The second subset of numerical computations shown in Fig. 25 is computed with  $\beta = 10\%$  and  $f_{Ti} = 0.5$ ;

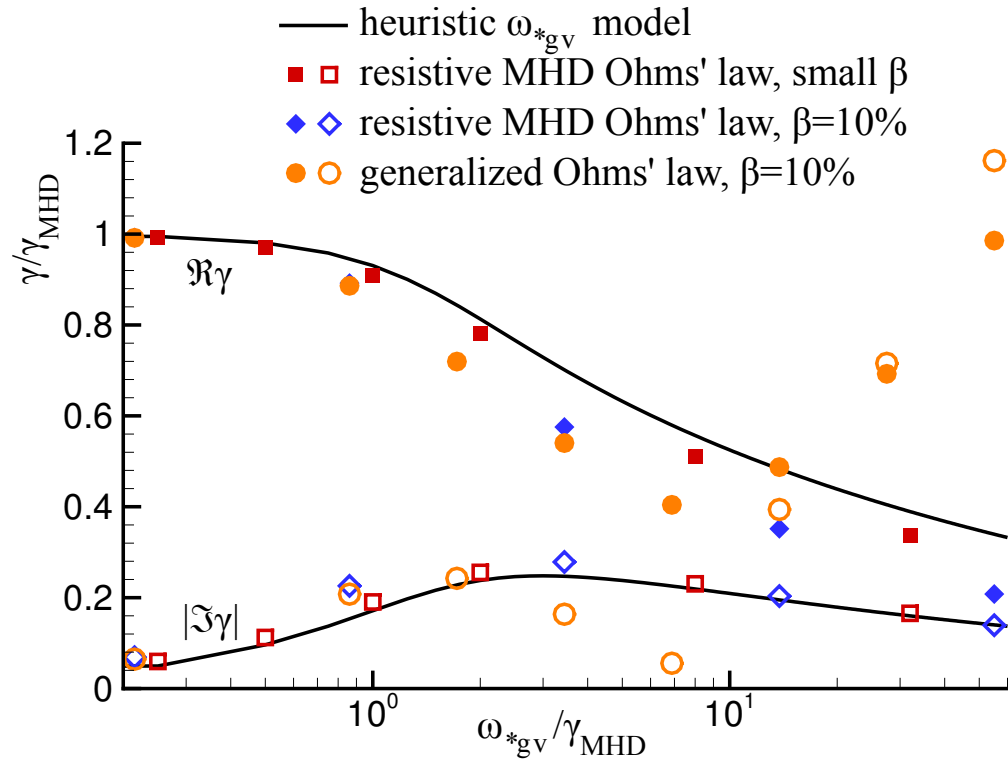


Figure 25: A comparison of  $\Re\gamma$  (top curve, filled symbols) and  $|\Im\gamma|$  (bottom curve, open symbols) between the heuristic  $\omega_{*gv}$  model and three sets of numerical computations with  $S = 10^6$ ,  $P_m = 10^{-3}$  and ion gyroviscosity.

the Ohm's law is again resistive MHD. Although the heuristic model does not include coupling between parallel flow and perturbed pressure, we observe that there is semi-quantitative agreement with the heuristic model under-predicting the stabilizing effect at large- $\omega_{*gv}$  values.

The third subset of computations uses the generalized Ohm's law, Eqn. (2.27), and essentially the same parameters as the computations shown in Fig. 23 except that  $S = 10^6$  and  $P_m = 10^{-3}$ . The results for the real growth rate are similar to those with  $\beta = 10\%$  and the resistive-MHD Ohm's law up to  $\omega_{*gv}/\gamma_{MHD} \simeq 10$  where the real frequency changes sign as the KAW-type effects become important. Note that  $\omega_{*gv}$  is proportional to the ion-sound gyroradius and in our computations,  $\omega_{*gv}/\gamma_{MHD} \simeq 315k\rho_s$ . Thus, the gyroviscous contribution becomes important at  $k\rho_s \simeq 3.2 \times 10^{-3}$ , before KAW responses occur, and loses significance for  $k\rho_s \gtrsim kl \simeq 7 \times 10^{-2}$ .

The regime boundaries from the  $S = 10^6$  results are consistent with the  $S = 8 \times 10^4$  results for warm ions shown in Fig. 23. For these cases  $\omega_{*gv} \simeq \gamma_{MHD}$  at  $k\rho_s = 5 \times 10^{-3}$ , and we conclude that a single-fluid MHD model captures the physics when  $\omega_{*gv} < \gamma_{MHD}$ , the drift regime begins when  $\omega_{*gv} \gtrsim \gamma_{MHD}$ , and KAW decoupling effects dominate when  $\rho_s \gtrsim l$ .

## 12 Cylindrical structure

### 12.1 Eigenfunction components

We now examine in additional detail two sets of cases, each set composed of both a warm- and cold-ion case, from the linear growth rate scan shown in Fig. 23. In particular we choose a set near the single-fluid limit for cold ions but in the intermediate  $\omega_{*gv}$ -drift regime for warm ions with  $k\rho_s = 0.035$ , and a set with  $k\rho_s = 0.17$  where the KAW decoupling is significant. These cases roughly correspond to the range of MST experimental parameters, see Tab. 3. In our subsequent nonlinear discussion we will examine the set of cases with  $k\rho_s = 0.17$  in more detail, and our multihelicity modeling of Part V is run with  $k\rho_s = 0.17$  and warm ions.

As described in Sec. 10.2, two-fluid effects alter the phases of the tearing eigenfunction as a function of radius, so the single-fluid phase relations are not valid. In Figs. 26 and 27 we plot two different sets of computed eigenfunction components for different physical parameters. The first set corresponds to the non-zero perturbations in the single-fluid limit ( $\Re\tilde{B}_r, \Im\tilde{B}_\perp, \Im\tilde{B}_\parallel$ ), and the second set ( $\Im\tilde{B}_r, \Re\tilde{B}_\perp, \Re\tilde{B}_\parallel$ ) is non-zero

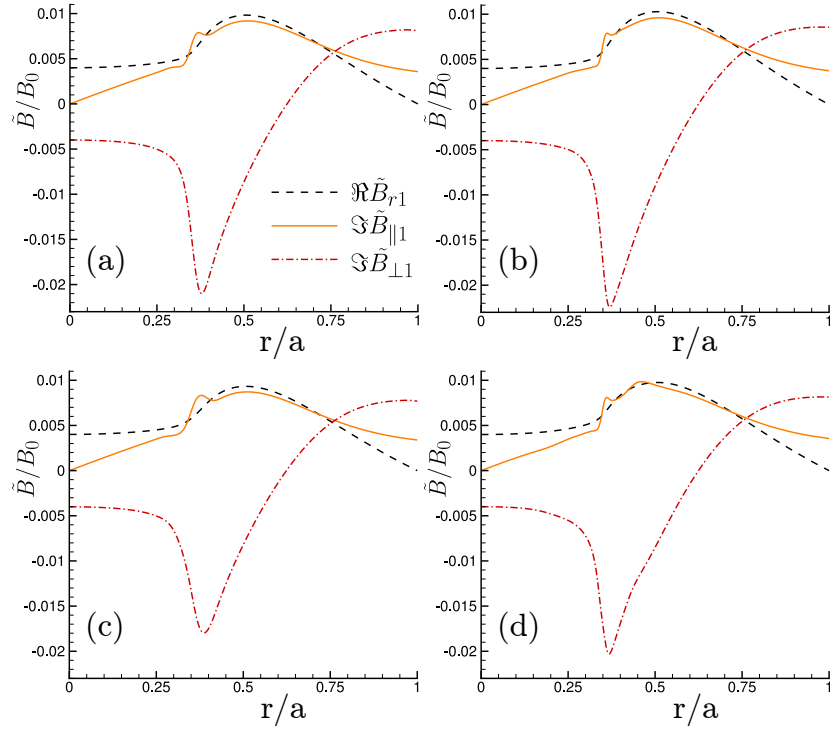


Figure 26: Eigenmode components of  $\tilde{\mathbf{B}}$  in phase with a single-fluid eigenfunction for computations with  $S = 8 \times 10^4$ ,  $\beta = 0.1$  and (a)  $k\rho_s = 0.035$  and cold ions, (b)  $k\rho_s = 0.17$  and cold ions, (c)  $k\rho_s = 0.036$  and warm ions, and (d)  $k\rho_s = 0.17$  and warm ions.

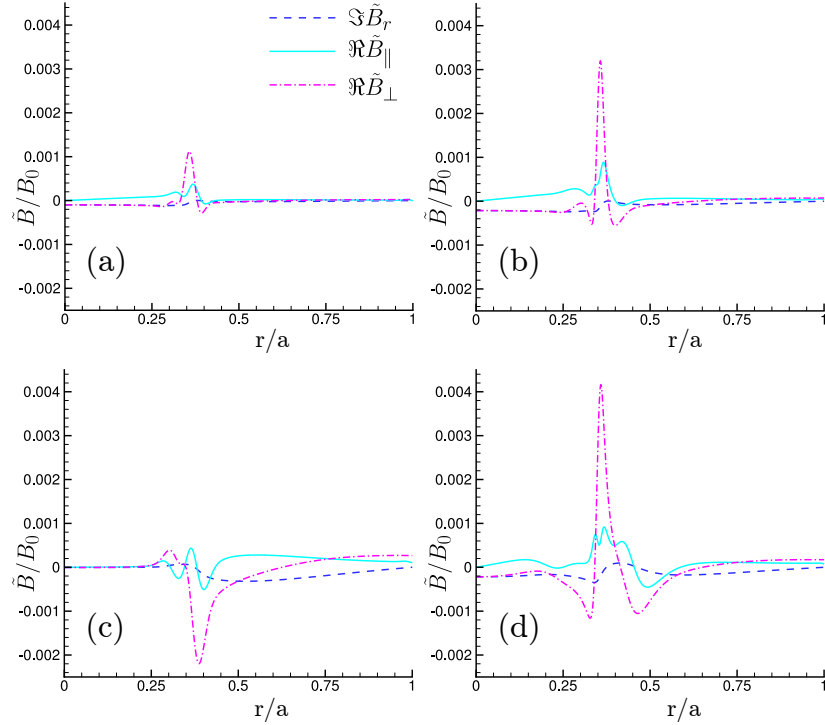


Figure 27: Eigenmode components of  $\tilde{\mathbf{B}}$  out of phase with a single-fluid eigenfunction for computations with  $S = 8 \times 10^4$ ,  $\beta = 0.1$  and (a)  $k\rho_s = 0.035$  and cold ions, (b)  $k\rho_s = 0.17$  and cold ions, (c)  $k\rho_s = 0.035$  and warm ions, and (d)  $k\rho_s = 0.17$  and warm ions.

only when two-fluid effects are considered. The linear magnetic components of the first set at  $S = 8 \times 10^4$  are plotted in Fig. 26 for  $k\rho_s = 0.035$  and  $k\rho_s = 0.17$  with warm and cold ions. The amplitude of the eigenfunction has been normalized such that  $\Re\tilde{B}_r(0) = 0.004B_0$  for comparison with the nonlinear plots discussed in Part IV. Note that the profile and relative amplitude of the  $(\Re\tilde{B}_r, \Im\tilde{B}_\perp, \Im\tilde{B}_\parallel)$  components in our cylindrical cases are largely unchanged by the two-fluid effects.

In contrast with the slab results, the cylindrical cases do not have a clear quadrupole field from  $\Re\tilde{B}_\parallel$ . We surmise that in addition to the fourth term on the RHS of the parallel induction equation, Eqn. (11.2), which is responsible for the quadrupole field, the contribution from  $\omega_{*H}$  and the third term on the RHS are significant and distort  $\Re\tilde{B}_\parallel$  (which is determined by Eqn. (5.24) in slab cases). For all cylindrical cases, the parallel component of the magnetic field in phase with a single-fluid eigenfunction,  $\Im\tilde{B}_\parallel$ , is not small nor solely determined by  $-B_0\nabla_\perp \cdot \tilde{\mathbf{v}}$ . As seen from the second term on the RHS of Eqn. (11.2), it has contributions from  $\tilde{v}_r$  when the equilibrium magnetic field gradient and poloidal curvature are non-zero at the resonant surface.

The magnetic-field components out of phase with the single-fluid eigenfunction produce a current-density perturbation  $(\Im\tilde{J}_r, \Re\tilde{J}_\perp, \Re\tilde{J}_\parallel)$  that is in phase with the flows associated with reconnection. These non-zero out-of-phase components of  $\tilde{\mathbf{J}}$  demonstrate that the electron flow required for reconnection decouples from the ion flow as  $\rho_s$  is increased. Figures 28 and 29 compare components relevant to a reconnecting electron and ion flow, as well as their separation,  $-\tilde{\mathbf{J}}/n_0e$ . At  $k\rho_s = 0.17$ , the electron inflow and outflow are comparable to the relevant components of  $-\tilde{\mathbf{J}}/n_0e$  near the resonant surface, and the ion flows are much smaller. This is in contrast to the smaller- $\rho_s$  results, where the ion and electron flows are closely coupled, especially with cold ions. We note that the x-point outflow velocity is an order of magnitude larger than the inflow velocity, consistent with the ordering of Sec. 4 where  $\tilde{v}_r \sim \mathcal{O}(\epsilon^0)$  and  $\tilde{v}_\perp \sim \mathcal{O}(\epsilon^{-1})$ . In the cases with cold ions, the peak of the outflow velocity is only slightly shifted from the resonant surface, indicating that the asymmetry of the cylindrical geometry has only a moderate influence. In the warm-ion  $k\rho_s = 0.17$  case, the peak of  $\tilde{v}_\perp$  shifts outward, and the ion flows do not penetrate all the way to the resonant surface. We surmise that the oscillations in radius are part of the cylindrical drift-tearing-like behavior when the equilibrium curvature and gradient effects are important.

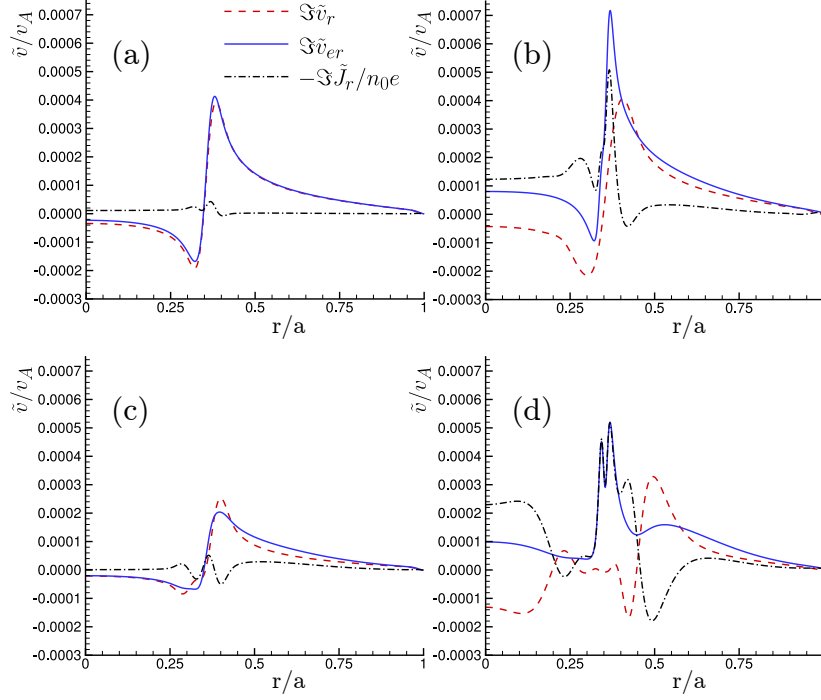


Figure 28: Linear electron and ion reconnecting flows and the difference,  $\tilde{\mathbf{J}}/ne$ . The radial components (x-point inflow) are displayed for computations with  $S = 8 \times 10^4$ ,  $\beta = 0.1$  and (a)  $k\rho_s = 0.035$  and cold ions, (b)  $k\rho_s = 0.017$  and cold ions, (c)  $k\rho_s = 0.035$  and warm ions, and (d)  $k\rho_s = 0.17$  and warm ions.

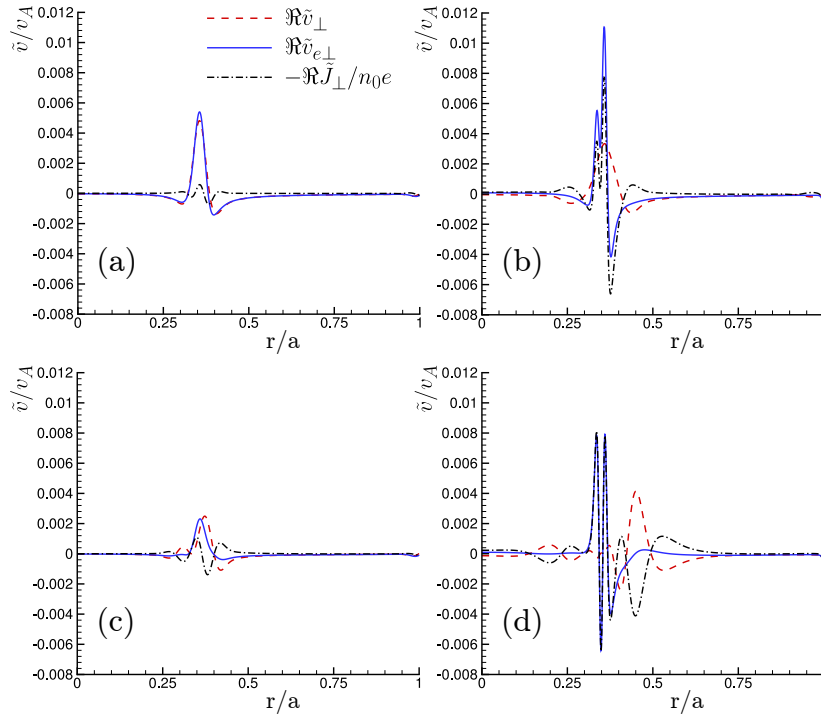


Figure 29: Linear electron and ion reconnecting flows and the difference,  $\tilde{\mathbf{J}}/ne$ . The perpendicular components (x-point outflow) are shown for computations with  $S = 8 \times 10^4$ ,  $\beta = 0.1$  and (a)  $k\rho_s = 0.035$  and cold ions, (b)  $k\rho_s = 0.17$  and cold ions, (c)  $k\rho_s = 0.035$  and warm ions, and (d)  $k\rho_s = 0.17$  and warm ions.

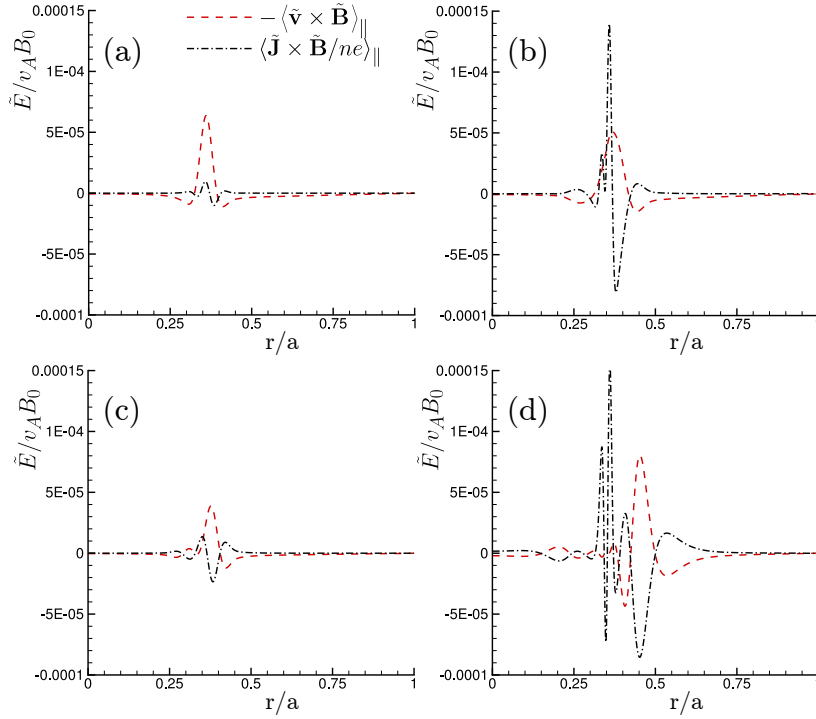


Figure 30: The dynamo electric fields inferred from the linear eigenmodes for computations with  $S = 8 \times 10^4$ ,  $\beta = 0.1$  and (a)  $k\rho_s = 0.035$  and cold ions, (b)  $k\rho_s = 0.17$  and cold ions, (c)  $k\rho_s = 0.035$  and warm ions, and (d)  $k\rho_s = 0.17$  and warm ions.

## 12.2 Dynamo contribution to the electric field inferred from the linear mode

With nonlinear evolution, correlated fluctuations of electron flows and magnetic field can modify the mean field via the generation of a dynamo emf as described by Eqn. (3.5) in Sec. 3.1. Together, the first two terms on the RHS of Eqn. (3.5) are the fluctuation-induced dynamo emf,  $\mathbf{E}_f$ . The first of these terms represents the MHD-dynamo effect, while the second is the Hall-dynamo effect.

Figure 30 shows the parallel component of the dynamo emfs calculated from the linear eigenfunctions, where parallel is with respect to the equilibrium magnetic field. In the cold-ion small- $\rho_s$  regime, case (a), where ion and electron flows are coupled, the Hall dynamo is small and the MHD dynamo dominates. Since the MHD and Hall dynamo are flux-surface averages, the results follow from the relationship between the phases of the fluctuation components that determine the cross product in the quadratic dynamo terms. As discussed in Sec. 12.1, in the single-fluid limit the perpendicular component of reconnecting ion flow,  $\tilde{v}_{\perp}(r)$ , and the radial component of the magnetic perturbation,  $\tilde{B}_r(r)$ , as well as the pair of the functions  $\tilde{v}_r(r)$

and  $\tilde{B}_\perp(r)$ , are in phase and contribute to the MHD-dynamo electric field. However, in the single-fluid limit the perpendicular and radial components of the current perturbation are out of phase with respect to the corresponding magnetic components; thus, the Hall dynamo vanishes. In contrast, the Hall contribution is significant in the two-fluid regimes (b and d) where the electron and ion fluids decouple and a fraction of the perturbed current arises in phase with the corresponding magnetic components. This effect is described in more detail for slab geometry in Ref. [23].

With cold ions and  $k\rho_s = 0.17$ , Fig. 30(b), the Hall dynamo peaks near the rational surface and adds to the MHD dynamo. Away from the rational surface, they tend to cancel. The peaked structure of the Hall dynamo near the rational surface qualitatively agrees with the analytic prediction at large  $\rho_s$  in Ref. [23]. However, the Hall dynamo is an even function about the resonant surface in slab geometry with a symmetric  $\lambda$  profile, whereas it is an odd function in our cylindrical cases. The inclusion of warm ions and ion gyroviscosity results in further decoupling of the ion and electron fluids and appreciable Hall dynamo even at small  $\rho_s$ , as shown in Fig. 30(c). With warm ions and  $k\rho_s = 0.17$ , case (d), the Hall dynamo is more significant, and strongly peaked at the resonant surface with fine structure. Figures 28(d) and 29(d) demonstrate that the ions do not penetrate to the resonant surface, and an eddy forms on the outboard side. Figure 30(d) shows that the resulting MHD dynamo also shifts outward, but it is largely canceled by the Hall dynamo.

## 13 Discussion

Our linear results confirm the tearing ordering of slab theory for two-fluid cases, verify the NIMROD code relative to this theory, and extend the theory into the cylindrical regime where we find important drift effects related to the magnetic-field gradient and poloidal curvature. With respect to the gyroviscous drift which affects the ion fluid, we note its form, Eqn. (11.10), is remarkably similar to the  $\nabla B$  and curvature drifts found from consideration of single-particle orbits, Eqns. (1.3) and (1.5), where we may estimate  $v_i \simeq \sqrt{T_i/m_i}$ . Unlike the  $\mathbf{E} \times \mathbf{B}$  drift, the  $\nabla B$  and curvature drifts cause the ion and electrons to move in opposite directions, and it is not surprising to find a drift-tearing response similar to that caused by diamagnetic effects as reviewed in Sec. 5.1. Additionally unlike tokamak configurations, these drift effects are significant for pinch profiles as the dominant  $\nabla B$  and curvature drifts are aligned with the flux surfaces as described in Sec. 1.4.

As the tearing perturbation grows to significant amplitude and the growth rate slows as described in Sec. 6.1, the semi-collisional tearing-layer width broadens ( $l \sim \Delta' \delta^2 \sim \Delta' / S\gamma\tau_A$ ), although eventually the linear

tearing ordering is no longer valid. As the layer width broadens, we expect our KAW-mediated linear cases which initially have  $\rho_s \gtrsim l$  will transition back to the collisional regime where  $\rho_s < l$ . Thus to the extent that our linear observations are relevant to the nonlinear regime, for large islands which evolve slowly we do not expect the KAW and  $\omega_{*H}$  effects to be significant. However, the gyroviscous drift is important when  $\gamma \lesssim \omega_{*gv}$  and as the growth of the perturbation slows our linear considerations predict that this drift effect increases in significance. Additionally, unlike the diamagnetic drift which is limited by flattening of pressure profile upon nonlinear saturation (Refs. [53, 54, 56], reviewed in Sec. 6.2), we do not expect the  $\nabla B$  and poloidal curvature profiles and thus  $\omega_{*gv}$  to be greatly modified.

## Part IV

# Nonlinear single-helicity tearing

## 14 Island structure in a cylinder

We now consider results from fully nonlinear cylindrical computations, where the perturbations modify the mean field via the dynamo emf and the mode saturates. As described in Sec. 9.2, we use a small aspect ratio,  $R/a = 0.505$ , such that our dynamics model the evolution of a single mode with  $m = 1$  that is roughly equivalent to the  $m = 1, n = 6$  mode in MST. We run the computations through the Rutherford stage described in Sec. 6.1 (Ref. [50]), where the nonlinear profile modification affects the growth of the mode, to a nearly steady final state. Figure 31 plots the island width in time for cold and warm ions at  $S = 8 \times 10^4$  with  $k\rho_s = 0.17$ . Early in the nonlinear evolution, the island-width evolution is characteristic of the Rutherford stage with nearly linear growth:  $dw/dt = A\Delta'\eta/\mu_0$  where  $w$  is the island width and  $A$  is a coefficient of order unity. Spectral broadening to  $m \geq 2$  is allowed in the simulations, but it is not observed to be significant.

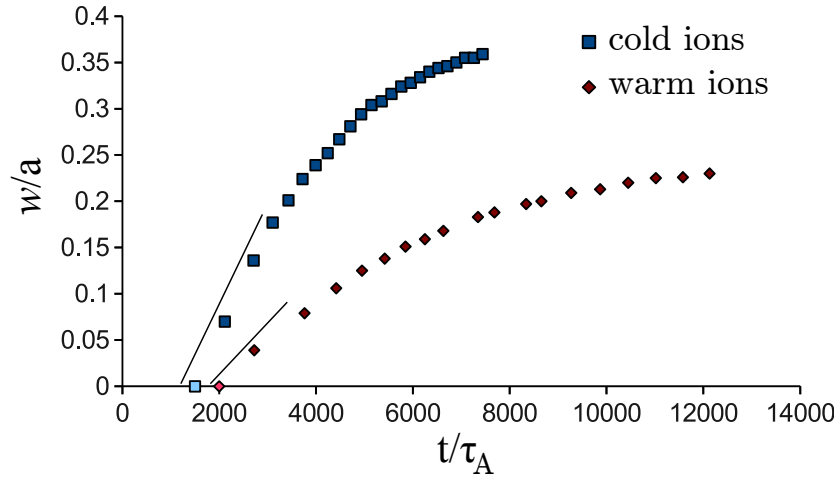


Figure 31: The island width as a function of time for computations with warm- and cold-ion models and  $k\rho_s = 0.17$ ,  $S = 8 \times 10^4$  and  $\beta = 0.1$ . The lighter colored data points at  $w(t) = 0$  represent the earliest indications of nonlinear evolution.

As discussed in Sec. 10.2, the linear MHD eigenfunction can be normalized such that  $\Im\tilde{B}_r(r) = \Re\tilde{B}_\perp(r) = \Re\tilde{B}_\parallel(r) = 0$ . This relation among the phases of the components is approximately valid for the nonlinear

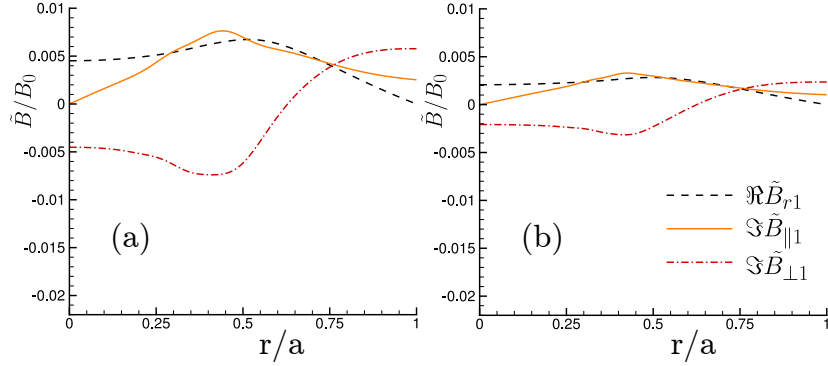


Figure 32: Components of  $\tilde{\mathbf{B}}$  from a saturated island in phase with a single-fluid eigenfunction for computations with  $S = 8 \times 10^4$ ,  $\beta = 0.1$ ,  $k\rho_s = 0.17$  and (a) cold ions and (b) warm ions.

saturated structures. The dominant part of the magnetic-field perturbation, for the  $k\rho_s = 0.17$  cases at  $S = 8 \times 10^4$ , is  $\Re\tilde{B}_r(r)$ ,  $\Im\tilde{B}_\perp(r)$  and  $\Im\tilde{B}_\parallel(r)$  which are in phase with the single-fluid eigenfunction. (See Fig. 32) Including the effect of ion gyroviscosity from warm ions reduces the saturation amplitude in the  $k\rho_s = 0.17$  cases, although the shape of the perturbations is largely unchanged. This result is not sensitive to the Lundquist number, at least in the conditions tested numerically between  $S = 5000$  and  $8 \times 10^4$ . For both the warm- and cold-ion cases, the shape of the perturbations is reminiscent of the linear results in Fig. 26 with the sharper features washed out. A notable difference is the large peak of  $\Im\tilde{B}_\perp$  that is only present in the linear results. This can be qualitatively explained through use of the  $\nabla \cdot \mathbf{B} = 0$  constraint. One expects that  $\Im\tilde{B}_\perp$  scales like  $\Re\tilde{B}_r/kw$  in the nonlinear stage, whereas it scales like  $\Re\tilde{B}_r/kl$  in the linear stage. Thus, relative to  $\Re\tilde{B}_r$ , the peak of  $\Im\tilde{B}_\perp$  is expected to be  $\sim l/w$  smaller in the nonlinear stage.

The saturated magnetic perturbations which are out of phase with the single-fluid eigenfunction are plotted in Fig. 33. The amplitude of the out-of-phase components is two orders of magnitude smaller than the saturated in-phase magnetic components. This contrasts with the linear results (Fig. 27), where the magnitude of the out-of-phase magnetic perturbations are approximately one third of the corresponding in-phase component magnitude. In the linear cases, the large out-of-phase magnetic components are associated with induction through the relatively large, decoupled, reconnecting flows. In contrast the flows are much smaller in the saturated state, as they only advect enough flux into the island to balance the resistive dissipation.

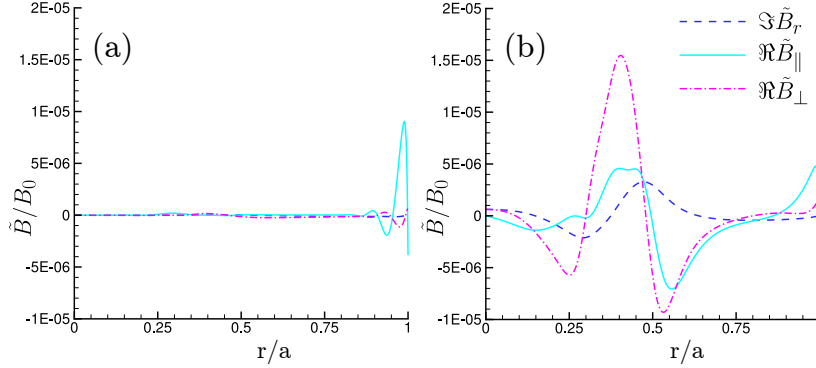


Figure 33: Components of  $\tilde{\mathbf{B}}$  from a saturated island out of phase with a single-fluid eigenfunction for computations with  $S = 8 \times 10^4$ ,  $\beta = 0.1$ ,  $k\rho_s = 0.17$  and (a) cold ions and (b) warm ions.

## 14.1 Helical projection method

To help visualize the saturated states, we project the single-helicity perturbations onto a helical surface that captures the variations across the magnetic island. We make a parametric definition of a set of nested surfaces in cylindrical coordinates,

$$\left\{ r, \frac{2\pi m\zeta}{m^2 + (nr/R)^2} - h, \frac{nr^2}{R} \frac{2\pi\zeta}{m^2 + (nr/R)^2} + \frac{mR}{n}h \right\} \quad (14.1)$$

where  $0 \leq r \leq a$  is the radial coordinate,  $0 \leq \zeta \leq 1$  is a normalized helical coordinate along a given helical surface, and  $0 \leq h \leq (na/R)^2 (2\pi / [m^2 + (na/R)^2])$  is a helical-surface label. The projection of the single-helicity perturbations onto these surfaces is independent of surface choice. A single helical surface is given by a fixed value of  $h$  and can be defined as

$$H_h(r, \theta, z) = \frac{nr}{R}\theta - \frac{m}{r}z + \left( \frac{nr}{R} + \frac{m^2 R}{rn} \right) h = 0. \quad (14.2)$$

We note that variations in the  $\hat{\mathbf{k}}$  direction are captured on each helical surface as  $\mathbf{k} \cdot \nabla H_h = 0$ , but variations in  $\hat{\mathbf{r}}$  are not captured on a single helical surface, as  $\hat{\mathbf{r}} \cdot \nabla H_h \neq 0$ . The surface mapped out at constant  $\zeta$  is

$$H_\zeta(r, \theta, z) = m\theta + \frac{n}{R}z - 2\pi\zeta = 0. \quad (14.3)$$

As  $\hat{\mathbf{r}} \cdot \nabla H_\zeta = 0$ , we conclude that variations in  $\hat{\mathbf{r}}$  merely move between the surfaces at constant  $\zeta$ . Since all the  $H_h$  surfaces are identical, we choose one ( $h = 0$ ) and project the  $\hat{\mathbf{r}}$  and  $\hat{\mathbf{k}}/L(r)$  vector components, where  $L(r)$  is the helix length at a given radius, onto this surface.

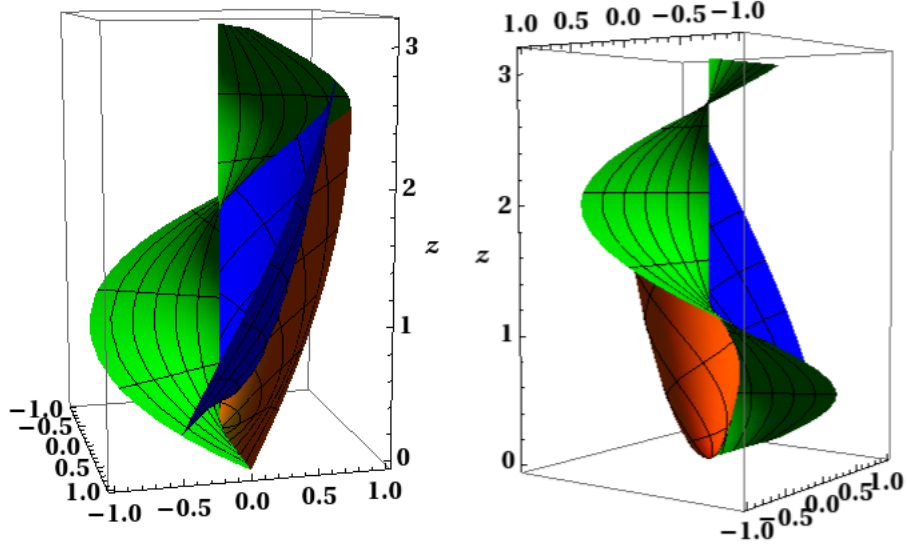


Figure 34: Helical surfaces  $H_h$  with  $h = 0$  (orange) and  $h = 0.1$  (blue), and  $H_\phi$  with  $\mu = 0$  (green) for a cylinder with  $R/a = 0.505$ . Two views are presented.

It is illustrative to consider the trivial case of the helical surfaces for a  $m = 0$  mode. The constant- $h$  surfaces then become the  $rz$  planes with  $\chi = h$ , and for this particular case  $r \cdot H_h = 0$ . The constant- $\mu$  surfaces are the  $r\chi$  planes with  $z = 2\lambda R\mu n$ . Note that  $0 \leq z \leq 2\lambda R n$ , thus only one x-point and one o-point are captured on the surface for any  $n$ .

Two helical surfaces,  $H_h$ , for the  $m = 1, n = 1$  mode with  $h = 0$  and  $h = 0.1$  are plotted in Fig. 34, along with the surface  $H_\phi$  for  $\mu = 0$ . Helical quantities are constant on the  $H_{\phi=0}$  surface by definition (see Eqn. (14.3)). The  $H_h$  surfaces are axially bounded by the  $H_{\phi=0}$  surface and thus they are axially periodic.

## 14.2 Flow structures

Returning to our nonlinear results, Fig. 35 shows the helical projection for the full magnetic-field streamlines. To verify our helical-projection method, the width measured from these plots has been compared to the results of a puncture plot produced with magnetic-field-line tracing. As one would expect from the smaller magnetic perturbation in Fig. 32(b), the  $k\rho_s = 0.17$  case with warm ions exhibits a smaller island saturation width than the cold-ion case. Table 4 lists the saturated island width for a larger parameter scan at  $S = 5000$ , as well as the two cases at  $S = 8 \times 10^4$ . The scan shows that for the warm-ion,  $k\rho_s = 0.035$  case and all the cold-ion cases, the island width is determined by physics included in the single-fluid model. However, the

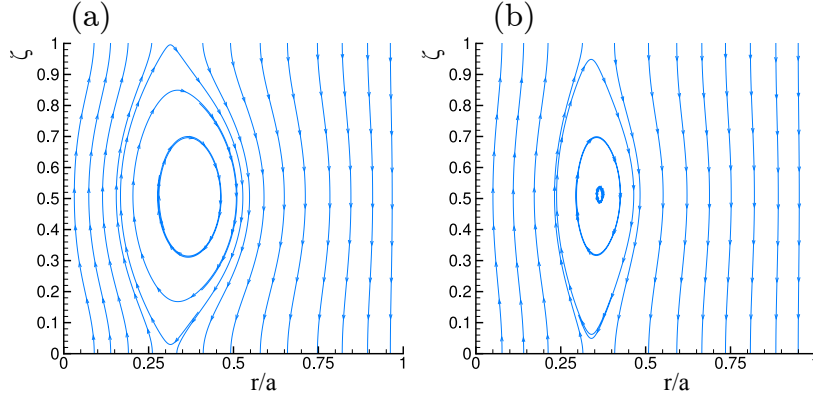


Figure 35: ‘Streamlines’ of a helical projection of  $\mathbf{B}_{eq} + \tilde{\mathbf{B}}$  for computations with  $S = 8 \times 10^4$ ,  $\beta = 0.1$ ,  $k\rho_s = 0.17$  and (a) cold ions and (b) warm ions.

$k\rho_s$	$S$	$w/a$ (cold)	$w/a$ (warm)
single-fluid	5000	0.36	
0.035	5000	0.36	0.36
0.17	5000	0.36	0.24
0.17	$8 \times 10^4$	0.36	0.24
0.70	5000	0.36	0.21

Table 4: Magnetic-island widths at saturation as a function of  $\rho_s$  for cases with cold and warm ions at  $\beta = 0.1$ .

island width decreases as  $\rho_s$  is increased in the warm-ion cases.

Steady single-helicity conditions require a helical electrostatic-field configuration arising from the reconnecting flows [73, 74] as well as helical force balance. Our results show that the Hall term in Ohm’s law does not significantly modify this electrostatic configuration when ions are cold. Thus, the final magnetic field perturbation amplitude is not affected by  $\rho_s$ . How gyroviscous effects from warm ions modify the island force balance and thus the saturated width is discussed in Sec. 15.2.

After nonlinear saturation, advection of magnetic flux into the island continues to balance resistive diffusion. This flow, plotted in Figs. 36 and 37, is analogous to the equilibrium pinch flow in establishing an Ohmic steady state. Comparing the figures, we note that the general shape of the electron flows is relatively unchanged by the warm-ion effects; however, their amplitude is reduced. The eddies are larger in the cold-ion case to sustain the larger island against dissipation. The narrow structure of the linear flows is replaced by a radially broad eddy in the saturated state. The flows in the saturated nonlinear cases are roughly an order

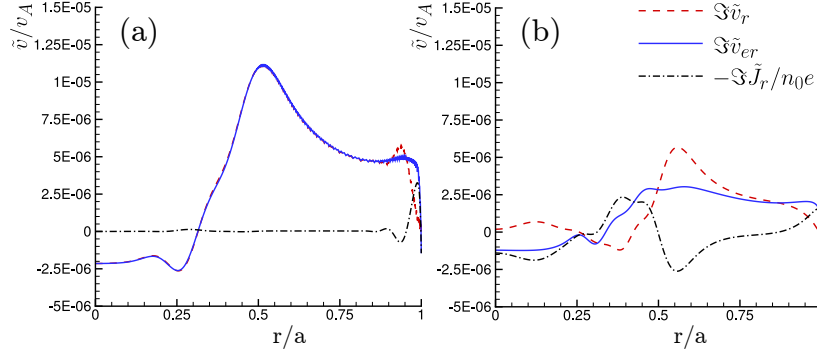


Figure 36: Electron and ion reconnecting flows and the difference,  $\tilde{\mathbf{J}}/ne$ . The radial components (x-point inflow) are displayed for computations with  $S = 8 \times 10^4$ ,  $\beta = 0.1$ ,  $k\rho_s = 0.17$  and (a) cold ions and (b) warm ions.

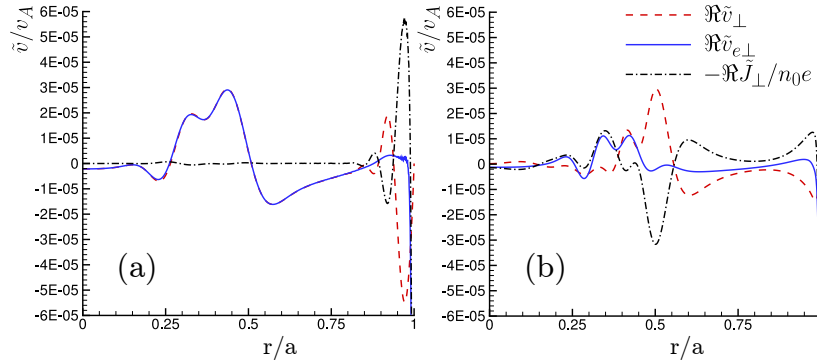


Figure 37: Electron and ion reconnecting flows and the difference,  $\tilde{\mathbf{J}}/ne$ . The perpendicular components (x-point outflow) are displayed for computations with  $S = 8 \times 10^4$ ,  $\beta = 0.1$ ,  $k\rho_s = 0.17$  and (a) cold ions and (b) warm ions.

of magnitude smaller in amplitude than their linear counterparts (Figs. 28 and 29) scaled by the magnetic-perturbation amplitude. However, we find that the ratio of the perturbed kinetic to magnetic energy of the saturated state is only a factor of two less than that of the linear state, due to the broad flow structure in the nonlinear state.

In Fig. 38 we project the vectors and streamlines of the ion flows onto a helical surface, along with the streamlines of the magnetic field. The contributions from the axisymmetric flows are not included. The eddies in the cold-ion case support reconnection, and as Figs. 36(a) and 37(a) show, they are coupled with the electrons. The eddies in the warm-ion case are decoupled and out of phase with a reconnecting flow.

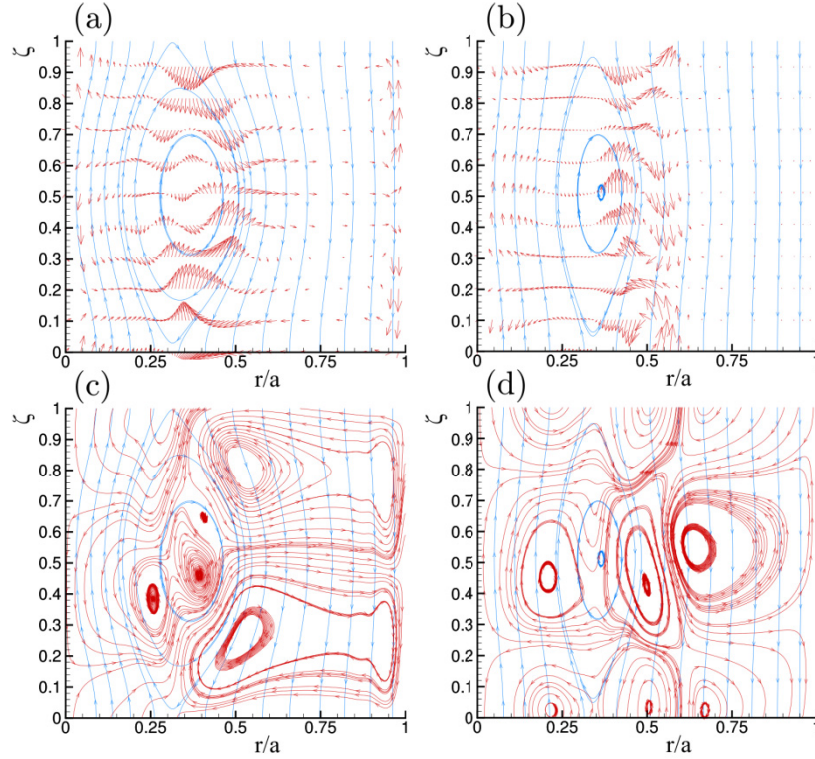


Figure 38: Streamlines of a helical projection of  $\mathbf{B}_{eq} + \mathbf{B}$  (blue) for computations of a saturated island with  $S = 8 \cdot 10^4$ ,  $\kappa = 0.1$ ,  $k\rho_s = 0.17$ . The frames also show ion flow vectors (red) for (a) cold- and (b) warm-ion conditions, where the same vector length corresponds to a 10 greater magnitude in the warm-ion plot. Frames (c) and (d) plot the ion-flow streamlines (red) with cold- and warm-ion models, respectively.

Plots of the electron-flow patterns are dominated by the contribution from the current-density perturbation that is out of phase with the flow supporting reconnection, and are not shown.

## 15 Cylindrical dynamo emfs and force balance

### 15.1 Dynamo emfs at saturation

The island structure in the saturated state can be directly related to the conventional picture of Fig. 16, unlike the linear cases where the perturbation is too small to affect the magnetic topology. The flow pattern of Fig. 38(a) is qualitatively similar to the flows sketched in Fig. 16 and interacts with the perturbed magnetic fields to produce the fluctuation-induced dynamo emf. It is straightforward to qualitatively determine  $\mathbf{E}_f = \mathbf{v}_e \times \mathbf{B}$  from Fig. 16. One expects an induced  $E_f$  aligned with  $\mathbf{J}_0$  at the rational surface, with

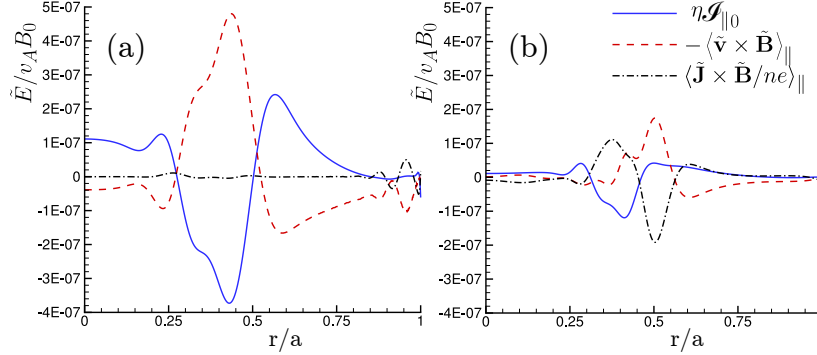


Figure 39: The fluctuation-induced dynamo electric fields and mean current modification at island saturation for computations with  $S = 8 \times 10^4$ ,  $\beta = 0.1$ ,  $k\rho_s = 0.17$  and (a) cold ions and (b) warm ions.

contributions from  $\tilde{B}_r$  and  $\tilde{v}_{e\perp}$  above and below the o-point. Away from the rational surface, there is an induced  $E_{f\parallel}$  anti-parallel to  $\mathbf{J}_0$  from the interaction of  $\tilde{B}_\perp$  and  $\tilde{v}_{er}$ .

As described in Secs. 3.1 and 6.1, in the saturated state the dynamo emf drives a nonlinear axisymmetric current density,  $\mathcal{J}_0 \equiv \langle \mathbf{J} \rangle - \mathbf{J}_{eq}$  (The initial equilibrium field is denoted by the subscript ‘*eq.*’), that is associated with profile changes:

$$\mathbf{E}_f = -\langle \tilde{\mathbf{v}} \times \tilde{\mathbf{B}} \rangle + \left\langle \frac{\tilde{\mathbf{J}} \times \tilde{\mathbf{B}}}{n_0 e} \right\rangle \simeq -\eta \mathcal{J}_0. \quad (15.1)$$

The dynamo emfs and induced current are plotted in Fig. 39. The combined dynamo emfs produce an axisymmetric current perturbation that primarily reduces  $J_{\parallel 0}$  inside the island and increases it outside. The Hall dynamo is relevant only when the flows decouple; thus in the saturated cold-ion state with coupled flows, the MHD dynamo is dominant. In the warm-ion case the ion flows are modified, as shown in Fig. 38(b); however, the electron flows maintain a flow pattern resembling Fig. 16, as demonstrated in Figs. 36 and 37. The Hall dynamo is significant with warm ions and the mean-current modification is smaller, which is consistent with the smaller island size.

From Figs. 30 and 39, we note that the Hall dynamo must vanish at some point in the nonlinear evolution when ions are cold. To examine this effect, Fig. 40 shows the island size and dynamo emf for the cold-ion case at different stages of nonlinear growth. The Hall dynamo becomes small relative to the MHD dynamo approximately when the island width becomes larger than  $d_i = 0.17a$ . In the linear cases, the two-fluid scales must be compared with the linear tearing layer width,  $l$ , which is small, whereas in the nonlinear stage the

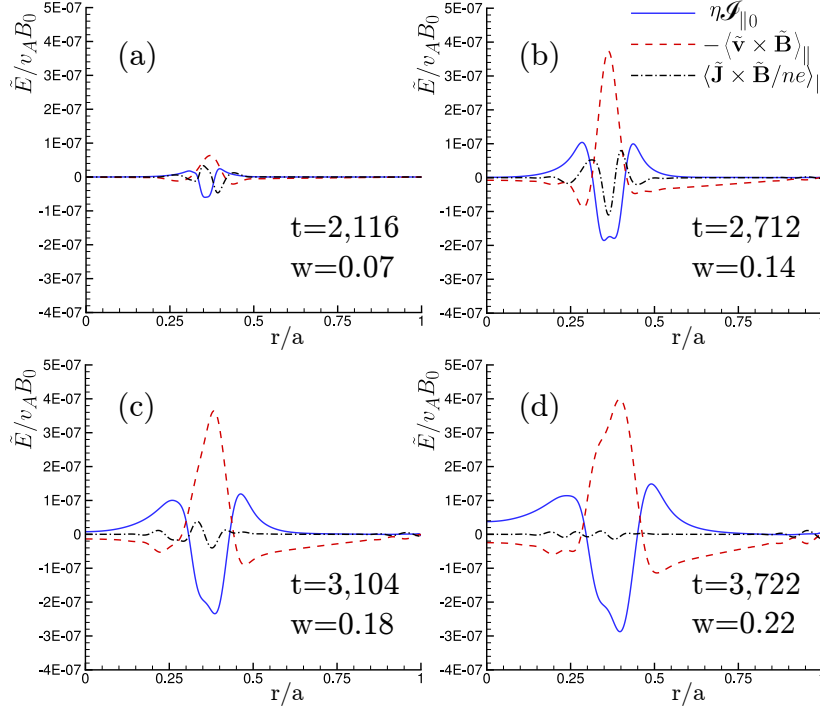


Figure 40: The fluctuation-induced dynamo electric fields and mean current modification for computations with  $S = 8 \times 10^4$ ,  $\beta = 0.1$ ,  $k\rho_s = 0.17$  and cold ions at different times: (a)  $t = 2,116\tau_A$ , (b)  $t = 2,712\tau_A$ , (c)  $t = 3,431\tau_A$  and (d)  $t = 3,722\tau_A$ .

two-fluid scales are compared with the island width,  $w$ , which can be considerably larger than  $l$ .

## 15.2 Island force balance

In Rutherford theory for the resistive MHD evolution of islands (Sec. 6.1), the perturbed current produces a third-order  $\mathbf{J} \times \mathbf{B}$  force, where the ordering refers to the perturbation amplitude, that counteracts the linear forces driving the island growth [50]. In order to illustrate this effect in our computation, we express the  $m = 1$  force-balance equation as

$$\rho_0 \frac{d\tilde{\mathbf{v}}}{dt} \cong \tilde{\mathbf{f}}_d + \tilde{\mathbf{f}}_3 - \nabla \cdot \mathbf{\Pi} \quad (15.2)$$

where  $\tilde{\mathbf{f}}_d$  is the driving force, and  $\tilde{\mathbf{f}}_3$  is the third-order force as defined in Sec. 6.1.

The driving, third-order, and ion-gyroviscous perpendicular forces in phase with a reconnecting flow are plotted in Fig. 41. Contributions from the inertial and isotropic viscous terms are small and are not shown. With cold ions, saturation results when the secondary force balances the driving force. This is the

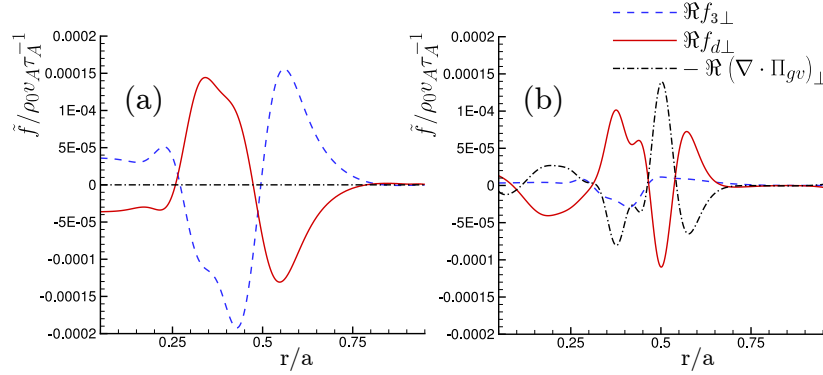


Figure 41: The driving, third-order and ion-gyroviscous perpendicular forces in phase with a reconnecting flow for computations with  $S = 8 \times 10^5$ ,  $\beta = 0.1$ ,  $k\rho_s = 0.17$  and (a) cold ions and (b) warm ions.

same balance that occurs with a resistive-MHD model. However with warm-ion effects, gyroviscosity plays a significant role in opposing the driving force, as shown in Fig. 41(b). The current profile modification required to balance  $\tilde{\mathbf{f}}_d$  is smaller as  $\tilde{\mathbf{f}}_3$  and  $\nabla \cdot \mathbf{\Pi}_{gv}$  combine to oppose the driving force. Thus warm-ion cases with  $k\rho_s > 0.035$  have a reduced saturation amplitude and a smaller total dynamo emf at saturation relative to resistive MHD. Additionally, because the gyroviscous forces prevent alignment of current density and magnetic field, the Hall dynamo remains active in the saturated state, as observed in the previous section.

As emphasized throughout the discussion of the tearing structure, the two-fluid effects mix the phases of the perturbations compared to a single-fluid model. Figure 42 shows that Eqn. (11.6) is still a good approximation for the gyroviscous force in the saturated state. As the Laplacian operator does not mix the phases, the stabilizing ion-gyroviscous force in phase with the reconnecting flow, such as in Fig. 41, is out of phase with the flow eddy that produces it. Figure 38(b) demonstrates that the dominant ion eddies are out of phase with the reconnecting flows with warm ions. Thus the force balance out of phase with the reconnecting flow is significant. These flow eddies are produced by the interaction of the ion-gyroviscous force resulting from the ion flow in phase with reconnection and the Lorentz forces related to the decoupling, where the perturbations have the phases  $(\Im \tilde{B}_r, \Re \tilde{B}_\perp)$  and  $(\Im \tilde{J}_r, \Re \tilde{J}_\perp)$ . Figures 33, 36 and 37 show that the perturbations with these phases are nonzero in the warm-ion saturated state.

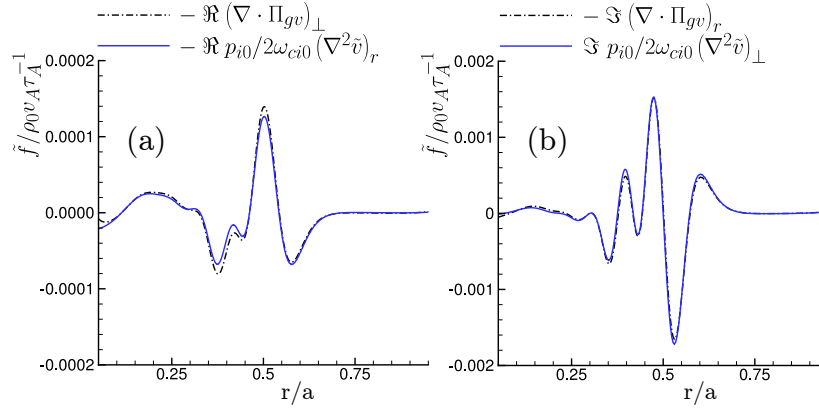


Figure 42: The perpendicular, (a), and radial, (b), ion-gyroviscous stress as well as the leading order terms expressed in Eqn. 11.6 for a computation of the saturated island with  $S = 8 \times 10^4$ ,  $\beta = 0.1$ ,  $k\rho_s = 0.17$  and warm ions.

## 16 Discussion

Our linear and nonlinear single-helicity cases do not represent the dynamic relaxation events observed in RFPs, which result from strong nonlinear interaction among tearing perturbations of multiple resonant helicities. However, because ion and electron temperatures are comparable in the experiment, we expect that the  $\omega_{*gv}$  drift influences island widths, possibly reducing the mode coupling and magnetic stochasticity that occurs during and between relaxation events. An experimental measurement of the relative phase between the magnetic perturbation and the ion flow could be compared to the predicted phases from this study in order to empirically determine the importance of the  $\omega_{*gv}$  drift to a particular discharge.

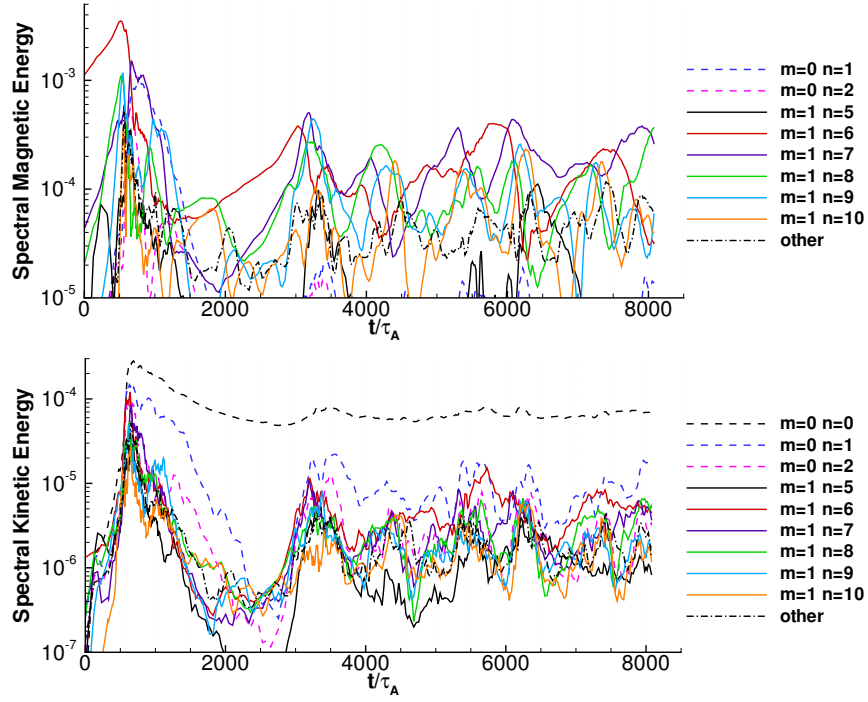
Our findings may have more direct relevance to RFP discharges achieving QSH and to profile-control experiments [75, 76]. As ion temperature increases with improved confinement, it may lead to a self-reinforcing process where the  $\omega_{*gv}$  drift increases, further limiting the magnetic perturbations. Additionally, QSH discharges are often associated with the dominance of the innermost resonant mode, and we note the poloidal curvature and the gradient of the magnetic field are relatively weak near the magnetic axis. Other modes would be subject to a larger drift effect, so there may be a natural tendency to produce QSH. Further study with a FLR model and transport effects is needed to clarify the influence of the  $\omega_{*gv}$  drift effects on these improved confinement discharges and in standard multi-helicity RFP dynamics.

## Part V

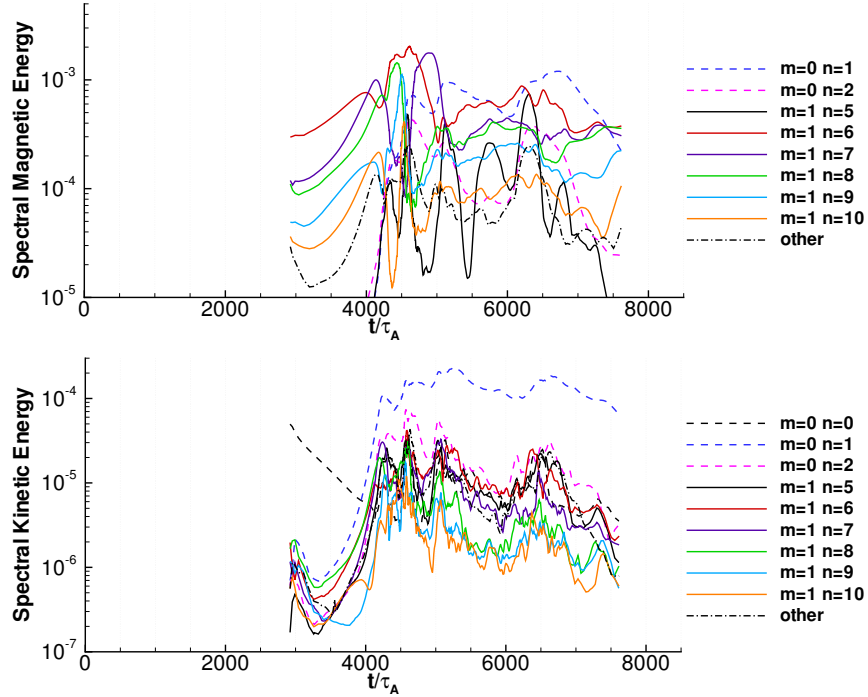
# Multi-helicity dynamics

We now turn to modeling of plasma behavior with an aspect ratio comparable to MST ( $R/a \simeq 3$ ), and thus full multi-mode dynamics. As described in Sec. 3.1, previous RFP computation has typically been performed with single-fluid models. Our two-fluid results differ in key aspects, which we believe bring them closer to the physical processes present in experiment. In particular in Sec. 17, we show that mode amplitudes are reduced relative to single-fluid modeling - an effect that is associated with the stabilizing gyroviscous effects described in Parts III and IV. In Sec. 18 we discuss the MHD- and Hall-dynamo emfs in our two-fluid computations and show both are significant during relaxation. We also perform an analysis of the measurements by Ding et al. (Ref. [25]) which compare reasonably well with our computations. The momentum transport mediated by the forces from the Maxwell stress associated with the Hall dynamo and the Reynolds stress is analyzed in Sec. 19. Similar to the measurements by Kuritsyn et al., the computed fluctuation-induced stresses exhibit radial variation and generally oppose each other (Ref. [16]). The computed redistribution of parallel momentum from these stresses during a relaxation event also compares well to experimental measurements.

An overview of our modeling is given by the spectral magnetic and kinetic energies plotted in Fig. 43. Figure 43(a) shows the result of our two-fluid computation with  $S = 8 \times 10^4$ ,  $\rho_s = 0.05a$ ,  $\beta = 0.1$  and  $P_m = 1$ , and Fig. 43(b) plots the result of a single-fluid computation initialized from the two-fluid state at  $t = 2,921\tau_A$ . The parameters of the single-fluid computation are identical to the two-fluid, only the model equations differ. The value of  $\rho_s$  on axis is the same as our  $k\rho_s = 0.17$  single-helicity cases, however as our multihelicity cases exhibit many modes over a range of wave-numbers, we normalize the  $\rho_s$  value by the minor radius. With regard to the two-fluid computation, a large initial-relaxation event occurs at  $t \simeq 650\tau_A$  as characterized by a spike in the magnetic- and kinetic-mode energies. After this event, the spectral energies are lower, indicating partial stabilization of the profile. There are additional relaxation events as the computation progresses (see  $t \simeq 3,250\tau_A$ ,  $t \simeq 5,800\tau_A$  and  $t \simeq 7,900\tau_A$ ), however the amplitude of the spectral energies remains much smaller than the initial event. The subsequent relaxation produces significant  $m = 1$  and  $6 \leq n \leq 8$  activity, but only during the initial event are  $m = 0$  modes excited to large amplitude. The kinetic energy spectrum is broader than the magnetic, and considerable mean kinetic energy is generated by the first event and sustained throughout the computation. Additionally, although the  $m = 0$ ,  $n \geq 1$  magnetic energy remains small during the plasma evolution subsequent to the initial event, the  $m = 0$ ,  $n \geq 1$  kinetic



(a) Magnetic (top) and kinetic (bottom) spectral energies for our two-fluid computation.



(b) Magnetic (top) and kinetic (bottom) spectral energies for our single-fluid computation.

Figure 43: Magnetic and kinetic spectral energies as a function of time for the (a) two-fluid and (b) single-fluid multi-helicity computations with  $S = 8 \times 10^4$ ,  $\rho_s = 0.05a$ ,  $\beta = 0.1$  and  $P_m = 1$ . Values are normalized such that the mean magnetic energy is approximately 1, where the mean magnetic energy has temporal variations of less than 1% in our computations.

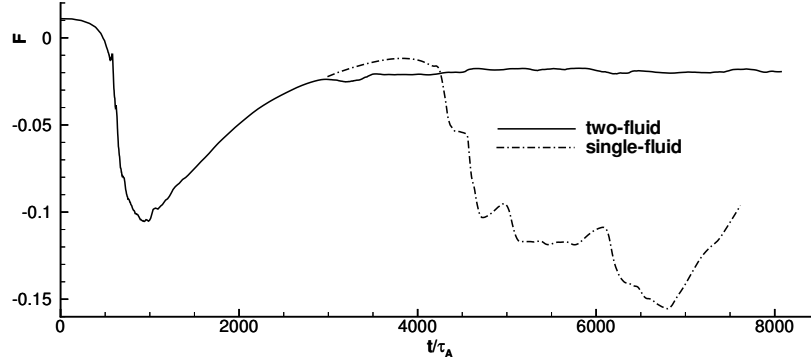
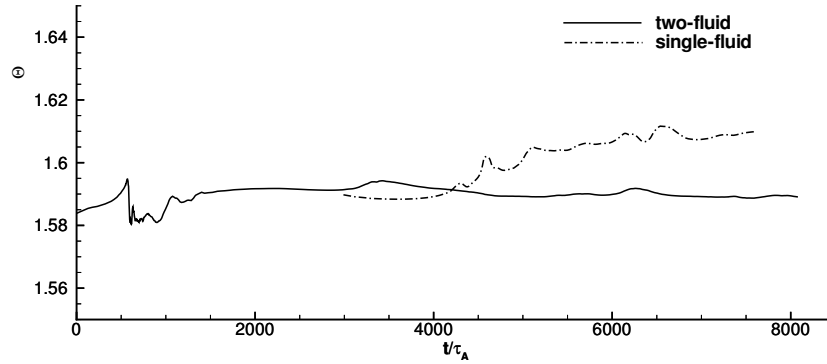
(a) Field-reversal parameter  $F$ , Eqn. 3.9(b) Normalized current  $\Theta$ , Eqn. 3.8

Figure 44: Plots of the (a) Field-reversal parameter and (b) normalized current for our two- and single-fluid computations.

is large. Comparing and contrasting the spectral energies between our two- and single-fluid modeling, we note three aspects: (1) The magnetic spectral energies are larger in the single-fluid computation, although in general the kinetic spectral energies remain in the same range as the two-fluid case. (2) The energy of the mean flows in the single-fluid computation is immediately damped, however the  $m = 0$ ,  $n = 1$  kinetic energy remains large similar to the two-fluid modeling. (3) The relaxation event that occurs at  $t \simeq 3,250\tau_A$  in the two-fluid case is delayed until  $t \simeq 4,100\tau_A$  with the single-fluid model, and the  $m = 0$ ,  $n = 1$  magnetic energy is excited to significant amplitude relative to the two-fluid computation.

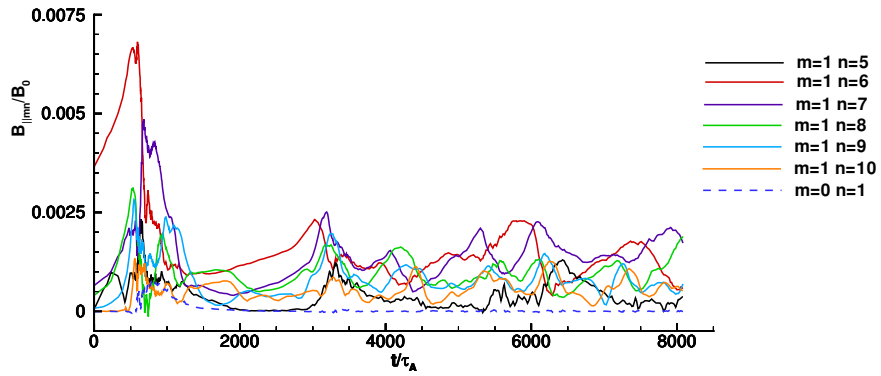
## 17 Mode amplitudes

### 17.1 Experimental comparison

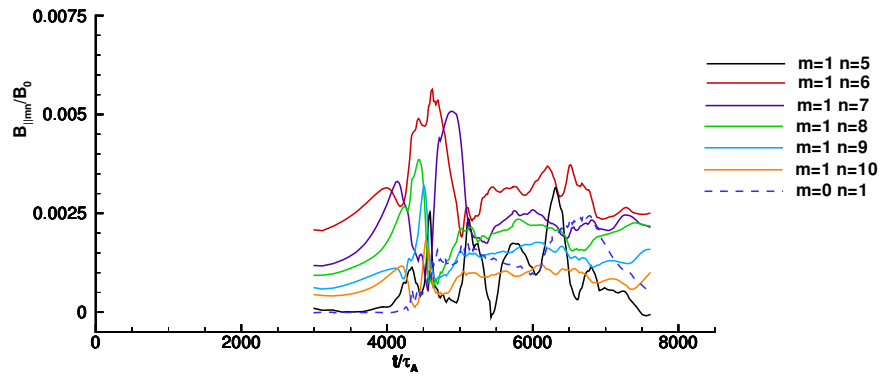
Figures 44 and 45 show time traces of  $F$  and  $\Theta$  and the amplitude of  $\tilde{B}_{\parallel}(a)$  decomposed by mode, respectively, as a function of time for both our single- and two-fluid cases. Similar to the behavior of the spectral magnetic energies, the amplitude of the  $\tilde{B}_{\parallel}(a)$  is much larger during the initial relaxation event relative to the subsequent evolution in the two-fluid computation, and the initial event is comparable in amplitude to the result obtained with a single-fluid model. Given the dominance of the mean poloidal magnetic field at the wall, we may compare  $\tilde{B}_{\parallel}(a)$  to the experimentally measured values of  $\tilde{B}_{\theta}(a)$  by Ding et al. in Fig. 5. Using the normalization  $B_0 \simeq 0.4$  T for the 400 kA experimental discharges they measure, we find  $\tilde{B}_{\parallel}(a)/B_0 = 0.0025$  is equivalent to 10 Gs. It is natural to compare the two-fluid initial-relaxation-event and the event with the single-fluid model to the  $F = -0.22$  experimental cases, as significant  $m = 0$  activity is present. The mode amplitudes in the computations are larger by approximately a factor of 1.75 when compared with the experimental measurements, even though the current drive in the computation ( $\Theta \simeq 1.6$ ) is slightly less than the experimental cases ( $\Theta \simeq 1.7$ ). Alternatively, we may compare the subsequent behavior ( $t \gtrsim 2,000$ ) of the two-fluid computation with the  $F \simeq 0$  measurements, as little  $m = 0$  mode activity is present. In terms of amplitude, there is remarkable similarity between the computation and experiment where both have mode amplitudes of approximately 10 Gs. However, the  $m = 1, n = 5$  dominates the dynamics in the experiment, whereas the  $m = 1, n = 6, 7$  are dominant in the computations. Given Eqn. 1.12, this indicates the parallel current on-axis is smaller and thus the profile is more relaxed in the experiment.

### 17.2 Equilibria and island force balance

As the  $m = 0, n = 1$  mode mediates three-wave coupling between the dominant  $m = 1$  modes of our computations,  $n = 6$  and  $7$ , the amplitude of  $m = 0$  activity can significantly alter the relaxation dynamics. We will study the initial (large  $m = 0$  activity) and subsequent (small  $m = 0$  activity) relaxation events of our two-fluid computation in more detail by evaluating quantities around the peak in the kinetic-energy spectrum associated with each event:  $612\tau_A \leq t \leq 684\tau_A$  and  $3,178\tau_A \leq t \leq 3,332\tau_A$ , see Fig. 43. Equilibrium quantities associated with these time windows are plotted in Fig. 46. The safety factor in the core is comparable between the two time windows, however the reversal surface location differs; it is located at  $r \sim 0.8a$  during  $612\tau_A \leq t \leq 684\tau_A$  and  $r \sim 0.9a$  during  $3,178\tau_A \leq t \leq 3,332\tau_A$ . The parallel current profile dynamics mirror the safety factor. There is very little variation in the core between the different



(a) Two-fluid computation



(b) Single-fluid computation

Figure 45: The amplitude of  $\tilde{B}_{||}$  (a) for the  $m = 0, n = 1$  and the  $m = 1, 5 \leq n \leq 10$  modes as a function of time for our (a) two-fluid and (b) single-fluid computations.

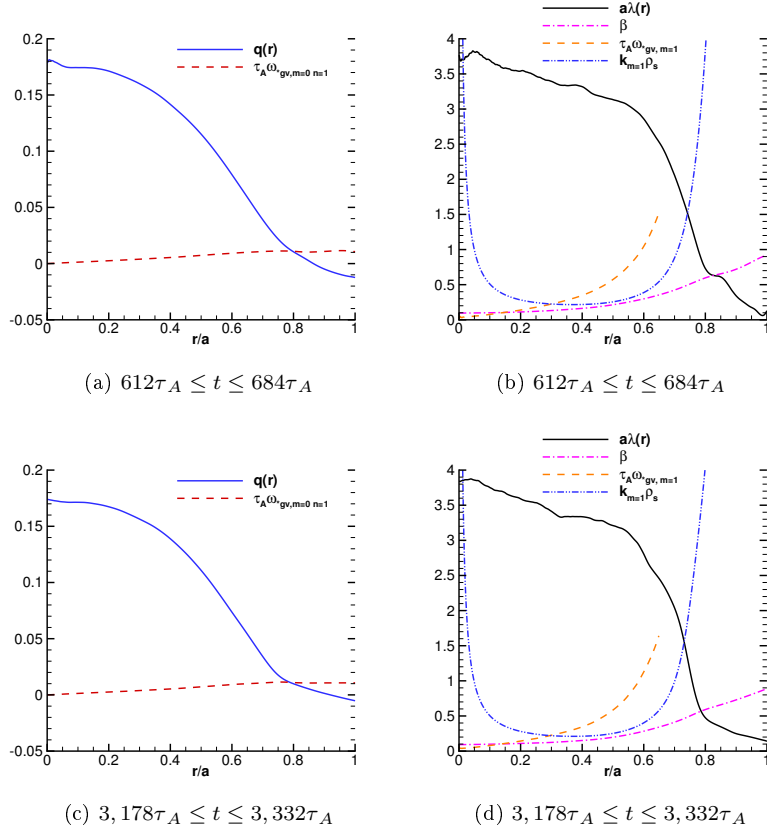


Figure 46: The (a,c) safety-factor and gyroviscous frequency for the  $m = 0$ ,  $n = 1$  mode profiles, and the (b,d) parallel-current, the gyroviscous frequency for the resonant  $m = 1$  modes, and the  $\beta$  profiles from the two-fluid computation are shown for two time periods. The top plots (a,b) are averaged over the time range  $612\tau_A \leq t \leq 684\tau_A$ , and the bottom plots (c,d) are averaged over  $3,178\tau_A \leq t \leq 3,332\tau_A$ .

times and small differences in the edge. The parallel current profile for  $r > 0.6a$  during the initial relaxation is more radially distributed with a flatter gradient at  $r \simeq 0.8a$  than during  $3,178\tau_A \leq t \leq 3,332\tau_A$ .

The profile of  $k_{m=1}\rho_s$  is also plotted in Fig. 46, where we compute  $k_{m=1}$  for the mode resonant at a given radial location such that

$$k_{m=1} = \sqrt{\frac{1}{r^2} + \frac{1}{q^2 R^2}}. \quad (17.1)$$

The  $k_{m=1}\rho_s$  profile diverges in two locations, as  $r \rightarrow 0$  and as  $q \rightarrow 0$ . Our first-order FLR model of ion gyroviscosity breaks down when  $k_{m=1}\rho_s$  approaches unity, and we do not expect the  $m = 1$  ion dynamics to be accurately modeled. The range of validity with respect to the  $m = 1$  mode is roughly  $0.1a \lesssim r \lesssim 0.65a$ , where the ion gyroradius is strictly less than the ion-sound gyroradius,  $\rho_i < \rho_s$  (for our cases with equal specie's temperature,  $\rho_i$  is smaller than  $\rho_s$  by a factor of  $\sqrt{2}$ ). Figure 56 in Appendix shows the resonant

surface location as a function of time for a collection of modes, and we note  $m = 1$  modes with  $6 \leq n \leq 20$  are resonant within the range of  $m = 1$  validity. These modes dominate our computations as larger- $k$  modes are both strongly damped (the dissipation scales as  $k^2$ ), and, as described in Sec. 4, the most unstable tearing modes are those with longer wavelengths. Thus we argue our model sufficiently captures the current-drive core dynamics. In our constant-equilibrium-pressure cases, the plasma- $\beta$  profile increases by roughly a factor of 9 at the wall relative to the core from magnetic-field amplitude variation. However, the experimental pressure profile is typically peaked in the core such that  $\beta$  is constant if not decreasing. As  $\rho_s \sim \sqrt{\beta}$ , the inclusion of a more realistic pressure profile would lead to smaller values of  $k_{m=1}\rho_s$  in the edge, although it would not eliminate the divergence as  $q \rightarrow 0$ .

Also plotted in Fig. 46 are the gyroviscous frequency profiles (Eqn. 11.10) for the  $m = 0, n = 1$  ( $k_\perp = 1/R$ ) and  $m = 1$  ( $k_\perp = k_{m=1}$ ) modes. Similar to the behavior of  $k_{m=1}\rho_s$ ,  $\omega_{*gv,m=1}$  diverges as  $q \rightarrow 0$  and the resonant axial mode number  $n \rightarrow \infty$ , and it is only plotted for  $r \leq 0.65a$  where  $k_{m=1}\rho_s \lesssim 0.5$ . From our linear theory, we expect the gyroviscous stabilization to be significant between  $0.5a \lesssim r \lesssim 0.65a$  where the  $m = 1, 10 \lesssim n \lesssim 20$  modes are resonant. Although the  $k_{m=1}\rho_s$  profile diverges as  $r \rightarrow 0$ , the  $\omega_{*gv}$  profile remains finite as both  $b_\theta$  and  $B'_0$  vanish. The gyroviscous frequency for the  $m = 0$  mode (left plots in Fig. 46) is small in comparison to the higher- $k$   $m = 1$  modes (right plots), and thus the linear theory predicts the stabilizing influence of the gyroviscous force is much smaller for the  $m = 0$  mode.

In Sec. 15.2 we examine terms of the helical momentum equation that establish the saturated-island force-density balance. In order to determine the influence of gyroviscosity in our multihelicity computations we make a similar decomposition, however the decomposition of forces into driving and third-order is no longer possible as there is no well-defined initial equilibrium. In addition, unlike our single-helicity results, nonlinear contributions to the helical momentum equation are large in our multi-helicity computations. Thus we decompose the forces into the linear contribution,

$$\mathbf{F}_{lin} = \tilde{\mathbf{J}} \times \mathbf{B}_0 + \mathbf{J}_0 \times \tilde{\mathbf{B}} - \nabla \tilde{p} - \mathbf{v}_0 \cdot \nabla \tilde{\mathbf{v}} - \tilde{\mathbf{v}} \cdot \nabla \mathbf{v}_0, \quad (17.2)$$

the nonlinear contribution from  $\mathbf{J} \times \mathbf{B}$ , and the gyroviscous force.

These terms in the perpendicular-force-balance equation for the  $m = 0, n = 1$ , and  $m = 1, n = 6$  and 10 modes are plotted in Fig. 47. These plots represent the forces governing the x-point outflow of each mode, and are averaged over the time windows corresponding to the initial and the subsequent relaxation events in the two-fluid computation. Alternatively, we could have chosen to plot the radial forces governing the x-point

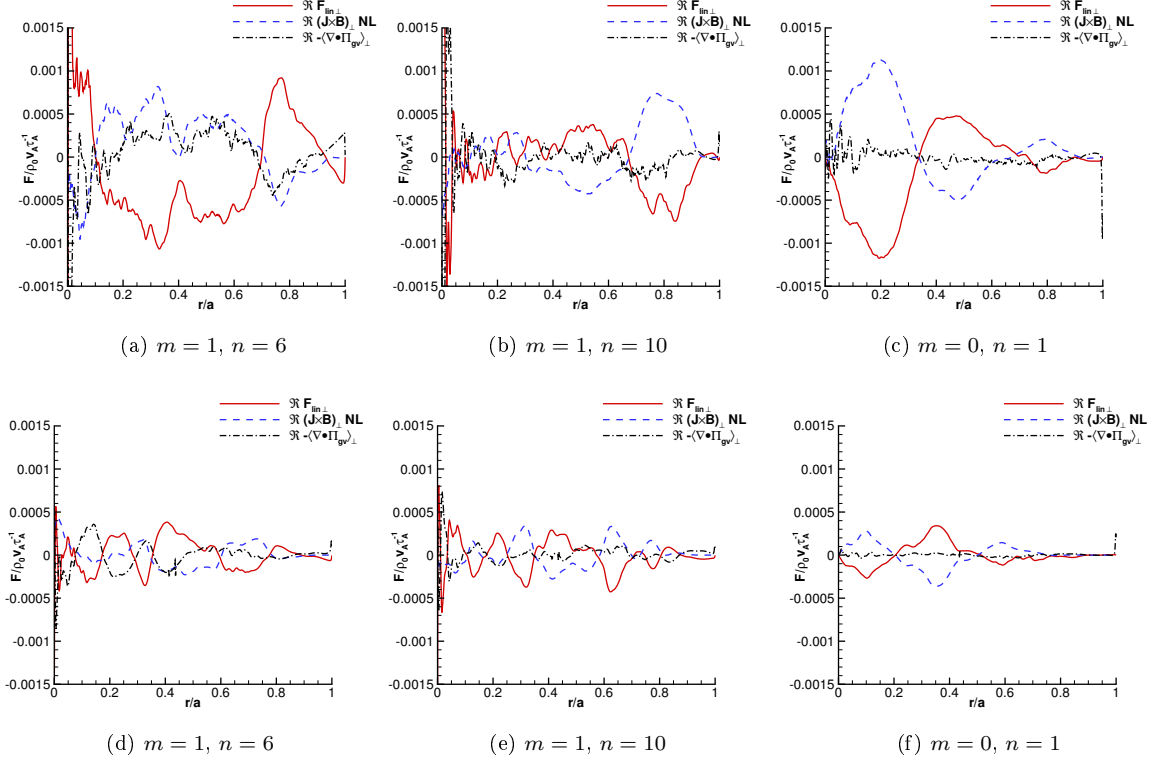


Figure 47: The perpendicular force balance for the (a,d)  $m = 1, n = 6$ , (b,e)  $m = 1, n = 10$ , and the (c,f)  $m = 0, n = 1$  modes during the (a-c) initial,  $612\tau_A \leq t \leq 684\tau_A$ , and (d-f) subsequent,  $3,178\tau_A \leq t \leq 3,332\tau_A$ , relaxation events.

inflow. For all modes in both time windows, the linear and nonlinear forces are significant. However, the gyroviscous force makes only a small contribution to the  $m = 0, n = 1$  force balance. It is more significant for the core modes and is particularly large for the  $m = 1, n = 6$  mode. The small influence of gyroviscosity on the  $m = 0$  mode agrees with the considerations of linear theory where  $\omega_{*gv,m=0}$  is small relative to  $\omega_{*gv,m=1}$  (Fig. 46).

### 17.3 $m = 0$ magnetic energy drive

The equilibria and force-balance considerations indicate that gyroviscous stabilization is not directly responsible for the lack of significant  $m = 0, n = 1$  magnetic-mode excitation after  $t \simeq 2,000\tau_A$  in the two-fluid computation. In order to investigate the relatively small  $m = 0, n = 1$  magnetic-mode amplitude further, we consider the spectral-magnetic-energy exchange. As shown in Appendix E, the time-rate of change of the

magnetic energy may be written as

$$\frac{\partial B^2}{\partial t 2\mu_0} = - \left[ \nabla \cdot \left( \frac{\mathbf{E} \times \mathbf{B}}{\mu_0} \right) + \mathbf{E} \cdot \mathbf{J} \right], \quad (17.3)$$

where the first term on the RHS is the Poynting flux, and the second represents coupling to the kinetic energy. Given the quadratic nature of these quantities, we may decompose volume-averaged according to contributions from a Fourier expansion. For example, the contribution to the magnetic energy from each mode becomes  $\langle\langle B_{m,n} B_{m,n}^* / \mu_0 \rangle\rangle$ , where  $\langle\langle \rangle\rangle$  indicates a volume average. After applying our conducting wall boundary conditions, the Poynting flux vanishes, and the time-rate of change of the volume-averaged spectral magnetic energy may be written as

$$\frac{\partial}{\partial t} \left\langle \left\langle \frac{B_{m,n} B_{m,n}^*}{\mu_0} \right\rangle \right\rangle = - \langle\langle \mathbf{E}_{m,n} \cdot \mathbf{J}_{m,n}^* + \mathbf{E}_{m,n}^* \cdot \mathbf{J}_{m,n} \rangle\rangle. \quad (17.4)$$

The spectral-magnetic-energy drive, the RHS of Eqn. (17.4), for the  $m = 0, n = 1$  mode is shown in Fig. 48 for both (a,b) the two-fluid and (c) single-fluid computations. This drive is decomposed in terms of the linear and nonlinear contributions from the  $m = 0, n = 1$  Ohm's law. We find the dynamics are dominated by the  $\mathbf{v} \times \mathbf{B}$ , Hall and resistive terms, and other contributions are not plotted.

During the initial relaxation event, shown in Fig. 48(a), we see the mode is initially driven (positive  $-\langle\langle \mathbf{E} \cdot \mathbf{J} \rangle\rangle$ ) from  $550\tau_A$  to  $800\tau_A$  and then damped (negative  $-\langle\langle \mathbf{E} \cdot \mathbf{J} \rangle\rangle$ ) during  $800\tau_A \lesssim t \lesssim 1,500\tau_A$ . The energy drive is provided through contributions from both the nonlinear Hall and MHD terms similar to the MST measurements described in Refs. [40, 41]. The large nonlinear drive is the result of three-wave coupling between the core-resonant  $m = 1$  modes with neighboring  $n$  numbers. There are temporal differences between the nonlinear Hall and MHD terms however, the Hall term is large and positive for period of  $50\tau_A$  during the mode-activity peak, and later it reverses sign and drains energy from the mode. In contrast, the nonlinear MHD term is almost strictly a driving term and is active for a period of approximately  $250\tau_A$ . The linear MHD term tends to oppose changes in the magnetic energy; during the initial driven period it is negative, and later it is positive in the damped period. Similar to behavior of our single-helicity cases where we find cancellations between  $\mathbf{v}$  and  $\mathbf{J}/ne$  lead to opposing MHD and Hall terms, the linear Hall contribution tends to drive the mode and partially cancels the stabilizing influence of the linear MHD term. The resistive contribution  $-\langle\langle \eta J^2 \rangle\rangle$  is strictly a damping term and makes a significant contribution when the mode magnetic amplitude is large.

Through the two-fluid evolution during the subsequent relaxation event,  $2,921\tau_A \leq t \leq 4,000\tau_A$  (Fig.

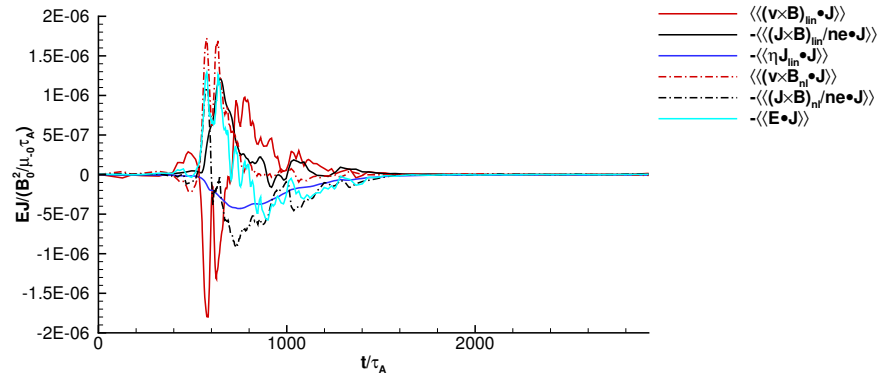
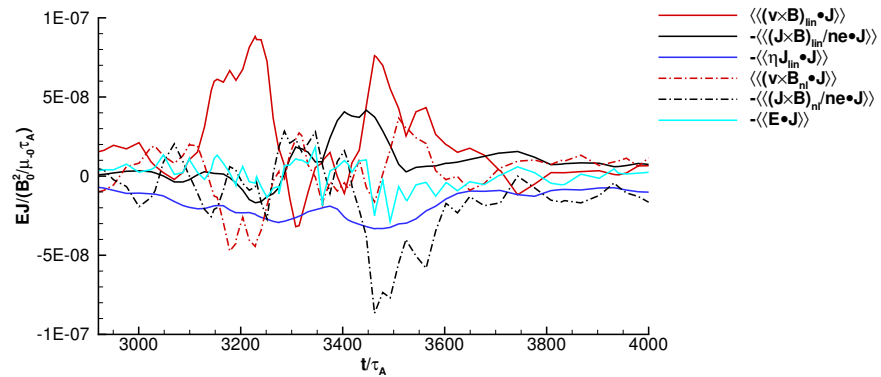
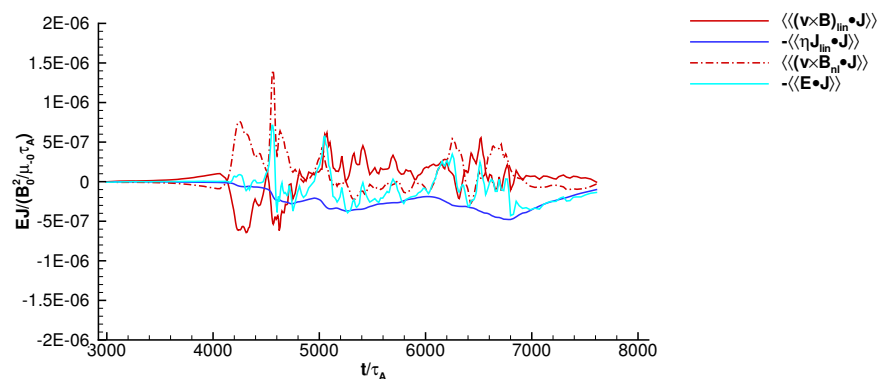
(a) Two-fluid computation for  $0 \leq t \leq 2,921\tau_A$ (b) Two-fluid computation for  $2,921\tau_A \leq t \leq 4,000\tau_A$ ; vertical axis scale differs(c) Single-fluid computation for  $2,921\tau_A \leq t \leq 8,100\tau_A$ 

Figure 48: Spectral energy transfer rate for the  $m = 0$ ,  $n = 1$  mode. The two-fluid computation is split between (a) the early time where large  $m = 0$ ,  $n = 1$  and (b) the later half of the computation where the  $m = 0$ ,  $n = 1$  mode remains suppressed. In (c) the single-fluid case is shown.

48(b)), all terms in the decomposition of  $-\langle\langle\mathbf{E}\cdot\mathbf{J}\rangle\rangle$  are small. There are small driving contributions from the linear terms, but not enough to significantly excite the  $m = 0$  magnetic perturbation. We conclude that it is not gyroviscous stabilization, but rather lack of a nonlinear drive that explains the small  $m = 0$  magnetic amplitudes after the initial relaxation event.

Figure 48(c) shows the spectral-magnetic-energy drive for the single-fluid computation. As the Hall term is not present in this computation, its contributions are not shown. Associated with the significant  $m = 1$  mode magnetic amplitudes, there is a large nonlinear  $\mathbf{v}\times\mathbf{B}$  drive during  $4000 - 5000\tau_A$ . The linear  $\mathbf{v}\times\mathbf{B}$  term tends to oppose changes in the mode energy as in the two-fluid case.

## 18 Electric-field dynamics

### 18.1 Dynamo emfs and profile modification

Figure 49 shows the parallel dynamo emfs and associated profile modification at  $612\tau_A \leq t \leq 684\tau_A$  and  $3,178\tau_A \leq t \leq 3,332\tau_A$ . In both time windows, the combined dynamo emf acts to flatten the current profile by driving parallel current in the edge, and reducing it in the core. The MHD- and Hall-dynamo emfs are of comparable amplitude. The measurements of Ding et al. find a fivefold decrease in the amplitude of the Hall dynamo between MST discharges with  $F = -0.22$  and  $F = 0$ . Our results are similar as the initial event has  $F \simeq -0.11$  and a Hall dynamo emf that is approximately a factor of eight larger than during the subsequent relaxation event with  $F \simeq 0.02$ .

It is clear from Fig. 49 that the sum of the dynamo emfs do not balance the resistive term from the perturbed mean current. This is natural as the multi-helicity plasma evolution remains dynamic throughout time and never approaches a steady state, unlike our single-mode modeling. The dynamo emfs are much larger than the perturbed mean current during a short time window around the relaxation events, and they are small in the quiescent periods between events.

The contributions from specific modes to the dynamo emfs are shown in Fig. 50. In general each mode flattens the current profile around its resonant surface by reducing the current on the radially-inward side and driving current on the radially-outward side (resonant-surface locations are plotted in Fig. 56, in Appendix H). For example, the Hall dynamo from the  $m = 1, n = 6$  mode is positive on the radially-inward side relative to its resonant surface, and is negative on the outward side for both the initial ( $F \simeq -0.11, r_s \sim 0.3a$ ) and subsequent ( $F \simeq -0.02, r_s \sim 0.2a$ ) relaxation events. As each mode incrementally transfers the current outward, their collective effect is a global redistribution of the parallel-current profile.

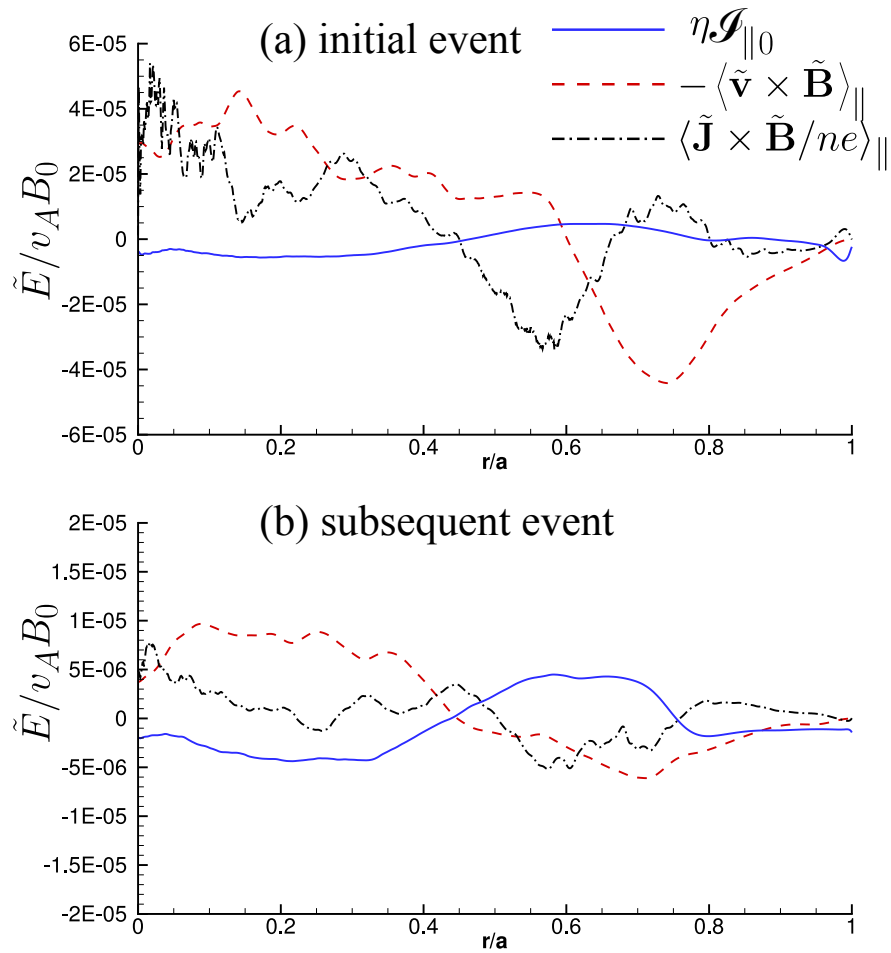


Figure 49: Time-averaged dynamo emfs and current-profile modification during the (top) initial,  $612\tau_A \leq t \leq 684\tau_A$ , and (bottom) subsequent,  $3,178\tau_A \leq t \leq 3,332\tau_A$ , relaxation events.

Both the Hall- and MHD-dynamo emfs are significant near each mode resonant surface. Similar to the behavior of the composite dynamo emfs (Fig. 49), the amplitude of the contributions from each mode to the dynamo emfs (Fig. 50) are smaller in the  $F \simeq -0.02$  event relative to the  $F \simeq -0.11$  event. For example, both the MHD- and Hall-dynamo emfs are reduced by a factor of four during the  $F \simeq -0.02$  time window.

With respect to the MHD dynamo, the significant amplitude of the dynamo emfs at mode resonant surfaces seen in Fig. 50 contradicts the discussion of Ding et al.. They point out the parallel MHD dynamo emf may be approximated as

$$\langle \tilde{\mathbf{v}} \times \tilde{\mathbf{B}} \rangle_{\parallel} = \langle \tilde{v}_r \tilde{B}_{\perp} \rangle - \langle \tilde{v}_{\perp} \tilde{B}_r \rangle \simeq - \langle \tilde{v}_{\perp} \tilde{B}_r \rangle \quad (18.1)$$

motivated by the ordering  $\tilde{B}_{\perp} \sim \tilde{B}_r$  and  $\tilde{v}_r \ll \tilde{v}_{\perp}$ . As discussed in Sec. 4, these assumptions are valid for tearing perturbations where the flow ordering results simply from the aspect ratio of the inflow,  $k_{\perp}^{-1}$ , to the outflow which is radially localized in the layer. They then use the property that tearing modes are nearly incompressible,

$$\nabla \cdot \tilde{\mathbf{v}} = \frac{1}{r} \frac{\partial}{\partial r} (r \tilde{v}_r) + ik_{\perp} \tilde{v}_{\perp} + ik_{\parallel} \tilde{v}_{\parallel} \simeq 0, \quad (18.2)$$

to relate  $\tilde{v}_{\perp}$  to  $\tilde{v}_{\parallel}$  by assuming that all terms proportional to  $\tilde{v}_r$  are again small. Their result is an MHD-dynamo emf which is proportional to  $k_{\parallel}$  and small at the mode resonant surface. We argue that given the flow aspect-ratio ordering,  $\tilde{v}'_r$  ( $\simeq -ik_{\perp} \tilde{\phi}'$  for linear theory) is comparable to  $\tilde{v}_{\perp}$  ( $\tilde{\phi}'$ ) near the resonant surface. As the last term ( $ik_{\parallel} \tilde{v}_{\parallel}$ ) on the RHS of Eqn. (18.2) vanishes at  $r_s$  by definition, there is instead a balance between  $\tilde{v}_{\perp}$  and  $\tilde{v}'_r$ . Thus nothing precludes the MHD-dynamo emf at the resonant surface from being significant as observed in our computations, and it may be expressed as  $-\langle i\tilde{v}'_r \tilde{B}_r \rangle / k_{\perp}$ .

## 18.2 Experimental comparison

Using values of  $B_0 \simeq 0.4$  T and  $v_A \simeq 2 \times 10^6$  m/s for the 400 kA discharges analyzed by Ding et al., the measured amplitude of the  $m = 1, n = 6$  Hall dynamo emf in Figs. 6 and 7 of 40 V/m corresponds to  $\tilde{E}/v_A B_0 = 5 \times 10^{-5}$  in our normalized units. The amplitude of the  $m = 1, n = 6$  Hall-dynamo emf at the resonant surface in our computation during the initial relaxation event,  $\tilde{E}/v_A B_0 \simeq 4 \times 10^{-5}$  (Fig. 50(a)), is remarkably similar. Additionally, the Hall-dynamo emf measurements during an  $F = 0$  relaxation event have an amplitude of 10V/m, a factor of four less than the  $F = -0.22$  measurements (See Fig. 11 in Ref. [25]). This behavior is similar to the  $4\times$  reduction in amplitude between our  $F \simeq -0.02$  and  $F \simeq -0.11$  events discussed in the last section. However, there are also some discrepancies between the experimental

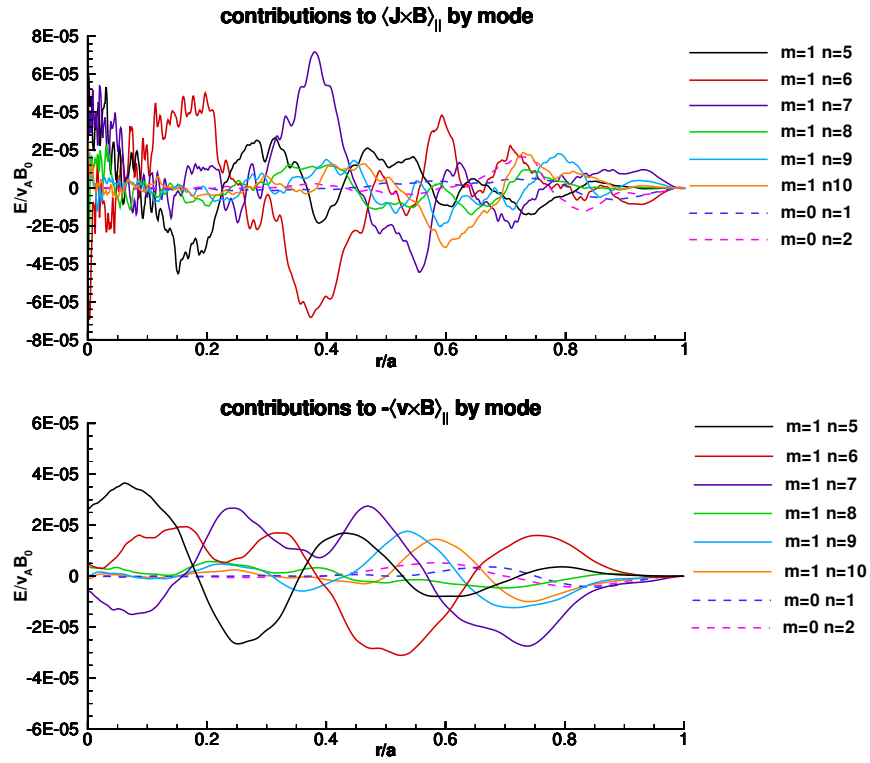
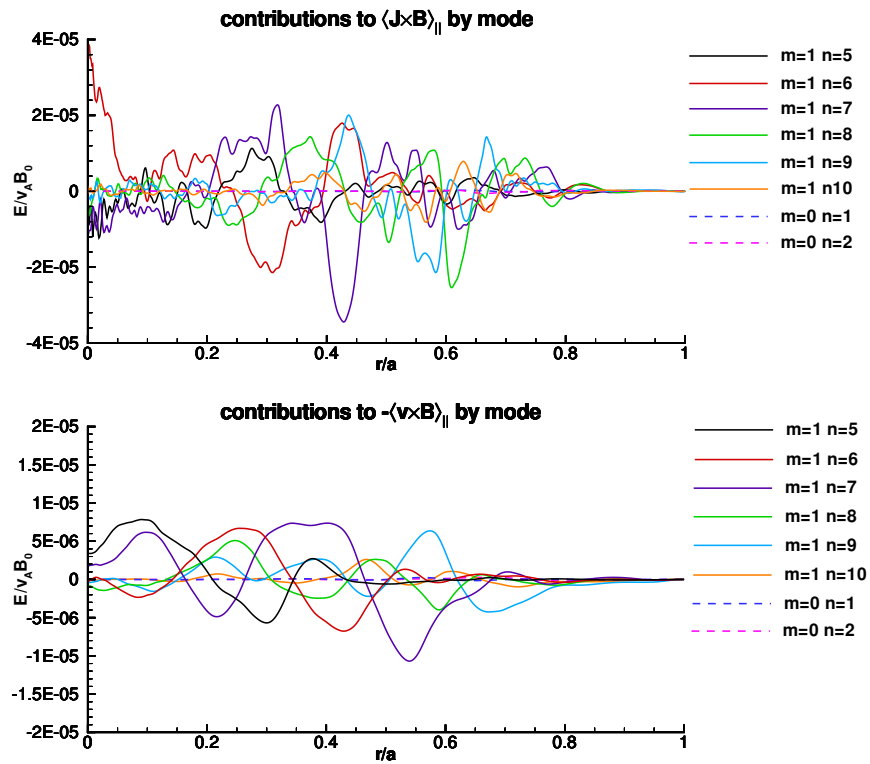
(a)  $612\tau_A \leq t \leq 684\tau_A$ ; note vertical scale differs(b)  $3,178\tau_A \leq t \leq 3,332\tau_A$ ; note vertical scale differs

Figure 50: Contributions to the Hall and MHD dynamo emfs from individual modes averaged over (a) the initial relaxation event,  $612\tau_A \leq t \leq 684\tau_A$ , and (b) the subsequent relaxation event,  $3,178\tau_A \leq t \leq 3,332\tau_A$ .

measurements and our computations. In particular, the measurements show a Hall-dynamo emf which is strictly positive, and radially localized within  $r_s \pm 0.1a$ . Whereas we find the emf has a radially-distributed influence and changes sign roughly near  $r_s$  with both negative and positive contributions.

Ding et al. decompose the Hall-dynamo emf and argue that a single term proportional to the correlation of  $\langle \tilde{B}_r, \tilde{B}'_\theta \rangle$  dominates. However, as described in detail in Appendix G, we argue that this term is one of two important contributions to the parallel Hall dynamo emf. To be more specific, after elimination of  $\tilde{B}_z$  with the  $\nabla \cdot \tilde{\mathbf{B}}$  constraint the poloidal component of the Hall dynamo emf may be written as

$$\mu_0 \langle \tilde{\mathbf{J}} \times \tilde{\mathbf{B}} \rangle_\theta = \left( \frac{2}{r} + \frac{\partial}{\partial r} \right) \langle \tilde{B}_r, \tilde{B}_\theta \rangle, \quad (18.3)$$

and the axial component of the Hall dynamo may be written as

$$\mu_0 \langle \tilde{\mathbf{J}} \times \tilde{\mathbf{B}} \rangle_z = -\frac{Rm}{rn} \frac{\partial}{\partial r} \langle \tilde{B}_r, \tilde{B}_\theta \rangle + \frac{R}{n} \left( \left\langle \frac{i\tilde{B}'_r}{r}, \tilde{B}_r \right\rangle + \langle i\tilde{B}''_r, \tilde{B}_r \rangle \right). \quad (18.4)$$

We may project these decomposed components into the parallel direction to find

$$\mu_0 \langle \tilde{\mathbf{J}} \times \tilde{\mathbf{B}} \rangle_\parallel = \left[ C_1 + C_2 \frac{\partial}{\partial r} \right] \langle \tilde{B}_r, \tilde{B}_\theta \rangle + C_3 \left\langle \frac{i}{r} \frac{\partial}{\partial r} (r\tilde{B}'_r), \tilde{B}_r \right\rangle \quad (18.5)$$

where

$$\begin{aligned} C_1 &= \frac{B_{0\theta}}{B_0} \frac{2}{r}, \\ C_2 &= \frac{B_{0\theta}}{B_0} - \frac{B_{0z}}{B_0} \frac{Rm}{rn}, \text{ and} \\ C_3 &= \frac{B_{0z}}{B_0} \frac{R}{n}. \end{aligned}$$

After use of the product rule for the derivatives, the five terms of Eqn. (18.5) are plotted in Fig. 51 for the  $m = 1, n = 6$  mode of our two-fluid case. The sum of the five terms in the decomposition are exactly equal to the Hall dynamo calculated from a straightforward correlation of  $\tilde{J}$  and  $\tilde{B}$ . Aside from terms that become large as  $r \rightarrow 0$  and cancel, the dominant contributions come from the term proportional to  $\langle \tilde{B}_r, \tilde{B}'_\theta \rangle$  and the term proportional to  $\langle i\tilde{B}''_r, \tilde{B}_r \rangle$ . We find the term neglected by Ding et al.,  $\langle i\tilde{B}''_r, \tilde{B}_r \rangle$ , is significant in our computational results. These terms largely tend to cancel as a function of radius for both the initial and subsequent relaxation events. As described earlier, the measurement of the amplitude of the  $\langle \tilde{B}_r, \tilde{B}'_\theta \rangle$  term in Figs. 6 and 7 of 40 V/m corresponds to  $\tilde{E}/v_A B_0 = 5 \times 10^{-5}$  in our normalized units. Comparison with

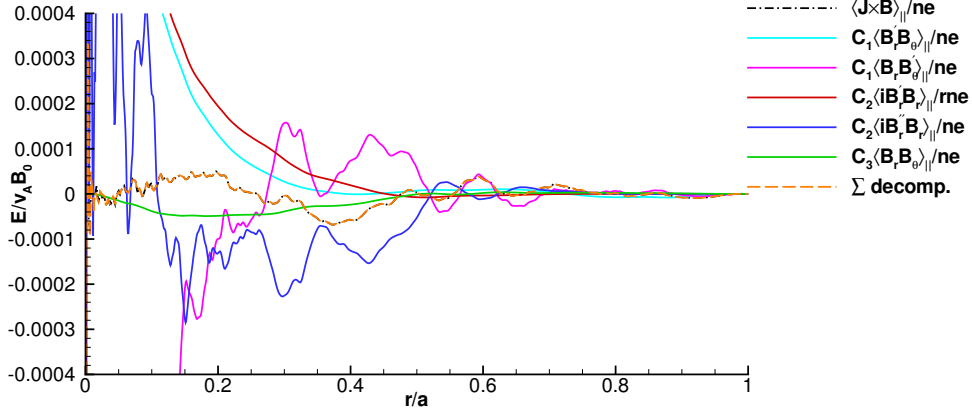
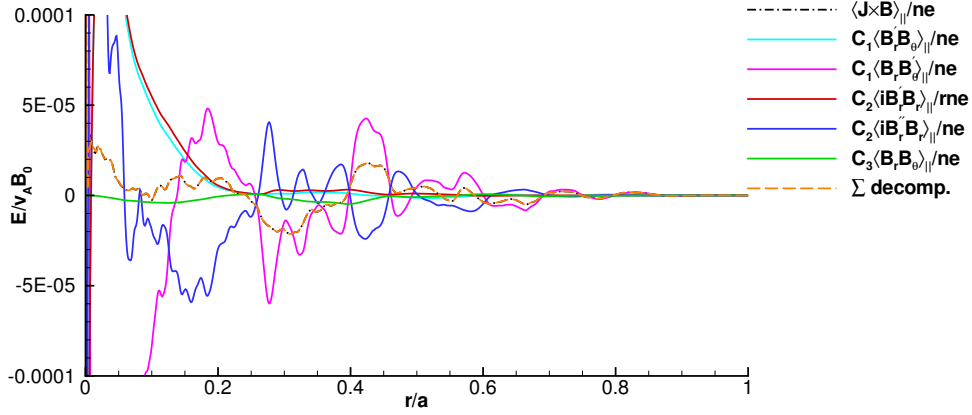
(a)  $612\tau_A \leq t \leq 684\tau_A$ ; note vertical scale differs(b)  $3,178\tau_A \leq t \leq 3,332\tau_A$ ; note vertical scale differs

Figure 51: Decomposition of the Hall-dynamo emf into the terms of Eqn. (18.5) during the initial and subsequent relaxation events.

Fig. 51 shows this value is comparable in amplitude to our computations during  $3,178\tau_A \leq t \leq 3,332\tau_A$  and four times smaller than the value during  $612\tau_A \leq t \leq 684\tau_A$ . The experimental measurement predicts a bell curve profile with a width of approximately  $0.2a$  centered at the resonant surface. In our computations  $\langle \tilde{B}_r, \tilde{B}'_{\theta} \rangle$  has considerable spatial variation, but is largely positive and localized to the mode resonant surface ( $r_s \simeq 0.3a$  during  $612\tau_A \leq t \leq 684\tau_A$  and  $r_s \simeq 0.2a$  during  $3,178\tau_A \leq t \leq 3,332\tau_A$ ).

The term  $\langle i\tilde{B}'_r, \tilde{B}_r \rangle$  is only nonzero if the complex phase of  $\tilde{B}_r$  varies as a function of radius. To illustrate, we write  $\tilde{B}_r = A \exp(-i\phi)$  where  $A(r)$  is a real and  $\phi(r)$  is the complex phase. Derivatives of  $\tilde{B}_r$  are then

$$\tilde{B}'_r = A' \exp(-i\phi) - i\phi' A \exp(-i\phi) \quad (18.6)$$

and

$$\tilde{B}_r'' = A'' \exp(-i\phi) - i(2\phi' A' + A\phi'') \exp(-i\phi) - A\phi'^2 \exp(-i\phi) , \quad (18.7)$$

and the correlated quantities are

$$\langle i\tilde{B}_r', \tilde{B}_r \rangle = A^2 \phi' \quad (18.8)$$

and

$$\langle i\tilde{B}_r'', \tilde{B}_r \rangle = 2\phi' A' A + A^2 \phi'' . \quad (18.9)$$

The significance of the  $\langle i\tilde{B}_r'', \tilde{B}_r \rangle$  term is not related to the size of  $\tilde{\psi}''$  from tearing ordering (in which case it would be associated with a term proportional to  $A''$ ), but rather due to the radial variation of the complex phase of  $\tilde{B}_r$ . For our linear slab cases, this effect is small (See Fig. 21 where  $\Im\tilde{B}_r \simeq 0$ ). However, the  $\omega_{*qv}$ - and  $\omega_{*H}$ -drift effects in our linear single-helicity cylindrical cases cause a distortion of the phase of the perturbation (Figs. 26 and 27). In addition, nonlinear effects from multi-mode interaction may cause further distortion.

## 19 Momentum transport

### 19.1 Flow profiles and mean forces

Associated with the Hall-dynamo emf is a force from the fluctuation-induced Maxwell stress. We find that this force, along the fluctuation-induced Reynolds stress and viscous forces, is able to generate significant mean flow in our computations. Figure 52 shows the parallel flow as a function of time and radius for our two-fluid computation, where the flow profile is nearly zero at  $t = 0$ . Associated with each relaxation event, there is flow driven in the parallel direction in the core, and flow driven in the anti-parallel direction mid-radius. Between the events, there is a slow diffusion of the driven flows. The components of the flow profile, in both cylindrical and magnetic coordinates, are shown in Fig. 53 at (a)  $612\tau_A \leq t \leq 684\tau_A$  and (b)  $3,178\tau_A \leq t \leq 3,332\tau_A$ . The parallel flow is considerably larger during the initial relaxation event in comparison to the subsequent event. Both events also generate a perpendicular flow profile that is associated with a mean electrostatic potential.

The mean parallel flow is largely unaffected by forces from the mean fields as the parallel component of  $\mathbf{J}_0 \times \mathbf{B}_0$  vanishes by definition, and  $\nabla p_0$  has only a radial component. Components of the mean momentum equation are plotted in Fig. 54: the advective term,  $\mathbf{v}_0 \cdot \nabla \mathbf{v}_0$ , the force densities from the Reynolds and

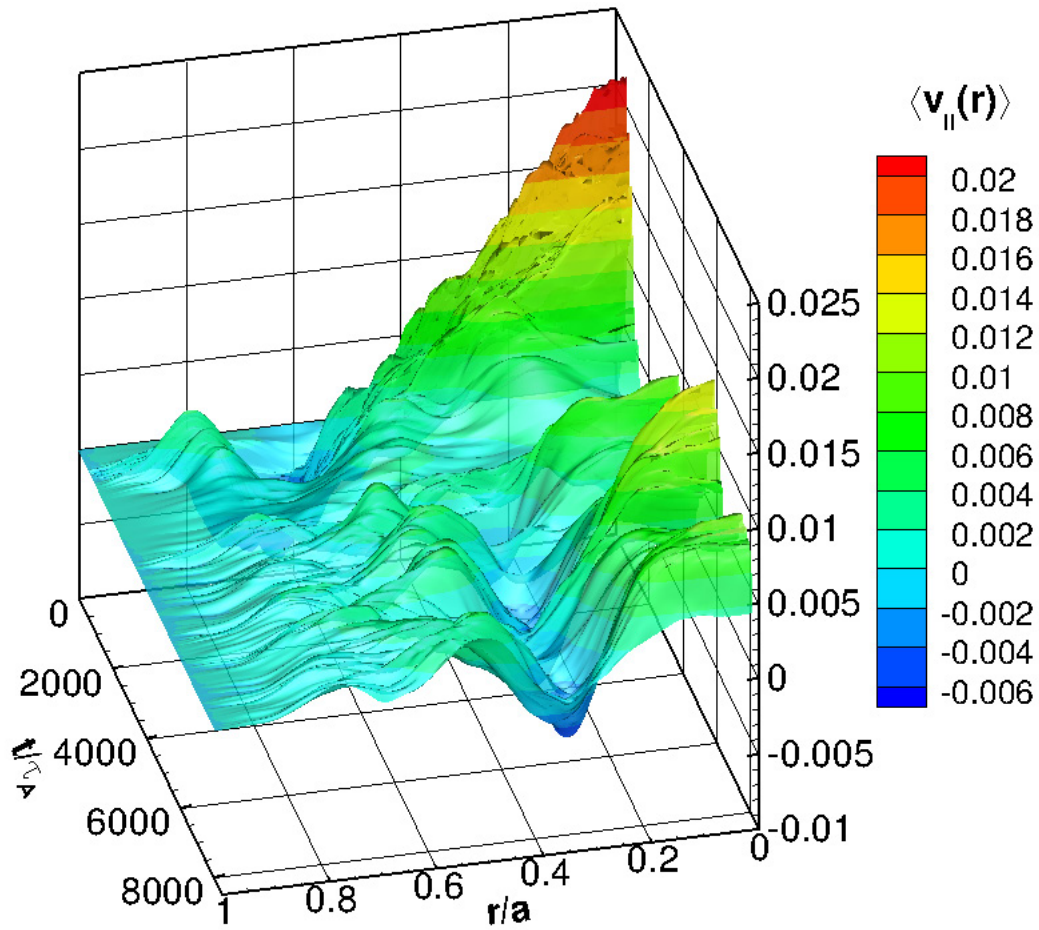


Figure 52: Mean parallel flow speed as a function of time and radius for the two-fluid computation.

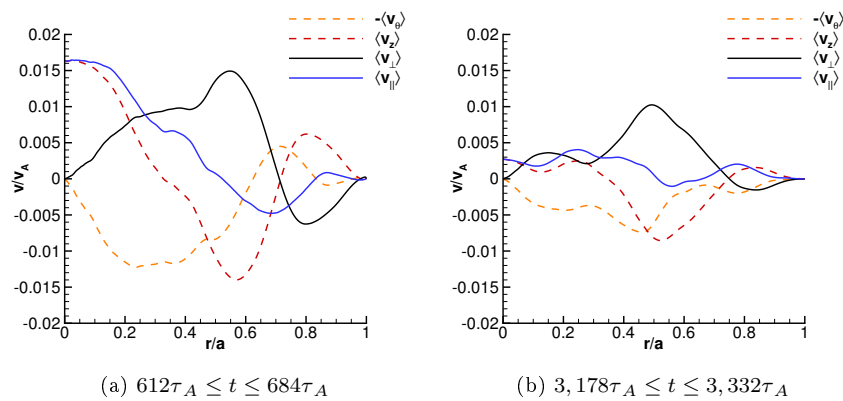


Figure 53: Flows profiles generated during the (a) initial,  $612\tau_A \leq t \leq 684\tau_A$ , and (b) subsequent,  $3,178\tau_A \leq t \leq 3,332\tau_A$ , relaxation events in our two-fluid computation.

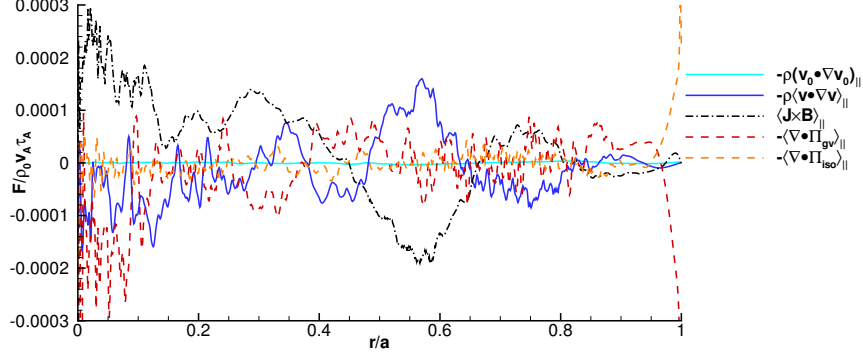
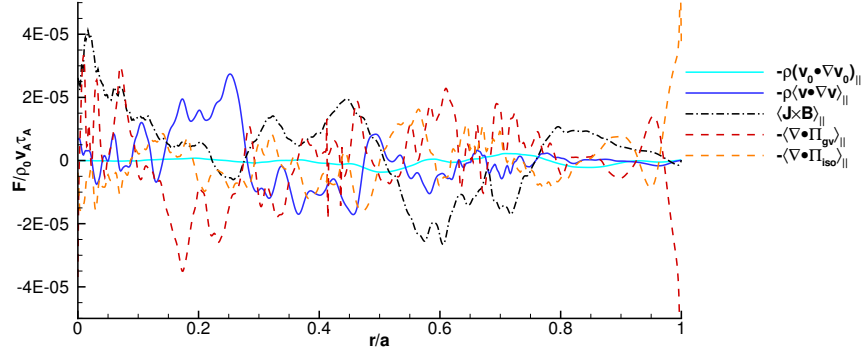
(a)  $612\tau_A \leq t \leq 684\tau_A$ (b)  $3,178\tau_A \leq t \leq 3,332\tau_A$ 

Figure 54: Mean parallel forces during the (a) initial,  $612\tau_A \leq t \leq 684\tau_A$ , and (b) subsequent,  $3,178\tau_A \leq t \leq 3,332\tau_A$ , relaxation events in our two-fluid computation.

Maxwell stress, and the viscous forces. The mean advective term is small in both time windows, and the dominant forces are from the correlation of the fluctuations associated with the relaxation event. Similar to the dynamo emfs, the force densities are roughly a factor of four smaller during the subsequent relaxation event relative to the initial event.

As shown in Appendix E, the model equations for our computations conserve momentum up to viscous interaction with the wall,

$$\frac{\partial}{\partial t} \langle \langle m_i n v_z \rangle \rangle = -\frac{2}{a} \langle \mathbf{\Pi}_{rz} \rangle|_{r=a} \quad (19.1)$$

and

$$\frac{\partial}{\partial t} \langle \langle m_i n v_\theta \rangle \rangle = -\frac{2}{a} \langle \mathbf{\Pi}_{r\theta} \rangle|_{r=a} . \quad (19.2)$$

After significant momentum is radially transported during the initial relaxation event, these viscous drags cause net momentum generation as shown in Fig. 55. However, our computations apply no-slip boundary

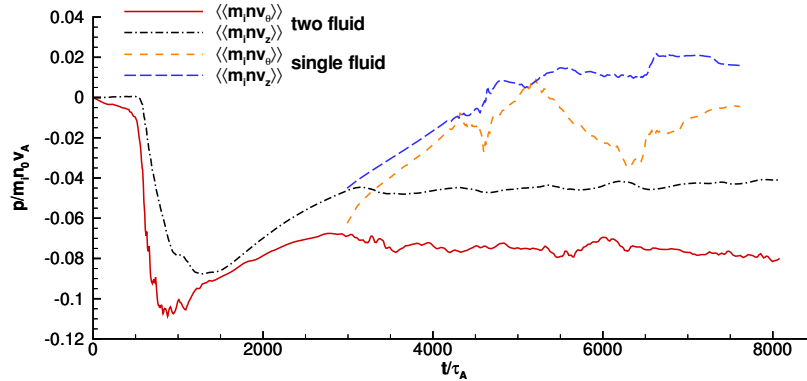


Figure 55: Axial and poloidal momentum as a function of time for our two- and single-fluid computations.

conditions on the perturbed velocity at the wall ( $\tilde{v}(a) = 0$ ), and we do not expect the net momentum generation to be representative of the experiment without more detailed boundary modeling. As seen in the figure, the net momentum generated by the two-fluid model is sustained through the computation, whereas it quickly decays from its initial level to much smaller values in our single-fluid case.

## 19.2 Experimental comparison

We expect our two-fluid modeling to capture the momentum profile changes from the nonlinear stresses during a relaxation event. The measurements from the low-current discharges studied by Kuritsyn et al. have  $B_0 \simeq 0.2$  T and  $n \simeq 10^{19}$  m $^{-3}$ , thus  $v_A \simeq 10^6$  m/s. The measured characteristic flow speed of 10 km/s is then equivalent to  $\tilde{v}/v_A = 0.01$  in our normalized units. In Fig. 9 we see the parallel flow at  $r = 0.3a$  is driven in the parallel direction by 20 km/s and the parallel flows at  $r = 0.5a$  and  $r = 0.66a$  are driven in the anti-parallel direction by 10 and 20 km/s, respectively. These changes compare favorably with those from our computations. In Fig. 53(a) we see the parallel flow is increased by  $0.01v_A$  at  $r = 0.3a$ , and decreased by approximately  $0.005v_A$  at  $r = 0.5a$  and  $0.66a$  as the flow profile is nearly zero at  $t = 0$ . Although the momentum transport in the computations is reduced by approximately a factor of two relative to the experiment, there is semi-quantitative agreement. Additionally, as shown in Fig. 12 when the  $m = 0$  is not excited during a relaxation event, there is little measured change in the core rotation speed. The flows generated in the computation during the subsequent relaxation event is significantly smaller (Fig. 53(b)), and Fig. 52 shows that the parallel flow profile does not change as significantly for  $t > 2000\tau_A$  relative to the initial relaxation event.

Kuritsyn et al. measured the forces from the Maxwell and Reynolds stresses, Figs. 10 and 11. They find

these forces are significant near relaxation events, and tend to oppose each other with a radially-varying structure. During the initial relaxation event in our computation, Fig. 54(a), the forces from the Maxwell and Reynolds stresses are also largely opposed with radial variation in their structure. The magnitude of the force densities may be compared as well, and using the same parameters as the previous paragraph, we note that  $10 \text{ N/m}^3$  is equivalent to  $\tilde{F}/\rho_0 v_A \tau_A^{-1} = 0.00016$ . Thus, the forces in the edge are approximately a factor of three smaller in the computations relative to the experiment.

## 20 Discussion

Our computations reproduce many two-fluid aspects measured in MST, however given the pinch parameter of  $\Theta \simeq 1.6$  (Fig. 44), it is natural to expect more significant  $m = 0$  mode activity. The computations do not have a pressure profile, and this addition would add three effects: (1) interchange drive, (2) a flat or decreasing  $\beta$  profile, and (3) diamagnetic-drift effects. We expect the interchange drive may destabilize modes resonant near the reversal surface where the pressure gradient is the largest, and a decreasing  $\beta$  profile would limit  $\omega_{*gv}$  stabilization and two-fluid decoupling effects near the edge. Although the diamagnetic-drift effects may be stabilizing, including the pressure gradient could produce  $m = 0$  mode activity through increased linear and nonlinear drives.

In addition, our computations use  $\beta = 0.1$  on the geometric axis, which is greater than the value of the experimental discharges by at least a factor of two (see Tab. 3). Thus the  $k\rho_s$  profile is slightly larger in our computations than that in the experiment, as  $k\rho_s \sim \sqrt{\beta}$ . As the stabilizing ion gyroviscous effect becomes smaller as  $k\rho_s$  decreases (Part IV), we expect computations with smaller  $\beta$  may exhibit larger  $m = 1$  mode amplitudes, and possibly greater nonlinear  $m = 0$  mode drive.

Another aspect of the experiment not present in the computations is the toroidal and poloidal gaps on the nearly-perfectly-conducting shell. With a toroidal gap, the plasma could generate a mean poloidal emf which modifies the otherwise fixed total amount of toroidal flux in the computation. This effect is certainly significant in the experiment where the toroidal flux changes by as much as 10% during relaxation.

Although our computations do not incorporate these potentially important effects, they still represent a significant development in two-fluid device-scale RFP modeling. The inclusion of two-fluid effects expands the parameter space from resistive MHD, where it may be characterized by the boundary electric fields ( $\Theta$  drive),  $S$  and aspect ratio, to an additional parameter space characterized by  $\beta$  and  $d_i$ . Resistive MHD does model some finite- $\beta$  effects through the coupling of pressure described in Sec. 4.3, however the two-fluid

model captures effects beyond resistive MHD: fluid-decoupling, KAW-mediated-tearing, and gyroviscous effects. Our studies show these effects are important with RFP experimental parameters. Although our multi-helicity computation only explores one location in this larger parameter space,  $\beta = 0.1$  and  $d_i = 0.17a$ , it clearly produces rich effects not present with a single-fluid model. There is substantial qualitative and quantitative agreement with the experimental measurements on the fluctuation amplitude, Hall-dynamo emf, and parallel-momentum transport, even though some parameters only approximate MST conditions, and  $S$  is at least a factor of ten smaller in our computations.

## Part VI

# Conclusions

## 21 Summary of results

Our main results are the discovery of new cylindrical FLR effects on tearing modes. In Secs. 21.1 and 21.2, we detail the new linear and nonlinear effects introduced by cylindrical geometry. Our new results show there are drifts in pinch profiles proportional to  $\nabla B$  and curvature after the linearization of an extended-MHD model without the use of a large-aspect-ratio approximation. These drifts lead to a stabilizing drift-tearing response. The linearization of ion gyroviscosity produces to the drift that affects the ion flow, and even when nonlinear effects are significant we find the gyroviscous force can supplement the third-order forces described by Rutherford ([50]) leading to a reduced island saturation amplitude. In our multi-mode two-fluid computation, which is similar to MST, we find both qualitative and quantitative agreement with MST measurements that are not captured by a single-fluid model (Sec. 21.3). This indicates that first-order FLR effects are essential to RFP modeling. Our results represent both code verification, where we find numerical growth rates from the NIMROD code match the result from linear slab two-fluid tearing theory, and partial code validation through comparison to experimental MST measurements

### 21.1 Drift effects on the linear tearing mode

Our linear computations demonstrate that first-order FLR effects such as ion-electron decoupling and ion gyroviscosity impact tearing-mode dynamics at parameters that are relevant to RFP experiments. Previous studies in slab geometry show KAW mediation of the tearing mode increases the growth rate when  $\rho_s \gtrsim l$  [46, 14, 49]. Relative to slab cases, the ion flow is modified by a drift from the gyroviscous stress that is associated with the gradient and poloidal curvature of the magnetic field with warm ions. The growth rate of the tearing mode is reduced in this intermediate drift regime where  $\omega_{*gv} \gtrsim \gamma$ , which occurs at lower- $\rho_s$  values than the transition from the collisional regime to the semi-collisional regime ( $\rho_s \sim l$ ). These  $\omega_{*gv}$ -drift contributions are much larger in pinch profiles than they are in large aspect-ratio tokamaks, where the poloidal curvature and the variation of the ion gyrofrequency profile are weaker.

In the large- $\rho_s$  regime,  $\rho_s \gtrsim l$ , we find a drift in the parallel induction equation again characterized by  $\nabla B$  and curvature in addition to the terms that lead to KAW effects. In this regime, the decoupled electron

fluid governs the dynamics of the mode, and our numerical results show that the cold- and warm-ion cases approach the same growth rate. Therefore, the modeling of ion dynamics is less important where  $\rho_s$  is largest, and the first-order ion FLR modeling should provide a reasonably good approximation over the entire parameter range.

## 21.2 Reduction of the saturated island width through FLR effects

In the nonlinear regime with experimentally-relevant conditions, the island width and characteristic scale lengths are significantly larger than  $\rho_s$ , so first-order modeling is well justified. With warm ions the nonlinear gyroviscous force supplements the perturbed nonlinear Lorentz force and reduces the island saturation width. This contrasts with our cold-ion results and with previous drift-tearing studies for large-island evolution with a diamagnetic drift where the island saturation width is the same as resistive MHD [53, 54, 56]. The curvature and gradient of the magnetic field are not greatly modified by the nonlinear island evolution, so the gyroviscous-drift effects are also relatively unchanged, unlike the pressure gradient that is important for diamagnetic-drift effects. We suspect this stabilizing effect could produce a self-reinforcing cycle where reduced magnetic-perturbation amplitudes lead to improved confinement and a hotter plasma, which in turn increases  $\rho_s$  and further reduces the magnetic-perturbation amplitudes. Additionally, because the gyroviscous forces balance Lorentz forces, the Hall terms remain significant with warm ions, unlike the results computed for cold ions. With warm ions, the ion flows are substantially distorted by the gyroviscous stress, and the dominant eddy is out of phase with the flow responsible for reconnection.

## 21.3 Multi-helicity results

Our two-fluid multi-mode results model the nonlinear interaction of multiple current-driven tearing modes. However they do not include transport effects, and thus we do not expect a self-reinforcing cycle of mode stabilization. With  $\rho_s = 0.05a$ , a value within the range of RFPs, we find mode amplitudes are suppressed relative to a single-fluid computation. This suppression is related to the gyroviscous stabilization effect that we analyzed for a single mode. Although for some large- $n$ ,  $m = 1$  modes  $k\rho_s$  is greater than one, our linear and nonlinear results indicate the ion dynamics ceases to matter at large  $k\rho_s$  and our first-order FLR model still captures the electron-MHD physics which govern the mode evolution. In addition, the  $m = 1$  core-resonant tearing modes, which are the most unstable modes in RFPs and tend to have the largest perturbed amplitudes, have small  $k\rho_s$  and are within the model's range of validity.

The dynamics with a two-fluid model produce effects beyond single-fluid modeling. Both the Hall and

MHD dynamos are significant in our two-fluid computation. The magnitude and sign of the Hall dynamo qualitatively agree with MST experimental measurements. Associated with the Hall dynamo is a Maxwell stress. Our computation finds the force from the Maxwell stress is generally opposed to the force from the Reynolds stress. This result, the amplitudes of these forces, and the associated momentum transport during a relaxation event match experimental measurements. Our results indicate a potentially bright future for RFP fluid modeling, where the inclusion of a more realistic pressure profile, and transport and boundary effects has the potential to significantly improve the predictability of nonlinear macroscopic RFP simulation.

# Appendix

## A Formulary

Frequencies ( $1/t$ )	
Gyro-	$\omega_{c\alpha} =  q_\alpha  B / m_\alpha$
Plasma	$\omega_{p\alpha} = \sqrt{n q_\alpha^2 / \epsilon_0 m_\alpha}$
Speeds ( $L/t$ )	
Thermal	$v_{T\alpha} = \sqrt{k_B T_\alpha / m_\alpha}$
Sound	$c_s = \sqrt{\Gamma k_B (T_i + T_e) / m_i}$
Alfvén	$v_A = B / \sqrt{\mu_0 \rho}$
Lengths ( $L$ )	
Skin depth	$d_\alpha = c / \omega_{p\alpha} = \sqrt{m_\alpha / \mu_0 n_\alpha e^2}$
Particle gyroradius	$\rho_\alpha = v_{T\alpha} / \omega_{c\alpha}$
Ion sound gyroradius	$\rho_s = c_s / \omega_{ci} = \sqrt{\Gamma \beta / 2} d_i$
Debye	$\lambda_D = v_{Te} / \omega_{pe} = \sqrt{\epsilon_0 k_B T_e / n_e q_e^2}$
Tearing skin depth	$\delta = \sqrt{a^2 / \gamma \tau_A S + d_e^2}$
Tearing layer width (small- $\Delta'$ )	$l \simeq \Delta' \delta^2$
Times ( $t$ )	
Alfvén	$\tau_A(L) = L / v_A = L \sqrt{\mu_0 \rho} / B$
Resistive	$\tau_R(L) = \mu_0 L^2 / \eta$
Viscous	$\tau_V(L) = L^2 / \nu_\perp$
Electron collision	$\tau_e = 4 \epsilon_0^2 \sqrt{\pi^3 m_e k_B^3 T_e^3} / \sqrt{2} \Lambda q_i^2 q_e^2 n_i$
Ion collision	$\tau_i = 4 \epsilon_0^2 \sqrt{\pi^3 m_i k_B^3 T_i^3} / \Lambda q_i^4 n_i$

## Dimensionless parameters

---

Lundquist number	$S = \tau_R/\tau_A$
Prandtl number	$P_m = \mu_0\nu_\perp/\eta$
Hartmann number	$H = S/P_m = \sqrt{\tau_R\tau_V}/\tau_A$
Plasma $\beta$	$\beta = 2\mu_0p/B$
Cylindrical safety factor	$q(r) = rB_{z0}/R_0B_{\theta0}$
Parallel current	$a\lambda = a\mu_0\mathbf{J} \cdot \mathbf{B}/B^2$

Diffusivities ( $L^2/t$ )

---

Resistive	$\eta/\mu_0 = m_e/\mu_0n_e e^2\tau_e = d_e^2/\tau_e$
Perpendicular viscous	$\nu_\perp = 3k_B T_i/10m_i\tau_i\omega_{ci}^2 = 3v_{Ti}^2/10\tau_i\omega_{ci}^2$
Parallel viscous	$\nu_\parallel = 0.96\tau_i k_B T_i/m_i = 0.96v_{Ti}^2\tau_i$

Wavelengths ( $1/L$ )

---

Cylindrical wave-vector	$\mathbf{k} = \hat{\theta}m/r + \hat{z}n/R$
-------------------------	---

## B Definitions of notation

We use the following definitions of notation:

$$\begin{aligned}
A(r, \theta, \phi) &\equiv A_0(r) + \tilde{A}(r, \theta, \phi) \\
A_0(r) \equiv \langle A(r, \theta, \phi) \rangle &\equiv \frac{1}{(2\pi)^2} \int A(r, \theta, \phi) d\theta d\phi \\
\langle\langle A \rangle\rangle &\equiv \frac{(2\pi)^2}{V} \int \langle A(r, \theta, \phi) \rangle r dr = \frac{1}{V} \int A(r, \theta, \phi) dV \\
\tilde{A}(r, \theta, \phi) &\equiv \tilde{A}_0(r) + \sum_{n=1}^{\infty} \tilde{A}_{0,n}(r) e^{in\phi} + \tilde{A}_{0,n}^*(r) e^{-in\phi} \\
&\quad + \sum_{m=1}^{\infty} \sum_{n=-\infty}^{\infty} \tilde{A}_{m,n}(r) e^{im\theta+in\phi} + \tilde{A}_{m,n}^*(r) e^{-im\theta-in\phi} \\
\langle \tilde{A}(r, \theta, \phi) \rangle &\equiv \tilde{A}_0(r) \\
A_0(r, t) &\equiv A_{eq}(r) + \tilde{A}_0(r, t) \\
\hat{\mathbf{b}} &\equiv \mathbf{B}/|B| .
\end{aligned}$$

For linear cases with  $n \neq 0$ ,

$$A_0(r) = A_{eq}(r) . \tag{B.1}$$

## C Model equations

These are the equations that constitute the model:

$$\frac{\partial \mathbf{B}}{\partial t} = -\nabla \times \mathbf{E} , \quad (\text{C.1})$$

$$m_i n \frac{d\mathbf{v}}{dt} = \mathbf{J} \times \mathbf{B} - \nabla p - \nabla \cdot (\mathbf{\Pi}_{gv} + \mathbf{\Pi}_{\parallel}) - \nabla \cdot \nu m_i n \mathbf{W} , \quad (\text{C.2})$$

$$\frac{dn}{dt} = -n \nabla \cdot \mathbf{v} + D_n \nabla^2 n , \quad (\text{C.3})$$

and

$$\frac{n}{\Gamma - 1} \frac{dk_B T}{dt} = -p \nabla \cdot \mathbf{v} + \nabla \cdot \chi n \nabla k_B T . \quad (\text{C.4})$$

They are completed with the relations:

$$\mathbf{E} = -\mathbf{v} \times \mathbf{B} + \frac{\mathbf{J} \times \mathbf{B}}{ne} - \frac{\nabla p_e}{ne} + \eta \mathbf{J} + \frac{m_e}{ne^2} \frac{\partial \mathbf{J}}{\partial t} , \quad (\text{C.5})$$

$$\mu_0 \mathbf{J} = \nabla \times \mathbf{B} , \quad (\text{C.6})$$

$$\nabla \cdot \mathbf{B} = 0 , \quad (\text{C.7})$$

$$\mathbf{\Pi}_{gv} = \frac{m_i p_i}{4eB} \left[ \hat{\mathbf{b}} \times \mathbf{W} \cdot (\mathbf{I} + 3\hat{\mathbf{b}}\hat{\mathbf{b}}) - (\mathbf{I} + 3\hat{\mathbf{b}}\hat{\mathbf{b}}) \cdot \mathbf{W} \times \hat{\mathbf{b}} \right] , \quad (\text{C.8})$$

$$\mathbf{\Pi}_{\parallel} = -\frac{3}{2} m_i n \nu_{\parallel} \mathbf{b} \cdot \mathbf{W} \cdot \hat{\mathbf{b}} \left[ \hat{\mathbf{b}}\hat{\mathbf{b}} - \frac{\mathbf{I}}{3} \right] , \quad (\text{C.9})$$

and

$$\mathbf{W} = \nabla \mathbf{v} + \nabla \mathbf{v}^T - (2/3) \mathbf{I} \nabla \cdot \mathbf{v} . \quad (\text{C.10})$$

## D Parallel electric field assumptions

Considerable attention is devoted to the parallel electric field. This field has no contribution from  $\mathbf{v}_{e0} \times \mathbf{B}_0$  after the  $\hat{b}_0 \cdot$  operation. Using the generalized Ohm's law, Eqn. C.5, we may express the parallel electric field as

$$\langle E \rangle_{\parallel} = -\langle \tilde{\mathbf{v}} \times \tilde{\mathbf{B}} \rangle_{\parallel} + \hat{b}_0 \cdot \left\langle \frac{\mathbf{J} \times \mathbf{B}}{ne} \right\rangle - \hat{b}_0 \cdot \left\langle \frac{\nabla p_e}{ne} \right\rangle + \eta J_{0\parallel} + \frac{m_e}{ne^2} \frac{\partial J_{0\parallel}}{\partial t}. \quad (\text{D.1})$$

Contributions to the Hall and  $\nabla p_e$  terms proportional to  $\tilde{n}$  and from electron inertia are found to be small in our computations and may be neglected. Given  $\hat{b}_0 \cdot (\nabla p_{e0}/n_0e)$  vanishes, the mean parallel electric field to good approximation is

$$E_{0\parallel} \simeq -\langle \tilde{\mathbf{v}} \times \tilde{\mathbf{B}} \rangle_{\parallel} + \left\langle \frac{\tilde{\mathbf{J}} \times \tilde{\mathbf{B}}}{n_0e} \right\rangle_{\parallel} + \eta \mathbf{J}_{0\parallel}. \quad (\text{D.2})$$

## E Conservation laws

### E.1 Momentum

$$\begin{aligned}
\frac{\partial}{\partial t} \langle \langle m_i n \mathbf{v} \rangle \rangle &= \left\langle \left\langle m_i \mathbf{v} \frac{\partial n}{\partial t} + m_i n \frac{\partial \mathbf{v}}{\partial t} \right\rangle \right\rangle \\
&= - \int dV \left[ m_i \mathbf{v} (\nabla \cdot (n \mathbf{v})) + m_i n \left( \mathbf{v} \cdot \nabla \mathbf{v} - \frac{\nabla \times \mathbf{B}}{\mu_0} \times \mathbf{B} + \nabla p + \nabla \cdot \mathbf{\Pi} \right) \right] \\
&= - \int dV \nabla \cdot \left[ m_i n \mathbf{v} \mathbf{v} - \frac{\mathbf{B} \mathbf{B}}{\mu_0} + \left( \frac{B^2}{2\mu_0} + p \right) \mathbf{I} + \mathbf{\Pi} \right] \\
&= - \int d\mathbf{S} \cdot \left[ m_i n \mathbf{v} \mathbf{v} - \frac{\mathbf{B} \mathbf{B}}{\mu_0} + \left( \frac{B^2}{2\mu_0} + p \right) \mathbf{I} + \mathbf{\Pi} \right] \tag{E.1}
\end{aligned}$$

Applying the boundary conditions used in our computations (Sec. 9.3), we may write  $\frac{\partial}{\partial t} \langle \langle m_i n v_z \rangle \rangle = -\hat{z} \cdot \int d\mathbf{S} \cdot \mathbf{\Pi}$ . Thus total momentum is conserved up to viscous interaction with the wall.

### E.2 Magnetic energy density

$$\begin{aligned}
\frac{\partial}{\partial t} \frac{B^2}{2\mu_0} &= \frac{\mathbf{B} \cdot \partial \mathbf{B}}{\mu_0 \partial t} = - \frac{\mathbf{B} \cdot \nabla \times \mathbf{E}}{\mu_0} = - \left[ \nabla \cdot \left( \frac{\mathbf{E} \times \mathbf{B}}{\mu_0} \right) + \mathbf{E} \cdot \frac{\nabla \times \mathbf{B}}{\mu_0} \right] \\
&= - \left[ \nabla \cdot \left( \frac{\mathbf{E} \times \mathbf{B}}{\mu_0} \right) + \mathbf{E} \cdot \mathbf{J} + \epsilon_0 \mathbf{E} \cdot \frac{\partial \mathbf{E}}{\partial t} \right] \\
&\simeq - \left[ \nabla \cdot \left( \frac{\mathbf{E} \times \mathbf{B}}{\mu_0} \right) + \mathbf{E} \cdot \mathbf{J} \right] \tag{E.2}
\end{aligned}$$

where the approximation on the last line is equivalent to ignoring displacement current in Ampere's law.

### E.3 Kinetic energy density

$$\begin{aligned}
\frac{\partial}{\partial t} \left( \frac{\rho_i v_i^2}{2} + \frac{\rho_e v_e^2}{2} \right) &= \sum_{\alpha} \left( \rho_{\alpha} \mathbf{v}_{\alpha} \cdot \frac{\partial \mathbf{v}_{\alpha}}{\partial t} + \frac{\rho_{\alpha} v_{\alpha}^2}{2} \frac{\partial n_{\alpha}}{\partial t} \right) \\
&= \sum_{\alpha} \left[ -\nabla \cdot \left( \frac{\rho_{\alpha} v_{\alpha}^2}{2} \mathbf{v}_{\alpha} \right) - \mathbf{v}_{\alpha} \cdot (\nabla p_{\alpha} + \nabla \cdot \mathbf{\Pi}_{\alpha}) + n_{\alpha} q_{\alpha} \mathbf{v}_{\alpha} \cdot \mathbf{E} - n q_{\alpha} \mathbf{v}_{\alpha} \eta \mathbf{J} \right] \\
&\simeq -\nabla \cdot \left( \frac{m_i n v^2}{2} \mathbf{v} \right) - \mathbf{v} \cdot (\nabla p + \nabla \cdot \mathbf{\Pi}_i) + \frac{\mathbf{J}}{ne} \cdot \nabla p_e + \mathbf{E} \cdot \mathbf{J} - \eta \mathbf{J}^2 \tag{E.3}
\end{aligned}$$

$$= -\mathbf{v} \cdot \nabla p + \frac{\mathbf{J}}{ne} \cdot \nabla p_e + \mathbf{E} \cdot \mathbf{J} - \eta \mathbf{J}^2 + \mathbf{\Pi}_i : \nabla \mathbf{v} - \nabla \cdot \left( \frac{m_i n v^2}{2} \mathbf{v} + \mathbf{\Pi}_i \cdot \mathbf{v} \right) \tag{E.4}$$

where the we use  $n_e \simeq n_i \simeq n$ ,  $\mathbf{v}_i \simeq \mathbf{v}$ ,  $m_e \ll m_i$ , and  $\mathbf{v}_e \simeq \mathbf{v} - \mathbf{J}/ne$  on the third line. On the fourth line, the first two terms are exchanges with internal energy (As we shall see since we set  $p_i \simeq p_e \simeq p$ , such that the ion flow advection and compression determine  $p_e$ , the second term is a loss term), the third an exchange with magnetic energy, and the fourth and fifth are Ohmic and viscous dissipation. The last two terms are kinetic and viscous fluxes.

#### E.4 Internal energy density

$$\frac{1}{\Gamma-1} \frac{\partial p}{\partial t} = \frac{1}{\Gamma-1} \left[ k_B T \frac{\partial n}{\partial t} + n k_B \frac{\partial T}{\partial t} \right] \quad (\text{E.5})$$

$$= -\frac{k_B T}{\Gamma-1} [\nabla \cdot (n\mathbf{v}) - D_n \nabla^2 n] - \frac{n}{\Gamma-1} \mathbf{v} \cdot \nabla k_B T - p \nabla \cdot \mathbf{v} + \nabla \cdot \chi n \nabla k_B T \quad (\text{E.6})$$

$$= -\frac{1}{\Gamma-1} [\mathbf{v} \cdot \nabla p + \Gamma p \nabla \cdot \mathbf{v}] + \frac{k_B T D_n}{\Gamma-1} \nabla^2 n + \nabla \cdot \chi n \nabla k_B T \quad (\text{E.7})$$

$$= \mathbf{v} \cdot \nabla p - \frac{\Gamma}{\Gamma-1} \nabla \cdot (p\mathbf{v}) + \frac{k_B T D_n}{\Gamma-1} \nabla^2 n + \nabla \cdot \chi n \nabla k_B T \quad (\text{E.8})$$

If we instead use separate equations for  $p_e$  and  $p_i$ , the internal energy density becomes

$$\frac{1}{\Gamma-1} \left( \frac{\partial p_i}{\partial t} + \frac{\partial p_e}{\partial t} \right) = \mathbf{v} \cdot \nabla p - \frac{\mathbf{J}}{ne} \cdot \nabla p_e - \frac{\Gamma}{\Gamma-1} \nabla \cdot (p_i \mathbf{v}_i + p_e \mathbf{v}_e) + \frac{k_B T D_n}{\Gamma-1} \nabla^2 n + \nabla \cdot \chi n \nabla k_B T \quad (\text{E.9})$$

and we recover the  $\mathbf{J} \cdot \nabla p_e / ne$  term from the kinetic energy density. Additionally, if we include heating through  $Q_e$ , the viscous and Ohmic dissipation in kinetic energy density equation become electron heating terms.

Assuming the heating terms are included and a separate electron pressure equation is used, the total volume integrated energy is

$$\begin{aligned}
\frac{\partial}{\partial t} \left\langle \left\langle \frac{B^2}{2\mu_0} + \frac{\rho_i v_i^2}{2} + \frac{\rho_e v_e^2}{2} + \frac{1}{\Gamma-1} \frac{\partial p}{\partial t} \right\rangle \right\rangle &= - \int dV \nabla \cdot \left( \frac{\mathbf{E} \times \mathbf{B}}{\mu_0} + \frac{m_i n v^2}{2} \mathbf{v} + \mathbf{\Pi}_i \cdot \mathbf{v} + \frac{\Gamma p \mathbf{v}}{\Gamma-1} - \chi n \nabla k_B T \right) \\
&= - \int dS \cdot \left( \frac{\mathbf{E} \times \mathbf{B}}{\mu_0} + \frac{m_i n v^2}{2} \mathbf{v} + \mathbf{\Pi}_i \cdot \mathbf{v} + \frac{\Gamma}{\Gamma-1} p \mathbf{v} - \chi n \nabla k_B T \right) \\
&= \int dS \left( \frac{E_{loop} B_\theta}{\mu_0} + \chi n k_B \frac{\partial T}{\partial r} \right).
\end{aligned}$$

For the last line, we have applied our conducting-wall, no-slip boundary conditions, and assumed cylindrical geometry with a purely toroidal loop voltage. Energy enters the system through the loop voltage, and leaves through thermal losses to the wall. For our system the heating terms are not included, and when energy is dissipated through viscosity or resistivity, it leaves the system.

## F Gyroviscous Mathematica code

Our heuristic linear model considers the effect of nearly incompressible flows represented by a stream function,  $\tilde{\mathbf{v}} = \hat{\mathbf{b}} \times \nabla \tilde{\phi}$ , orders radial derivatives of  $\tilde{\phi}$  as  $\epsilon^{-1}$ , and makes Taylor expansions of the axisymmetric quantities in  $x = r - r_s$ , where  $|x|$  is of order  $\epsilon$ . All other quantities, including the wavenumber  $k$ , are of order  $\epsilon^0$ . Thus we may write

$$\hat{\mathbf{b}} \rightarrow \hat{\mathbf{b}}_s + x \hat{\mathbf{b}}'_s + \frac{1}{2} x^2 \hat{\mathbf{b}}''_s + \dots \quad (\text{F.1})$$

$$\mathbf{k} \rightarrow \mathbf{k}_s + x \mathbf{k}'_s + \frac{1}{2} x^2 \mathbf{k}''_s + \dots \quad (\text{F.2})$$

$$\frac{1}{r_s} \rightarrow \frac{1}{r_s} - \frac{x}{r_s^2} + \frac{x^2}{r_s^3} + \dots \quad (\text{F.3})$$

where the subscript  $s$  indicates evaluation at the resonant surface and  $k_{\parallel s} = \hat{\mathbf{b}}_s \cdot \mathbf{k}_s = 0$ .

The calculation of the parallel gyroviscous torque, described in Sec. 11.2, has been performed both by hand and with Mathematica. The Mathematica code is given here for reference. Comments are indicated as (\* Comment \*), input to Mathematica is bold, and output is in regular font.

## Begin Mathematica 7.0 code

```

<< VectorAnalysis`
SetCoordinates[Cylindrical[r,  $\theta$ , z]]
Cylindrical[r,  $\theta$ , z]

(* Define b_hat and k, expansion can be done later *)
b:={0, bp[r], bz[r]}
(* k includes the 1/r in kp implicitly through the 1/r in d/d $\phi$  terms, *)
(* thus the units of kz are 1/L and kp is dimensionless. *)
k:={0, kp, kz}
(* Perp direction *)
Perp:=Cross[b, {1, 0, 0}]
{0, bz[r], -bp[r]}
(* Define transform to kperp and kpar *)
KRules = {{kp  $\rightarrow$  r * (bp[r] * kpar[r] + bz[r] * kperp[r]), kz  $\rightarrow$  (kpar[r] * bz[r] - kperp[r] * bp[r])}};

(* Stream function representation for v. *)
stream:= $\phi$ [r] * Exp[I * k.{r,  $\theta$ , z}]
v = Cross[b, Grad[stream]];
(* Check v_r *)
Simplify[v[[1]] * Exp[-I * k.{r,  $\theta$ , z}]//.KRules]
{-i (bp[r]2 + bz[r]2) kperp[r] $\phi$ [r]}
(* Check v_perp *)
Simplify[Dot[Perp, v] * Exp[-I * k.{r,  $\theta$ , z}]//.KRules]
{(bp[r]2 + bz[r]2)  $\phi$ '[r]}

```

(\* Mathematica does not have a cylindrical  $\nabla$ (vector) operator built in. \*)

(\* We construct one, and the following is a quick check. \*)

vt:={vr[r] \* Exp[I \* k.{r,  $\theta$ , z}], vp[r] \* Exp[I \* k.{r,  $\theta$ , z}], vz[r] \* Exp[I \* k.{r,  $\theta$ , z]}}

TableForm[Simplify[(Transpose[{Grad[vt[[1]], Grad[vt[[2]],

Grad[vt[[3]]}] + {{0, 0, 0}, {-vt[[2]]/r, +vt[[1]]/r, 0}, {0, 0, 0}}) \* Exp[-I \* k.{r,  $\theta$ , z}]]]

$vr'[r]$	$vp'[r]$	$vz'[r]$
$-\frac{vp[r]-ikpvr[r]}{r}$	$\frac{ikpvp[r]+vr[r]}{r}$	$\frac{ikpvz[r]}{r}$
$ikzvvr[r]$	$ikzvp[r]$	$ikzvz[r]$

(\* Find the  $\nabla v$  tensor with the stream function representation. \*)

$\nabla v = \text{Transpose}[\{\text{Grad}[v[[1]], \text{Grad}[v[[2]], \text{Grad}[v[[3]]]\}] + \{0, 0, 0\}, \{-v[[2]]/r, v[[1]]/r, 0\}, \{0, 0, 0\}\};$

(\* Compute the rate of strain tensor  $W$ . \*)

$W = \nabla v + \text{Transpose}[\nabla v] - \text{IdentityMatrix}[3] * 2 * \text{Div}[v]/3;$

(\* Checks of  $W$  \*)

Simplify[Tr[W]]

0

$W == \text{Transpose}[W]$

True

(\* Compute  $bxW$  and  $Wxb$  \*)

$bxW = \text{Inner}[\text{Times}, \text{LeviCivitaTensor}[3], b, \text{Plus}, 2].W;$

$Wxb = W.\text{Transpose}[\text{Inner}[\text{Times}, \text{LeviCivitaTensor}[3], b, \text{Plus}, 3]];$

$\text{partPi1} = bxW.(\text{IdentityMatrix}[3] + 3 * \text{Outer}[\text{Times}, b, b]);$

$\text{partPi2} = (\text{IdentityMatrix}[3] + 3 * \text{Outer}[\text{Times}, b, b]).Wxb;$

(\* Use the transpose property in the gyroviscous  $\Pi$  as a check \*)

Simplify[Transpose[partPi1] + partPi2]

{{0, 0, 0}, {0, 0, 0}, {0, 0, 0}}

(\* Assemble the  $\Pi_{gv}$  tensor, here  $C[r]$  is the coefficient,  $p_{i0}/4\omega_{ci}$ . \*)

$$\Pi = C[r] * (\text{bxW} - \text{Wxb});$$

(\* Check that the gyroviscous  $\Pi$  is traceless \*)

$$\text{Simplify}[\text{Tr}[\Pi]]$$

0

(\* We define the cylindrical divergence of a tensor, and make a quick check \*)

$$\Pi_t := \text{Transpose}[\{\{\pi_{rr}[r], \pi_{pr}[r], \pi_{zr}[r]\}, \{\pi_{rp}[r], \pi_{pp}[r], \pi_{zp}[r]\}, \{\pi_{rz}[r], \pi_{pz}[r], \pi_{zz}[r]\}\} * \text{Exp}[I * k.\{r, \theta, z\}]]$$

(\* Check of the radial component \*)

$$\text{Simplify}[(\text{Div}[\text{Transpose}[\Pi_t][[1]]] - \Pi_t[[2, 2]]/r) * \text{Exp}[-I * k.\{r, \theta, z\}]]$$

$$\frac{-\pi_{pp}[r] + ik_p \pi_{pr}[r] + \pi_{rr}[r] + ik_{zr} \pi_{zr}[r] + r \pi_{rr}'[r]}{r}$$

(\* Check of the poloidal component \*)

$$\text{Simplify}[(\text{Div}[\text{Transpose}[\Pi_t][[2]]] + \Pi_t[[2, 1]]/r) * \text{Exp}[-I * k.\{r, \theta, z\}]]$$

$$\frac{ik_p \pi_{pp}[r] + \pi_{pr}[r] + \pi_{rp}[r] + ik_{zr} \pi_{zp}[r] + r \pi_{rp}'[r]}{r}$$

(\* Check of the axial component \*)

$$\text{Simplify}[(\text{Div}[\text{Transpose}[\Pi_t][[3]]]) * \text{Exp}[-I * k.\{r, \theta, z\}]]$$

$$\frac{ik_p \pi_{pz}[r] + \pi_{rz}[r] + ik_{zr} \pi_{zz}[r] + r \pi_{rz}'[r]}{r}$$

(\* Compute  $-\nabla \cdot \Pi$ . This is still the unreduced expression. \*)

$$\text{Div}\Pi = -\{\text{Div}[\text{Transpose}[\Pi][[1]]] - \Pi[[2, 2]]/r, \text{Div}[\text{Transpose}[\Pi][[2]]] + \Pi[[2, 1]]/r, \text{Div}[\text{Transpose}[\Pi][[3]]]\};$$

(\* We now expand  $\text{bp}[r]$ ,  $\text{bz}[r]$ ,  $C[r]$ ,  $\text{kperp}[r]$ ,  $\text{kpar}[r]$  and  $r$  by  $x = r - r_s$  where  $x \sim \epsilon \ll 1$ . \*)

$$\text{bpt}[x\_]:= \text{bp0} + \text{bp1} * x + \text{bp2}/2 * x^2 + O[\epsilon]^3$$

$$\text{bzt}[x\_]:= \text{bz0} + \text{bz1} * x + \text{bz2}/2 * x^2 + O[\epsilon]^3$$

$$\text{Ct}[x\_]:= \text{C0} + \text{C1} * x + \text{C2}/2 * x^2 + O[\epsilon]^3$$

$$\text{kperpt}[x\_]:= \text{kperp0} + \text{kperp1} * x + \text{kperp2}/2 * x^2 + O[\epsilon]^3$$

(\*  $\text{kpar0}=0$  by definition. \*)

$$\text{kpart}[x\_]:= \text{kpar1} * x + \text{kpar2}/2 * x^2 + O[\epsilon]^3$$

$$\text{invr}[x\_]:= 1/r_s - x/r_s^2 + x^2/r_s^3 + O[\epsilon]^3$$

```

TaylorExp = {{bp[r] → bpt[ε * x], bp'[r] → bpt'[ε * x], bp''[r] → bpt''[ε * x],
bz[r] → bzt[ε * x], bz'[r] → bzt'[ε * x], bz''[r] → bzt''[ε * x],
C[r] → Ct[ε * x], C'[r] → Ct'[ε * x], C''[r] → Ct''[ε * x],
kperp[r] → kperpt[ε * x], kperp'[r] → kperpt'[ε * x], kperp''[r] → kperpt''[ε * x],
kpar[r] → kpart[ε * x], kpar'[r] → kpart'[ε * x], kpar''[r] → kpart''[ε * x]}};
ROrdering = {{r → 1/rinv, rinv → invr[ε * x]}};
(* Rules for the ordering *)
PhiOrdering = {{φ[r] → φo, φ'[r] → dφo/ε, φ''[r] → ddφo/ε^2, φ'''[r] → dddφo/ε^3, φ''''[r] → ddddφo/ε^4}};
AllRules = Join[KRules, PhiOrdering, TaylorExp, ROrdering, 2];

```

(\* Use  $1 - b_z^2 + b_p^2 = d|b|/dr = 0$  to simplify. \*)

```
BRules = {{bz0 → Sqrt[1 - bp0^2], bz1 → -bp0 * bp1/bz0}};
```

(\* Apply the ordering to the radial force \*)

```
DivIIr = (Simplify[ε^3 * DivII[[1]] * Exp[-I * k.{r, θ, z}]]/.AllRules) + O[ε]^3;
radDivIIpoly = CoefficientList[DivIIr, ε];
```

(\* Radial  $O(\epsilon^{-3})$  gyroviscous force \*)

```
Simplify[radDivIIpoly[[1, 1]]/.BRules]
```

```
{2C0dddφo}
```

(\* Radial  $O(\epsilon^{-2})$  gyroviscous force \*)

```
Simplify[radDivIIpoly[[1, 2]]/.BRules]
```

```
{ $\frac{2(C0dddφo+C1rs(ddφo+dddφox))}{rs}$ }
```

(\* Apply the ordering to the perpendicular force \*)

```
DivIIp = (Simplify[ε^3 * ({0, bz0, -bp0}.DivII) * Exp[-I * k.{r, θ, z}]]/.AllRules) + O[ε]^3;
```

```
perpDivIIpoly = CoefficientList[DivIIp, ε];
```

(\* Perpendicular  $O(\epsilon^{-3})$  gyroviscous force \*)

```
Simplify[perpDivIIpoly[[1, 1]]/.BRules]
```

```
{0}
```

(\* Perpendicular  $O(\epsilon^{-2})$  gyroviscous force \*)

Simplify[perpDivIIpoly[[1, 2]]//.BRules]

{2iC0dd $\phi$ okperp0}

(\* Perpendicular  $O(\epsilon^{-1})$  gyroviscous force \*)

Simplify[perpDivIIpoly[[1, 3]]//.BRules]

$$\left\{ \frac{2i(C1kperp0rs(2d\phi o+dd\phi ox)+C0((1+bp0^2)d\phi okperp0+dd\phi okperp1rsx))}{rs} \right\}$$

(\* Apply the ordering to the parallel force \*)

DivII $t$  = (Simplify[ $\epsilon^3 * (b.DivII) * Exp[-I * k.\{r, \theta, z\}]$ ]//.AllRules) +  $O[\epsilon]^3$ ;

parDivIIpoly = CoefficientList[DivII $t$ ,  $\epsilon$ ];

(\* Parallel  $O(\epsilon^{-3})$  gyroviscous force \*)

Simplify[parDivIIpoly[[1, 1]]//.BRules]

{0}

(\* Parallel  $O(\epsilon^{-2})$  gyroviscous force \*)

Simplify[parDivIIpoly[[1, 2]]//.BRules]

{0}

(\* Compute the unreduced  $-\hat{b} \cdot \nabla \times \nabla \cdot \Pi_{gv}$ . \*)

ParCurlDivII = b.Curl[DivII];

(\* Apply the ordering. \*)

ParCurlDivII $t$  = (Simplify[ $\epsilon^3 * ParCurlDivII * Exp[-I * k.\{r, \theta, z\}]$ ]//.AllRules) +  $O[\epsilon]^2$ ;

ParCurlDivIIpoly = CoefficientList[ParCurlDivII $t$ ,  $\epsilon$ ];

(\*  $O(\epsilon^{-3})$  parallel gyroviscous torque \*)

Simplify[ParCurlDivIIpoly[[1, 1]]//.BRules]

{0}

(\*  $O(\epsilon^{-2})$  parallel gyroviscous torque \*)

Simplify[ParCurlDivIIpoly[[1, 2]]//.BRules]

$$\left\{ \frac{2idd\phi okperp0(bp0^2C0+2C1rs)}{rs} \right\}$$

## G Dynamo emf component derivation

Given a Fourier expansion of perturbed quantities in the poloidal and toroidal directions,

$$\begin{aligned} \tilde{A}(r, \theta, \phi) = \tilde{A}_0(r) + \sum_{n=1}^{\infty} \left( \tilde{A}_{0,n}(r) e^{in\phi} + \tilde{A}_{0,n}^*(r) e^{-in\phi} \right) \\ + \sum_{m=1}^{\infty} \sum_{n=-\infty}^{\infty} \left( \tilde{A}_{m,n}(r) e^{im\theta+in\phi} + \tilde{A}_{m,n}^*(r) e^{-im\theta-in\phi} \right) \end{aligned} \quad (\text{G.1})$$

where  $\phi = z/R$ , the flux surface average of the product of two fluctuating quantities  $\langle \tilde{A}\tilde{B} \rangle$  may be written in terms of the complex coefficients of the expansion as

$$\begin{aligned} \langle \tilde{A}\tilde{B} \rangle = \frac{1}{(2\pi)^2} \int \tilde{A}\tilde{B} d\theta d\phi = \tilde{A}_0\tilde{B}_0 + \sum_{n=1}^{\infty} \left( \tilde{A}_{0,n}^*\tilde{B}_{0,n} + \tilde{A}_{0,n}\tilde{B}_{0,n}^* \right) \\ + \sum_{m=1}^{\infty} \sum_{n=-\infty}^{\infty} \left( \tilde{A}_{m,n}^*\tilde{B}_{m,n} + \tilde{A}_{m,n}\tilde{B}_{m,n}^* \right). \end{aligned} \quad (\text{G.2})$$

Measurements of the dominant contribution to dynamo emf often involve a single set of mode numbers at a radial location. For example, in the core, the  $m = 1$ ,  $n = 6$  mode is typically dominant, and these are the mode numbers of the fluctuating quantities measured by Ding et al. We now assume the mode numbers are specified, drop the  $m, n$  subscript and define the operator

$$\langle \tilde{A}, \tilde{B} \rangle = \tilde{A}^*\tilde{B} + \tilde{A}\tilde{B}^* = 2\Re\tilde{A}\tilde{B} + 2\Im\tilde{A}\Im\tilde{B}. \quad (\text{G.3})$$

Thus mean-field contributions from a quadratic product are present if and only if both the perturbed coefficients with identical mode numbers are non-zero and not  $90^\circ$  out of phase in the complex plane. The  $\langle \cdot, \cdot \rangle$  operator has the following useful properties:

- $\langle i\tilde{A}, \tilde{A} \rangle = 0$
- $\langle \tilde{A}, \tilde{B} \rangle = \langle \tilde{B}, \tilde{A} \rangle$
- $\langle \tilde{A} + \tilde{B}, \tilde{C} \rangle = \langle \tilde{A}, \tilde{C} \rangle + \langle \tilde{B}, \tilde{C} \rangle$
- $\langle R\tilde{A}, \tilde{B} \rangle = \langle \tilde{A}, R\tilde{B} \rangle = R\langle \tilde{A}, \tilde{B} \rangle$  where  $R$  is a real number
- $\langle i\tilde{A}, \tilde{B} \rangle = -\langle \tilde{A}, i\tilde{B} \rangle$
- $\langle \partial\tilde{A}/\partial r, \tilde{B} \rangle + \langle \tilde{A}, \partial\tilde{B}/\partial r \rangle = \partial\langle \tilde{A}, \tilde{B} \rangle/\partial r$

We expand the Hall dynamo emf in terms of the poloidal and toroidal components similar to Ding et al. in Ref. [25], where the divergence of  $\mathbf{B}$  constraint,

$$\nabla \cdot \tilde{\mathbf{B}} = \frac{1}{r} \frac{\partial}{\partial r} (r \tilde{B}_r) + \frac{im}{r} \tilde{B}_\theta + \frac{in}{R} \tilde{B}_z = 0, \quad (\text{G.4})$$

is used extensively. Their derivation incorrectly assumes  $\langle i\tilde{A}, \tilde{B} \rangle = \langle \tilde{A}, i\tilde{B} \rangle$ ,  $\langle i\tilde{A}', \tilde{A} \rangle = \langle i\tilde{A}'', \tilde{A} \rangle = 0$ , and has an arithmetic mistake, all of which are corrected here. This expansion yields

$$\begin{aligned} \mu_0 \langle \tilde{\mathbf{J}} \times \tilde{\mathbf{B}} \rangle_\theta &= \mu_0 \langle \tilde{J}_\phi, \tilde{B}_r \rangle - \mu_0 \langle \tilde{J}_r, \tilde{B}_z \rangle \\ &= \left\langle \frac{1}{r} \frac{\partial}{\partial r} (r \tilde{B}_\theta) - \frac{im}{r} \tilde{B}_r, \tilde{B}_r \right\rangle - \left\langle \frac{im}{r} \tilde{B}_z - \frac{in}{R} \tilde{B}_\theta, \tilde{B}_z \right\rangle \\ &= \left\langle \frac{1}{r} \frac{\partial}{\partial r} (r \tilde{B}_\theta), \tilde{B}_r \right\rangle + \left\langle \frac{in}{R} \tilde{B}_\theta, \tilde{B}_z \right\rangle \\ &= \left\langle \tilde{B}_r, \frac{1}{r} \frac{\partial}{\partial r} (r \tilde{B}_\theta) \right\rangle - \left\langle \tilde{B}_\theta, \frac{in}{R} \tilde{B}_z \right\rangle \\ &= \left\langle \tilde{B}_r, \frac{1}{r} \frac{\partial}{\partial r} (r \tilde{B}_\theta) \right\rangle + \left\langle \tilde{B}_\theta, \frac{1}{r} \frac{\partial}{\partial r} (r \tilde{B}_r) \right\rangle \\ &= \left( \frac{2}{r} + \frac{\partial}{\partial r} \right) \langle \tilde{B}_r, \tilde{B}_\theta \rangle, \end{aligned} \quad (\text{G.5})$$

which agrees with the expression in Ref. [16], and

$$\begin{aligned} \mu_0 \langle \tilde{\mathbf{J}} \times \tilde{\mathbf{B}} \rangle_z &= \mu_0 \langle \tilde{J}_r, \tilde{B}_\theta \rangle - \mu_0 \langle \tilde{J}_\theta, \tilde{B}_r \rangle \\ &= \left\langle \frac{im}{r} \tilde{B}_z - \frac{in}{R} \tilde{B}_\theta, \tilde{B}_\theta \right\rangle - \left\langle \frac{in}{R} \tilde{B}_r - \tilde{B}'_z, \tilde{B}_r \right\rangle \\ &= \left\langle \frac{im}{r} \frac{R}{in} \left( -\frac{1}{r} \frac{\partial}{\partial r} (r \tilde{B}_r) \right), \tilde{B}_\theta \right\rangle - \left\langle \frac{R}{in} \frac{\partial}{\partial r} \left( \frac{1}{r} \frac{\partial}{\partial r} (r \tilde{B}_r) + \frac{im}{r} \tilde{B}_\theta \right), \tilde{B}_r \right\rangle \\ &= -\frac{Rm}{rn} \left\langle \frac{1}{r} \frac{\partial}{\partial r} (r \tilde{B}_r), \tilde{B}_\theta \right\rangle + \frac{R}{n} \left\langle i \frac{\partial}{\partial r} \left( \frac{1}{r} \frac{\partial}{\partial r} (r \tilde{B}_r) \right), \tilde{B}_r \right\rangle - \frac{Rm}{n} \left\langle \frac{\partial}{\partial r} \left( \frac{\tilde{B}_\theta}{r} \right), \tilde{B}_r \right\rangle \\ &= -\frac{Rm}{rn} \left( \left\langle \frac{1}{r} \frac{\partial}{\partial r} (r \tilde{B}_r), \tilde{B}_\theta \right\rangle + \left\langle \frac{1}{r} \frac{\partial}{\partial r} (r \tilde{B}_\theta), \tilde{B}_r \right\rangle - \frac{2}{r} \langle \tilde{B}_\theta, \tilde{B}_r \rangle \right) \\ &\quad + \frac{R}{n} \left\langle i \left( \frac{\tilde{B}'_r}{r} + \tilde{B}''_r \right), \tilde{B}_r \right\rangle \\ &= -\frac{Rm}{rn} \frac{\partial}{\partial r} \langle \tilde{B}_r, \tilde{B}_\theta \rangle + \frac{R}{n} \left( \left\langle \frac{i \tilde{B}'_r}{r}, \tilde{B}_r \right\rangle + \langle i \tilde{B}''_r, \tilde{B}_r \rangle \right). \end{aligned} \quad (\text{G.6})$$

As the parallel component is of particular interest, we project these components to find

$$\begin{aligned} \mu_0 \langle \tilde{\mathbf{J}} \times \tilde{\mathbf{B}} \rangle_{\parallel} &= \frac{B_{0\theta}}{B_0} \mu_0 \langle \tilde{\mathbf{J}} \times \tilde{\mathbf{B}} \rangle_{\theta} + \frac{B_{0z}}{B_0} \mu_0 \langle \tilde{\mathbf{J}} \times \tilde{\mathbf{B}} \rangle_z \\ &= \frac{B_{0\theta}}{B_0} \left[ \frac{2}{r} + \left( 1 - \frac{B_{0z} R m}{B_{0\theta} r n} \right) \frac{\partial}{\partial r} \right] \langle \tilde{B}_r, \tilde{B}_{\theta} \rangle + \frac{B_{0z} R}{B_0 n} \left\langle \frac{i}{r} \frac{\partial}{\partial r} (r \tilde{B}'_r), \tilde{B}_r \right\rangle. \quad (\text{G.7}) \end{aligned}$$

Alternatively, the axial Hall dynamo contribution may be more conveniently written in terms of  $\tilde{B}_z$  instead of  $\tilde{B}_{\theta}$ , as this formulation avoids contributions from  $\tilde{B}'_r$ :

$$\begin{aligned} \mu_0 \langle \tilde{\mathbf{J}} \times \tilde{\mathbf{B}} \rangle_z &= \mu_0 \langle \tilde{J}_r, \tilde{B}_{\theta} \rangle - \mu_0 \langle \tilde{J}_{\theta}, \tilde{B}_r \rangle \\ &= \left\langle \frac{i m}{r} \tilde{B}_z - \frac{i n}{R} \tilde{B}_{\theta}, \tilde{B}_{\theta} \right\rangle - \left\langle \frac{i n}{R} \tilde{B}_r - \tilde{B}'_z, \tilde{B}_r \right\rangle \\ &= \left\langle \frac{i m}{r} \tilde{B}_z, -\frac{r}{i m} \left( \frac{i n}{R} \tilde{B}_z + \frac{1}{r} \frac{\partial}{\partial r} (r \tilde{B}_r) \right) \right\rangle + \langle \tilde{B}'_z, \tilde{B}_r \rangle \\ &= \left\langle \tilde{B}_z, \frac{1}{r} \frac{\partial}{\partial r} (r \tilde{B}_r) \right\rangle + \langle \tilde{B}'_z, \tilde{B}_r \rangle \\ &= \left( \frac{1}{r} + \frac{\partial}{\partial r} \right) \langle \tilde{B}_r, \tilde{B}_z \rangle. \end{aligned}$$

## H Supplemental multi-helicity plots

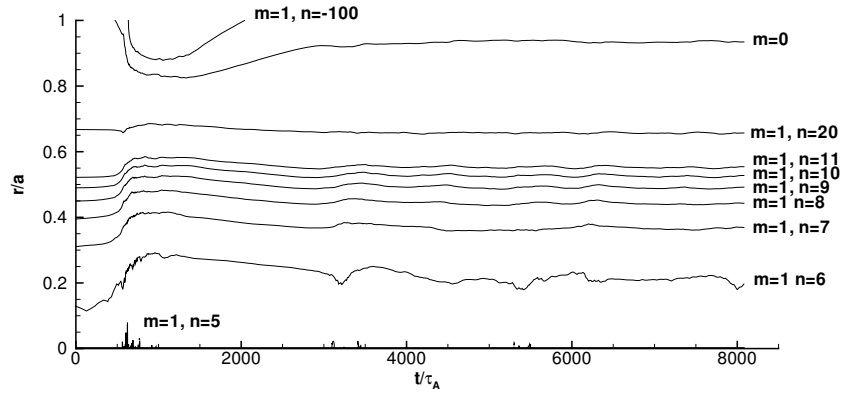


Figure 56: Rational surface location by mode versus time for our two-fluid computation.

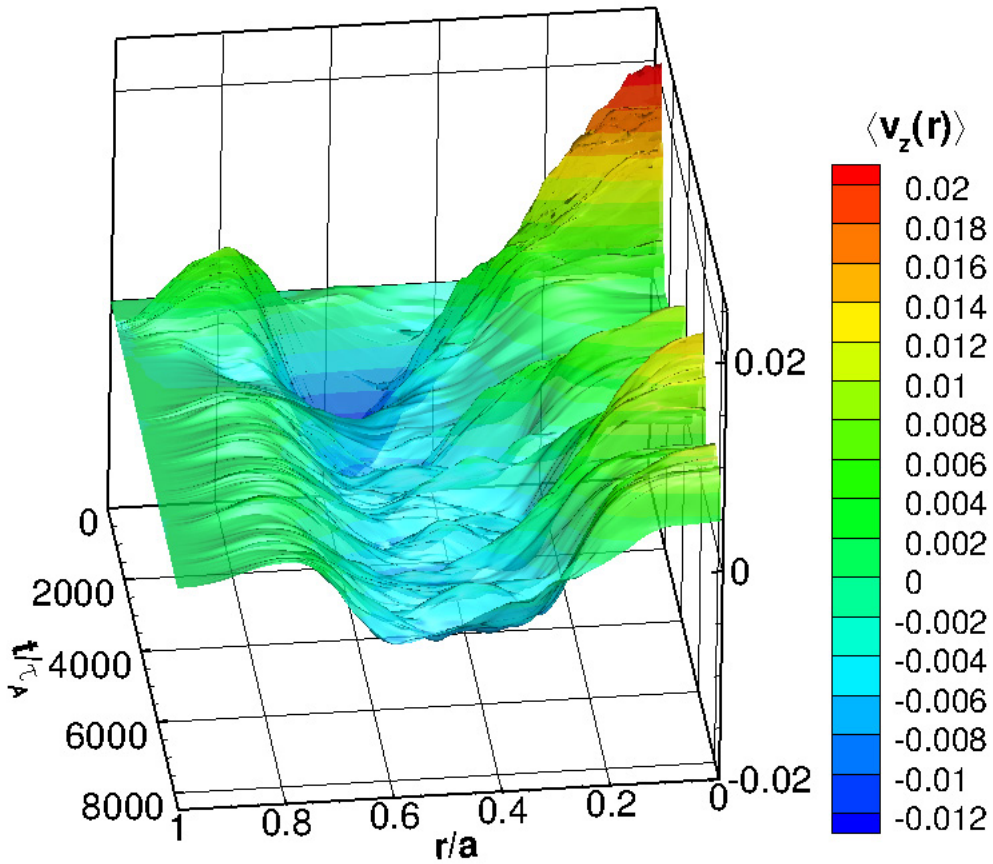


Figure 57: Mean axial flow speed as a function of time and radius for the two-fluid computation.

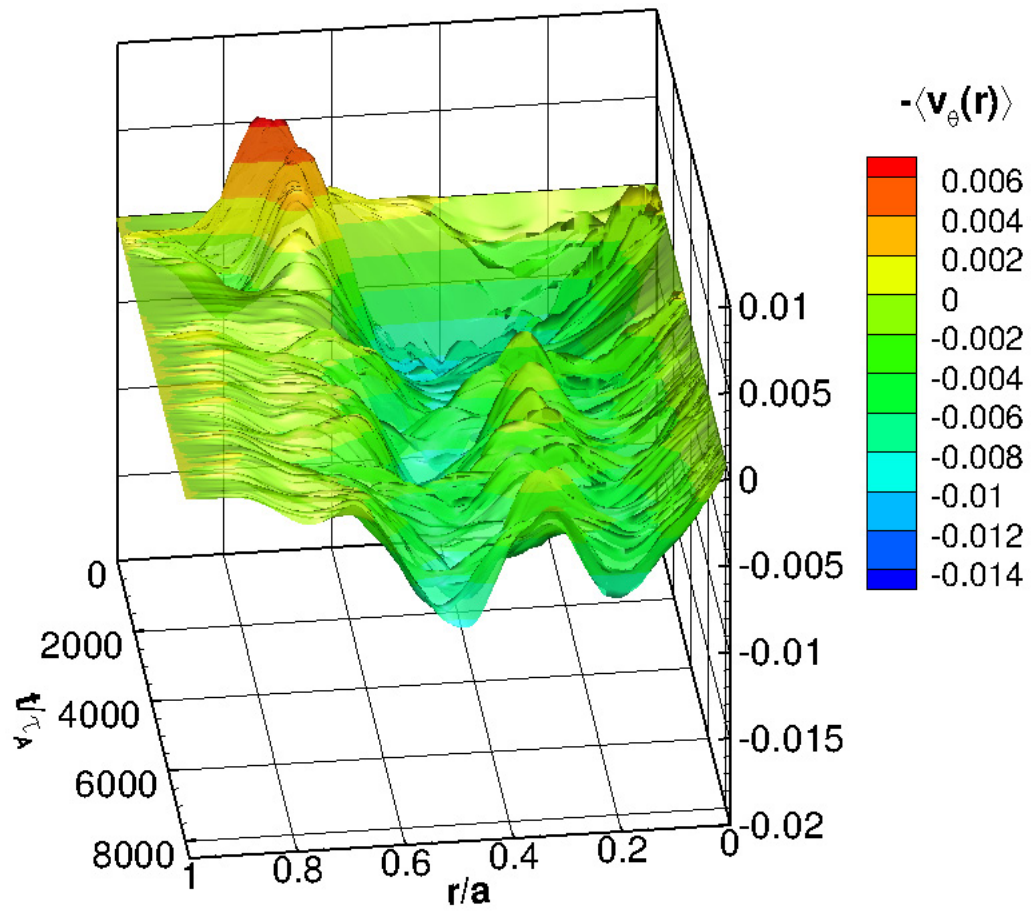


Figure 58: Mean poloidal flow speed as a function of time and radius for the two-fluid computation.

## I References

- [1] R D Hazeltine and J D Meiss. *Plasma Confinement*. Dover, 2003.
- [2] D D Schnack. *Lectures in Magnetohydrodynamics*. Springer, 2009.
- [3] T J M Boyd and J J Sanderson. *The Physics of Plasmas*. Cambridge University Press, 2003.
- [4] J D Lawson. Some criteria for a power producing thermonuclear reactor. *Proceedings of the Physical Society. Section B*, 70(1):6, 1957.
- [5] J B Taylor. *Bundle divertors and topology*. Technical Report CLM-R 132, Culham Laboratory, 1974.
- [6] Jr. Lyman Spitzer. The stellarator concept. *Physics of Fluids*, 1(4):253–264, 1958.
- [7] V D Shafranov. *Review of Plasma Physics*, volume 2. Consultants Bureau, New York, 1966.
- [8] Harold Grad. Toroidal containment of a plasma. *Physics of Fluids*, 10(1):137–154, 1967.
- [9] E. C. Howell and C. R. Sovinec. NIMEQ: MHD Equilibrium Solver for NIMROD. *APS Meeting Abstracts*, November 2008.
- [10] H P Furth, J Killeen, and M N Rosenbluth. Finite-resistivity instabilities of a sheet pinch. *Phys. Fluids*, 6:459, 1963.
- [11] S I Braginskii. *Transport Properties in a Plasma in Review of Plasma Physics*, volume 1. Consultants Bureau, New York, 1965.
- [12] Peter J. Catto and Andrei N. Simakov. A drift ordered short mean free path description for magnetized plasma allowing strong spatial anisotropy. *Physics of Plasmas*, 11(1):90–102, 2004.
- [13] A N Kaufman. Plasma viscosity in a magnetic field. *Phys. Fluids*, 3(4):610, 1960.
- [14] V. V. Mirnov, C. C. Hegna, and S. C. Prager. Two-fluid tearing instability in force-free magnetic configuration. *Physics of Plasmas*, 11(9):4468–4482, 2004.
- [15] R N Dexter, D W Kerst, T W Lovell, S C Prager, and J C Sprott. The madison symmetric torus. *Fusion Technol.*, 19:131, 1991.
- [16] A Kuritsyn, G Fiksel, A F Almagri, D L Brower, W X Ding, M C Miller, V V Mirnov, S C Prager, and J S Sarff. Measurements of the momentum and current transport from tearing instability in the madison symmetric torus reversed-field pinch. *Phys. Plasmas*, 16:055903, 2009.

- [17] D A Ennis, D Craig, S Gangadhara, J K Anderson, D J Den Hartog, F Ebrahimi, G Fiksel, and S C Prager. Local measurements of tearing mode flows and the magnetohydrodynamic dynamo in the madison symmetric torus reversed-field pinch. *Phys. Plasmas*, 17:082102, 2010.
- [18] D C Robinson. Tearing-mode-stable diffuse-pinch configurations. *Nucl. Fusion*, 18:939, 1978.
- [19] J. A. Holmes, B. A. Carreras, P. H. Diamond, and V. E. Lynch. Nonlinear dynamics of tearing modes in the reversed field pinch. *Physics of Fluids*, 31(5):1166–1179, 1988.
- [20] Y L Ho and G G Craddock. Nonlinear dynamics of field maintenance and quasiperiodic relaxation in reversed-field pinches. *Phys. Fluids*, 3(3):030721, 1991.
- [21] H K Moffatt. *Magnetic Field Generation in Electrically Conducting Fluids*. Cambridge University Press, 1978.
- [22] D. D. Schnack, E. J. Caramana, and R. A. Nebel. Three-dimensional magnetohydrodynamic studies of the reversed-field pinch. *Physics of Fluids*, 28(1):321–333, 1985.
- [23] V V Mirnov, C C Hegna, and S C Prager. A hall dynamo effect driven by two-fluid tearing instability. *Plasma Phys. Rep.*, 29(7):566, 2003.
- [24] R A Nebel. In S Ortoloni and E Sindoni, editors, *Proceedings of the Physics of Alternative Magnetic Confinement Schemes*, page 611. Societa Italiana di Fisica, Editrice Compositori, Bologna, Italy, 1991.
- [25] W. X. Ding, D. L. Brower, B. H. Deng, A. F. Almagri, D. Craig, G. Fiksel, V. Mirnov, S. C. Prager, J. S. Sarff, and V. Svidzinski. The hall dynamo effect and nonlinear mode coupling during sawtooth magnetic reconnection. *Physics of Plasmas*, 13(11):112306, 2006.
- [26] L Woltjer. A theorem on force-free magnetic fields. *P. Natl. Acad. Sci.*, 44(6):489, 1958.
- [27] L Woltjer. Hydromagnetic equilibrium ii. stability in the variational formulation. *P. Natl. Acad. Sci.*, 45(6):769, 1959.
- [28] M. D. Kruskal and R. M. Kulsrud. Equilibrium of a magnetically confined plasma in a toroid. *Physics of Fluids*, 1(4):265–274, 1958.
- [29] J. B. Taylor. Relaxation and magnetic reconnection in plasmas. *Rev. Mod. Phys.*, 58(3):741–763, Jul 1986.

- [30] H. Ji, S. C. Prager, and J. S. Sarff. Conservation of magnetic helicity during plasma relaxation. *Phys. Rev. Lett.*, 74(15):2945–2948, Apr 1995.
- [31] L. Turner. Hall effects on magnetic relaxation. *IEEE T. Plasma Sci.*, 14(6):849–857, 1986.
- [32] L. C. Steinhauer and A. Ishida. Relaxation of a two-specie magnetofluid. *Phys. Rev. Lett.*, 79(18):3423–3426, Nov 1997.
- [33] C. C. Hegna. Self-consistent mean-field forces in turbulent plasmas: Current and momentum relaxation. *Physics of Plasmas*, 5(6):2257–2263, 1998.
- [34] L. C. Steinhauer and A. Ishida. Relaxation of a two-species magnetofluid and application to finite-beta flowing plasmas. *Physics of Plasmas*, 5(7):2609–2622, 1998.
- [35] S. M. Mahajan and Z. Yoshida. Double curl beltrami flow: Diamagnetic structures. *Phys. Rev. Lett.*, 81(22):4863–4866, Nov 1998.
- [36] Shuichi Ohsaki and Zensho Yoshida. Variational principle with singular perturbation of hall magneto-hydrodynamics. *Physics of Plasmas*, 12(6):064505, 2005.
- [37] W. X. Ding, D. L. Brower, D. Craig, B. H. Deng, G. Fiksel, V. Mirnov, S. C. Prager, J. S. Sarff, and V. Svidzinski. Measurement of the hall dynamo effect during magnetic reconnection in a high-temperature plasma. *Phys. Rev. Lett.*, 93(4):045002, Jul 2004.
- [38] W. A. Newcomb. Hydromagnetic stability of a diffuse linear pinch. *Annals of Physics*, 10(2):232 – 267, 1960.
- [39] B. Coppi, J. M. Greene, and J. L. Johnson. Resistive instabilities in a diffuse linear pinch. *Nuclear Fusion*, 6(2):101, 1966.
- [40] S. Choi, D. Craig, F. Ebrahimi, and S. C. Prager. Cause of sudden magnetic reconnection in a laboratory plasma. *Phys. Rev. Lett.*, 96(14):145004, Apr 2006.
- [41] T. D. Tharp, A. F. Almagri, M. C. Miller, V. V. Mirnov, S. C. Prager, J. S. Sarff, and C. C. Kim. Measurements of impulsive reconnection driven by nonlinear hall dynamics. *Physics of Plasmas*, 17(12):120701, 2010.
- [42] Bruno Coppi. Influence of gyration radius and collisions on hydromagnetic stability. *Physics of Fluids*, 7(9):1501–1516, 1964.

- [43] D. Biskamp. Drift-tearing modes in a tokamak plasma. *Nuclear Fusion*, 18(8):1059, 1978.
- [44] S. C. Cowley, R. M. Kulsrud, and T. S. Hahm. Linear stability of tearing modes. *Physics of Fluids*, 29(10):3230–3244, 1986.
- [45] D. Grasso, M. Ottaviani, and F. Porcelli. Linear stability and mode structure of drift tearing modes. *Physics of Plasmas*, 8(10):4306–4317, 2001.
- [46] J. F. Drake and Y. C. Lee. Kinetic theory of tearing instabilities. *Physics of Fluids*, 20(8):1341–1353, 1977.
- [47] L. Zakharov and B. Rogers. Two-fluid magnetohydrodynamic description of the internal kink mode in tokamaks. *Physics of Fluids B: Plasma Physics*, 4(10):3285–3301, 1992.
- [48] B. N. Rogers, R. E. Denton, J. F. Drake, and M. A. Shay. Role of dispersive waves in collisionless magnetic reconnection. *Phys. Rev. Lett.*, 87(19):195004, Oct 2001.
- [49] Eduardo Ahedo and Jesus J Ramos. Parametric analysis of the two-fluid tearing instability. *Plasma Physics and Controlled Fusion*, 51(5):055018, 2009.
- [50] P. H. Rutherford. Nonlinear growth of the tearing mode. *Physics of Fluids*, 16(11):1903–1908, 1973.
- [51] N. Arcis, D. F. Escande, and M. Ottaviani. Rigorous approach to the nonlinear saturation of the tearing mode in cylindrical and slab geometry. *Physics of Plasmas*, 13(5):052305, 2006.
- [52] N. Arcis, D. F. Escande, and M. Ottaviani. Saturation of a tearing mode in zero-beta full magnetohydrodynamics. *Physics of Plasmas*, 14(3):032308, 2007.
- [53] D. Biskamp. Non-linear quenching of diamagnetic and gyroviscous effects in tearing modes. *Nuclear Fusion*, 19(6):777, 1979.
- [54] D. A. Monticello and R. B. White. Nonlinear drift tearing modes. *Physics of Fluids*, 23(2):366–371, 1980.
- [55] R. D. Hazeltine and H. R. Strauss. Tokamak heat transport due to tearing modes. *Phys. Rev. Lett.*, 37(2):102–104, Jul 1976.
- [56] Bruce D. Scott, A. B. Hassam, and J. F. Drake. Nonlinear evolution of drift-tearing modes. *Physics of Fluids*, 28(1):275–277, 1985.

- [57] Bruce D. Scott, J. F. Drake, and A. B. Hassam. Nonlinear stability of drift-tearing modes. *Phys. Rev. Lett.*, 54(10):1027–1030, Mar 1985.
- [58] J. F. Drake, Jr. T. M. Antonsen, A. B. Hassam, and N. T. Gladd. Stabilization of the tearing mode in high-temperature plasma. *Physics of Fluids*, 26(9):2509–2528, 1983.
- [59] Bruce D. Scott and A. B. Hassam. Analytical theory of nonlinear drift-tearing mode stability. *Physics of Fluids*, 30(1):90–101, 1987.
- [60] M. Kotschenreuther, R. D. Hazeltine, and P. J. Morrison. Nonlinear dynamics of magnetic islands with curvature and pressure. *Physics of Fluids*, 28(1):294–302, 1985.
- [61] J. R. King, C. R. Sovinec, and V. V. Mirnov. First-order finite-larmor-radius effects on magnetic tearing in pinch configurations. *Physics of Plasmas*, 18(4):042303, 2011.
- [62] C.R. Sovinec, A.H. Glasser, T.A. Gianakon, D.C. Barnes, R.A. Nebel, S.E. Kruger, S.J. Plimpton, A. Tarditi, M.S. Chu, and the NIMROD Team. Nonlinear magnetohydrodynamics with high-order finite elements. *J. Comp. Phys.*, 195:355, 2004.
- [63] W G Strang and G J Fix. *Analysis of the Finite Elements Method (Prentice-Hall Series in Automatic Computation)*. Prentice Hall, 1973.
- [64] M. O. Deville, P. F. Fischer, and E. H. Mund. *High-Order Methods for Incompressible Fluid Flow (Cambridge Monographs on Applied and Computational Mathematics)*. Cambridge University Press, 2002.
- [65] C R Sovinec, D D Schnack, A Y Pankin, D P Brennan, H Tian, D C Barnes, S E Kruger, E D Held, C C Kim, X S Li, D K Kaushik, S C Jardin, and the NIMROD Team. Nonlinear extended magnetohydrodynamics simulation using high-order finite elements. *Journal of Physics: Conference Series*, 16(1):25, 2005.
- [66] C.R. Sovinec and J.R. King. Analysis of a mixed semi-implicit/implicit algorithm for low-frequency two-fluid plasma modeling. *Journal of Computational Physics*, 229(16):5803 – 5819, 2010.
- [67] Y. Saad. *Iterative Methods for Sparse Linear Systems, Second Edition*. Society for Industrial and Applied Mathematics, 2003.

- [68] Xiaoye S. Li and James W. Demmel. Superlu-dist: A scalable distributed-memory sparse direct solver for unsymmetric linear systems. *ACM Transactions on Mathematical Software*, 29(2):110–140, June 2003.
- [69] R Courant, K O Friedrichs, and H Lewy. *Math. Ann.*, 100:32, 1928.
- [70] P. Zhu, D. D. Schnack, F. Ebrahimi, E. G. Zweibel, M. Suzuki, C. C. Hegna, and C. R. Sovinec. Absence of complete finite-larmor-radius stabilization in extended mhd. *Phys. Rev. Lett.*, 101(8):085005, Aug 2008.
- [71] J. F. Drake and Y. C. Lee. Nonlinear evolution of collisionless and semicollisional tearing modes. *Phys. Rev. Lett.*, 39(8):453–456, Aug 1977.
- [72] V.V. Mirnov, C.C. Hegna, S.C. Prager, C.R. Sovinec, and H. Tian. Two fluid dynamo and edge-resonant  $m=0$  tearing instability in reversed field pinch. *Proc. of the 21st IAEA Conf.*, TH/P3-18, 2006.
- [73] D. Bonfiglio, S. Cappello, and D. F. Escande. Dominant electrostatic nature of the reversed field pinch dynamo. *Phys. Rev. Lett.*, 94(14):145001, Apr 2005.
- [74] S. Cappello, D. Bonfiglio, and D. F. Escande. Magnetohydrodynamic dynamo in reversed field pinch plasmas: Electrostatic drift nature of the dynamo velocity field. 13(5):056102, 2006.
- [75] J.S. Sarff, A.F. Almagri, J.K. Anderson, T.M. Biewer, A.P. Blair, M. Cengher, B.E. Chapman, P.K. Chattopadhyay, D. Craig, D.J. Den Hartog, F. Ebrahimi, G. Fiksel, C.B. Forest, J.A. Goetz, D. Holly, B. Hudson, T.W. Lovell, K.J. McCollam, P.D. Nonn, R. O’Connell, S.P. Oliva, S.C. Prager, J.C. Reardon, M.A. Thomas, M.D. Wyman, D.L. Brower, W.X. Ding, S.D. Terry, M.D. Carter, V.I. Davydenko, A.A. Ivanov, R.W. Harvey, R.I. Pinsker, and C. Xiao. Tokamak-like confinement at a high beta and low toroidal field in the mst reversed field pinch. *Nuclear Fusion*, 43(12):1684, 2003.
- [76] P. Martin, L. Marrelli, G. Spizzo, P. Franz, P. Piovesan, I. Predebon, T. Bolzonella, S. Cappello, A. Cravotta, D.F. Escande, L. Frassinetti, S. Ortolani, R. Paccagnella, D. Terranova, the RFX team, B.E. Chapman, D. Craig, S.C. Prager, J.S. Sarff, the MST team, P. Brunzell, J.-A. Malmberg, J. Drake, the EXTRAP T2R team, Y. Yagi, H. Koguchi, Y. Hirano, the TPE-RX team, R.B. White, C. Sovinec, C. Xiao, R.A. Nebel, and D.D. Schnack. Overview of quasi-single helicity experiments in reversed field pinches. *Nuclear Fusion*, 43(12):1855, 2003.